Ministero dell'Istruzione, dell'Università
e della Ricerca

Università degli Studi
di Palermo

Innovative smart materials designed for environmental purposes

Ph.D. Thesis

Giuseppe Cavallaro

PhD Degree in Chemical Sciences – XXIV Course

2011 – 2013

TABLE OF CONTENTS

Preface

This Ph.D. thesis entitled “Innovative smart materials designed for environmental purposes” was initiated in January 2011 and finalized in December 2013. The study was almost carried out at University of Palermo (Department of Chemistry and, successively, Department of Physics and Chemistry), and some experiments were done at the Institute of Micromanifacturing of the Louisiana Tech University (USA) during a scientific stage of 6 months.

The thesis reports fundamental physico-chemical insights on composite materials based on environmental friendly resources, such as nanoclays and biopolymers. Particular attention was focused on Halloysite nanotubes (HNTs). In detail, the thesis includes eight chapters. The first one summarizes the properties and the current applications of green materials (nanoclays, biopolymers and their composites). Chapter 2 reports the physico-chemical studies of biopolymer/laponite systems in aqueous phase describing the structural and the thermodynamic features that influence the interactions between the two components. Chapters 3 and 4 are dedicated on the physico-chemical characterization of functionalized HNTs and hybrid gel beads, respectively. Experiments on the potential applications (decontamination and biotechnology) of these materials are reported in the Chapter 5. Physico-chemical studies of bionanocomposites based on nanoclays are described in the Chapter 6 in order to evaluate the effectiveness as biocompatible packaging by correlating the macroscopic properties to the microscopic ones. The physico-chemical characterization of plasticized nanocomposite films, reported in the Chapter 7, was done with the motivation to estimate their performances in material science. Lastly, Chapter 8 outlines the most important insights provided by this thesis.

The experiments performed at Louisiana Tech University concern the studies of functionalized HNTs for biotechnological and micromanifacturing purposes. The functionalization of HNTs with biopolymers was done also at Louisiana Tech University. Small Angle Neutron Scattering (SANS) experiments were carried out at ILL in Grenoble and at BENSC in Berlin.

The details on the experimental data and on the used equipments were omitted but they can be found in the attached related papers (Chapter 10).

Acknowledgements

I would like to thank all the people who assisted me during the PhD period. In particular, I am grateful to prof. A. Gianguzza and dr. G. Lazzara who supervised me at University of Palermo. I thank prof. Milioto who gave me the opportunity to work in her laboratories. I am grateful to prof. Y. Lvov who supervised me at Louisiana Tech University and for the stimulating discussions on the perspective of halloysite. I gratefully acknowledge dr. S. Prevost and dr. I. Grillo for the assistance in performing SANS experiments and prof. M. Gradzielski who helped me in the analysis of SANS data.

1. Green materials

1.1 Introduction

The gradual environmental degradation of the earth is mainly due to the excessive and irresponsible exploitation of the natural available resources. To the light of this situation, nowadays there is a simultaneous and growing interest in developing new materials and innovative process technologies that can reduce the environmental impact on the ecosystems.

Specifically, the researchers have focused their attention on renewable and no toxic natural resources to face key environmental problems, like the accumulation of urban wastes and water pollution. Among the natural resources, biopolymers and nanoclays appear really promising.

As far as the accumulation of the urban wastes is concerned, the principal cause is the wide use of petroleum based plastics generating a relevant environmental impact because of their non degradability. Moreover, the disposal of plastic wastes by incineration increases carbon dioxide amount and, in some cases, generates toxic products which contribute to the global warming and the city pollution. Biodegradable materials can provide a solution to the environmental impact of solid waste produced from fossil fuel. Within this topic, for instance, biopolymers, forming films, may be used in wrapping and packaging materials. Nevertheless, their use is often limited because of fast degradation and, in some cases, of unsatisfactory mechanical properties.[1]The combination of biopolymeric matrix and nanoclays may generate new sustainable materials, so called bionanocomposites, with excellent and unique properties.[2]

Futhermore, both biopolymers and nanoclays can be used as adsorbent materials of organic and inorganic contaminants. Therefore, they represent a cheap alternative to the activated carbon as waste-water decontaminants. Biopolymers as well as gel beads composed of polymers or polymer mixtures with sequestrant capabilities were proposed to capture contaminants from the aqueous phase.[3,4]

The high specific surface makes the nanoclays very efficient to remove pollutant from water.[5] Advancements have been reached on the use of organo-clays as sorbents to remediate organic contamination.[6,7]

On this basis, nanoclays and biopolymers must be considered green materials really interesting for their potential environmental applications. Moreover, their combination may generate new materials with smart properties matching the great advantage to be composed of macromolecules, derived from renewable resources and nanoparticles, environmental friendly.

1.2 Nanoclays

The nanoclays are alumino-silicate particles which present at least one dimension on the nanometric scale. From the mineralogical view-point they belong to the family of phyllosilicates composed of tetrahedral and octahedral sheets. The tetrahedral sheet consists of silicon-oxygen tetrahedra linked to neighboring tetrahedra by sharing three corners, resulting in a hexagonal network; the remaining fourth oxygen of each tetrahedron belongs also to adjacent octahedral sheet. The latter is usually composed of aluminum or magnesium in six-fold coordination with oxygen from the tetrahedral sheet and with hydroxyl groups. The thickness of each layers is ca. 1 nm and the lateral dimensions may change from 300 Å to several microns. Several layers may be joined in a clay crystallite by interlayer cations, van der Waals force, electrostatic force, or by hydrogen bonding. These layers organize themselves to form stacks with a regular van der Walls gap called the interlayer or the gallery. The different arrangement of the tetrahedral and octahedral sheets allowed us to classify the clays in three categories: 1:1, 2:1 and 2:1:1 phyllosilicates. The 1:1 phyllosilicates, like kaolinite and halloysite, have one tetrahedral and one octahedral sheet per clay layer; as concerns the 2:1 clay minerals, each layer consists of one octahedral sheet sandwiched between the two tetrahedral sheets. Examples are given by montmorillonite, laponite and illite. Finally, the 2:1:1 phyllosilicates, like cloisite, are composed of an octahedral sheet adjacent to a 2:1 layer. Because of the isomorphous substitutions the clays may have a charge in tetrahedral and octahedral sheets influencing their layered structure. Isomorphous substitution is the replacement of an element with another element in mineral crystal without modifying its chemical structure. For example, Al^{3+} can replace Si^{4+} in tetrahedral coordination, and Al^{3+} replaced by Mg^{2+} or by Fe^{2+} and Mg^{2+} replaced by Li^{+} may occur in octahedral coordination. The presence of these charges are counterbalanced by ions situated in the interlayer. Recently the nanoclays have attracted growing interest in material science due to their versatile features of large surface area, high porosity, and tunable surface chemistry which enabled these nanomaterials to be utilized as catalysts,[8,9,10], in electronic devices,[11] for entrapment of hydrophilic and lipophilic active agents,[12,13,14] and as a nanofillers for polymers.[15,16,17,18] Moreover, the nanoclays are largely employed in pharmaceutical applications[19] and in water decontamination[5,20,21] because of their sorption ability and biocompatibility. Within this field, halloysite and laponite are new emerging clays with unique properties and appealing perspectives.

1.3 Halloysite

Halloysite is an economically viable clay material that can be mined from deposits as a raw mineral. The most widely available halloysites are from the deposits in Northland (New Zealand) and in Dragon Mine (Utah – USA). Geological settings are also present in China, Turkey and Australia.

Halloysite is a 1:1 phyllosilicate with a chemical formula of $Al_2Si_2O_5(OH)_4{\cdot}2H_2O$ which is similar to kaolinite except for the presence of an additional water monolayer between the adjacent clay layers.[18] As shown in Figure 1.3.1, the presence of the interlayer water molecules determines an increase of the spacing in the multilayer walls from 7 Å to 10 Å. The principal form of Halloysite is a hollow tubular morphology in the submicrometer range (Fig 1.3.1) It is currently unclear the reason that flat kaolinite rolls into Halloysite nanotubes (HNTs).[18] We can suppose that the neighboring alumina and silica layers together with their two interlayer water molecules create a packing disorder causing them to curve and roll up, forming multilayer tubes. It is reported that the HNTs walls are formed by the rolling of 15-20 aluminosilicate layers.[14] They are quite polydisperse in size; their length varies from 0.2 and 1 μm while the inner and outer diameters are ca. 1-30 nm and 30-50 nm, respectively.[14] The HNTs external surface is composed of Si−O−Si groups, whereas the internal surface consists of a gibbsite-like array of Al−OH groups. This difference results in a negatively charged outer surface and a positively charged inner lumen in the pH range between 2 and 8.[22]

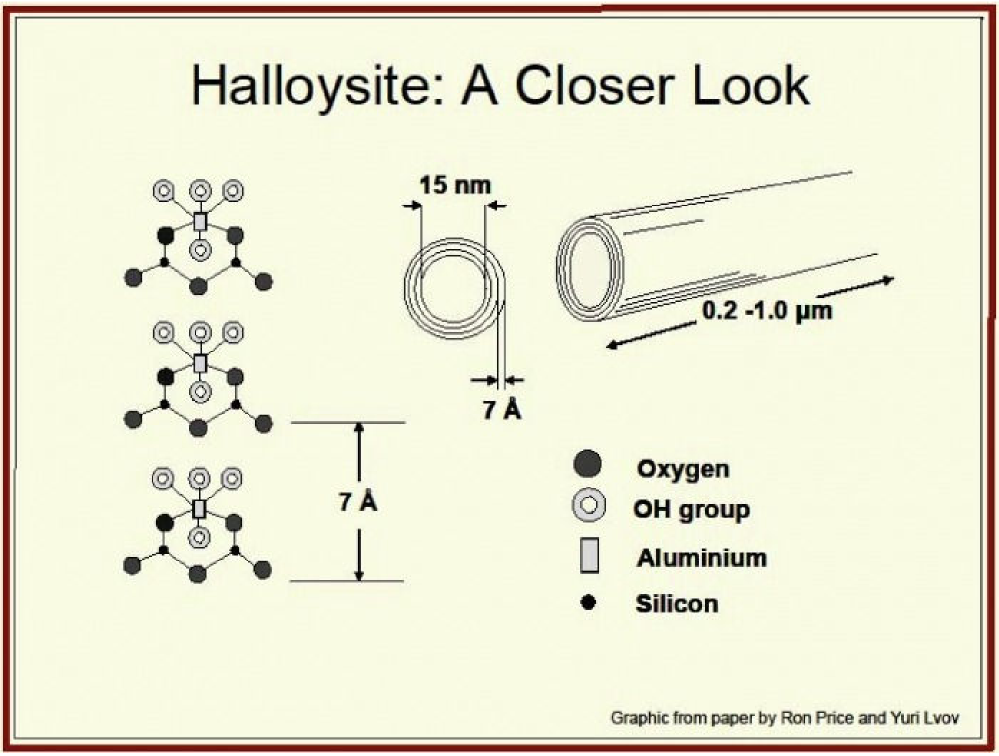

Figure 1.3.1 Mineralogy and structure of Halloysite

Because of their morphology and chemistry, HNTs are appropriate materials in numerous applications over different fields. Within this topic, it is important to evidence that unlike other tubular materials such as boron nitride, metal oxide, or carbon nanotubes, Halloysite is a natural and biocompatible nanomaterial,[19] which makes it attractive for specific environmental purposes. Moreover, Halloysite is far cheaper than the other tubular nanoparticles. The cost of HNTs and carbon nanotubes is \$4 and \$500 per kg, respectively. Therefore, it is reasonable to expect that these nanoclays can achieve a massive industrial application over the next years.

As concerns the environmental purposes, the HNTs are good adsorbent materials towards both inorganic and organic contaminants and, consequently, they can be considered a smart alternative to the traditional methods used for the water decontamination. It was studied the HNTs efficiency to remove organic dyes, like Neutral Red[20] and Methyl Violet,[5] and ammonium ions[23] from the aqueous phase.

The HNTs are perspective biocompatible materials for biotechnological research because their cavity can be used to encapsulate biologically active molecules, such as biocides and drugs. In 2001 Price et al. first demonstrated that the HNTs are proper nanocontainers for Tetracycline, Khellin, and Nicotinamide Adenine Dinucleotide.[24] HNTs were used as nanoreactors for biomimetic reactions[9,25] and to synthesize insulated silver nanorods employed as antimicrobial additives for polymer composites.[10]

Self-healing protective coatings were prepared by loading HNTs cavity with corrosion inhibitors such as benzotriazole.[13,26] In this case inhibitors are released upon formation of the paint cracks and terminate metal corrosion. The release control of the inhibitors with end stoppers was exploited.[27]

It is important to evidence that many applications of Halloysite as nanocontainer depend on its lumen size. Recently, HNTs with an enlarged cavity were prepared by a selective etching of alumina sheets[22,28] that consists into their dissolution by means of an acidic treatment. The HNTs, etched with sulfuric acid, showed a four times increase of the benzotriazole loading.[22]

Concerning the material science, Halloysite application as nanofiller in polymer composites represents an efficient strategy to develop new nanomaterials with excellent properties from the physico-chemical view point. Filling polymers with HNTs improves the composites mechanical properties as demonstrated for styrene-butadiene rubber,[29], epoxy resin,[30] polymethylmethacrylate,[31] and natural polymers.[15] Literature reports that the addition of HNTs prevents the cracking in the drying latex films.[32] Polystyrene[33] and polyamide[34] filled with well dispersed HNTs exhibited a thermal and a mechanical reinforcement of the polymer matrix. Composite materials with humidity control ability were prepared by using HNTs as filler.[35] Recently, researchers[16,15,36,37,38] have focused their attention on doping polymers from renewable resources with HNTs in order to design new biocompatible packaging materials which can be an alternative to the petroleum based plastics. Futhermore, HNTs application as nanofillers in polymer composites allows to control the sustained release of chemically and biologically active compounds loaded into their lumens. This is promising to develop functional polymeric nanocomposites with anticorrosion[13,39,40] and antibacterial functions.[10,41]

Other potential Halloysite applications include bioimplants, such as biomaterial for dentistry and for bone tissue scaffolds[42] and catalytic supports.[43] For instance, HNTs were used as catalyst support for the platinum in the synthesis of allyl-ended hyperbranched organic silicone resins.[44] The functionalization of the Halloysite external surface allows to obtain catalyst supports for the metallopor-phyrin[45] immobilization and the heterogeneous atom transfer polymerization of methyl methacrylate (MMA) into poly(methyl methacrylate) (PMMA) by using CuBr as catalyst.[46]

Finally, the combination of Halloysite and fly ash determines the formation of geopolymers (or inorganic polymers).[47] the development of these materials is an important step for the production of environmental friendly cements.

1.4 Laponite

Laponite is a synthetic crystalline 2:1 phyllosilicate with crystal structure and composition closely similar to the natural smectite clay hectorite. It is manufactured by Rockwood Additives Ltd (formerly Laporte Ind. Ltd.), Cheshire UK, and Southern Clay Products, Inc., Gonzales, Texas.

Its molecular formula is $Si_8(Mg_{5.45}Li_{0.4})O_{20}(OH)_4Na_{0.7}$. Single laponite crystals are disk shaped and nearly uniform, typically 25 nm in diameter and 0.92 nm in the thick, much smaller than natural clays (Figure 1.4.1). Within a single crystal, each sheet of octahedrally coordinated aluminum or magnesium oxide is sandwiched between two layers of tetrahedrally coordinated silica. A laponite disk shows an overall net negative charge of 700 electron charges (the crystal faces have negative charge, while the edges have small pH-dependent positive charge, typically 10% of the negative charge). The negative charge, due to isomorphous substitution in the octahedral sheet, is balanced by interlayer cations which are predominantly Na^+. Suspensions of laponite are observed to undergo a transition from a fluid-like sol to a solid-like gel instead of forming a liquid-crystalline phase.[48,49] Above a concentration of 2 wt% laponite readily hydrates and swells to form a thixotropic gel in water[50] which can be used as cleaning materials of artifacts. Laponite is employed in many commercial products such as toothpaste, cosmetics, and personal care products as well as thickening agent in paints and ointments. The very large specific surface area (160 m^2 g^{-1}) renders laponite nanodisks an efficient adsorbent material for contaminants. It is demonstrated that laponite removes some dyes, like cristal violet (CV),[21] from the aqueous phase. Laponite can be used in many pharmaceutical applications as carrier system for drug delivery and cancer therapy. For example, itraconazole[51,52] and doxorubicin[53] were able to be incorporated into laponite interlayer and their release was very slow. Laponite doped with poly(lactic co-glycolic acid) is very efficient to encapsulate amoxicillin.[54]

Within the material science topic, laponite is used as filler for designing nanocomposites (solid or hydrogel) with interesting properties. It is observed that copolymer/laponite systems are versatile materials with a large flexibility of their macroscopic properties based on the control of their nanostructure.[55] The filling of laponite in the starch/poly vinyl alcohol blend enhances the tensile strength and decreases the water vapor permeability regardless of the relative humidity. Therefore, these films can be potentially used as biocompatible packaging even in high humidity conditions.[56] Poly(Nisopropylacrylamide)/laponite hydrogel composites are appealing biomaterials because of their excellent and unique mechanical properties; specifically, a self-reinforcement after large deformation was observed for the gel with high clay content.[57]

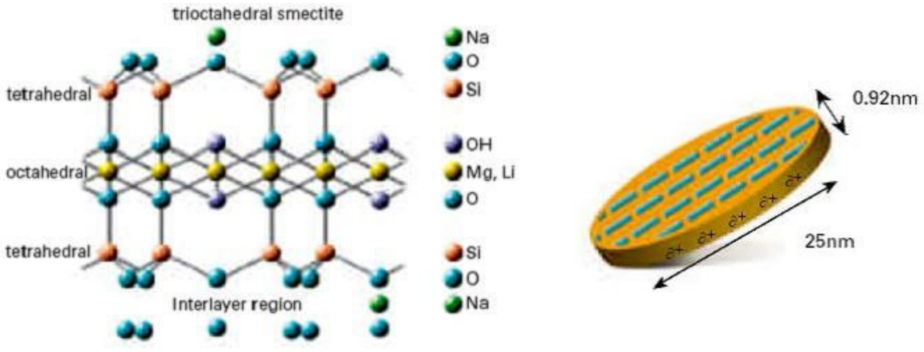

Figure 1.4.1 Laponite structure (left) and schematic representation of a negatively charged disk like Laponite particle (right).

Finally, laponite is used for the encapsulation/entrapment of homogeneous inorganic catalysts.[58]

1.5 Biopolymers

Biopolymers are chain-like molecules made up of repeating chemical blocks which are obtained from renewable sources. They can be classified into three main categories:

- biopolymers extracted from the biomass, such as cellulose, pectins and starch.
- biopolymers produced by microorganisms, like the polyhydroxyalkanoates.
- synthetic biopolymers obtained by manipulating renewable and natural resources. Polylactic acid synthesized from the starch is an example.

Because of their naturally occurring structure, biopolymers are fully capable of biodegradation at accelerated rates. In other words, the organic components undergo to fast degradation induced by a biological system (especially for enzymatic action) determining the release of carbon dioxide, water, minerals and new biomass.

Their biodegradability and renewability make these materials environmental friendly alternatives to the plastics based on fossil fuel in many fields, such as packaging, engineering and textile industry. Moreover, biopolymers are very abundant in the nature and, therefore, they can be potentially also advantageous also from the economic view-point. A study[2] evidenced that, in the next decades, the natural polymers will be cheaper than the traditional plastics because of the progressive increase of the petroleum costs.

Pectins, alginates, cellulose and their derivates are some examples of appealing biopolymers.

1.6 Pectins

Pectins form a family of complex polysaccharides present in all plant primary cell walls. The main constituent is the homogalacturonate, which is a linear chain of 1,4-linked α-D-galactopyranosyluronic acid residues where some of the carboxyl groups are methylated. The polymeric chain presents also Rhamnogalacturonan-I (RG-I). On the basis of the methyl esterification degree (DE), these biopolymers are classified as high-methoxy pectins (HM) and low-methoxy pectins (LM). In detail, HM and LM pectins have a DE value higher and lower than 50%, respectively.

Pectins are extracted predominantly from fruits (apple pulp and citrus peel). The extraction method is rather simple; it occurs acid aqueous solution at pH comprised between 1.5 and 3.0 and temperature between 60 and 100 °C.

The most attractive property of pectins for industrial applications is their gelling activity. Pectins of high DE have been developed into hydrogels for drug delivery[59] and biosorption of heavy metals.[60] Pectins are employed as stabilizers in food industry and cosmetics determining positive effect on the human health, such as lowering of cholesterol, reduction of the cancer[61] and stimulation of the immunological response.[62] Moreover, these biopolymers are used to develop biodegradable films with interesting physico-chemical properties. Films based on pectin and additives (such as poly(vinyl alcohol), chitosan, etc.) can be potentially used as water-soluble pouches for detergents, softeners, and medical delivery.[2] Pectin blended with high amylase starch and glycerol generates edible films with a large interval of mechanical properties[63] and excellent oxygen barrier capability.[64] Pectin-protein composite films may be used in wrapping and packaging materials for situations where moderate mechanical strength and low water vapor transmission are required.[65]

1.7 Alginates

Alginates are water-soluble polysaccharides consisting of alternating segments of 1-4 linked β-D-mannuronic acid and α-L-guluronic acid. The proportion and distribution of these segments, along with their relative sequencing, determines the chemical and physical properties of the alginates.[66]

These biopolymers are quite abundant in nature since they occur both as a structural component of the cellular walls in marine brown algae (specifically *Laminariales and Fucales*), comprising up to 40% of the dry matter, and as capsular polysaccharides in soil bacteria, such as *Pseudomonas Aeruginosa*.[67]

The alginates are mostly obtained by the extraction from the algal thallus using Green and Gloahec-Herter methods.[67]

The industrial applications of alginates are correlated to their ability to retain water and their gelling.[68] Alginate gels are used in many pharmaceutical applications, such as wound dressing, control release drugs, and immobilization matrices for cells or other materials. Alginates present an affinity toward multivalent cations such as Ca^{+2} leading to the formation of ionically cross-linked alginate gels.[69]

Alginate gel beads are efficient in the removal of dyes, such as victoria blue[70] and methylene blue.[71]

Finally, alginates can be used to produce biodegradable films for food packaging because of their unique colloidal and excellent membrane-forming properties.[72]

1.8 Cellulose derivatives

Cellulose is the most abundant biopolymer on Earth, which makes it also the most common organic compound. Annual cellulose synthesis by plants is close to 10^{12} tons. Plants contain approximately 33% cellulose whereas wood contains around 50 per cent and cotton contains 90%.

Cellulose is a linear and fairly rigid homopolymer consisting of D-anhydroglucopyranose units. These units are linked together by β-(1→4) glycosidic bonds formed between C-1 and C-4 of adjacent glucose moieties.

This biopolymer is extensively used as a raw material in the paper industry in the production of paper products; nevertheless, the utilization in chemical industry is often limited because of its poor solubility in water and organic solvents. Therefore, it is chemically modified yielding products widely used in different industrial sectors, food and cosmetics.[73]

Within this field, the etherification of the cellulose leads to obtain synthetic biopolymers which are very promising in numerous applications. Examples of commercial cellulose ethers are hydroxypropylcellulose (HPC) and sodium carboxymethylcellulose (CMC). HPC is obtained by linking the propylene oxide to the anhydroglucose hydroxyl groups. There are different HPC on the basis of the molecular weight and substitution degree. The physico-chemical behavior of HPC is well known based also on its rather high solubility in water although it is hydrophobically modified. HPC undergoes phase separation upon heating,[74] and forms liquid crystals.[75] This polymer was used in the consolidation of waterlogged woods and it was revealed very efficient even if optimization of the impregnation process was necessary.[76] HPC is used in preparing organic–inorganic nanocomposites because it ensures the stabilization and the homogeneous dispersions of inorganic salts.[77] HPC/HNTs nanocomposites showed interesting physico-chemical properties, such as thermal stability and wettability.[16]

Finally, HPC assembled with poly(acrylic acid) onto nanoparticles provided long term stability microcapsules for controlled drug delivery applications.[78]

CMC is a cellulose derivative with carboxymethyl groups ($–CH_2–COONa$) bonded to some of the hydroxyl groups on cellulose backbone. The presence of polar carboxyl groups renders the cellulose soluble, chemically reactive and strongly hydrophilic. Because of these characteristics, CMC is very attractive and promising in superabsorbent fields.[79,80] This biopolymer was widely used for several industrial applications such as drug delivery, textile printing, paper industry, detergents, food, and oil well drilling operations.[81,82]

Recently, the research has been addressed to the preparation of hybrid nanocomposites based on CMC and various nanoparticles, such as copper complexes,[83] silver nanoparticles[84] and layered double hydroxide.[85] Their potential applications involve the material science as well as the biotechnology.

1.9 Biocompatible nanocomposites

Nanocomposites are a class of materials composed of nanoparticles dispersed in a polymer matrix. The intercalation of a vinylic monomer into the montmorillonite, occurred in 1961 by Blumstein, represents the starting point of the development of these nanomaterials. Nevertheless, the nylon 6/montomoriillonite nanocomposite, prepared by Okada in 1988 in Toyota laboratories, is the first industrial application.[86]

These nanomaterials have drawn considerable research interest because of their consistent improvement in physical, thermal, mechanical, and electroactive properties compared to those of pristine polymers.[87,88]

As concerns the performances of hybrid nanomaterials, it is well known that they are strongly dependent on the matrix/filler interactions so that the shape of the nanoparticles plays a crucial role on the improvement of the physico-chemical properties compared to those of pristine polymers. Therefore, we distinguish three different types of nanoparticles: isodimensional, nanotube (or nanodisks) and sheet which present three, two and one dimensions in the nanoscale, respectively. Nanotubes and isodimensional nanoparticles maximize the interactions between polymer and filler and, therefore, they favor the improvement of the performance with respect to the pristine polymer materials.[89]

As concerns the structure, nanocomposites may be divided into three main different categories in dependence of the miscibility degree between matrix and filler. Specifically, nanocomposites structure can be:

- *Tactoid*. A complete separation between polymer and nanoparticles is observed. To obtain material with improved physico-chemical properties compared to the pristine polymer the filler loading must be very large.
- *Intercalated*. The nanocomposites present an ordered structure of alternating polymer and inorganic fillers layers. They show a partial miscibility.
- *Exfoliated*. The filler is completely and uniformly dispersed into the polymer matrix. It is a system with a complete miscibility. Due to the high interface area between the two components, the polymer/nanoparticles interactions are very strong favoring the improvement of the physico-chemical properties. In this case, small amounts of filler are efficient to develop nanomaterials with good performance.

The peculiar structure of the nanocomposites is influenced by both the characteristics (chemistry and geometry) of the pristine components and the method of preparation (polymerization in situ, melt blending and the casting method).

1.10 Aims and objective of the study

The combination of different environmental friendly resources represents an innovative route to obtain very efficient adsorbent materials which can be used for the entrapment of contaminants, gas and biocides.

Within this issue, the objective of this study was to design, prepare and characterize from the physic-chemical view point innovative hybrid green materials based on nanoclays with interesting properties for environmental and technological applications. It is well known that the functionalization of nanoclays by using polymers and/or surfactants determines an enhancement of the adsorption ability towards both inorganic and organic molecules. For example, laponite nanodisks grafted with no ionic copolymers are very efficient to solubilize phenol.[6] The modification of the HNTs external surface by hexadecyltrimethylammonium is a successful route to obtain nanomaterials able to adsorb naphatalene[90] and Cr (VI).[91] Recently, the functionalization of the HNTs inner surface by octadecylphosphonic acid[92] and dopamine derivates[25] was investigated to create a hydrophobic HNTs lumen with adsorption ability towards non polar contaminants. This thesis was addressed to create innovative adsorbent materials based on the HNTs inner surface functionalization with anionic surfactants and polymers. The surfactant/HNTs hybrid nanomaterials must be considered a new class of tubular inorganic micelles. The tubule clay micelle-like absorbent offers additional features with respect to the conventional organic micelles, such as chemical and mechanical stability as well as the possibility to produce this material in large quantities. The micellar features of modified HNTs are associated to their unique architecture where the hydrophobic cavity allows the solubilization of hydrophobic guest molecules by partitioning from a polar solvent while the polar external surface provides stability of the nanoparticles dispersion in water. It was demonstrated that the functionalization of lumen with anionic surfactant determines an increase of the HNTs aqueous colloidal stability because of the neutralization of the inner positive charges.[93] This latter finding is crucial for HNTs applications in decontamination, biotechnology and material science. An extended physico-chemical study on the functionalized HNTs provided insights on the structure of these hybrid nanomaterials which influence the aqueous colloidal stability as well as the adsorption ability. Alkanoate surfactants (attached papers III – IX) were used with the motivation to develop new inorganic micelles able to solubilize both aliphatic and aromatic hydrocarbons. The HNTs lumen modified with fluorinated surfactants (attached paper VIII) was exploited as oxygen reservoir nanocontainers.

The HNTs functionalization with anionic polymers was explored to increase the aqueous colloidal stability because of new drilling petroleum formulations and micromanifacturing applications.

Extensively thermodynamic and structural studies of aqueous HPC/laponite system (attached paper II) discriminated the driving forces which control the interactions between the two components. The good colloidal stability of aqueous laponite dispersions endowed to perform these studies.

Gel beads based on biopolymers, such as chitosan, pectins and alginates, and their mixtures have been recently proposed to capture contaminants from the aqueous phase.[94,95] In order to increase the solubilization ability, a part of work was focused on the preparation and characterization of composite gel beads based on biopolymers (pectins and alginates) and HNTs.[96,97] Their adsorption ability towards a inorganic and organic contaminants was investigated (attached papers V – VI). Finally, the thesis was also dedicated to the development of biopolymer/nanoclay composite film which could be used as biocompatible packaging. The macroscopic properties of the bionanocomposites obtained from the aqueous casting method were correlated with their microscopic structure (attached papers I - IV). Plasticized bionanocomposites were prepared to improve the mechanical performances (attached paper VII).

2. Aqueous biopolymer/laponite mixtures

2.1 Physico-chemical studies of aqueous biopolymer/laponite systems

Physico-chemical studies (attached paper II) of aqueous biopolymer/laponite systems were carried out by means of different techniques, such as Isothermal Titration Calorimetry (ITC), Differential Scanning Calorimetry (DSC), densitometry, Dynamic Light Scattering (DLS) and and surface tension experiments. The measurements were performed in dependence of the concentration of both the polymer and the nanofiller. Temperature and inorganic salts were selected as additional parameters because they trigger the adsorption process.

The thermodynamic properties (ITC, DSC and densitometry) are suitable for evidencing the forces controlling the distribution of the nanofiller into the aqueous polymer matrix, while the DLS technique is sensitive to the biopolymer/nanoclay mesostructures through the diffusion behaviour. In addition, surface tension evidences phenomena present at the interface.

Let us analyse in detail the above mentioned properties and the insights provided by them.

2.2 Thermodynamic properties

As examples, ITC curves of the heat of interaction per mole of HPC (ΔH_i) as functions of the polymer/laponite mole ratio ($R_{HPC:L}$) for the HPC + laponite + water ternary mixtures at variable temperature and ionic strength are reported in Figure 2.2.1.

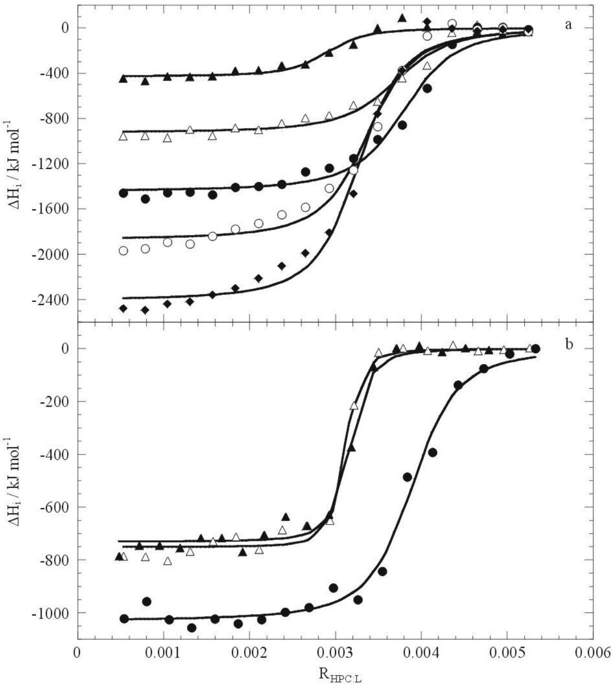

Figure 2.2.1. Heat of interaction per mol of HPC as functions of the HPC/laponite unit cell moles ratio in the absence (a) and the presence (b) of salts. a: 5 °C (▲), 15 °C (Δ), 25 °C (●), 35 °C (○) and 45 °C (♦). b: LiCl (▲), NaCl (●), KCl (Δ) all 5 mmol kg^{-1} and 15 °C. Lines are best fits.

In general, each ΔH_i vs $R_{HPC:L}$ sigmoidal curve evidences a single adsorption process successfully interpreted by means of a model assuming that a number (Z) of polymer molecules adsorb onto the solid nanoparticles that contain a certain number of equivalent sites, as sketched in Figure 2.2.2.

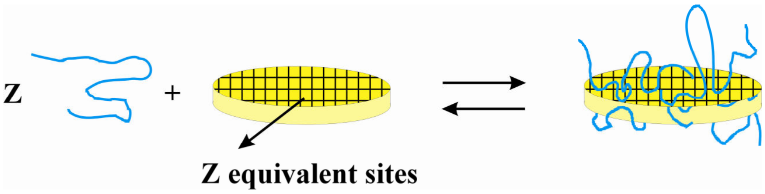

Figure 2.2.2. Sketch representation of the polymer adsorption equilibrium onto laponite.

The fitting of the experimental data provides the equilibrium constant (K_{ads}), Z and the enthalpy of adsorption per mole of polymer ($\Delta H°_{ads}$). Thereby, standard free energy ($\Delta G°_{ads}$) and entropy ($\Delta S°_{ads}$) for the adsorption process are calculated as

$$\Delta G°_{ads} = - RT \ln K_{ads} \qquad T\Delta S°_{ads} = \Delta H°_{ads} - \Delta G°_{ads} \qquad (2.2.1)$$

The adsorption of a polymer at the solid/liquid interface involves a series of microscopic aspects. From the energetic view-point, one observes the partial rupturing of the water-polymer and water-nanoparticle bonds and the formation of polymer-nanoparticle interactions. Given that $\Delta H°_{ads}<0$ (Figure 2.2.3), the polymer-nanoparticle interactions are the dominant effect, while the strong entropy decrease for the HPC adsorption onto laponite evidences that the constraints of the polymer motion at the solid/liquid interface is the dominant entropic factor (Figure 2.2.3).

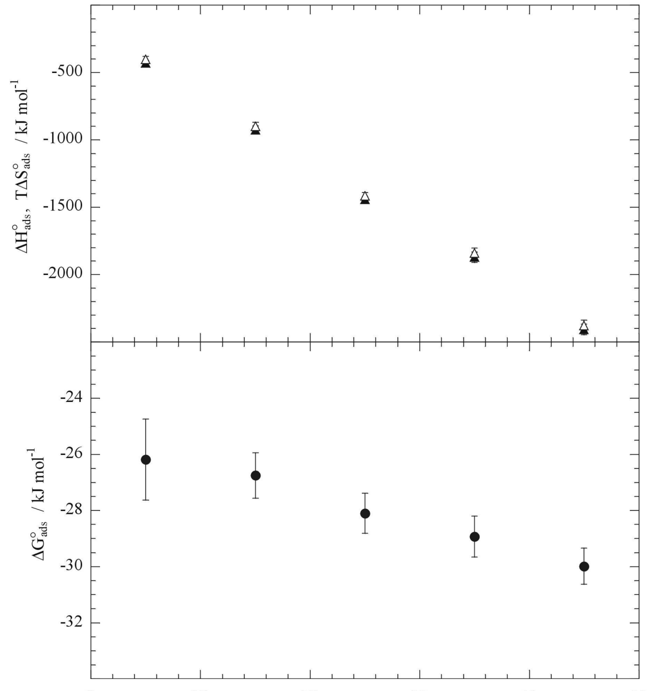

Figure 2.2.3. Standard free energy (●), enthalpy (▲) and entropy (Δ) (○) for the HPC adsorption onto laponite in water at various temperatures.

Temperature change affects the adsorption process and the results confirm the depicted thermodynamic pathway. The decrease of both $\Delta S°_{ads}$ and $\Delta H°_{ads}$ with temperature (Figure 2.2.3) agrees with the idea that upon heating the water structure is partially lost and therefore the water-polymer interactions are weaker and the entropic contribution of the polymer de-hydration due to the adsorption is less important.

Similar findings were drawn from volumetric studies on aqueous pectin/laponite systems.[15] In such a situation it occurred: 1) the adsorption of the biomacromolecule onto the laponite surface controlled by the interactions between the negative surface charge of the nanofiller and the -OH and -COOH groups of the biomacromolecule as well as the hydrogen ions; and 2) the folding and compacting of the biomacromolecule at the solid/liquid interphase enhanced by its adsorption. Moreover, the temperature effect was amazing because apparently null expansibility of laponite was determined.

The general thermodynamic considerations drawn for the adsorption equilibrium in water are still valid in the presence of salts (LiCl, NaCl and KCl) as showed in Figure 2.2.4.

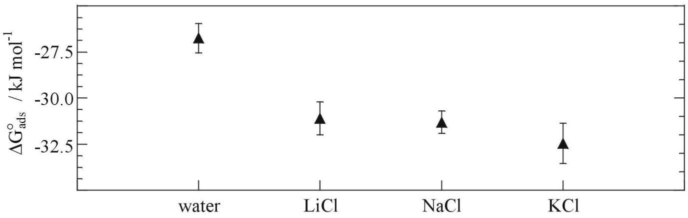

Figure 2.2.4. Standard free energy for the HPC adsorption onto laponite in water and in the presence of LiCl, NaCl and KCl all at 5 mmol kg^{-1} and 15 °C.

It is intriguing the effect of the cation nature on the enthalpy and entropy changes as LiCl and KCl increase ΔH°_{ads} while NaCl decreases the ΔH°_{ads} value with respect to the value in water (Figure 2.2.5).

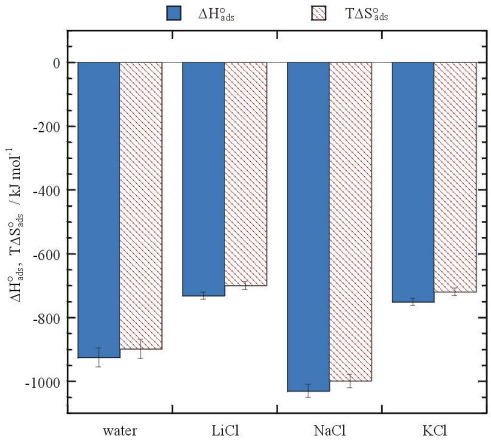

Figure 2.2.5. Standard enthalpy and entropy for the HPC adsorption onto laponite in the absence and the presence of LiCl, NaCl and KCl all at 5 mmol kg^{-1} and 15 °C.

Such a different behavior can be explained to the light of the Na^+ ions release from the laponite surface. Under our experimental conditions and considering a charge of -700e for each disk,[98] one calculates a sodium concentration in solution due to the laponite dissociation equal to ca. 4 mmol kg^{-1}. This value is comparable to the concentration of the added salt and therefore one expects that the ion release is reduced in the presence of NaCl due to the common ion effect. Therefore the positive contribution of the laponite dissociation to ΔH°_{ads} is expected to be smaller in the presence of NaCl than in water. This argument explains the peculiarity of ΔH°_{ads} in NaCl with respect of other salts for which the common ion effect cannot be invoked.

The addition of KCl favours the aggregation of the clay platelets that is reduced by the polymer wrapping the laponite nanodisks.[15]

DSC studies evidenced that the addition of laponite generates a strong effect on the cloud temperature (t_C) of HPC describing a sigmoidal profile (Figure 2.2.7). The enlargement of the one-phase region by increasing the laponite concentration (C_L) may be a consequence of the HPC adsorption onto the solid surface.

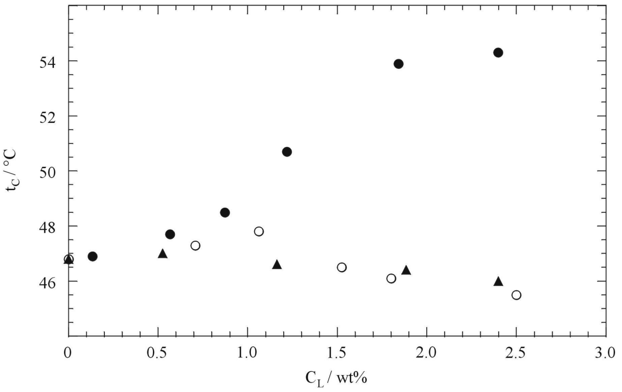

Figure 2.2.7. Dependence on the laponite concentration for temperature and enthalpy of the HPC phase separation in the absence (●) and the presence of NaCl 5 mmol kg^{-1} (○) and KCl 5 mmol kg^{-1} (▲).

Electrolytes play a relevant salting out effect. Xia et al.[99] ascribed such a phenomenon to the weakening of hydrogen bonding between HPC and water. The mechanism that salts act indirectly on HPC precipitation through its exclusion from the condensed phase was also invoked.[75]

2.3 Structural characteristics

The results for the HPC/laponite aqueous mixtures are rather interesting. The linear increase of the apparent hydrodynamic radius (Rh) with the HPC concentration is correlated to the polymer adsorption at the laponite surface. In fact, the laponite particle covered by HPC has a slower dynamics than the bare laponite and it maintains a sufficient scattering intensity. The maximum change in Rh is of ca. 20 nm and it is of the same order of magnitude of the change observed for adsorbing poly(ethylenglycols) with a molecular mass similar to the present HPC.[100] Such a small Rh change was interpreted in terms of a very flat polymer conformation at the interface.[100] This result is peculiar for polymer adsorbed onto disk-like shape nanoparticles as also evidenced by neutron scattering experiments.[99] The interactions between the laponite surface and the –OH group from the polymer evidenced by ITC agree with the DLS results and with the interpretation in terms of a flat HPC layer highly in contact with the particle.

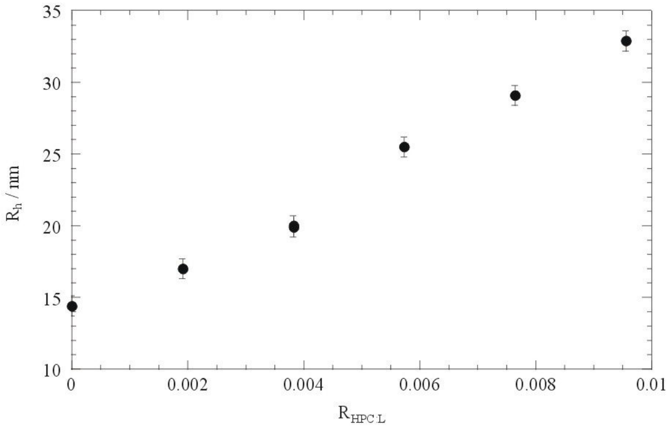

Figure 2.3.1. Apparent hydrodynamic radius of HPC/laponite mixtures in aqueous phase as a function of their mole ratio.

2.4 Correlation between surface tension and bulk properties

The surface tension (γ) reveals the adsorption process occurring in the bulk phase. As Figure 2.4.1a illustrates, HPC strongly lowers γ of water even at very low concentration.

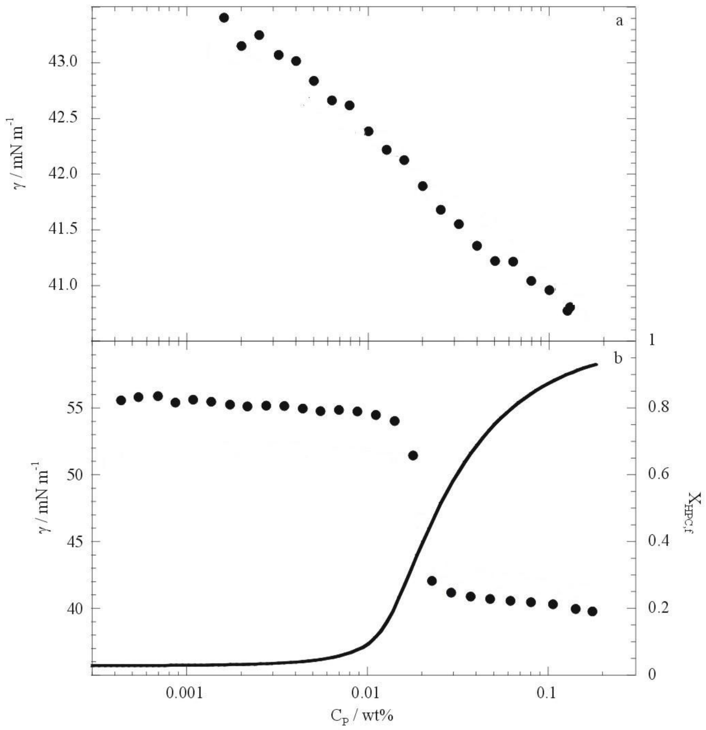

Figure 2.4.1. Surface tension as a function of the HPC concentration: a, the solvents are water (●); b, the solvents are water+laponite (●).The line is the fraction of non-adsorbed HPC calculated from ITC data.

The laponite addition dramatically alters not only the γ values but also the γ vs polymer concentration (C_P) slope. For a straightforward understanding of the γ vs C_P profile, the fraction of free HPC in solution ($X_{HPC,f}$) was calculated from ITC data. As Figure 2.4.1b illustrates, that $X_{HPC,f}$ is nearly negligible at low C_P while it increases reaching a nearly unitary value at larger concentration. It is interesting that the shape of the curves in Figure 2.4.1b are rather similar and that to the sharp $X_{HPC,f}$ change corresponds the γ sharp decrease. To the light of this evidence one concludes that the step-like change in the γ vs C_P profile in the presence of laponite reflects the saturation of the nanoparticles surface and that the laponite covered by the polymer is not surface active or, at least, it is less surface active than the polymer it-self.

3. Functionalized HNTs

3.1 Design of HNTs functionalization

A part of the PhD thesis work was done to design, prepare and characterize HNTs functionalized with anionic biopolymers such as alginate and CMC, and surfactants (attached papers III, VIII, IX), both anionic (sodium alkanoates and sodium perfluoroalkanoates with different chain length) and cationic (decyltrimethylammoniumbromide). The surfactant structures and acronyms are listed in Table 3.1.1.

Table 3.1.1. Surfactants used for the HNTs functionalization.

Name	Acronym	Structure
Sodium undecanoate	NaC11	$CH_3(CH_2)_{10}COONa$
Sodium dodecanoate	NaC12	$CH_3(CH_2)_{11}COONa$
Sodium tetradecanoate	NaC14	$CH_3(CH_2)_{12}COONa$
Sodium perfluoropentanoate	NaPFC5	$CF_3(CF_2)_4COONa$
Sodium perfluoroheptanoate	NaPFC7	$CF_3(CF_2)_6COONa$
Sodium perfluorooctanoate	NaPFC8	$CF_3(CF_2)_7COONa$
Decyltrimethylammonium bromide	DeTAB	$CH_3(CH_2)_9N(CH_3)_3Br$

The selective modification of both the outer and inner halloysite surfaces was deeply investigated. An extended physico-chemical study was performed with the aim at studying the effect of the functionalization on the aqueous colloidal stability of HNTs. The experimental procedure is reported in attached papers while in the following the physico-chemical insights are reported.

3.2 Physico-chemical characterization of HNTs functionalized by surfactants

One of the aim of the work was verifying the surfactant loading into the hybrids (Table 3.2.1) and for this purpose thermogravimetric (TG) experiments were carried out.

Table 3.2.1. Surfactant loading, diffusion coefficient and ζ-potential for surfactant/HNTs hybrid materials.[a]

	Surfactant loading	$D_t \times 10^{12}$	ζ potential
HNTs		0.9	-19
NaC11/HNTs	1.4	1.0	-28
NaC12/HNTs	8.0	0.9	-25
NaC14/HNTs	6.6	1.1	-34
NaPFC5/HNTs	0.3	1.2	-27
NaPFC7/HNTs	0.6	1.0	-29
NaPFC8/HNTs	0.9	0.9	-32
DeTAB/HNTs	0.3	3.4	+9

[a]Units are: surfactant loading, wt%; D_t, $m^2 s^{-1}$; ζ-potential, mV.

By keeping in mind the maximum loading value expected from the cavity size is ca. 10 %,[14] data in Table 3.2.1 show that for all the surfactants this value is never reached indicating the presence of void space into the hollow cavity. If one assumes that the adsorbed surfactant generates a monolayer considering the average specific area of the inner surface (6.9 $m^2 g^{-1}$)[22] and the occupied area of the surfactant with a carboxylate head group at the water/alumina interface (0.41 nm^2 molecule^{-1}),[101] one obtains a loading of 1.2 wt %. From these results one may deduce that some surfactants like NaC11 form monolayer into the lumen while other surfactants (like NaC12 and NaC14) generate structures, which require larger amounts of surfactant.

These findings were supported by Small Angle Neutron Scattering (SANS) experiments performed on pristine HNTs and hybrids. Figures 3.2.1 and 3.2.2 report the scattering curves in full contrast (D_2O as a solvent). It clearly appears that the general trends observed for pristine HNTs and NaC12/HNTs are rather similar with a high scattering intensity in the low regime of scattering vector (q) as expected for cylinders 700 nm long.

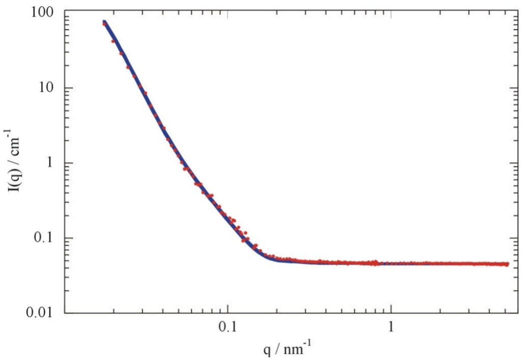

Figure 3.2.1. SANS curve for pristine HNTs dispersion.

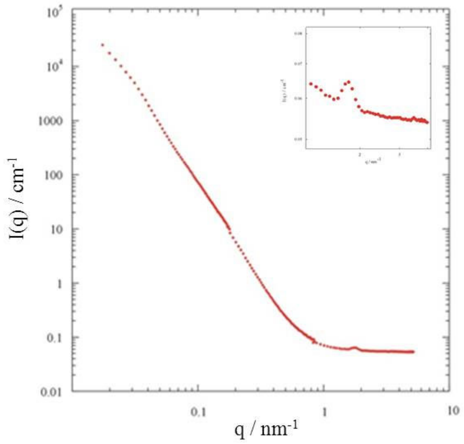

Figure 3.2.2. SANS curve for NaC12/HNTs dispersion.

The absence of oscillation agrees with the large size polydispersion of the material. A preliminary quantitative analysis of the data obtained for HNTs/D_2O shows that a good simulation of the scattering curve is obtained by assuming the form factor of hollow cylinders with a uniform scattering length density (SLD) and 19 nm, 70 nm and 500 nm for inner, outer radius and length, respectively. These values are in good agreement with the SEM findings. It is interesting to note that for the hybrid NaC12/HNTs system in D_2O, a peak appears at $q = 1.79$ nm^{-1}. The corresponding characteristic length calculated by the Bragg law is 3.5 nm. Based on the reported length of one NaC12 molecule (1.7 nm),[102] one may asses that this reflection is compatible with either the formation of layered structures or cylindrical packing of NaC12 within the HNTs lumen. In the case of NaC11/HNTs system in D_2O the scattering pattern does not show any evidence of surfactant organized structures.

One advantage of the SANS technique is the possibility to change the contrast between the solvent and the scattering objects by exchanging hydrogen with deuterium. In particular, we thought interesting to perform experiments in D_2O/H_2O mixture so that the clay nanoparticle SLD is matched. This experiment can straightforwardly highlight the surfactant organization in the hybrid material. To this aim the value of the SLD for HNTs was determined by measuring the total scattered intensity of several HNTs dispersions at variable D_2O/H_2O ratio (Figure 3.2.3). On this basis, dispersions of HNTs and NaC12/HNTs in D_2O/H_2O mixed solvent at the HNTs matching point (45 % D_2O) were prepared and investigated. As Figure 3.2.4 shows, the scattering intensity is nearly null for the HNTs dispersion while it is rather large for NaC12/HNTs. Although the quantitative analysis is in progress, these experiments confirm the presence of NaC12 organized structure into the HNTs lumen.

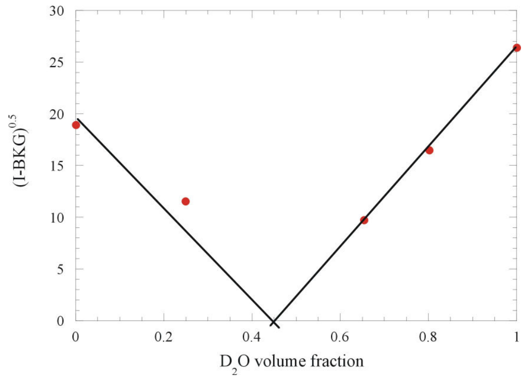

Figure 3.2.3. Determination of HNTs matching point.

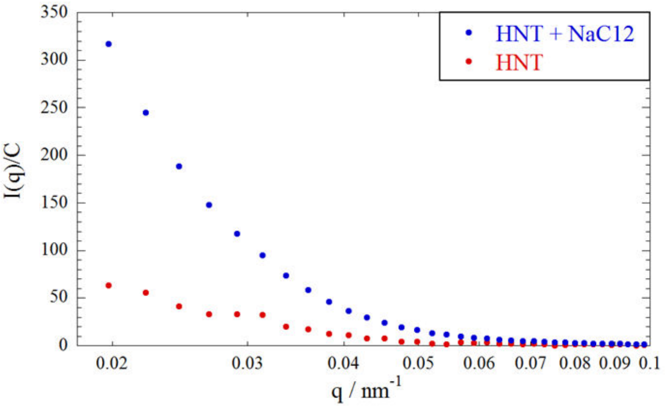

Figure 3.2.4. SANS curves in HNTs contrast matching conditions for pristine HNTs and NaC12/HNTs.

The SEM micrographs (examples of fluorinated surfactant/HNTs composites are reported in Figure 3.2.5) showed that the tubular shape of halloysite is preserved after the functionalization and the characteristic lengths are comparable to those for the pristine HNTs samples. The dried samples did not show any orientation of the anisotropic particles ruling out preferential interactions.

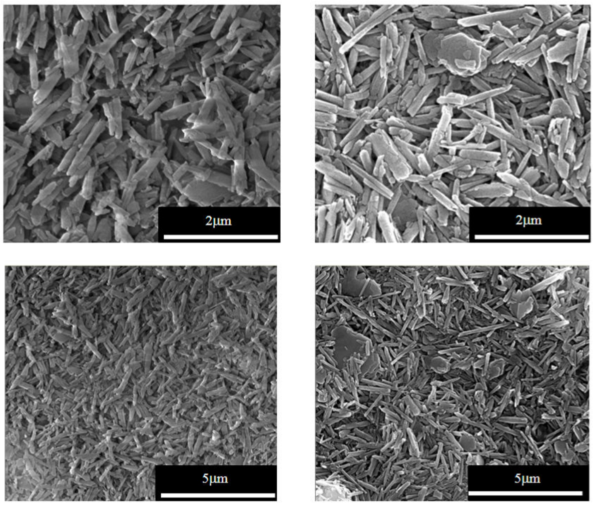

Figure 3.2.5. Scanning electron micrographs of NaPFC5/HNTs (left hand side) and NaPFC8/HNTs (right hand side).

The ζ-potential experiments revealed interesting consequences of the adsorption of surfactants onto HNTs. DeTAB produces an inversion of the HNTs charge with a ζ-potential of +9 mV while all anionic surfactants does enhance the negative ζ-potential (Table 3.2.1). These changes agree with the effective surfactant head group charge as positive alkylammonium bromide groups neutralize a certain number of negative sites of the external surface generating a total positive charge. The anionic surfactant entrapment into the HNTs lumen cancels out the inner positive charges and creates an increase in the total negative charge of HNTs. The prepared nanomaterials are expected to be stabilized in aqueous dispersion as a consequence of electrostatic repulsions.

As concerns the diffusion dynamics of functionalized HNTs, the anionic surfactant/HNTs nanostructures present values for the average translational diffusion coefficients (D_t) close to those reported[15] for bare HNTs in water (9×10^{-13} m^2 sec^{-1}) indicating that they possess the same diffusion dynamic behavior in water of single diffusive nanotubes while DeTAB/HNTs form large aggregates because of the hydrophobic attractive interactions generated by the chains of the cationic surfactant adsorbed onto the HNTs outer surface (Table 3.2.1).

The FTIR measurements proved the surfactant adsorption onto the HNTs as they evidence the characteristic bands of surfactant and HNTs into the solid samples. In the case of alkanoate surfactants, it is interesting to analyze the single sharp stretching band of the carboxylate group that is splitted into two peaks (1541.4 and 1578.1 cm^{-1}) for the hybrid (Figure 3.2.6). It likely occurs that sodium alkanoates entrapped into the lumen by attractive electrostatic forces interact preferentially with one oxygen atom and the delocalization of the negative charge along the carboxylate group is no more present. As concerns DeTAB, the bands for CH_2 asymmetric stretching mode and symmetric stretching mode (at 2927 and 2855 cm^{-1})[103] are shifted to 2918 and 2851 cm^{-1}, respectively (Figure 3.2.6) in the presence of HNTs. This is an indication of high packing of surfactant tails at the surface.

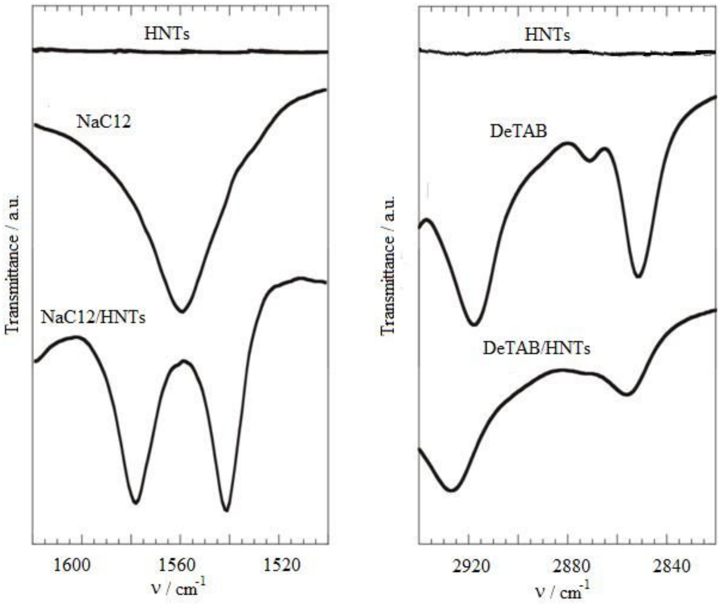

Figure 3.2.6. FTIR spectra of HNTs, surfactants and surfactant + HNTs hybrid materials.

3.3 Physico-chemical characterization of HNTs functionalized by polymers

This work was done at the Institute of Micromanifacturing of Louisiana Tech University (USA).

TG data provided that the polymer loading for CMC/HNTs and alginate/HNTs of 4.4 wt% and 2.9 wt%, respectively, that are consistent with the entrapment of polymers into the HNTs cavity. The thermal stabilization of ca. 15 °C as well as the unchanged water contact angle values observed for both biopolymers is a further indication of the encapsulation into the HNTs lumen.

The presence of both polymers increased the net negative charge of HNTs; in particular, the ζ-potential of CMC/HNTs and alginate/HNTs are -40 mV and -38 mV, respectively. These results are straightforwardly explained by invoking the neutralization of the positive charges of the Halloysite inner surface.[93]

The Rh of CMC/HNTs (Figure 3.3.1) decreases linearly with the concentration of the hybrid material in water ($C_{h,w}$). This trend reveals the repulsive electrostatic interactions between the nanoparticles; the Rh value extrapolated at infinite dilution (186 nm) indicates that the hybrid material does not aggregate in water and it diffuses as single nanotube. Therefore, hydrophobic attractive interactions between the chains of the polymer can be ruled out. Similar results were obtained for alginate/HNTs systems.

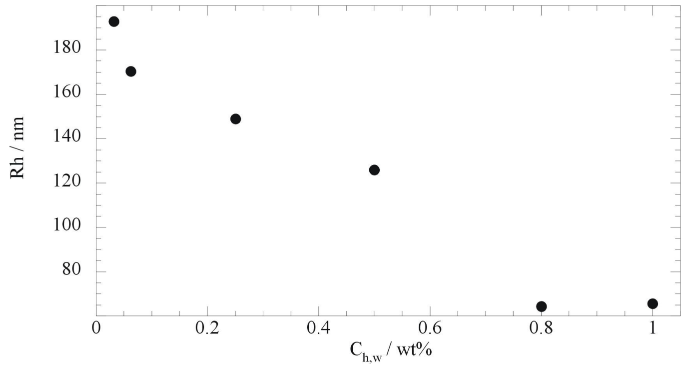

Figure 3.3.1. Apparent hydrodynamic radius of CMC/HNTs as a function of the dispersed material concentration in water.

The HNTs were successfully functionalized also with poly(styrene)sulfonate (PSS) for micromanifacturing purposes. The polymer loading determined by TG is 5.1 wt% and the ζ potential is -52 mV. These results, as well as the water contact angle experiments, agree with the polymer loading into the HNTs lumen.

3.4 Stability of functionalized halloysite in water

To evaluate the mechanism controlling the stabilization of the dispersion, the kinetics of sedimentation of pristine and functionalized HNTs in water was studied by means of turbidimetry.

Figure 3.4.1 shows that the sedimentation is highly influenced by the surfactant nature being strongly slowed down by NaC12. The turbidity value after equilibration follows the order NaC12>water>DeTAB indicating that the anionic surfactant is a proper and efficient stabilizing agent for the HNTs dispersion while DeTAB enhances the sedimentation.

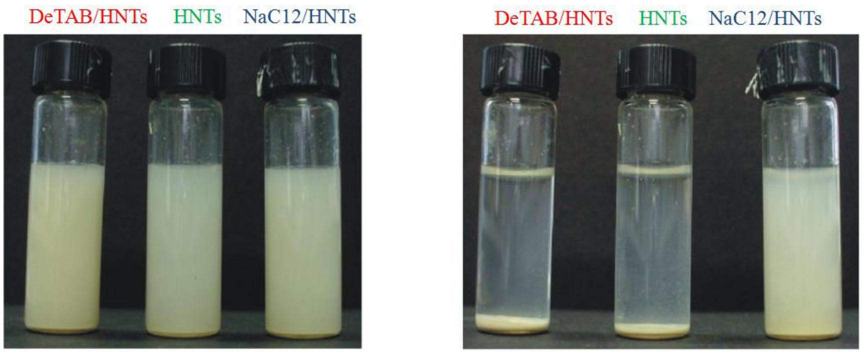

0 hours after mixing

40 hours after mixing

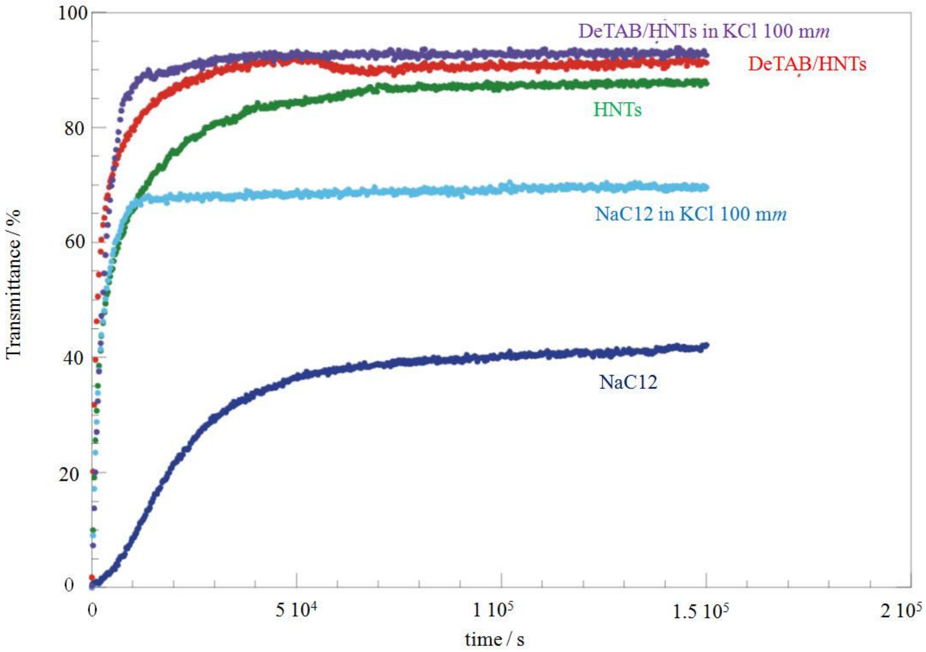

Figure 3.4.1. Photographs and transmittance at 600 nm as a function of time for HNTs and functionalized HNTs dispersions (1 wt%) in water and a water + KCl mixture 100 m*m*.

As evidenced by DLS, the DeTAB/HNTs system has the tendency to form aggregates. This phenomenon is absent in the presence of NaC12 entrapped into the HNTs lumen and therefore the NaC12/HNTs dispersion stability in water is higher. The electrostatic interactions evidenced by ζ-potential measurements bring to the same conclusions. Namely, the larger stability in the presence of NaC12 is explained in terms of the repulsive electrostatic forces enhancement between NaC12/HNTs. Moreover, the lower ζ-potential value for the DeTAB based system agrees with the worst dispersion stability.

To investigate the key role of the electrostatic interactions in controlling the stability of aqueous HNTs hybrid materials dispersions, we measured the turbidity under variable ionic strength conditions. NaC12/HNTs are strongly destabilized by KCl according to the salt screening effect while DeTAB/HNTs sedimentation is only slightly affected because the system is already destabilized in water (Figure 3.4.1).

It should be noted that the colloidal stability of modified HNTs is not straightly correlated to the loading degree for HNT/NaC12 and HNT/NaC14. However, high surfactant content into the lumen close to 10 % indicates the formation of surfactant self-organized structures into the cavity like, for instance, double-layers that maintaining the counterions do not contribute to the net charge of the nanoparticle and consequently to its electrostatic stabilization.

As concerns fluorinated surfactant/HNTs hybrids, Figure 3.4.2 reports the critical concentration (C^*_{LP}) above which the dispersion is stable because the highest packing of the nanotubes is approached and shorter distances between the nanoparticles are hindered by the electrostatic repulsions.

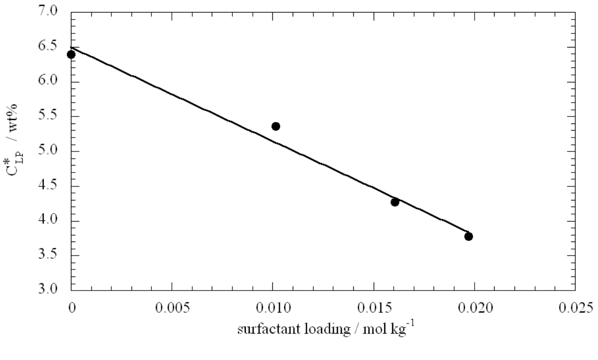

Figure 3.4.2. Critical concentration as a function of the surfactant loading for HNTs hybrid materials.

The linear decrease of C^*_{LP} with the loading reveals that each mole of adsorbed surfactant neutralizes an equivalent number of positive charges of the nanotubes inner surface generating a linear increase of the net negative charge of HNTs and therefore longer range interactions. It should be noted that a surfactant monolayer is likely formed for the fluorinated surfactant.

Figure 3.4.3 shows that the presence of both CMC and alginate strongly slows down the kinetics of sedimentation of HNTs. To the light of the ζ potential findings, the stabilization due to enhanced HNTs electrostatic repulsions is obtained.

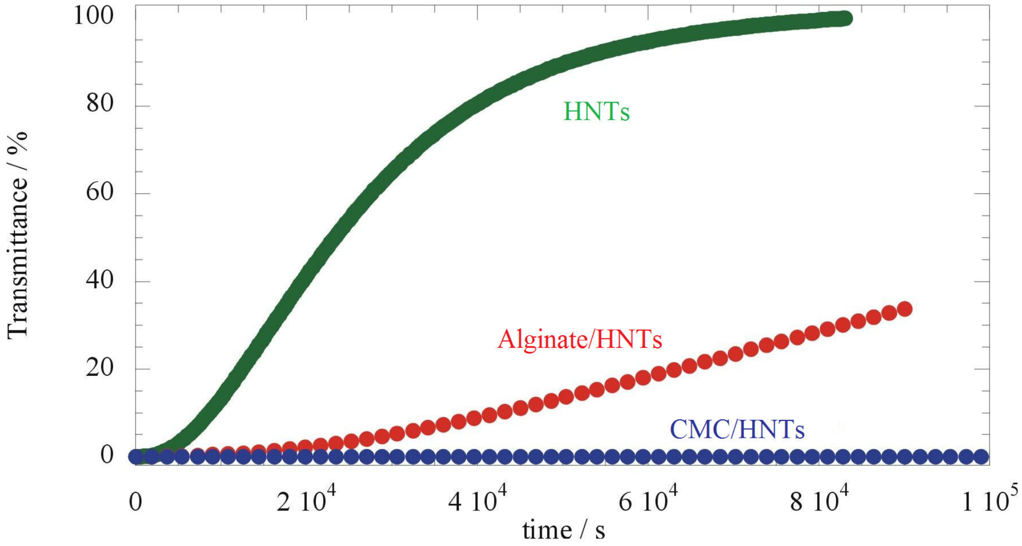

Figure 3.4.3. Transmittance at 600 nm as a function of time for HNTs and functionalized HNTs dispersions (1 wt%) in water.

Within this issue, a previous work[15] evidenced the strong interactions occurring between pectins and HNTs in aqueous media. Thermodynamic results indicated the loading of COO^- groups into the filler lumen and the wrapping of the biomacromolecule onto the HNTs surface occurring via the ion-dipoles attractive forces.

4. Hybrid Gel Beads

4.1 Design of hybrid gel beads based on biopolymers and HNTs

Novel hybrid gel beads with well defined and controlled size formed by alginate and HNTs were designed, prepared and characterized from the physico-chemical view-point (Attached paper V). The alginate/HNTs mass ratios were 1:1, 2:1 and 2:3. Composite gel beads based on alginate and pectin with variable ratio between the two components were prepared and characterized from the physic-chemical view point (Attached paper VI).

The thermogravimetry made it possible to determine the water content, the total as well as the local compositions of HNTs into the gel beads. These insights agree with the morphological studies performed by SEM. Dielectric spectroscopy evidenced that HNTs reduced the fluctuation of ions.

4.2 Physico-chemical characterization of alginate/HNTs hybrid gel beads

The gel beads size is not significantly influenced by the HNTs content whilst the transparency is reducing upon the addition of the clay mineral amount (Figure 4.2.1). Similarly, the size of the gel beads composed of chitosan and laponite are not affected by the addition of the nanoclay.[104]

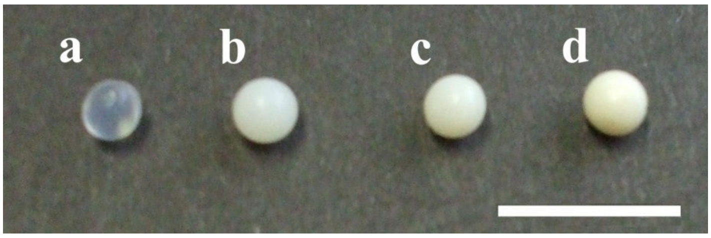

Figure 4.2.1. Optical images for hybrid gel beads at variable HNTs content: a, P_{HNTs}= 0 mass%; b, P_{HNTs} = 33.2 mass%; c, P_{HNTs} = 48.5 mass%; d, P_{HNTs} = 60.2 mass%. The bar is 1 cm.

The experimental HNTs mass fraction (P_{HNTs}) in the dried gel beads evidences that the filler is quantitatively entrapped into the gel beads and that the gel formation is faster than the HNTs diffusion into the calcium chloride solution. The HNTs presence influences the gel beads water content, which decreases upon incorporating the clay mineral into the beads. The SEM micrographies show that the dried bead possesses a rough surface with pores in the micrometer range (Figure 4.2.2a-c) that is similar to what observed in the absence of HNTs.[4]

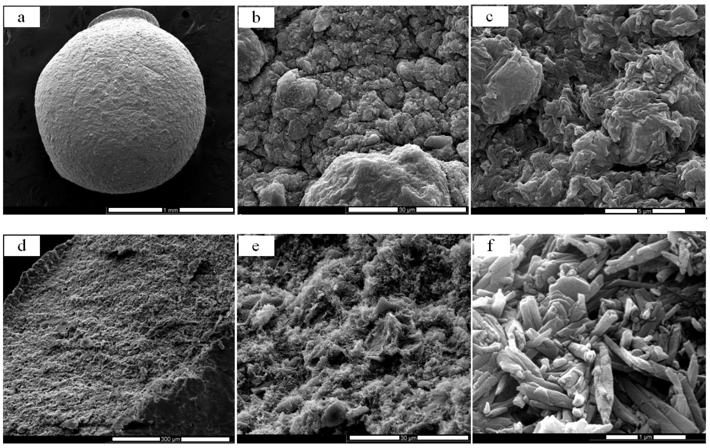

Figure 4.2.2. Scanning electron microscopy images of gel beads loaded with HNTs at P_{HNTs} = 33.2 mass%. a, b, c refer to the surface; d, e, f refer to the core.

Investigating the core structure of the dried gel bead (Figures 4.2.2d-f), the HNTs particles are more numerous than those at the surface as proved by TGA experiments due to the presence of larger amount of water.

Dielectric spectroscopy provides information on the molecular dynamics of systems by monitoring the relaxation processes. The gel beads showed a relaxation process in the MHz domain that is well identified as the maximum in the tanδ vs ν plot (Figure 4.2.3). Upon HNTs addition the peak position is shifted toward lower frequencies but the general profile is not altered. The relaxation frequency at the maximum (ν_{max}) shows a linear decrease with HNTs concentration in agreement with a reduced ions fluctuation generated by the nanotubes. Finally, the steep increase of the dielectric constant at low frequencies can be related to ionomer multiplets forming large aggregates with high polarizability observed in gels based on polyelectrolytes.[105]

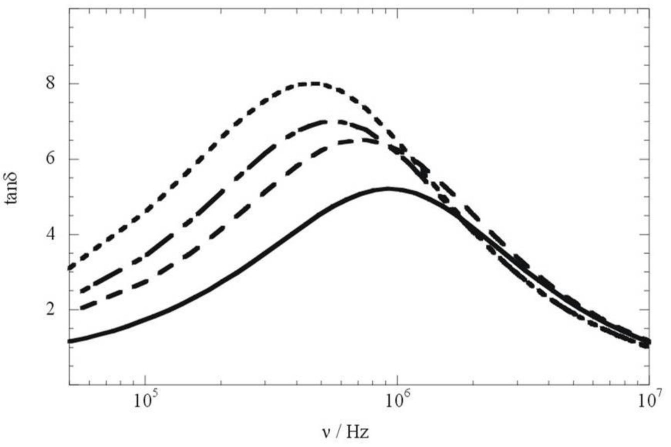

Figure 4.2.3. Dispersion factor as a function of the frequency for hybrid gel beads with variable HNTs content. (—),P_{HNTs} = 0 mass%; (– –), P_{HNTs} = 33.2 mass%; (- – -), P_{HNTs} = 48.5 mass%; (---),P_{HNTs} = 60.2 mass%.

4.3 Physico-chemical characterization of alginate/pectate hybrid gel beads

The following gel beads were prepared: simple alginate 2% (Ca-*A*) and mixed alginate 2% with pectin 1% (Ca-AP_1), pectin 1.5% (Ca-$AP_{1.5}$) and pectin 2% (Ca-AP_2). Surface SEM micrographies (Figure 4.3.1 reports Ca-AP2 gel bead as an example) show wrinkled surfaces of gel beads with creases and pores.

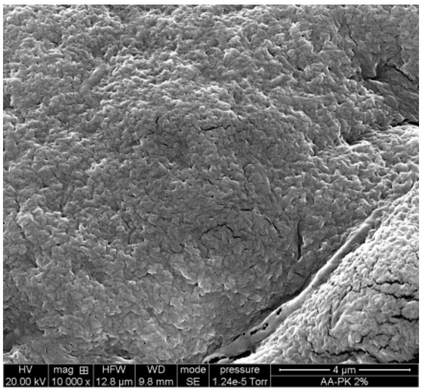

Figure 4.3.1. Surface scanning electron micrograph of Ca-AP_2

The density values of mixed gel beads are slightly lower respect to that of simple alginate gel beads, while the mechanical resistance of gel beads containing pectin is a little higher than that of Ca-*A* gel beads. The latter finding can be due to the higher concentration of biopolymers which contributes to make more compact the structure of the gel due to the higher number of cross-linking among the molecules of alginate, pectin and Ca^{2+} ions.

5. Functionalized HNTs and gel beads: applications

5.1 Applications

This part of the work was dedicated to the evaluation of the potential applications of functionalized HNTs and hybrid gel beads in fields like decontamination and biotechnology.

Alkanoate surfactant/HNTs hybrid nanomaterials were exploited as inorganic micelles to capture hydrocarbon and aromatic oils in the gaseous and the liquid states as well as in water (Attached papers III, IX). The solubilization experiments were perforomed on n-decane and toluene, which are organic compounds of environmental interest. The capability of NaC12/HNTs to encapsulate an apolar biocide in order to develop nanocontainer with potential biotechnological purposes was investigated. The ability of NaPF8/HNTs like non-foaming and oxygen reservoir was studied (Attached paper VIII). Finally, the capture capacity of hybrid gel beads was verified with the specific purpose of adsorbing dye and heavy metals from aqueous phase (Attached papers V, VI).

5.2 Solubilization ability of alkanoate surfactant/HNTs towards n-decane

The solubilization ability of surfactant/HNTs hybrid was verified by studying n-decane in the liquid and vapor states.

As concerns n-decane in vapor phase, both HNTs and the surfactant/HNTs exhibited a valuable adsorbed amount of n-decane which increases with temperature.

The adsorption constant (K_{ads}) are calculated as

$$K_{ads} = Q_{ads}/P_{vap} \qquad (5.2.1)$$

where Q_{ads} and P_{vap} are the adsorbed amount of n-decane (g of n-decane per 100 g of solid) and the vapor pressure, respectively.

The K_{ads} for all the investigated systems are illustrated in Figure 5.2.1.

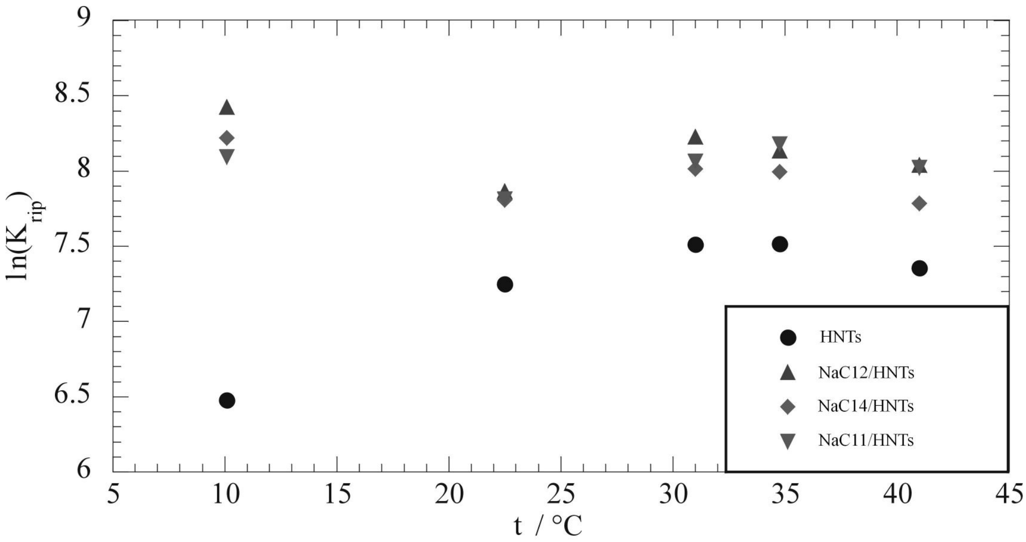

Figure 5.2.1. Adsorption constant of gaseous n-decane onto the solid substrate as a function of temperature.

The pristine nanotubes exhibit affinity towards n-decane that is rather small at low temperatures and it is definitely smaller than that of the hybrid materials. It appears surprising that the adsorption ability of the hybrid materials does not depend on the alkyl chain lengths of the surfactants. However, in spite the amount of the surfactant as well as the structures formed into the lumen are tail surfactants dependent, the inner micropolarity remains unaltered being anhydrous and with properties similar to the hydrocarbons. Therefore, one may conclude that NaC11/HNTs exhibits affinity towards gaseous n-decane in the same manner as NaC14/HNTs does even though it contains surfactant amount six times smaller.

DeTAB/HNTs is not able to entrap n-decane in agreement with the different surfactant structures. Anionic surfatant/HNTs possess a hydrophobic compartment evoking the formation of inorganic micelles.

Surface tension experiments on a lens of liquid n-decane in contact with an aqueous dispersion of pristine and functionalized HNTs were performed in order to mime the case of an aquifer contaminated by light non-aqueous phase liquids (Figure 5.2.2).

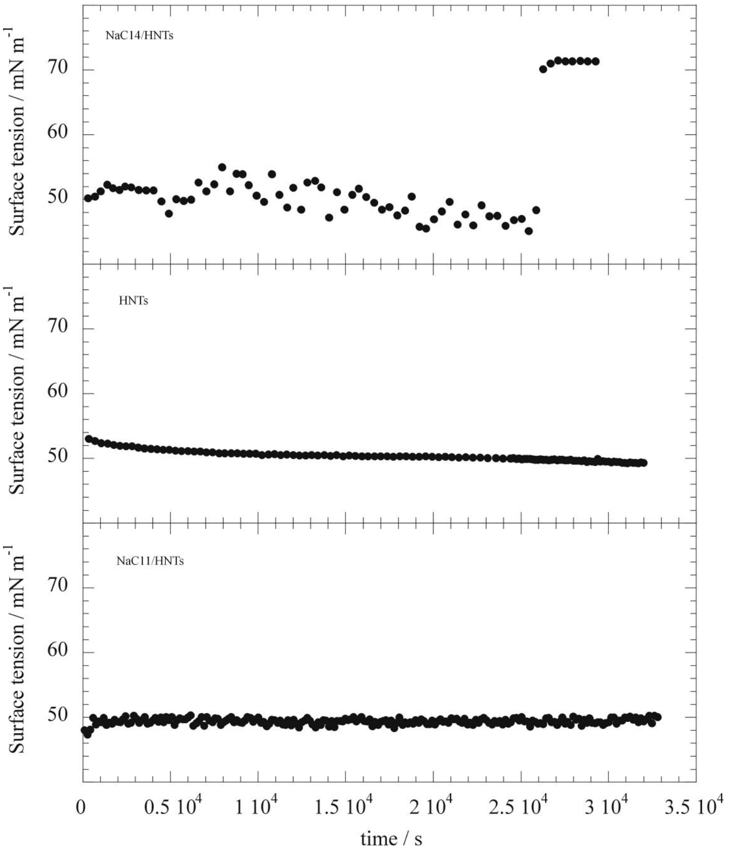

Figure 5.2.2. Surface tensions as functions of time of HNT, NaC11/HNTs and NaC14/HNTs dispersed in water in the presence of n-decane film.

Peculiar is the S-shaped trend for NaC14/HNTs which exhibits a value around 50 mN m^{-1} (due to the presence of n-decane at the interface) for severals hours thereafter it sharply increases reaching the water value (72 mN m^{-1}). Such a jump reveals the disappearance of n-decane and it was attributed to the entrapment into the hydrophobic cavity of the nanotubi. The adsorption onto the native HNTs is negligible. The efficiency of the hybrid surfactant/HNTs material specific of the surfactant tail, agrees with the fact NaC14 forms complex structures into the lumen of HNTs while NaC11 does monolayer.

5.3 Solubilization ability of alkanoate surfactant/HNTs towards toluene

The functionalized HNTs were also tested to entrap toluene solubilized in water at a concentration lower than its solubility. Figure 5.3.1 shows the difference of the removed toluene by the hybrid material, at variable aqueous concentration (C_{ads}), with respect to the pristine HNTs (ΔR). The surfactant tail tuned the affinity towards the oil; accordingly, higher alkyl chain surfactants exhibited a higher affinity towards toluene. Furthermore, the NaC11/HNTs system does not improve at all the encapsulation properties of HNTs. In spite the loaded amount of NaC12 into the HNTs lumen is slightly larger than that of NaC14, HNTs/NaC14 exhibits a larger solubilizing power indicating that the formed complex structures, likely double layers, possess an hydrophobicity established by the alkyl chain length.

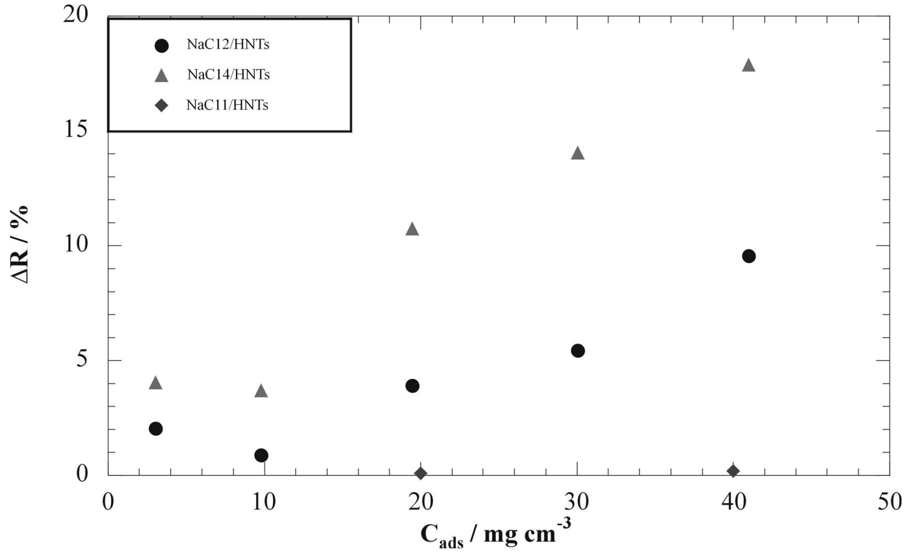

Figure 5.3.1. Toluene removal efficiency from aqueous dispersions of NaC11/HNTs, NaC12/HNTs and NaC14/HNTs calculated as percentage increment with respect to the removal obtained by pristine HNTs as a function of hybrid material concentration.

These results are in line with those obtained for the liquid n-decane solubilization corroborating the findings that the surfactant monolayer of NaC11/HNTs possess somewhat a hydrophilic character likely due to the presence of water while the more complex surfactant structures of NaC12/HNTs and NaC14/HNTs behave like conventional micelles.

5.4 Solubilization ability NaC12/HNTs towards antraquinone

The encapsulation ability of NaC12/HNTs hybrid towards the antraquinone (AQ) was investigated. AQ is an apolar biocide with a killing activity against the sulfate reductive bacteria. Figure 5.4.1 shows that the modified HNTs are more efficient than pristine HNTs to entrap AQ because of the hydrophobic lumen.

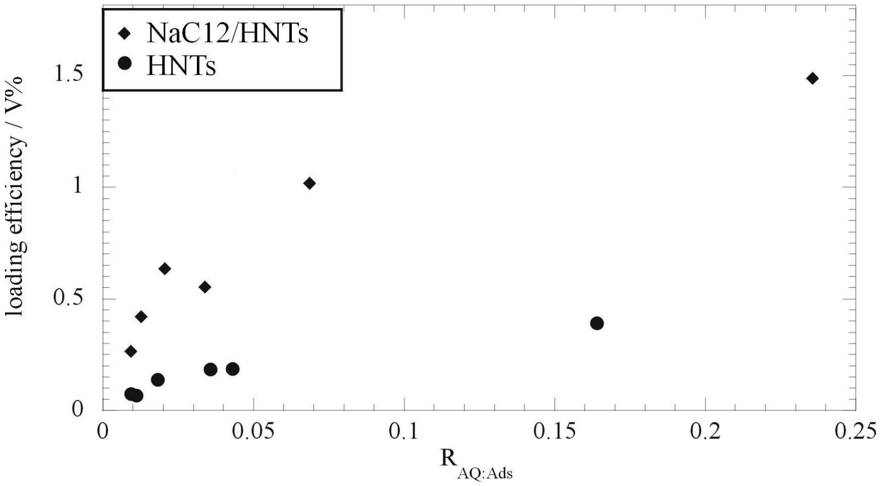

Figure 5.4.1. Antraquinone loading efficiency of HNT and HNT/NaC12 as function of the biocide/adsorbent material weight ratio

To evaluate the effectiveness of NaC12/HNTs as bionanocontainer release experiments of AQ in aqueous media were performed. Figure 5.4.2 evidences that the kinetics of AQ release is slower for the hybrid with respect to the pure HNTs. Even after 20 hours AQ was released from the hydrophobic lumen of HNT/NaC12. This finding was confirmed by the biological experiments.

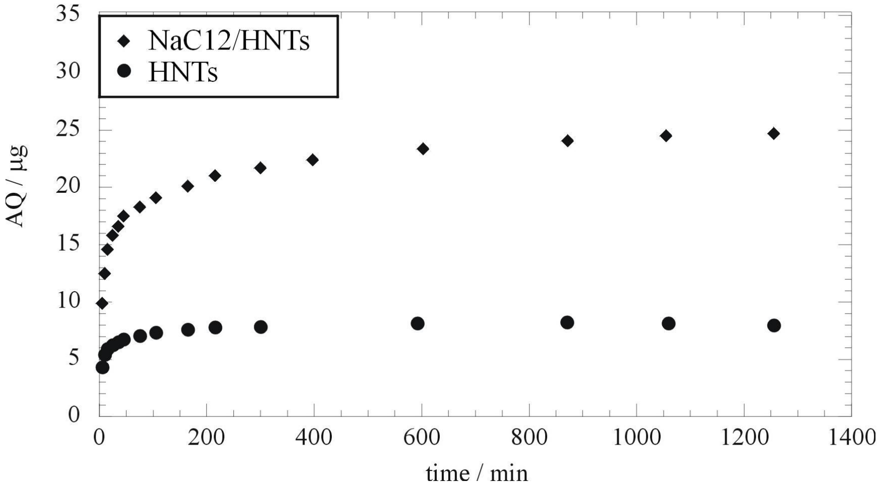

Figure 5.4.2. Release of AQ as function of time for pristine HNT and HNT/NaC12 with $R_{AQ:Ads} = 0.01$.

Antibacterial action towards *Desulfovibrio desulfuricans* was investigated by means of Fluorescein Diacetate (FDA) hydrolysis assay. The results, reported in Figure 5.4. 3, evidence that the AQ loaded nanotubes present a larger antibacterial action time with respect to the pure AQ. This finding is fundamental for potential biotechnological applications of these nanomaterials. Moreover, accordingly with the larger AQ loading, the killing bacterial activity of AQ loaded NaC12/HNTs is stronger compared to that of AQ loaded HNTs.

Currently, further biological experiments at Louisiana Tech University are in progress.

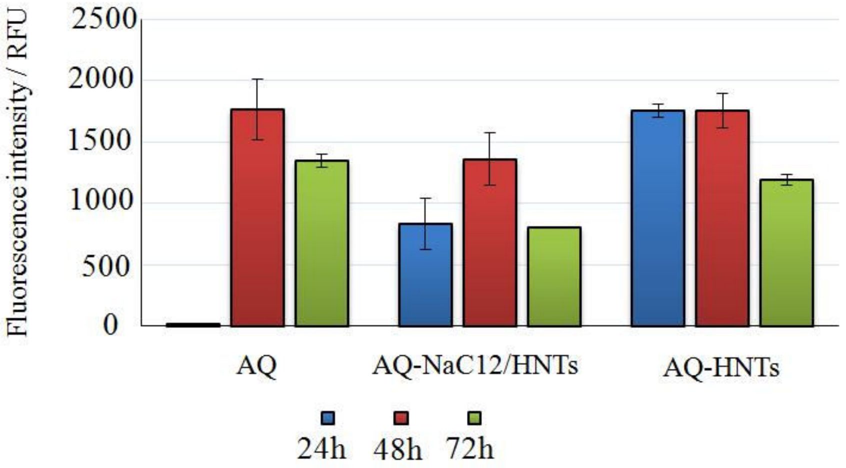

Figure 5.4.3. FDA hydrolysis assay results at different time for pure AQ, AQ loaded NaC12/HNTs and AQ loaded HNTs.

5.5 Oxygen reservoir ability of NaPFC8/HNTs

HNTs functionalized with fluorinated surfactants can be promising as oxygen nanoreservoir in aqueous media being that fluorinated solvents are able to solubilize large amount of gas. To explore this perspective, aqueous dispersions of both HNTs and NaPFC8/HNTs (2.0 wt%) were saturated with oxygen and left to equilibrate with air under vigorous stirring (1250 rpm) or static conditions. For the results collected under stirring (Figure 5.5.1), the time required for the O_2 concentration to halve its initial value ($t_{1/2}$) shows that the hybrid material behaves like an O_2 reservoir that releases the gas in water over time to contrast the desaturation of the aqueous dispersion resulting an efficient tool in retarding the O_2 desaturation.

It is impressive the key role played by the nanotubes on the oxygen release under static situations (Figure 5.5.1). Both HNTs and NaPFC8/HNTs are efficient in keeping the supersaturation state. Nevertheless, after 6 h the HNTs dispersion released ca. 50 % of O_2 while the hybrid nanotubes showed an oxygen loss of only ca. 10%. The strong enhancement of oxygen entrapment ability of the modified lumen is generated by the presence of only 0.86 wt% of surfactant into the HNTs, which corresponds to the concentration value of 5×10^{-5} mol kg^{-1} in water that is two order of magnitude smaller than the sodium perfluoroctanoate critical micellar concentration (0.05 mol kg^{-1}).[23]

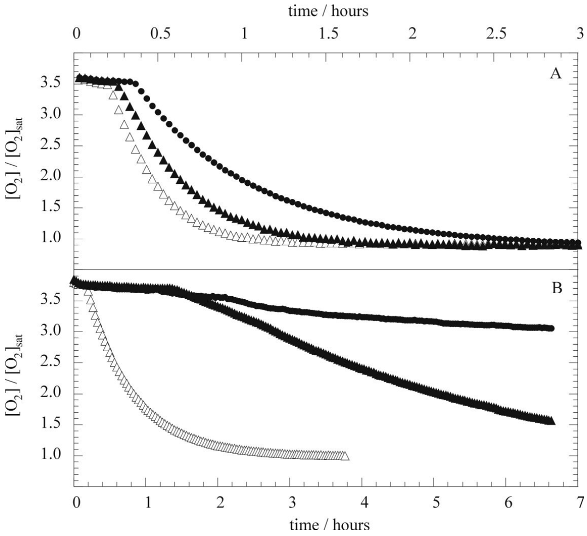

Figure 5.5.1. Oxygen concentration as a function of time in water (Δ) and in aqueous dispersions of HNTs (▲) and NaPFC8/HNTs (●). Data collected under magnetic stirring at 1250 rpm (A) and under static conditions (B).

5.6 Microchannels of aligned PSS/HNTs

As preliminary results, Figure 5.6.1 reports SEM photos of microchannels formed by PSS/HNTs and pristine HNTs. These structures were obtained by using the droplet casting method at 65 °C. It was observed that the functionalization of the HNTs cavity with PSS favors the nanotubes' alignment. The interpretation of these results can be made by considering the coffee ring effect and the Onsager theory for charged nanorods. Based on this theory the formation of a nematic phase is enhanced by increasing the charge of the nanoparticles. As reported in Chapter 3, the presence of PSS enhances the HNTs surface negative charge. The complete comprehension of these findings is still under investigation.

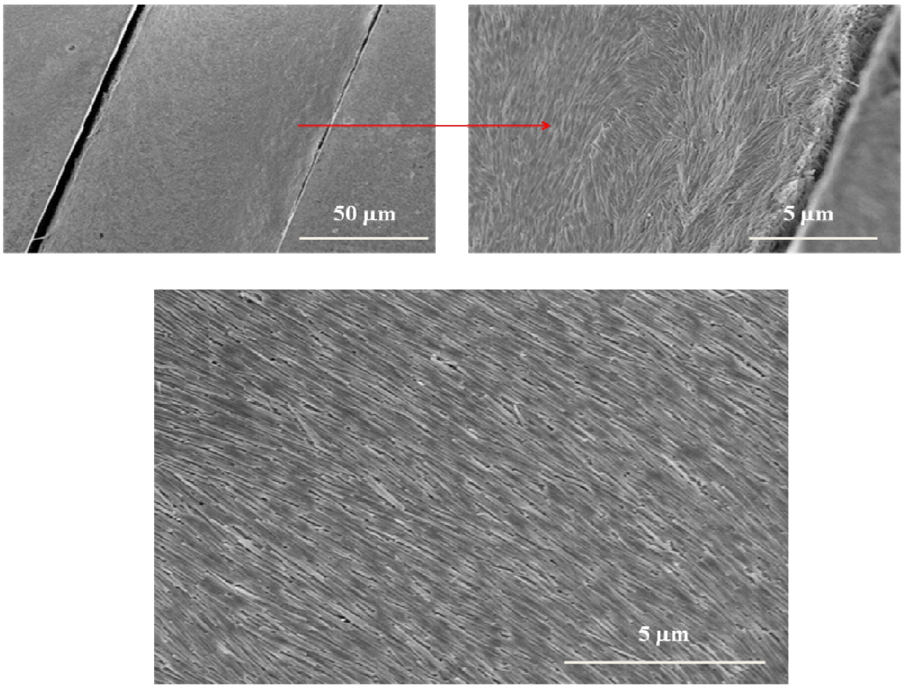

Figure 5.6.1. Scanning electron micrographs of PSS/HNTs structures obtained by droplet casting method at 65 °C.

5.7 Solubilization ability of alginate/HNTs gel beads towards crystal violet

The good adsorption efficiency of the composite gel beads is exhibited by the change in the adsorption generated by the gel loaded with clay minerals. As Figure 5.7.1 shows, HNTs enhances the gel beads ability in capturing CV; for instance, at the alginate/HNTs mass ratio of 2:1, at stoichiometric concentration of adsorbent material (C_s) = 0.25 and 0.50 mass%, the $R_{\%}$ value is increased by ca. 55 and 45 %, respectively. This sharp increase is even larger than that calculated by assuming the simple rule of mixtures (Figure 5.7.1) and it proves that the combination of HNTs and biopolymer generates synergistic effects in the adsorption properties of hybrids beads based on alginate.

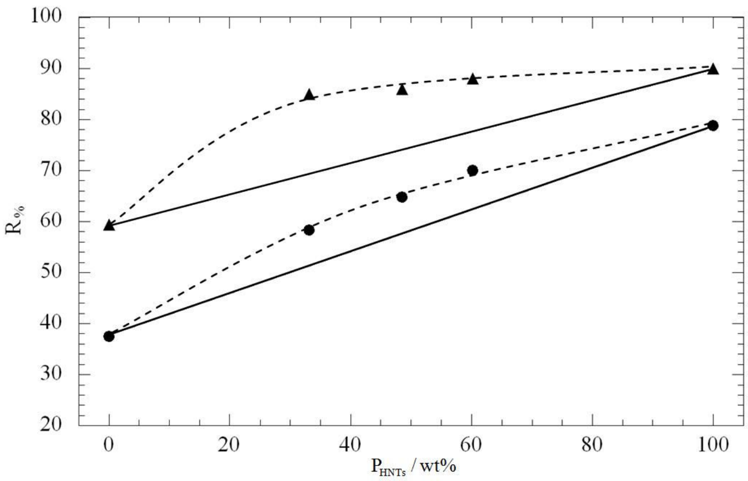

Figure 5.7.1 Dependence on HNTs concentration of percent of removed CV from aqueous phase calculated from data in Table 2. (●), C_s=0.25 mass% and (▲), C_s=0.5 mass%. Solid lines are calculated by rule of mixtures. Broken lines are guide for eyes.

5.8 Sorption ability of alginate/pectin hybrid gel beads towards Cd(II) and Cu(II)

The sorption process of Cd(II) and Cu(II) ions from solution by mixed alginate/pectin gel beads at different concentration ratios was evaluated on the basis of kinetic and equilibrium studies. The sorption process follows a pseudo second-order kinetic model and the adsorption capacity increases with the increasing of pectin percentage in the mixed alginate/pectin gel system. The Langmuir isotherm model fits equilibrium data better than the Freundlich model. Micrographies from SEM analysis (as an example Figure 5.8.1 reports Ca-AP_2 gel bead after the Cu^{2+} adsorption) show that the ions sorption makes the surfaces more wrinkled with many creases and pores. This peculiar morphology may be attributed to the shrinkage of the beads at higher metal concentrations.

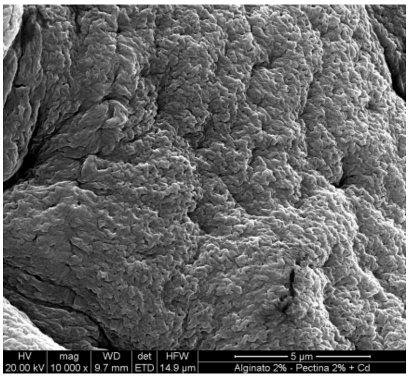

Figure 5.8.1 Surface scanning electron micrograph of Ca-AP_2 after Cu^{2+} sorption.

6. Bionanocomposites based on nanoclays

6.1 Biopolymer/nanoclay composite films

This chapter is focused on the studies of films based on HPC and HNTs (attached paper I). The films were prepared by casting method from aqueous solutions. The HNTs concentration (C_f) was systematically varied in a very extended range.

The morphological analysis was helpful to explain the nanomaterial features as well as the thermal stability, transparency, wettability and dielectric properties.

A previous extended physico-chemical study[15] on bionanocomposites based on nanoclays with different shape (HNTs, laponite nanodisks and kaolinite sheets) and pectins evidenced that HNTs are good candidates to form bionanocomposite films with interesting properties. The prepared composites exhibited evident differences in the macroscopic aspect.

The biocomposites based on HNTs and kaolinite showed compact mechanical features while those based on laponite (Figure 6.1.1) presented a structural deterioration.

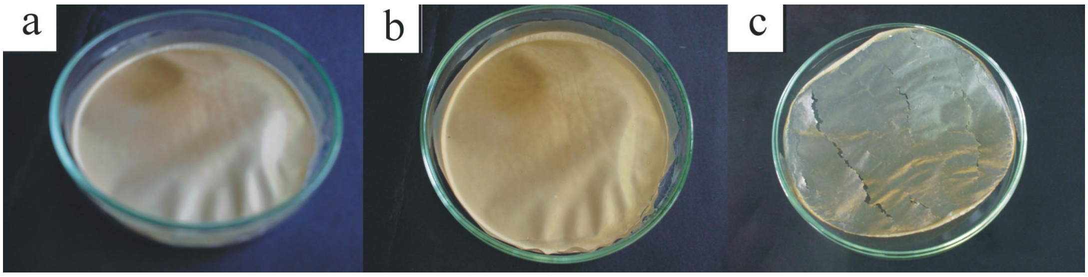

Figure 6.1.1. Films of nanocomposites formed by HM pectin and HNTs (a, C_f = 60%), kaolinite (b, C_f = 60%) and laponite (c, C_f = 30%). The diameter of the Petri dish is 9 cm.

6.2 Thermal and dielectric properties

The presence of small amounts of nanofiller causes the HPC thermal stabilization (up to 10 °C) while a further addition of HNTs (above $C_f \approx 20$ wt%) enhances the thermal degradation that occurs at temperature even 65 °C below degradation temperature (T_d) of pristine HPC.

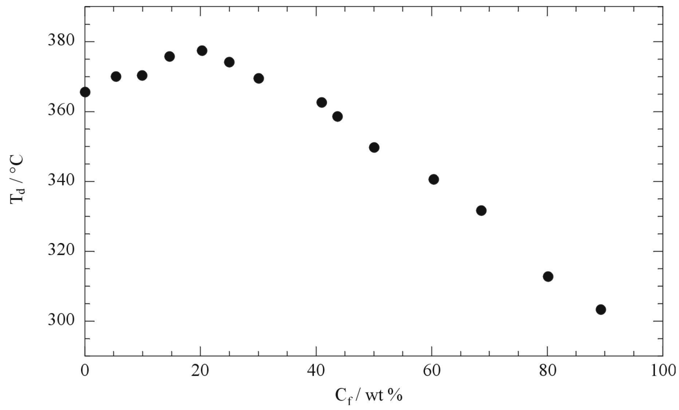

Figure 6.2.1. Degradation temperature as a function of the filler concentration for HPC/HNTs films.

According to the study of pectin/HNTs nanocomposites, the thermal stabilization of polymers in the presence of halloysite is generally observed[13,25] and ascribed to the entrapment of the volatile products (obtained from the polymer thermal decomposition) into the HNTs lumen. Moreover, commonly the effect on T_d of inorganic fillers in the polymeric matrices is discussed in terms of barrier effects towards both mass and heat transports; in particular, a composite material with well dispersed nanoparticles typically shows a thermal reinforcement. The opposite effect generated by HNTs is an indication of the structural change of the material.

By determining thermograms at variable heating rates the activation energy of HPC degradation was determined. Once again we observe two different behaviours occurring in the low and high concentration regimes and it was concluded that large amounts of nanotubes surprisingly enhance the thermal degradation of HPC.

The structural change on the HPC based nanocomposites occurring between the two regions agree with the dielectric properties. It was established that HPC shows the relaxation processes related to the local chain motion via the glucosidic bond (β-relaxation) and to the motion of the side groups attached to the glucosic unit of the polysaccharides (γ-relaxation) both in the range from 10^6 to 10^7 Hz.[21] Very recently, dielectric spectroscopy evidenced free water relaxation at ca. 10^{10} Hz for wet HPC samples.[22] To the light of these insights the dielectric constant (ε_r) and the dispersion factor (tanδ) data as functions of the frequency (ν) for HPC in the absence and the presence of HNTs evidence the polymer relaxation (examples are in Figure 6.2.2). The profile is strongly altered by the HNTs being that the peak is shifted toward lower frequencies and it becomes wider.

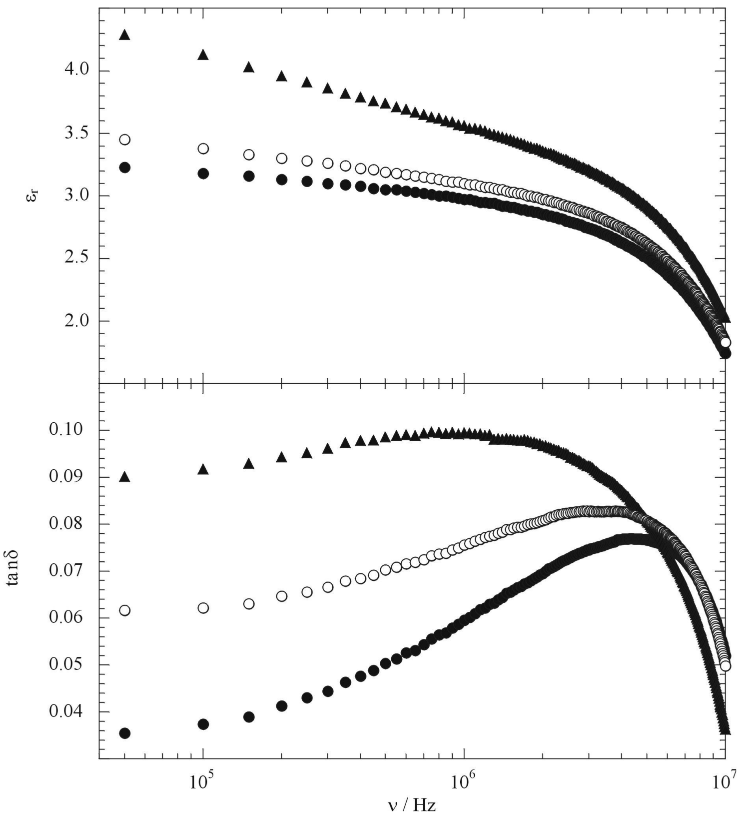

Figure 6.2.2. The dielectric constant and the dispersion factor as functions of the frequency for HPC/HNTs films at $C_f = 0$ wt % (●) , $C_f = 25$ wt % (○) and $C_f = 70$ wt % (▲).

Interesting insights are provided by the relaxation frequency at the maximum of tanδ (ν_{max}) vs C_f trend. As Figure 6.2.3 illustrates, ν_{max} slightly changes to $C_f \approx 20$ wt% thereafter it sharply decreases upon the HNTs addition. The decrease of ν_{max} is ascribable to the increase of the characteristic relaxation time and therefore to the reduced mobility of the polymer moiety in the presence of large amount of HNTs.

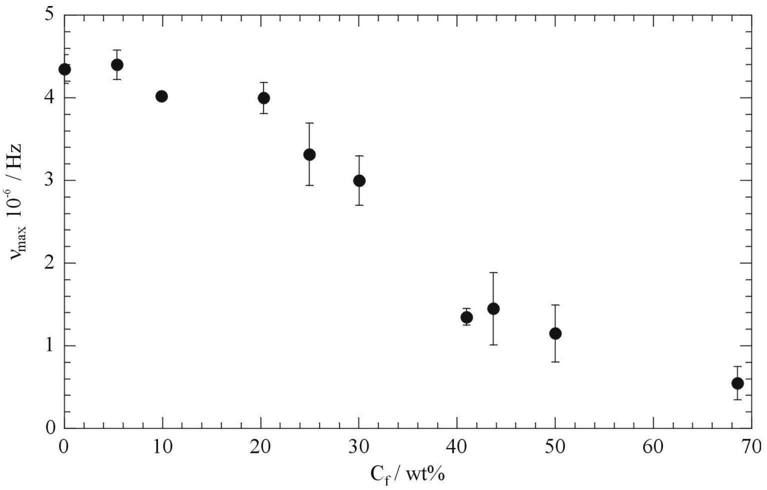

Figure 6.2.3. The relaxation frequency as a function of HNTs concentration for HPC/HNTs films.

6.3 Morphology

The morphology study evidenced the correlation between structure of the film and its properties. The morphology of the hybrid surfaces at both low and high HNTs content is very peculiar in the case of films based on HPC because the surface appears homogeneous and the presence of nanoparticles is rare. As evidenced in Figure 6.3.1, this morphology is very different from that of LM pectin/HNTs films which showed dispersed HNTs into the polymer matrix.[13]

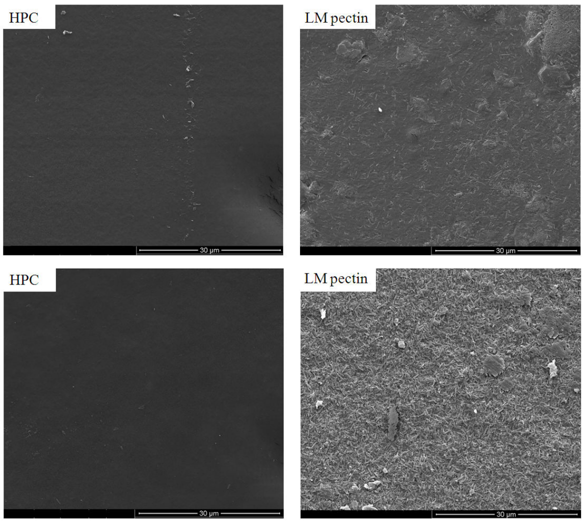

Figure 6.3.1. Scanning electron microscopy images of HPC/HNTs and LM pectin/HNTs films. The HNTs concentration is: top, C_f = 10 wt %; bottom, C_f = 60 wt %.

The SEM micrographies (Figure 6.3.2) of the edges of the nanocomposites in high filler content show that the nanotubes are well compacted between two smooth thin layers of HPC in a sandwich-like structure.

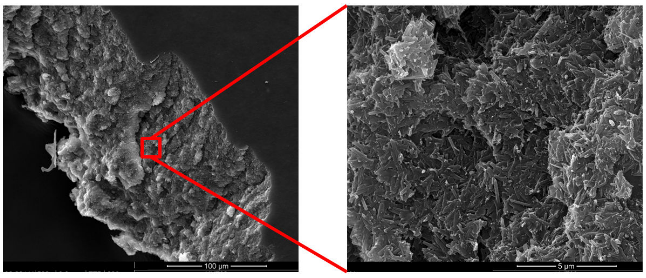

Figure 6.3.2. Scanning electron microscopy images of cross section of HPC/HNTs film $C_f = 60$ wt %.

One may conclude that the cluster formation is inhibited and that the nanotubes are well dispersed along to the plane directions of the film in the entire concentration range in agreement with SEM insights.

It has to be noted that in the case of HM pectin/HNTs system,[15] the such calculations reflected the organization into clusters of nanotubes (wrapped by the adsorbed pectin) with apparent radii progressively increasing upon the filler addition.

6.4 Surface property: wettability

As observed for LM pectin/HNTs composites, as general result, the water contact angle (ϑ) decreases over time while the drop volume and the contact area decreases and increases, respectively. Therefore, one can conclude that both spreading and water absorption occur during the experiment.

The initial water contact angle (ϑ_i) vs C_f trend evidences a minimum at $C_f \approx 15$ wt% (Figure 6.4.1) that may reflect the variation of the microstructures of the films surface generated by the HNTs, which apparently make the surface more hydrophilic in the low concentration regime and more hydrophobic at high loading. These results agree with the sandwich-like structure composed of two HPC layers incorporating the HNTs observed at high filler regime.

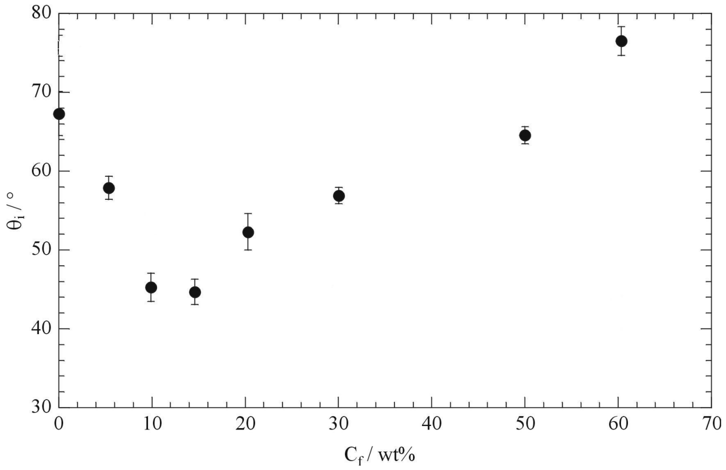

Figure 6.4.1. Dependence of the water contact angle at t=0 s on the filler concentration HPC/HNTs composites.

In principle, one may consider two effects: the HNTs surface concentration and the films surface roughness induced by HNTs. From SEM data one rules out the role of roughness because within the concentrations regime a very flat surface has been imaged. Therefore, the change in the polymer conformations induced by HNTs and the concentration of the species at the interface play the key role.

In the case of LM pectin/HNTs,[16] ϑ_i decreases with C_f because of the enhancement in the surface hydrophilicity as a consequence of the enrichment of the nanofillers at the interface.

7. Plasticized nanocomposites

7.1 Design of performant plasticized nanocomposites

To the light of the growing interest on the environmental and economic problems, nowdays the nanotechnology research has focused its attention on the development of bionanocomposites and sustainable polymer blends, namely, hybrid materials obtained by combining natural and biocompatible components which can be used in many applications, such as in packaging.

Within this issue, the physico-chemical study on poly(ethylene) glycol (PEG)20000/HNTs hybrid system (Attached paper IV) represented the starting point to develop plasticized nanocomposite films based on PEG 20000/LM pectin blend and HNTs (Attached paper VII). PEG 20000 was used as plasticizer to improve the performances of LM pectin/HNTs bionanocomposite films previously studied.[15] The casting method from water was used to prepare these materials. The filler content (C_f) and the LM pectin/PEG 20000 ratio (R_{pp}) were systematically changed. In particular, $R_{pp} = 1$ and $R_{pp} = 4$ were selected.

Properties of technological interest, such as thermal stability, wettability, tensile properties and water uptake behavior, were monitored and they were correlated to the structural features of the nanocomposites.

7.2 Physico-chemical investigation of PEG20000/HNTs

The PEG 20000/HNTs nanocomposites morphology (Figure 7.1.1) shows that the the filler is well dispersed into the polymer matrix on both the surface and the core of the material. At high C_f content, the nanocomposite clearly appears less compact with several irregular craters (having a size of ca. 10 μm) present on both the surface and the edge. Such a structure is consistent with results of enthalpy of PEG 20000 melting (ΔH_m) which decreases upon the addition of HNTs indicating a reduction of the polymer crystallinity. In fact, these results are interpreted by assuming that: 1) some segments of the adsorbed macromolecules are radiating away from the surface forming loops and tails; 2) the portion of the polymer in contact with the HNTs surface cannot melt because of constraints due to the nanoclay anchoring; and 3) the unbound polymer in the nanocomposites behaves like the pristine one.[106]

The addition of HNTs to PEG 20000 generates a monotonic decrease of polymer melting temperature (T_m) in the entire range of investigated composition ascribed to a good dispersion of the nanofiller into the polymeric matrix.[107]

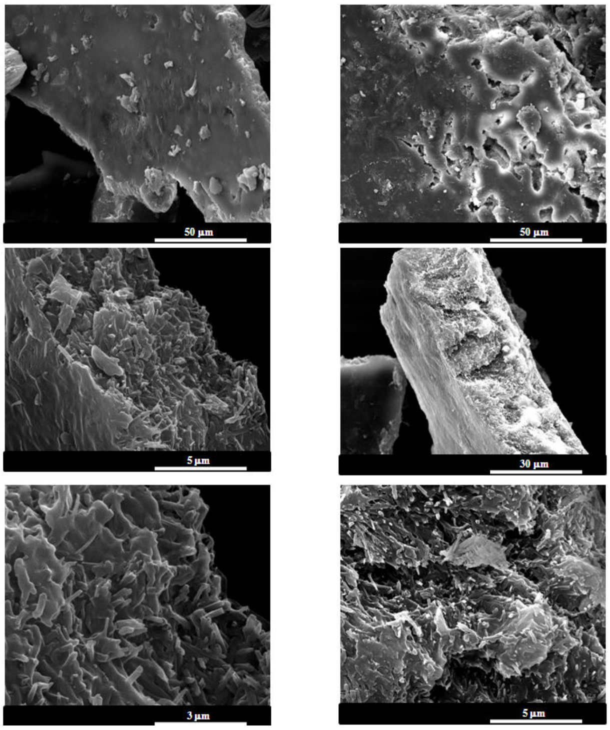

Figure 7.1.1. Scanning electron micrographs for nanocomposites at filler concentration of 10 wt% (left hand side) and 50 wt% (right hand side).

The effect of HNTs on the PEG 20000 resistance to thermal degradation is similar to that observed for HPC/HNTs films (Figure 7.1.2).

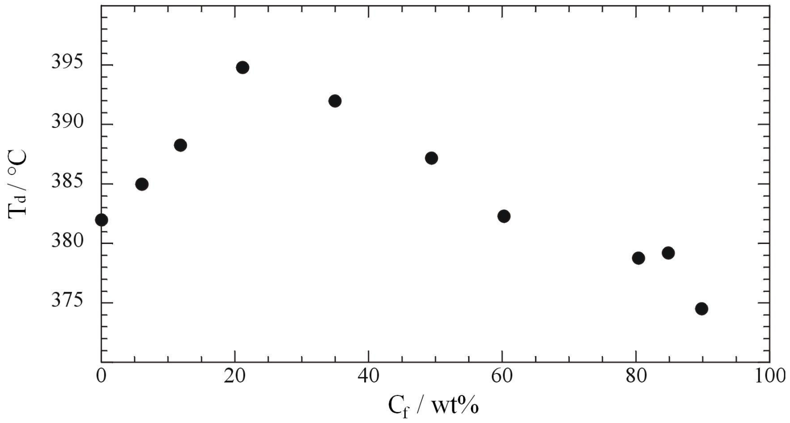

Fig. 7.1.2. PEG 20000 degradation temperature as a function of filler concentration.

These data were interpreted by invoking the compact structure at low C_f and a deteriorated structure at high C_f content.

7.3 Physico-chemical studies of LM pectin/PEG 20000 blend

The wettability of LM pectin/PEG blend film (R_{pp} =4) shows that the addition of the plasticizer caused a small but significant increase (ca. 5°) of LM pectin θ_i despite the PEG 20000 hydrophilic nature (Table 7.3.1). This effect is ascribable to the increase of the surface roughness as evidenced by SEM images (Figure 7.3.1) showing that the surface of the LM pectin/PEG 20000 blend is very rough with many craters (size of ca. 2 μm), while the LM pectin surface is smooth.

Table 7.3.1. The water contact angle at $\tau = 0$ for LM pectin, PEG 20000 and the LM pectin/PEG 20000 blend ($R_{pp} = 4$).

	θ_i
LM Pectin	75 ± 1
PEG 20000	28 ± 1
LM Pectin/PEG 20000 ($R_{pp} = 4$)	80 ± 2

Unit is: θ_i, °.

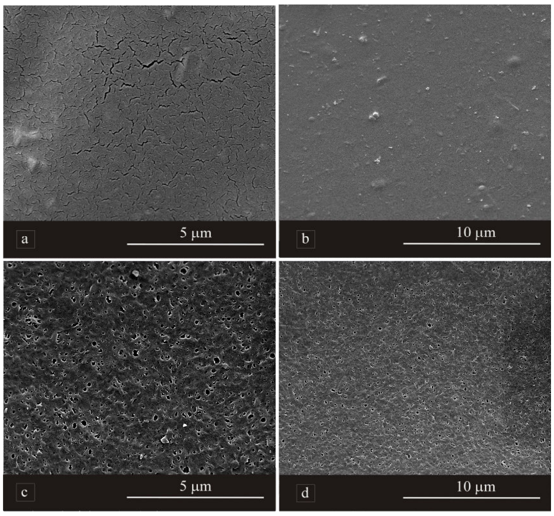

Figure 7.3.1. Scanning electron microscopy images for surface of pristine LM pectin (a,b) and LM pectin/PEG 20000 blend with R_{pp} = 4 (c,d).

Water uptake (WU%) of the blend at variable relative humidity (Rh%) (Table 7.3.2) showed that the water uptake (WU%) are lower than those for the LM pectin.

Table 7.3.2. Water uptake values at different relative humidity.

WU% (Rh = 33%)	WU% (Rh = 75%)	WU% (Rh = 97%)
LM Pectin		
3.6 ± 0.7	8.2 ± 0.8	14 ± 2
LM Pectin/PEG 20000 (R_{pp}=4)		
1.3 ± 0.3	5.0 ± 0.9	8 ± 1
LM Pectin/PEG 20000/HNTs (R_{pp}=4, C_f = 50.52 wt%)		
1.3 ± 0.1	4.7 ± 0.8	7 ± 1

The plasticization of LM pectin with PEG 20000 changed the tensile properties of the biopolymer. A similar result was also observed for chitosan/PEG 20000 blends.[108] The addition of PEG 20000 (R_{pp}=4) generated a slight improvement of the elastic modulus (ca. 10%) with respect to the pristine polymer,[15] while both the stress and the elongation at breaking point decreased.

7.4 Physico-chemical studies of plasticized bionanocomposites

The general trend of θ_i vs C_f (Figure 7.4.1) shows that over the low filler loading regime θ_i is nearly equal to that of the blend and for high regime θ_i sharply decreases in agreement with the enhancement of the surface hydrophilicity.

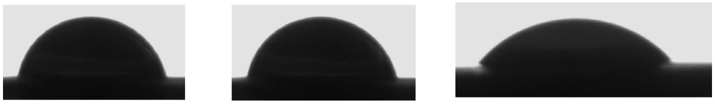

0 wt% 10 wt% 50 wt%

Figure 7.4.1. Optical images of water drops just after the deposition on bionanocomposites with R_{pp} = 4 and variable filler content.

These results were straightforwardly understood to the light of the morphological study (Figure 7.4.2) by taking into account the roughness and the population of HNTs at the interface.

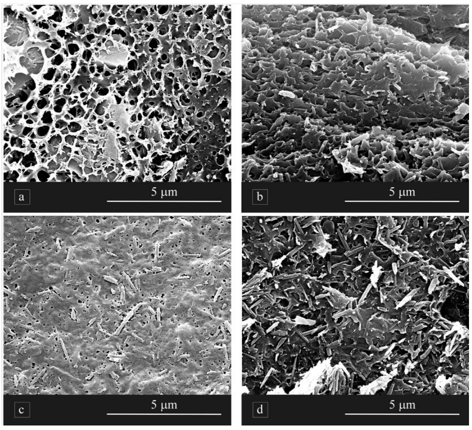

Figure 7.4.2. Scanning electron microscopy images of surface (a,c) and cross section (b,d) of bionanocomposites with R_{pp} = 4. The filler content is: top, C_f = 10 wt%; bottom, C_f = 30 wt%.

The addition of large amount of HNTs to the blend generated biomaterials with unaltered WU% (Table 7.3.2) in spite of the hydrophilic nature of the nanoclay. This is promising for applications in several field such as coatings for food conservation. As concerns the tensile properties, the elastic modulus increases upon HNTs addition (Figure 7.4.3) in agreement with the good dispersion of the filler into the polymer matrix.

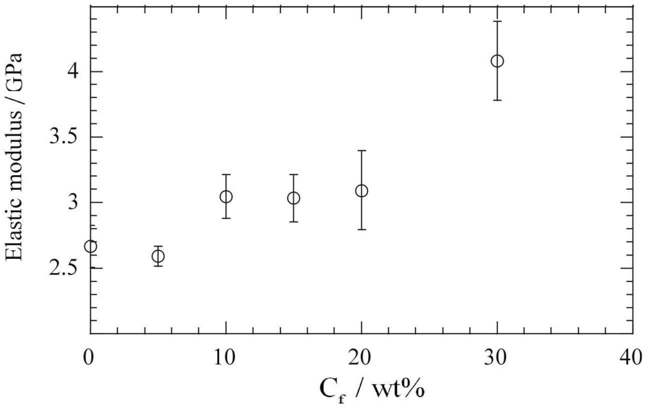

Figure 7.4.3. Elastic modulus of bionanocomposites with R_{pp} = 4 as function of filler content.

Bionanocomposites with R_{pp} = 1 were not studied by tensile tests because of their high fragility. The thermal behavior is rather intriguing. It appears that the LM pectin degradation temperature (T_{d1}) increases in the presence of HNTs with a larger slope for R_{pp}=4 (Figure 7.4.4) in agreement with the lumen encapsulation of the pectin degradation products delaying the mass transport. The PEG 20000 thermal destabilization (Figure 7.4.4) generated by the pectin proves that the HNTs hollows are no more available to incorporate the PEG 20000 degradation products.

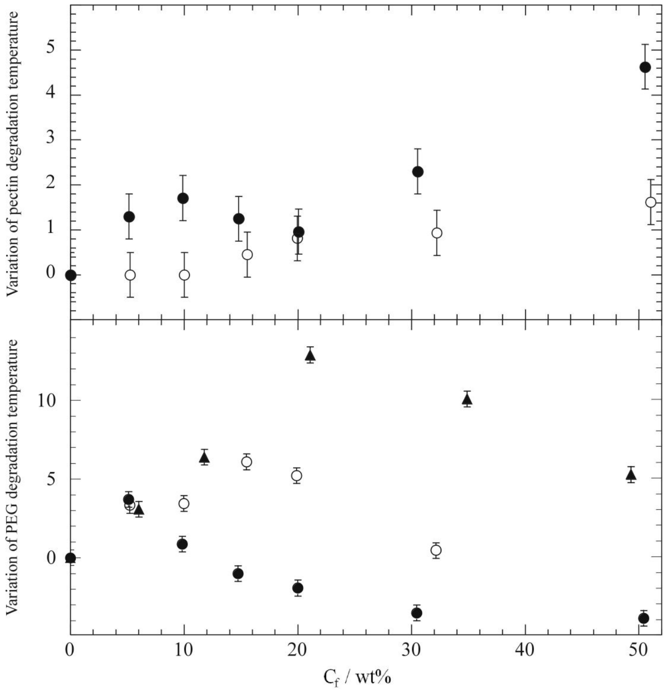

Figure 7.4.4. Variation of the degradation temperature of the pectin (top) and PEG 20000 (bottom) as function of the filler content for bionanocomposites with $R_{pp} = 0$ (▲), $R_{pp} = 1$ (○) and $R_{pp} = 4$ (●).

The addition of HNTs to the blends essentially did not modify the crystallinity of PEG 20000 so that one may conclude that competitive processes of HNTs/pectin and HNTs/PEG 20000 interactions take place and that the interactions of pectin with the nanoclay surface appears privileged.

8. Concluding remarks

Biopolymer/nanoclay composite films were successfully prepared by the casting method from water. The nature of the matrix and the shape of the filler exercise a key role on the morphological and macroscopic properties of the materials. In particular, it was observed that HNTs are proper fillers to develop composite films based on pectins and HPC. These materials are competitive with many traditional plastics from mechanical and thermal view point and, therefore, they are promising for packaging applications. Within this issue, the plasticization of pectin/HNTs films with PEG allowed us to tune the elastic properties. As concerns the morphological characteristics, a sandwich like structure and a uniform filler distribution were found for HPC/HNTs and pectin/HNTs nanocomposites, respectively (Scheme 1). A good correlation between the morphologies and some macroscopic properties, such as transparency and wettability, was observed.

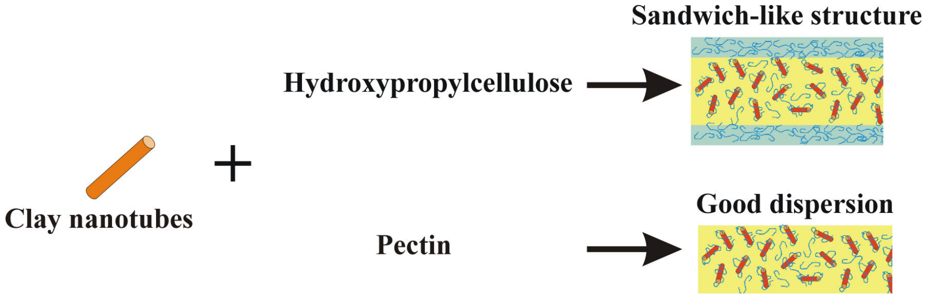

Scheme 1. Sketch representation of nanocomposites morphologies.

The physico-chemical studies on the aqueous mixtures used to prepare the bionanocomposite films showed that polymers are adsorbed onto the nanoclays surfaces endowing the formation of stable dispersions. In particular, an efficient stabilization of HNTs in water was evidenced by using anionic polymers, such as CMC, alginate, pectins and PSS, that are adsorbed into the lumen. Obtaining HNTs with a good aqueous colloidal stability is fundamental for decontamination and micromanifacture purposes. This approach was appreciated by companies and currently is tested for new applications in petroleum drilling formulations at *Schumbelger* (Texas – US). As concerns laponite, it was demonstrated that the adsorption of HPC onto the laponite surface is energetically favored and enthalpy driven. This process is triggered by temperature and/or inorganic salts, therefore it opens up to new routes for the control of polymer-nanoparticles interactions with the aim at obtaining smart materials.

New hybrid nanomaterials were prepared exploiting electrostatic forces between ionic surfactants with different head group charges and HNTs. It was demonstrated that the adsorption of negatively charged surfactant, even if it occurs at the inner surface of the HNTs, generates the higher stabilization effect of the nanotubes in water while either the cationic surfactant or the salt addition enhance the precipitation. Furthermore, the functionalization of the HNTs lumen endowed to develop inorganic micelles with an hydrophobic pocket able to solubilize aromatic and aliphatic hydrocarbons (Scheme 2). The modification of the HNTs cavity with anionic fluorinated surfactants leads to obtain oxygen nanoreservoirs. The incorporation of an apolar biocide into the HNTs lumen is the starting point for the development of geopolymers produced by LA Tech University and, currently, tested by NASA. Certainly, anionic surfactants/HNTs hybrids are very promising for environmental and biotechnological applications.

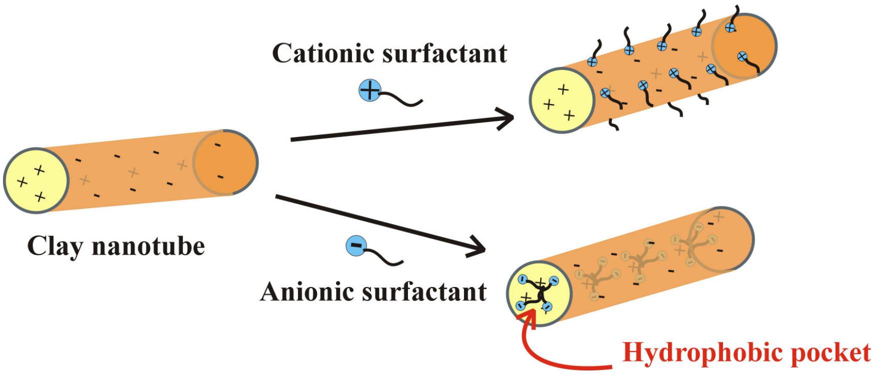

Scheme 2. Sketch representation of surfactant/HNTs structures.

9. Referencees

(1) Yu, L.; Dean, K.; Li, L. *Prog. Polym. Sci.* **2006**, *31*, 576–602.

(2) Tharanathan, R. N. *Trends Food Sci. Technol.* **2003**, *14*, 71–78.

(3) Nurchi, V. M.; Villaescusa, I. *Coord. Chem. Rev.* **2012**, *256*, 212–221.

(4) Peretz, S.; Cinteza, O. *Colloids Surf. Physicochem. Eng. Asp.* **2008**, *319*, 165–172.

(5) Liu, R.; Zhang, B.; Mei, D.; Zhang, H.; Liu, J. *Desalination* **2011**, *268*, 111–116.

(6) De Lisi, R.; Lazzara, G.; Milioto, S.; Muratore, N. *Langmuir* **2006**, *22*, 8056–8062.

(7) Luo, P.; Zhang, J.; Zhang, B.; Wang, J.; Zhao, Y.; Liu, J. *Ind Eng Chem Res* **2011**, *50*, 10246–10252.

(8) Barrientos-Ramírez, S.; Ramos-Fernández, E. V.; Silvestre-Albero, J.; Sepúlveda-Escribano, A.; Pastor-Blas, M. M.; González-Montiel, A. *Microporous Mesoporous Mater.* **2009**, *120*, 132–140.

(9) Shchukin, D. G.; Sukhorukov, G. B.; Price, R. R.; Lvov, Y. M. *Small* **2005**, *1*, 510–513.

(10) Abdullayev, E.; Sakakibara, K.; Okamoto, K.; Wei, W.; Ariga, K.; Lvov, Y. *ACS Appl Mater Interfaces* **2011**, *3*, 4040–4046.

(11) Wan, C.; Li, M.; Bai, X.; Zhang, Y. *J. Phys. Chem. C* **2009**, *113*, 16238–16246.

(12) Shamsi, M. H.; Geckeler, D. V. *Nanotechnology* **2008**, *19*, 075604.

(13) Abdullayev, E.; Price, R.; Shchukin, D.; Lvov, Y. *ACS Appl. Mater. Interfaces* **2009**, *1*, 1437–1443.

(14) Lvov, Y. M.; Shchukin, D. G.; Mohwald, H.; Price, R. R. *ACS Nano* **2008**, *2*, 814–820.

(15) Cavallaro, G.; Lazzara, G.; Milioto, S. *Langmuir* **2011**, *27*, 1158–1167.

(16) Cavallaro, G.; Donato, D. I.; Lazzara, G.; Milioto, S. *J Phys Chem C* **2011**, *115*, 20491–20498.

(17) Du, M.; Guo, B.; Jia, D. *Polym. Int.* **2010**, *59*, 574–582.

(18) Joussein, E.; Petit, S.; Churchman, J.; Theng, B.; Righi, b.; Delvaux, B. *Clay Min.* **2005**, *40*, 383.

(19) Vergaro, V.; Abdullayev, E.; Lvov, Y. M.; Zeitoun, A.; Cingolani, R.; Rinaldi, R.; Leporatti, S. *Biomacromolecules* **2010**, *11*, 820–826.

(20) Luo, P.; Zhao, Y.; Zhang, B.; Liu, J.; Yang, Y.; Liu, J. *Water Res.* **2010**, *44*, 1489–1497.

(21) De Lisi, R.; Lazzara, G.; Milioto, S.; Muratore, N. *Chemosphere* **2007**, *69*, 1703–1712.

(22) Abdullayev, E.; Joshi, A.; Wei, W.; Zhao, Y.; Lvov, Y. *ACS Nano* **2012**, *6*, 7216–7226.

(23) Zhao, Y.; Zhang, B.; Zhang, Y.; Wang, J.; Liu, J.; Chen, R. *Sep. Sci. Technol.* **2010**, *45*, 1066–1075.

(24) Shu, X. Z.; Shu, K. J. *J Microencapsul* **2001**, *18*, 713.

(25) Yah, W. O.; Xu, H.; Soejima, H.; Ma, W.; Lvov, Y.; Takahara, A. *J Am Chem Soc* **2012**, *134*, 12134–12137.

(26) Abdullayev, E.; Abbasov, V.; Tursunbayeva, A.; Portnov, V.; Ibrahimov, H.; Mukhtarova, G.; Lvov, Y. *ACS Appl. Mater. Interfaces* **2013**, *5*, 4464–4471.

(27) Abdullayev, E.; Lvov, Y. *J Mater Chem* **2010**, *20*, 6681–6687.

(28) Zhang, A.-B.; Pan, L.; Zhang, H.-Y.; Liu, S.-T.; Ye, Y.; Xia, M.-S.; Chen, X.-G. *Colloids Surf. Physicochem. Eng. Asp.* **2012**, *396*, 182–188.

(29) Guo, B.; Chen, F.; Lei, Y.; Liu, X.; Wan, J.; Jia, D. *Appl. Surf. Sci.* **2009**, *255*, 7329–7336.

(30) Ye, Y.; Chen, H.; Wu, J.; Ye, L. *Polymer* **2007**, *48*, 6426–6433.

(31) Wei, W.; Abdullayev, E.; Hollister, A.; Mills, D.; Lvov, Y. M. *Macromol. Mater. Eng.* **2012**, *297*, 645–653.

(32) Qiao, J.; Adams, J.; Johannsmann, D. *Langmuir* **2012**, *28*, 8674–8680.

(33) Lin, Y.; Ng, K. M.; Chan, C.-M.; Sun, G.; Wu, J. *J. Colloid Interface Sci.* **2011**, *358*, 423–429.

(34) Lecouvet, B.; Gutierrez, J. G.; Sclavons, M.; Bailly, C. *Polym. Degrad. Stab.* **2011**, *96*, 226–235.

(35) Dong, F.; Wang, J.; Wang, Y.; Ren, S. *J. Mater. Chem.* **2012**, *22*, 11093–11100.

(36) Cavallaro, G.; Lazzara, G.; Milioto, S. *Polym. Degrad. Stab.* **2013**, *98*, 2529–2536.

(37) Xie, Y.; Chang, P. R.; Wang, S.; Yu, J.; Ma, X. *Carbohydr. Polym.* **2011**, *83*, 186–191.

(38) Chang, P. R.; Xie, Y.; Wu; D.; Ma; X. *Carbohydr. Polym.* **2011**, *84*, 1426.

(39) Shchukin, D. G.; Lamaka, S. V.; Yasakau, K. A.; Zheludkevich, M. L.; Ferreira, M. G. S.; Mohwald, H. *J. Phys. Chem. C* **2008**, *112*, 958–964.

(40) Yuan, P.; Southon, P. D.; Liu, Z.; Green, M. E. R.; Hook, J. M.; Antill, S. J.; Kepert, C. J. *J. Phys. Chem. C* **2008**, *112*, 15742–15751.

(41) Joshi, A.; Abdullayev, E.; Vasiliev, A.; Volkova, O.; Lvov, Y. *Langmuir* **2012**, *29*, 7439–7448.

(42) Kelly, HM:; Deasy, PB.; Ziaka,, E.; Claffey, N. *Int J Pharm* **2004**, *274*, 167.

(43) Wang, L.; Chen, J.; Ge, L.; Zhu, Z.; Rudolph, V. *Energy Fuels* **2011**, *25*, 3408–3416.

(44) Zhang, D.; Huo, W.; Wang, J.; Li, T.; Cheng, X.; Li, J.; Zhang, A. *J. Appl. Polym. Sci.* **2012**, *126*, 1580–1584.

(45) Machado, G. S.; de Freitas Castro, K. A. D.; Wypych, F.; Nakagaki, S. *J. Mol. Catal. Chem.* **2008**, *283*, 99–107.

(46) Barrientos-Ramírez, S.; Oca-Ramírez, G. M. de; Ramos-Fernández, E. V.; Sepúlveda-Escribano, A.; Pastor-Blas, M. M.; González-Montiel, A. *Appl. Catal. Gen.* **2011**, *406*, 22–33.

(47) Zhang, Z.; Wang, H.; Yao, X.; Zhu, Y. *Cem. Concr. Compos.* **2012**, *34*, 709–715.

(48) Nelson, A.; Cosgrove, T. *Langmuir* **2004**, *20*, 2298–2304.

(49) De Lisi, R.; Gradzielski, M.; Lazzara, G.; Milioto, S.; Muratore, N.; Prévost, S. *J. Phys. Chem. B* **2008**, *112*, 9328–9336.

(50) Willenbacher, N. *J. Colloid Interface Sci.* **1996**, *182*, 501–510.

(51) Jung, H.; Kim, H.-M.; Choy, Y. B.; Hwang, S.-J.; Choy, J.-H. *Appl. Clay Sci.* **2008**, *40*, 99–107.

(52) Jung, H.; Kim, H.-M.; Choy, Y. B.; Hwang, S.-J.; Choy, J.-H. *Int. J. Pharm.* **2008**, *349*, 283–290.

(53) Wang, S.; Wu, Y.; Guo, R.; Huang, Y.; Wen, S.; Shen, M.; Wang, J.; Shi, X. *Langmuir* **2013**, *29*, 5030–5036.

(54) Wang, S.; Zheng, F.; Huang, Y.; Fang, Y.; Shen, M.; Zhu, M.; Shi, X. *ACS Appl. Mater. Interfaces* **2012**, *4*, 6393–6401.

(55) Lazzara, G.; Milioto, S.; Gradzielski, M.; Prevost, S. *J. Phys. Chem. C* **2009**, *113*, 12213–12219.

(56) Tang, X.; Alavi, S. *J. Agric. Food Chem.* **2012**, *60*, 1954–1962.

(57) Lian, C.; Lin, Z.; Wang, T.; Sun, W.; Liu, X.; Tong, Z. *Macromolecules* **2012**, *45*, 7220–7227.

(58) Kuźniarska-Biernacka, I.; Silva, A. R.; Carvalho, A. P.; Pires, J.; Freire, C. *Langmuir* **2005**, *21*, 10825–10834.

(59) Vandamme, T. .; Lenourry, A.; Charrueau, C.; Chaumeil, J.-C. *Carbohydr. Polym.* **2002**, *48*, 219–231.

(60) Mata, Y. N.; Blázquez, M. L.; Ballester, A.; González, F.; Muñoz, J. A. *Chem. Eng. J.* **2009**, *150*, 289–301.

(61) Jackson, C. L.; Dreaden, T. M.; Theobald, L. K.; Tran, N. M.; Beal, T. L.; Eid, M.; Gao, M. Y.; Shirley, R. B.; Stoffel, M. T.; Kumar, M. V.; Mohnen, D. *Glycobiology* **2007**, *17*, 805–819.

(62) Inngjerdingen, K. T.; Patel, T. R.; Chen, X.; Kenne, L.; Allen, S.; Morris, G. A.; Harding, S. E.; Matsumoto, T.; Diallo, D.; Yamada, H.; Michaelsen, T. E.; Inngjerdingen, M.; Paulsen, B. S. *Glycobiology* **2007**, *17*, 1299–1310.

(63) Coffin, D. R.; Fishman, M. L.; Ly, T. V. *J. Appl. Polym. Sci.* **1996**, *61*, 71–79.

(64) Coffin, D. R.; Fishman, M. L. *J. Appl. Polym. Sci.* **1994**, *54*, 1311–1320.

(65) Hassan-Nejad, M.; Ganster, J.; Bohn, A.; Pinnow, M.; Volkert, B. *Macromol. Symp.* **2009**, *280*, 123–129.

(66) Batchelor, H. .; Banning, D.; Dettmar, P. .; Hampson, F. .; Jolliffe, I. .; Craig, D. Q. . *Int. J. Pharm.* **2002**, *238*, 123–132.

(67) Pawar, S. N.; Edgar, K. J. *Biomaterials* **2012**, *33*, 3279–3305.

(68) Kumar Giri, T.; Thakur, D.; Alexander, A.; Ajazuddin; Badwaik, H.; Krishna Tripathi, D. *Curr. Drug Deliv.* **2012**, *9*, 539–555.

(69) Draget, K. I.; Skjåk-Bræk, G.; Smidsrød, O. *Int. J. Biol. Macromol.* **1997**, *21*, 47–55.

(70) Kumar, M.; Tamilarasan, R. *J. Chem. Eng. Data* **2013**, *58*, 517–527.

(71) Ai, L.; Li, M.; Li, L. *J. Chem. Eng. Data* **2011**, *56*, 3475–3483.

(72) Xiao, Q.; Tong, Q.; Lim, L.-T. *Carbohydr. Polym.* **2012**, *87*, 1689–1695.

(73) Fei, B.; Wach, R. A.; Mitomo, H.; Yoshii, F.; Kume, T. *J. Appl. Polym. Sci.* **2000**, *78*, 278–283.

(74) Robitaille, L.; Turcotte, N.; Fortin, S.; Charlet, G. *Macromolecules* **1991**, *24*, 2413–2418.

(75) Hamley, I. W. *Soft Matter* **2010**, *6*, 1863–1871.

(76) Giachi, G.; Capretti, C.; Macchioni, N.; Pizzo, B.; Donato, I. D. *J. Cult. Herit.* **2010**, *11*, 91–101.

(77) Bobowska, I.; Wojciechowski, P.; Halamus, T. *Polym. Adv. Technol.* **2008**, *19*, 1860–1867.

(78) Guan, Y.; Zhang, Y.; Zhou, T.; Zhou, S. *Soft Matter* **2009**, *5*, 842–849.

(79) Wang, W.; Wang, A. *Carbohydr. Polym.* **2010**, *82*, 83–91.

(80) Suo, A.; Qian, J.; Yao, Y.; Zhang, W. *J. Appl. Polym. Sci.* **2007**, *103*, 1382–1388.

(81) He, F.; Zhao, D. *Environ. Sci. Technol.* **2007**, *41*, 6216–6221.

(82) Hebeish, A.; Higazy, A.; El-Shafei, A.; Sharaf, S. *Carbohydr. Polym.* **2010**, *79*, 60–69.

(83) Basta, A. H.; El-Saied, H. *Carbohydr. Polym.* **2008**, *74*, 301–308.

(84) Song, J.; Birbach, N.; Hinestroza, J. *Cellulose* **2012**, *19*, 411–424.

(85) Yadollahi, M.; Namazi, H. *J. Nanoparticle Res.* **2013**, *15*, 1–9.

(86) Alexandre, M.; Dubois, P. *Mater. Sci. Eng. R Rep.* **2000**, *28*, 1–63.

(87) Jung, D. H.; Cho, S. Y.; Peck, D. H.; Shin, D. R.; Kim, J. S. *J. Power Sources* **2003**, *118*, 205–211.

(88) Lvov, Y.; Abdullayev, E. *Prog. Bionanocomposites Green Plast. Biomed. Appl.* **2013**, *38*, 1690–1719.

(89) LeBaron, P. C.; Wang, Z.; Pinnavaia, T. J. *Appl. Clay Sci.* **1999**, *15*, 11–29.

(90) Lee, S. Y.; Kim, S. J. *Appl. Clay Sci.* **2002**, *22*, 55–63.

(91) Jinhua, W.; Xiang, Z.; Bing, Z.; Yafei, Z.; Rui, Z.; Jindun, L.; Rongfeng, C. *Desalination* **2010**, *259*, 22–28.

(92) Yah, W. O.; Takahara, A.; Lvov, Y. M. *J Am Chem Soc* **2011**, *134*, 1853–1859.

(93) Cavallaro, G.; Lazzara, G.; Milioto, S. *J. Phys. Chem. C* **2012**, *116*, 21932–21938.

(94) De Stefano, C.; Gianguzza, A.; Piazzese, D.; Porcino, N.; Sammartano, S. *Biophys. Chem.* **2006**, *122*, 221–231.

(95) Escudero, C.; Fiol, N.; Villaescusa, I.; Bollinger, J.-C. *J. Hazard. Mater.* **2009**, *164*, 533–541.

(96) Cavallaro, G.; Gianguzza, A.; Lazzara, G.; Milioto, S.; Piazzese, D. *Appl. Clay Sci.* **2013**, *72*, 132–137.

(97) Cataldo, S.; Cavallaro, G.; Gianguzza, A.; Lazzara, G.; Pettignano, A.; Piazzese, D.; Villaescusa, I. *J. Environ. Chem. Eng.* **2013**, *1,* 1252–1260.

(98) Kollár, T.; Kónya, Z.; Pálinkó, I.; Kiricsi, I. *J. Mol. Struct.* **2001**, *563-564*, 417–420.

(99) Xia, X.; Tang, S.; Lu, X.; Hu, Z. *Macromolecules* **2003**, *36*, 3695–3698.

(100) Krug, R. R.; Hunter, W. G.; Grieger, R. A. *J. Phys. Chem.* **1976**, *80*, 2335–2341.

(101) Ruths, M.; Sjöblom, J.; Blokhus, A. M. *J. Colloid Interface Sci.* **1991**, *145*, 108–112.

(102) Patrick, H. N.; Warr, G. G.; Manne, S.; Aksay, I. A. *Langmuir* **1999**, *15*, 1685–1692.

(103) Zhao, Z.; Tang, T.; Qin, Y.; Huang, B. *Langmuir* **2003**, *19*, 9260–9265.

(104) Yang, H.; Hua, S.; Wang, W.; Wang, A. *Iran. Polym. J.* **2011**, *20*, 479–490.

(105) Osada, Y.; Khokhlov, A. *Polymer Gels and Networks*; Marcel Dekker.; New York, 2002.

(106) De Lisi, R.; Lazzara, G.; Milioto, S.; Muratore, N. *J. Therm. Anal. Calorim.* **2007**, *87*, 61–67.

(107) Stefanescu, E. A.; Schexnailder, P. J.; Dundigalla, A.; Negulescu, I. I.; Schmidt, G. *Polymer* **2006**, *47*, 7339–7348.

(108) Gunbas, I. D.; Aydemir Sezer, U.; Gülce İz, S.; Delilioğlu Gürhan, İ.; Hasirci, N. *Ind. Eng. Chem. Res.* **2012**, *51*, 11946–11954.

10. Curriculum Vitae

Personal and Education

Born: April 26, 1983 in Palermo (Italy)

30/10/2007. Bachelor Degree in “Environmental Sciences” at the University of Palermo, Faculty of Sciences. Defended thesis: “Methods for water decontamination”. The examination committee approved with *magna cum laude*.

25/11/2009. Master Degree in “Environmental Sciences” at the University of Palermo, Faculty of Sciences. Defended thesis: “Pectins and nanoclays: components of new sustainable materials. A thermal, mechanical, dielectric, optical and morphological study”. The examination committee approved with *magna cum laude* and remarked the excellent *curriculum studiorum*.

October 2010-December 2010. Research contract - Department of Physical Chemistry “F. Accascina”, University of Palermo (Italy).

01/01/2011-31/12/2013. Ph.D. student in Chemical Sciences - University of Palermo (Italy).

Grants

15/01/2011. “ECOST Action D43” to attend the “Training School: Fluids and Solid Interfaces”, Sofia (Bulgaria) 12 – 15 April 2011.

01/04/2011. “Associazione Italiana di Calorimetria ed Analisi Termica” to attend the *10th Mediterranean Conference on Calorimetry and Thermal Analysis*, Porto (Portugal) 24-27 July 2011.

Scientific Stages

December 2006-April 2007. Stage at the laboratory of *ARPA Sicilia* on analytical tecniques for the determination of inorganic and organic contaminants in wastewater. Palermo (Italy).

May 2009-June 2009. Stage at the laboratory of *TA Instruments* on dynamic mechanical analysis of viscoelastic materials.
Milan (Italy).

July 2009 – Septmber 2009. Stage at the laboratory of *Experimental Zooprophylactic Institute* on treatment of the urban waste.
Palermo (Italy).

April 2013 – October 2013. Research stage at the laboratories supervised by Prof. Yuri Lvov, *Institute of Micromanifacturing* at *Louisiana Tech University* (USA).

Seminars held at Abroad Institutions

18 September 2013. Speaker of the seminar "Aqueous colloidal stability and solubilization ability of ionic Surfactant/Clay nanotubes hybrids" held at *Louisiana Tech University* (USA)

Attendance at International Schools and Courses

01/09/2008-14/09/2008. "Italian-Russian School: Chemistry for the Environmental Monitoring and Protection" organized by *Russian Institute of Education and Ecological Researches*.
Palermo (Italy).

12/04/2011-15/04/2011. "Training School: Fluids and Solid Interfaces" organized within the European project ECOST Action D43 "Colloid and Interface Science Nanotechnology".
Sofia (Bulgaria).

19/06/2011-24/06/2011. "Summer School of Calorimetry 2011: Calorimetry and thermal methods in catalysis" organized by IRCELYON (Institut de Recherches sur la Catalyse et l'Environnement de Lyon) and CNRS (Centre national de la recherche scientifique).
Lyon (France).

08/03/2012-16/03/2012. *Berlin School on Neutron Scattering* held in *Lise Meitner Campus/Helmholtz-Zentrum Berlin für Materialien und Energie*.
Berlin (Germany).

14/12/2012-16/12/2012. "*1st Winter School - Renewable Energy Systems and Green Nanotechnologies for a Clean Environment"*
Drobeta-Turnu Severin (Romania).

15/04/2013 – 15/05/2013 "Nanofabrication by Self-Assembly" course held by Prof. Yuri Lvov at *Louisiana Tech University – Institute of Micromanifacturing*
Ruston (Louisiana – USA).

Experiments at Large Facilities

18/04/2012-22/04/2012. "*Institut Laue-Langevin*" Grenoble (France), Small Angle Neutron Scattering measurements (Instrument D11).

24/09/2012-28/09/2012. "*Institut Laue-Langevin*" Grenoble (France), Small Angle Neutron Scattering measurements (Instrument D11).

12/01/2013-19/01/2013. "*Helmholtz-Zentrum*" Berlin (Germany), Small Angle Neutron Scattering measurements (Instrument V4).

Organizing activities

14/12/2012-16/12/2012. Component of the organizing committee of "*1st Winter School - Renewable Energy Systems and Green Nanotechnologies for a Clean Environment"*
Drobeta-Turnu Severin (Romania).

27/08/2013-30/08/2013. Component of the organizing committee of " *The 2nd Central and Eastern European Conference for Thermal Analysis and Calorimetry".*
Vilnius (Lituania).

Publications

1) **G. Cavallaro**, G. Lazzara, S. Milioto
Dispersions of nanoclays of different shapes into aqueous and solid biopolymeric matrices. Extended physicochemical study
Langmuir 27, 1158, **2011**

2) **G. Cavallaro**, D. I. Donato, G. Lazzara, S. Milioto
A comparative thermogravimetric study of waterlogged archaeological and sound woods
J. Therm. Anal. Calorim. 104, 451, **2011**

3) **G. Cavallaro**, R. De Lisi, G. Lazzara, S. Milioto
Bionanocomposites based on pectins and halloysite nanotubes
ACS symposium 104, 83, **2011**

4) **G. Cavallaro**, D. I. Donato, G. Lazzara, S. Milioto
Films of halloysite nanotubes sandwiched between two layers of biopolymer: from the morphology to the dielectric, thermal, transparency, and wettability properties
J. Phys. Chem. C 115, 20491, **2011**

5) **G. Cavallaro**, G. Lazzara, S. Milioto
Aqueous phase/nanoparticles interface: hydroxypropyl cellulose adsorption and desorption triggered by temperature and inorganic salts
Soft Matter, *8*, 3627, **2012**

6) **G. Cavallaro**, G. Lazzara, S. Milioto
Exploiting the colloidal stability and solubilization ability of clay nanotubes/ionic surfactant hybrid nanomaterials.
J. Phys. Chem. C 116, 21932, **2012**

7) **G. Cavallaro**, D. I. Donato, G. Lazzara, S. Milioto
Determining the selective impregnation of waterlogged archaeological woods with poly(ethylene) glycols mixtures by differential scanning calorimetry
J. Therm. Anal. Calorim. 111, 1449, **2013**

8) **G. Cavallaro**,[a] R. De Lisi, G. Lazzara, S. Milioto
Polyethylene glycol/clay nanotubes composites: thermal properties and structure.
J. Therm. Anal. Calorim. 112, 383, **2013**

9) **G. Cavallaro**, A. Gianguzza, G. Lazzara, S. Milioto, D. Piazzese
Alginate-clay nanotubes hybrid gel beads.
Appl. Clay Sci. 72, 132*,* **2013**

10) M. Massaro, S. Riela, **G. Cavallaro**, M. L. Saladino, S. Agnello, R. Noto.
Properties and structural studies of multi-wall carbon nanotube-phosphate ester hybrids.
Int. J. Org. Chem. 3, 26, **2013**

11) **G. Cavallaro**, R. De Lisi, G. Lazzara, S. Milioto
Clay nanotubes/ionic surfactant: Smart hybrid nanomaterials for the solubilization of hydrophobic compounds in aqueous media
ACS symposium 108, 13, **2013**

12) S. Cataldo, **G. Cavallaro**, A. Gianguzza, G. Lazzara, A. Pettignano, D. Piazzese, I. Villaescusa
Kinetic and equilibrium study for cadmium and copper removal from aqueous solutions by sorption onto mixed alginate/pectin gel beads
J. Env. Chem. Eng. 1, 1252, **2013**

13) **G. Cavallaro**, G. Lazzara, S. Milioto
Sustainable nanocomposites based on halloysite nanotubes and pectin/polyethylene glycol blend
Polym. Degrad. Stab. 98, 2529, **2013**.

14) M. Massaro, S. Riela, **G. Cavallaro**, M. Gruttadauria, S. Milioto, R. Noto, G. Lazzara
Eco-friendly functionalization of natural halloysite clay nanotube with ionic liquids by microwave irradiation for Suzuki coupling reaction
J. Organomet. Chem. 749, 410, **2014**

15) **G. Cavallaro**, G. Lazzara, S. Milioto, G. Palmisan, F.Parisi
Halloysite Nanotube with Fluorinated Lumen: Non-Foaming Nanocontainer for Storage and Controlled Release of Oxygen in Aqueous Media
J. Colloid Int. Sci. 417, 66, **2014**

16) **G. Cavallaro**, G. Lazzara, S. Milioto, F.Parisi, V.Sanzillo
Modified Halloysite Nanotubes: nanoarchitectures for enhancing capture of oils from vapor and liquid phases
ACS Appl. Mater. Inter. **dx.doi.org/10.1021/am404693r**

17) Y. Zhao, W. Wei, **G. Cavallaro**, Y. Lvov
Controlled orientation and alignment in films of halloysite nanotubes by liquid-crystalline processing
Adv. Mater. **(in preparation)**

---

[a] Corresponding author

Congress communications

1) **G. Cavallaro**, R. De Lisi, G. Lazzara, S. Milioto
Bionanocomposites based on pectins and halloysite nanotubes: from the structure to the properties
XXXIX Congresso Nazionale di Chimica Fisica.
Stresa (Italy) 20-24 September 2010

2) **G. Cavallaro**,[b] G. Lazzara
Bionanocompositi pectina/nanotubi di argilla: uno studio chimico-fisico
Convegno Congiunto delle Sezioni Calabria e Sicilia della SCI
Palermo (Italy) 2-3 December 2010

3) **G. Cavallaro**, R. De Lisi, G. Lazzara, S. Milioto
Bionanocomposites based on pectins and halloysite nanotubes
241st ACS National Meeting & Exposition
Anaheim, California, (USA) 27-31 March 2011

4) **G. Cavallaro**,[b] R. De Lisi, G. Lazzara, S. Milioto
Interactions between nanoclays and biopolymers evidenced by extensive thermodynamic and structural studies
10th Mediterranean Conference on Calorimetry and Thermal Analysis
Porto (Portugal) 24-27 July 2011

5) **G. Cavallaro**, R. De Lisi, G. Lazzara, S. Milioto
Tuning the hydroxypropyl cellulose adsorption and desorption at the nanoparticle/water Interface by temperature and inorganic salts
10th Mediterranean Conference on Calorimetry and Thermal Analysis
Porto (Portugal) 24-27 July 2011

6) **G. Cavallaro**, D. I. Donato, G. Lazzara, S. Milioto
Thermogravimetric studies of archaeological woods
XXIV Congresso Nazionale della Società Chimica Italiana
Lecce (Italy) 11-16 September 2011

7) **G. Cavallaro**, R. De Lisi, G. Lazzara, S. Milioto
Nanoclays and biopolymers in aqueous solution and in solid state. Interactions and structure
XXIV Congresso Nazionale della Società Chimica Italiana
Lecce (Italy) 11-16 September 2011

8) **G. Cavallaro**, G. Lazzara, S. Milioto
Bionanocomposites based on natural polymers and nanoclays. An extended physico-chemical study to evidence the role of the polymer nature and the nanoclay shape
The 4th International Conference on Medical Geology (GEOMED 2011)
Bari (Italy) 20-25 September 2011

9) **G. Cavallaro**,[b] G. Lazzara, S. Milioto
Dispersioni di nanoargille in biofilms. Il ruolo chiave del polimero nel controllo della struttura.
Convegno Congiunto delle Sezioni Calabria e Sicilia della SCI
Messina (Italy) 1-2 December 2011

10) **G. Cavallaro**,[a] A. Gianguzza, G. Lazzara, S. Milioto, D. Piazzese
Alginate/halloysite nanotubes gel beads: innovative and advanced adsorbent biomaterials
"XXXIV National Congress on Calorimetry, Thermal Analysis and Applied Thermodynamics".
Rome (Italy), 5-8 June 2012

11) **G. Cavallaro**, G. Lazzara, S. Milioto
Is Calorimetry a crucial technique for studying innovative nanomaterials?
"XXXIV National Congress on Calorimetry, Thermal Analysis and Applied Thermodynamics".
Rome (Italy), 5-8 June 2012

12) **G. Cavallaro**, D.I. Donato, G. Lazzara, S. Milioto
DSC and TGA to evaluate the selective impregnation of waterlogged archaelogical woods with poly(ethylene) glycols mixtures.
"XXXIV National Congress on Calorimetry, Thermal Analysis and Applied Thermodynamics".
Rome (Italy), 5-8 June 2012

13) **G. Cavallaro**, G. Lazzara, S. Milioto
Calorimetry: a valuable tool for emerging smart nanomaterials.
"15th International Confederation for Thermal Analysis and Calorimetry"
Osaka (Japan), 20-24 August 2012

14) M. Massaro, S. Riela, **G. Cavallaro**, M. Gruttadauria, G. Lazzara, S. Milioto, R. Noto
Microwave-assisted functionalization of halloysite nanotube surface
"*XXXIV Congresso Nazionale della Divisione di Chimica Organica della Società Chimica Italiana*"
Pavia (Italy), 10-14 September 2012.

15) M. Massaro, S. Riela, **G. Cavallaro**, M. Gruttadauria, G. Lazzara, S. Milioto, R. Noto
Funzionalizzazione della superficie dell'allosite mediante riscaldamento a microonde
"12nd Sigma Aldrich Young Chemists Symposium"
Riccione (Italy), 1-3 October 2012.

16) **G. Cavallaro**, R. De Lisi, G. Lazzara, S. Milioto
Clay nanotubes/ionic surfactant: Smart hybrid nanomaterials for the solubilization of hydrophobic compounds in aqueous media
245th ACS National Meeting & Exposition
New Orleans, Louisiana, (USA) 7-11 April 2013

17) G. Lazzara, D.I. Donato, **G. Cavallaro**, S. Milioto
Thermal methods to evaluate consolidation of artworks
11th Mediterranean Conference on Calorimetry and Thermal Analysis
Atene (Grecia) 12-15 Giugno 2013

18) G. Lazzara, N. Armata, S. Cataldo, **G. Cavallaro**, F. Ferrante, A. Pettignano, L. Bernazzani, C. Duce, L. Ghezzi, M.R. Tinè, E. Bramanti, C. Ferrari, V. Ierardi, G. Mancini
Clay nanotubes for designing eco-compatible smart materials
11th Mediterranean Conference on Calorimetry and Thermal Analysis
Atene (Grecia) 12-15 Giugno 2013

19) **G. Cavallaro**, G. Lazzara, S. Milioto
Halloysite based material for enhanced solubilization
XLI Congresso Nazionale di Chimica Fisica
Alessandria (Italia) 23-27 Giugno 2013

20) **G. Cavallaro**, G. Lazzara, S. Milioto
Waterlogged archaeological wood: evaluation of consolidation treatments by calorimetry
XLI Congresso Nazionale di Chimica Fisica
Alessandria (Italia) 23-27 Giugno 2013

21) **G. Cavallaro**, G. Lazzara, S. Milioto
Sustainable plastics based on halloysite nanotubes and biopolymers
2nd CEEC-TAC conference
Vilnius (Lituania) 27-30 August 2013

22) **G. Cavallaro**, G. Lazzara, S. Milioto, F. Parisi
Clay Nanotube/Perfluorinated Surfactant Hybrid Materials
2nd CEEC-TAC conference
Vilnius (Lituania) 27-30 August 2013

23) **G. Cavallaro**, G. Lazzara, S. Milioto, F. Parisi
Paper consolidation with Halloysite nanotubes. TGA, DMA and contact angle investigations
2nd CEEC-TAC conference
Vilnius (Lituania) 27-30 August 2013

24) **G. Cavallaro**[a], G. Lazzara, Y. Lvov, S. Milioto, F. Parisi
Halloysite Nanotubes/Perfluoroctanote: an efficient consolidant and flame retardant for paper
247th ACS National Meeting & Exposition
Dallas, Texas (USA) 16 – 20 March 2014

25) Y. Zhao, W. Wei, **G. Cavallaro**, Y. Lvov
Controlled orientation and alignment in films of halloysite nanotubes by liquid-crystalline processing
247th ACS National Meeting & Exposition
Dallas, Texas (USA) 16 – 20 March 2014

---

[a] Poster presenter. [b] Speaker.

11. Attached papers

Attached I

THE JOURNAL OF
PHYSICAL CHEMISTRY C

ARTICLE

pubs.acs.org/JPCC

Films of Halloysite Nanotubes Sandwiched between Two Layers of Biopolymer: From the Morphology to the Dielectric, Thermal, Transparency, and Wettability Properties

Giuseppe Cavallaro, D. Ines Donato, Giuseppe Lazzara,* and Stefana Milioto

Department of Chemistry "S. Cannizzaro", University of Palermo, Viale delle Scienze, Parco D'Orleans II, 90128 Palermo, Italy

S *Supporting Information*

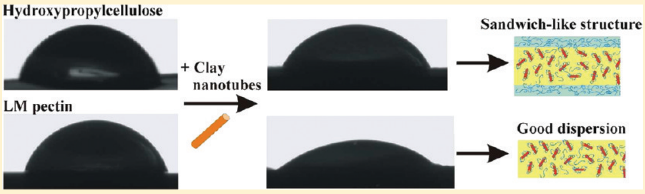

ABSTRACT: This study focused on the preparation and characterization of films based on biopolymers (hydroxypropylcellulose and low methoxyl pectin) and halloysite nanotubes (HNTs). The morphology is strongly dependent on the polymer nature. In particular, we observed a sandwich-like structure composed of two hydroxypropylcellulose layers incorporating the HNTs and a homogeneous distribution of the nanotubes into the low methoxyl pectin matrix. The different mesoscopic properties were invoked to explain the dielectric, thermal, and wettability properties of the corresponding films. Nanocomposites obtained by combining materials from renewable resources and HNTs is a challenging task in view of designing green materials with tunable barrier and delivery properties for specific purposes.

INTRODUCTION

During the last few decades, materials based on nanoclays have attracted large interest because their properties and morphologies may be tuned. Within this field, halloysite nanotubes (HNTs) are newly emerging clays with unique features[1] and appealing perspectives.[2] Halloysite is a naturally occurring hydrated polymorph of kaolinite, and it possesses a peculiar hollow tubular shape, which results from the wrapping of clay layer. The size of HNTs is quite polydisperse, ranging between 0.1 and 2 μm, whereas the outer and inner diameters are ca. 30−50 and 1−30 nm, respectively.[1] The low cost and the environmentally friendly nature make the HNTs competitive with the carbon nanotubes in several applications. The HNT use in controlled release, nanotemplating, and sorption was recently reviewed.[1] Loading the HNTs with anticorrosive agents for active coating protections was successfully done, and self-healing effect was achieved.[2−5] HNTs assembly by sequential adsorption with the polycations generated ordered multilayers.[6] The selective recognition of contaminants was done by using molecular imprinted polymer based on magnetic HNTs.[7] Because HNT is a green filler and a natural product, its use does not add any risk to the environment as other nanofillers in principle do.[2] Polystyrene[8] and polyamide[9] filled with well-dispersed HNTs exhibited a thermal and a mechanical reinforcement of the polymer matrix. Composites formed by clay tubes with nanoholes on the sidewalls were obtained by in situ mechanochemical polymerization of aniline in the presence of HNTs.[10] In some cases, the functionalization of HNTs by grafting appropriate organic molecules was designed with the aim at obtaining a nanoclay-based filler with a high compatibility with the polymer matrix.[11] Filling polymers from renewable resources with HNTs is a challenging task in view of designing new packaging materials. A recent review[12] reported that several biopolymeric materials may form films, but their use would be limited because of fast degradation and, in some cases, unsatisfactory mechanical properties.[13] To our knowledge, very few insights into biopolymers filled with HNTs are available.[14−17]

Hydroxypropyl cellulose (HPC) obtained from the chemical modification of the cellulose may be an interesting biopolymer matrix of investigation. It was tested in several applications as a consolidant of waterlogged woods[18] and drug delivery.[19]

Within this work, we prepared biofilms formed by HPC and HNTs, and we widely studied them by determining thermal stability, transparency, wettability, and dielectric properties. The morphology was helpful to explain the nanomaterial features. For a comparison purpose, some low methoxyl pectin/HNT composites were also investigated.

This work contributes to the knowledge on green nanocomposites, proving that materials with rather different mesoscopic structure can be designed by changing the biopolymer nature.

EXPERIMENTAL SECTION

Materials. Citrus pectin (with a low degree of methyl esterification, 24%, M_w = 30−100 kg mol^{-1}) and HPC (M_w = 80 kg mol^{-1}) were from Aldrich. HNTs was a gift from Applied Minerals. All the materials were used without further purification. Water was from reverse osmosis (Elga model Option 3) with a specific resistivity >1 MΩ cm.

Received: July 29, 2011
Revised: September 7, 2011
Published: September 14, 2011

Preparation of Nanocomposite Films. The aqueous polymer+filler mixtures were prepared as described elsewhere.[14] In brief, citrus pectin (LM pectin) or HPC were solubilized in water under stirring at 70 °C. The solutions were left to equilibrate at room temperature under stirring overnight. The final polymer concentration was evaluated by weight. Then, an appropriate amount of HNT was added to the polymer solution and kept under stirring overnight.

The well-dispersed aqueous mixture was poured in glass Petri dishes and heated at 80 °C for ~15 h to evaporate water until weight was constant. The films (with a thickness of ca. 0.06 mm) were easily removed from the supports and stored in a desiccator at room temperature; their thickness was measured with a micrometer ($\pm 10^{-3}$ mm). The composition of nanofillers (C_f) expressed as weight percent (grams of filler/100 grams of nanocomposite) was systematically changed.

Methods. *Dielectric Spectroscopy.* A Hewlett-Packard impedance analyzer (HP 4294A) equipped with HP 16451B dielectric test fixtures was used at 25.0 ± 0.1 °C. The frequency was changed from 50 kHz to 10 MHz. The dielectric constant (ε_r) and the dispersion factor ($\tan \delta$) were measured, and the electrical conductivity (σ) was calculated accordingly

$$\sigma = \varepsilon_r \varepsilon_0 \omega \tan \delta \qquad (1)$$

where ε_0 and ω are the vacuum permittivity and the angular frequency of the alternating current, respectively.

Thermogravimetry. A Q5000 IR apparatus (TA Instruments) under a nitrogen flow of 25 $\text{cm}^3\ \text{min}^{-1}$ for the sample and 10 $\text{cm}^3\ \text{min}^{-1}$ for the balance was used. The weight of each sample was ca. 10 mg. The measurements were carried out by heating the sample from room temperature to 900 °C at a rate of 10 °C min^{-1}. From these experiments, the following parameters were determined: (1) the water content from the mass loss up to 150 °C; (2) the polymer decomposition temperature (t_d) taken at the maximum of the first-order derivative curves of mass loss to temperature (DTG curves); and (3) the residual weight at 900 °C. The variation of the water content in the film with different HNT loadings is minute, and the residual weight clearly depends on C_f. (Data are in the Supporting Information.)

Experiments were also performed to determine the kinetics of degradation of the polymer in the films. To this aim, two procedures were followed: (1) the nonisothermal degradation was studied by changing heating rates (5, 10, 15, and 20 °C min^{-1}) and (2) the isothermal degradation was investigated by heating the sample to 310 °C with a fast ramp (500 °C min^{-1}) and keeping the isothermal condition until a constant weight was registered.

Scanning Electron Microscopy. The morphology of nanocomposites was studied using a microscope ESEM FEI QUANTA 200F. Before each experiment, the surface of the sample was coated with gold in argon by means of an Edwards Sputter Coater S150A to avoid charging under electron beam. Minimal electron dose condition was set to avoid damage of the sample.

Films Transparency. The experiments were carried out at 25.0 ± 0.1 °C by using an Analytic Jena Specord S 600 BU.

VIS-absorption spectra were recorded in the range from 400 to 800 nm. The attenuation coefficient (k) for each sample was computed as

$$k = A/(2.3 \times D) \qquad (2)$$

where A is the absorbance and D is the thickness of the rectangular film measured with a micrometer ($\pm 10^{-3}$ mm). For all of the investigated systems, the k values are almost independent of λ (examples are shown in the Supporting Information); therefore, the k at 750 nm (k_{750}) will be discussed hereafter. The simplest way to analyze the k_{750} data is based on the equation derived for spherical particles[20]

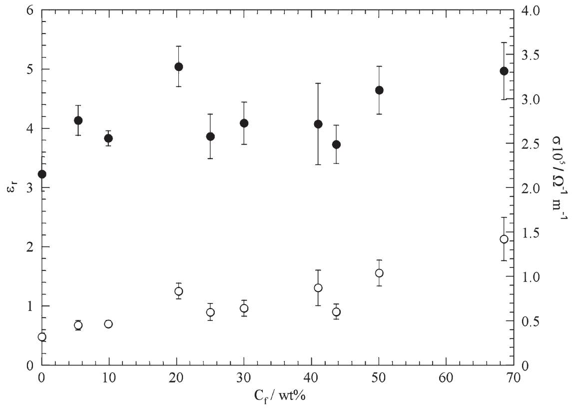

Figure 1. Dependence of the dielectric constant (●) and the electrical conductivity (○) of HPC/HNTs films on filler concentration.

$$k \propto \phi R \qquad (3)$$

where R is the radius of the equivalent spherical particles scattering light and ϕ is their volume fraction. It has to be noted that the HNT particles do not have a spherical shape; therefore, R assumes a more general meaning of an apparent radius of the spherical particle with the same scattering property of the nanotube.

Contact Angles. Contact angle measurements were performed by using an optical contact angle apparatus (OCA 20, Data Physics Instruments) equipped with a video measuring system having a high-resolution CCD camera and a high-performance digitizing adapter. SCA 20 software (Data Physics Instruments) was used for data acquisition. The films were fixed on top of a plane solid support and kept flat. The contact angle of water in air was measured by the sessile drop method. The water droplet volume was 6.0 ± 0.5 μL. Temperature was set at 25.0 ± 0.1 °C for the support and the injecting syringe as well. Images were collected 25 times per second, starting from the deposition of the drop to 40 s. From the data analysis, the contact angle, the volume, and the contact area of the drop were calculated. Five measurements at least were carried out on each film sample.

■ RESULTS

Dielectric Spectroscopy. This technique can provide information on the molecular dynamics of polymer systems monitoring the relaxation processes. Moreover, the dielectric properties of nanohybrids are of technological interest because they represent the capability to store/dissipate energy under the application of an electric field. Dielectric methods were extensively applied to cellulose and its derivatives.[21−23] The dielectric spectroscopy studies for the HPC/HNTs mixtures showed that at a certain frequency HNTs addition hardly affect both ε_r and σ, which is consistent with the HNTs polar nature and the increased number of charge carriers in their presence (Figure 1).

It was established that HPC shows the relaxation processes related to the local chain motion via the glucosidic bond

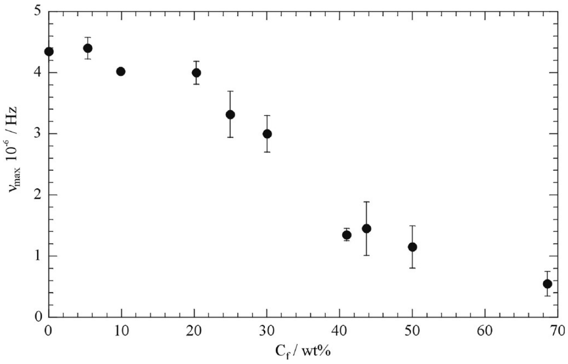

Figure 2. Relaxation frequency as a function of HNTs concentration for HPC/HNTs films.

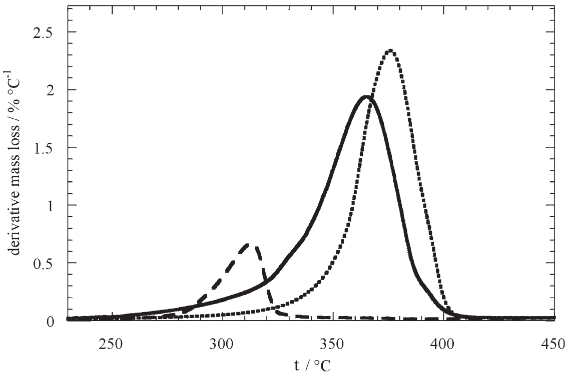

Figure 3. Thermal degradation rates as functions of temperature for HPC/HNTs films at $C_f = 0$ wt % (—), 15 wt % (---), and 80 wt % (− −).

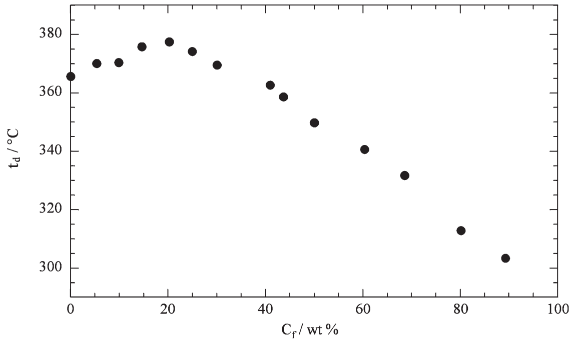

Figure 4. Degradation temperature as a function of the filler concentration for HPC/HNTs films.

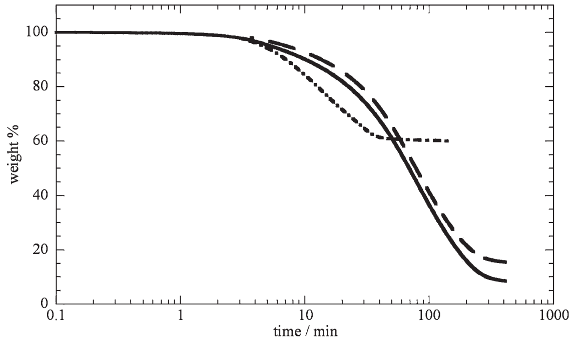

Figure 5. Isothermal degradation at 310 °C for pristine HPC (——) and HPC/HNTs films at $C_f = 10$ wt % (— —) and 60 wt % (— • —).

(β-relaxation) and to the motion of the side groups attached to the glucosic unit of the polysaccharides (γ-relaxation) both in the range from 10^6 to 10^7 Hz.[21] Very recently, dielectric spectroscopy evidenced free water relaxation at ca. 10^{10} Hz for wet HPC samples.[22] In light of these insights, one may state that ε_r and tan δ data as functions of the frequency (ν) for HPC in the absence and the presence of HNTs evidence the polymer relaxation (examples are in the Supporting Information). In particular, a maximum in the tan δ versus ν trend is evident in the correspondence of the inflection point in the ε_r versus ν curve. The profile is strongly altered by the HNTs being that the peak is shifted toward lower frequencies and it becomes wider. A similar effect was observed for the dielectric response of TiO_2-epoxy composite, and it was explained in terms of Maxwell—Wagner interfacial polarization.[24] Interesting insights are provided by the relaxation frequency at the maximum of tan δ (ν_{max}) versus C_f trend (Figure 2) because ν_{max} slightly changes to $C_f \approx 20$ wt %; thereafter, it sharply decreases upon the HNTs addition, reflecting a reduced local chain mobility in the presence of the nanotubes.

Thermal Degradation. Figure 3 reports DTG examples on the influence of HNTs on the thermal stability of HPC. Compared with the pristine HPC, the peak reflecting the polymer decomposition is shifted toward larger and lower temperatures for low and high C_f values, respectively. Such a peculiarity is clearly evidenced in the trend of t_d as a function of C_f (Figure 4). The presence of small amounts of nanofiller causes the HPC thermal stabilization (up to 10 °C), whereas a further addition of HNTs (above $C_f \approx 20$ wt %) enhances the thermal degradation that occurs at temperature even 65 °C below t_d of pristine HPC. For LM pectin/HNTs mixtures, t_d sharply increases within the regime of very high HNT loading.[14] The nanoparticles nature controls the thermal behavior of polymers.[14,25−27] In the presence of HNTs the thermal stabilization is generally observed,[14,25] and it is ascribed to the entrapment of the volatile products (obtained from the polymer thermal decomposition) into the HNTs lumen. Commonly, the effect on t_d of inorganic fillers in the polymeric matrices is discussed in terms of barrier effects toward both mass and heat transports; in particular, a composite material with well-dispersed nanoparticles typically shows a thermal enforcement. For a better understanding of the thermal degradation issue, we monitored the isothermal degradation at 310 °C for pristine HPC and nanocomposites at $C_f = 10$ and 60 wt %. As Figure 5 shows, the mass is constant during an induction period; afterward, it decreases, approaching a plateau. Of course the residual mass is larger the higher the amount of inorganic nondegradable filler. Compared with pristine HPC, the thermal decomposition at $C_f = 10$ wt % is slightly delayed, whereas it is strongly accelerated at $C_f = 60$ wt %; that confirms the t_d data.

Thermograms were also collected on the same samples at variable heating rates (β) to determine the activation energy (E_a) of degradation. The Flynn—Wall—Ozawa approach as well as the Friedman's methods are nonisothermal and model-free, allowing us to calculate E_a as a function of the extent of conversion (α) without making any assumption on the reaction mechanism. For this reason, they are widely used[14,28−31] in kinetic studies of thermal decomposition of nanocomposites and macromolecules.

In brief, the FWO method is based on the following integrated equation

$$\ln \beta = \left[\frac{AE_\alpha}{RG(\alpha)}\right] - 5.3305 - 1.0516\frac{E_\alpha}{RT} \qquad (4)$$

where $G(\alpha)$ is a function of the extent of conversion, A is the pre-exponential factor, R is the gas constant, and T is the absolute temperature. At a given α value, from the slope of the $\ln \beta$ versus $1/T$ plot, one can easily calculate E_a. As concerns the Friedman approach, the following equation was used

$$\ln\left(\beta\frac{d\alpha}{dT}\right) = \ln[Af(\alpha)] - \frac{E_\alpha}{RT} \qquad (5)$$

where $d\alpha/dT$ is the first derivative of α with respect to temperature and $f(\alpha)$ is a function of the extent of conversion that depends on the degradation mechanism. In this case, the E_a values at each α value are obtained from the slopes of the $\ln(\beta\ d\alpha/dT)$ versus $1/T$ plot.

It is worth noting that the results provided by the two methods are very similar, supporting the reliability of the data analysis. (E_a data from the FWO method are in the Supporting Information.) For all of the investigated nanocomposites, E_a does not depend on α (Figure 6), but it does strongly depend on composition. At C_f = 10 wt %, E_a is slightly larger than the corresponding value of the pure HPC, whereas at C_f = 60 wt %, the energetic barrier to the degradation process drops to almost zero value.

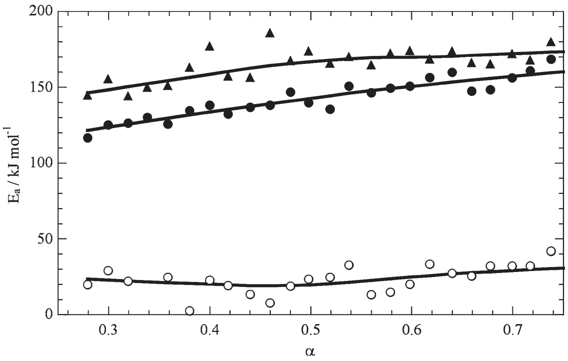

Figure 6. Activation energy as a function of the extent of conversion for the HPC/HNTs films at C_f = 0 wt % (●), 10 wt % (▲), and 60 wt % (○) obtained from the Friedman method. Lines are guide for eyes.

Films Morphology. SEM experiments were carried out to image the morphology of the film both at the surfaces and at the transverse section. The morphology of the hybrid surfaces at both low and high HNTs content is very peculiar in the case of films based on HPC because the surface appears homogeneous and the presence of nanoparticles is rare (Figure 7). Being that in the film preparation, which is a solvent casting method followed by evaporation of the solvent, one surface of the film was exposed to air while the other surface was in contact with the glass Petri dish, in some cases, we performed measurements on both face-sides of the film, and we did not evidence any difference on the general structure of the two sides (Figure 7). From these results, one may deduce that the sandwich-like structure is driven by interactions between the components of the films. This morphology is very different from that of LM pectin/HNTs films, which showed dispersed HNTs into the polymer matrix.[14] Furthermore, such a difference is magnified when the micrographs obtained for the same HNTs composition and at the same sensitivity scale for the HPC/HNTs and LM pectin/HNTs systems are compared (Figure 8). On one side, the surface film of LM pectin evidences HNTs that are well-distinguishable and recognizable; on the other side, the surface film of HPC is in general very smooth, burying the nanotubes well. The peculiar morphology of the HPC/HNTs films induced us to perform measurements onto the edges of the films to check the distribution of the nanoclay along the lateral profile. Figure 9 shows that the nanotubes are well-compacted between two smooth thin layers of HPC in a sandwich-like structure. This amazing result is opposite to that reported[14] for LM pectin/HNTs for which the nanoclay is equally distributed on the surface as well as along the edges.

In light of these findings, the interpretation of k_{750} can be easily done. Figure 10 illustrates that for HPC/HNTs films the k versus ϕ is a linear trend with a slope proportional to R (eq 3), indicating that clustering between scattering object is negligible. For the pectins/HNT nanocomposites, the cluster formation is controlled by percolation, and it is enhanced for pectin with a higher degree of methyl-esterification.[14]

Wettability of HPC/HNTs Films. The surface properties of the HPC/HNTs and LM pectin/HNTs films were determined by measuring the contact angles (ϑ) of water as a function of time (τ) at variable HNTs composition. As a general result, ϑ decreases over time (examples are given in Supporting Information), whereas the drop volume and the contact area decreases and increases, respectively (Figure 11). Similar findings were obtained for surfaces

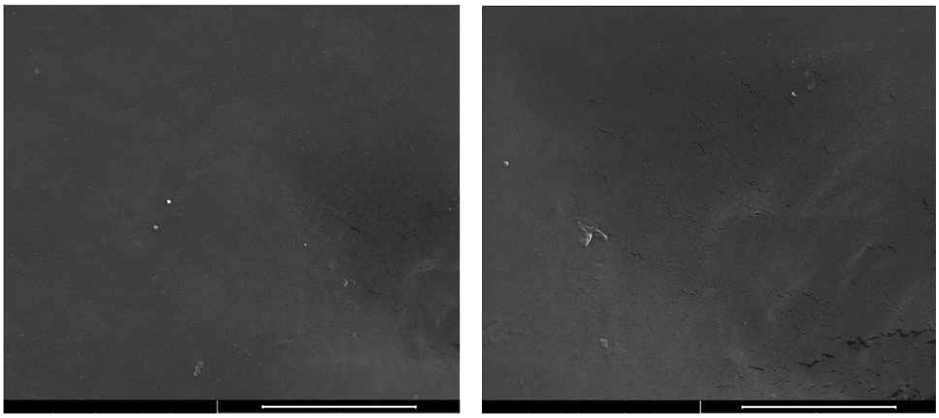

Figure 7. Scanning electron microscopy images of HPC/HNTs (C_f = 50 wt %) for surface in contact with air (left-hand side) and glass Petri dish (right-hand side). The bar is 10 μm.

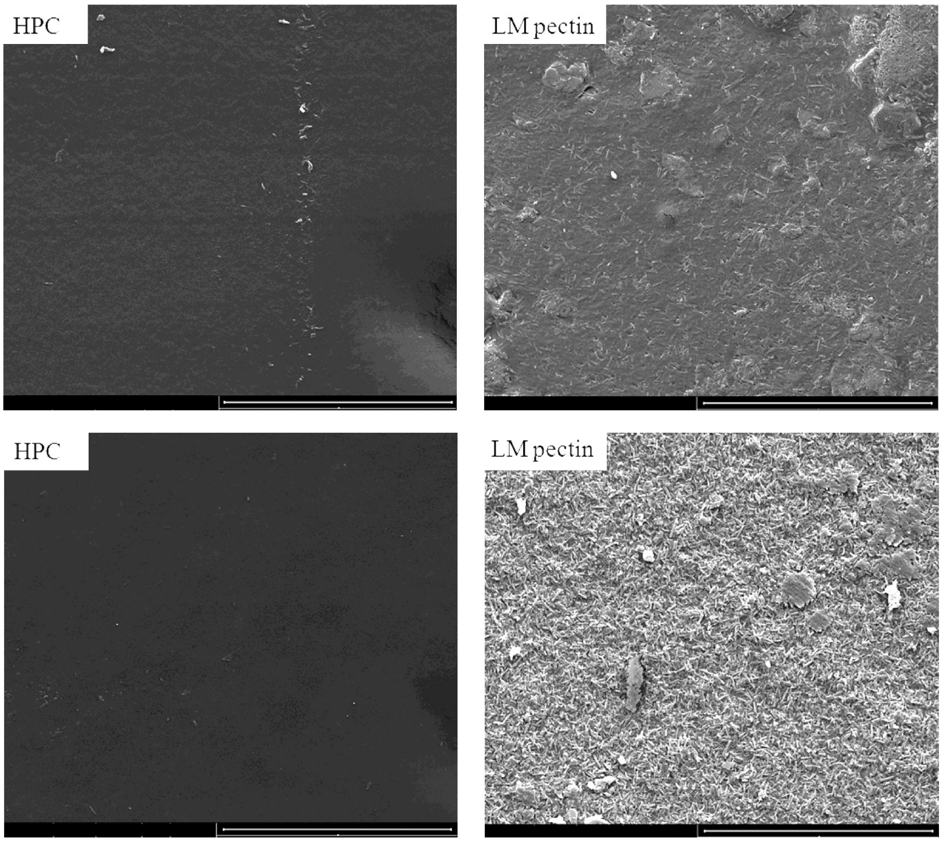

Figure 8. Scanning electron microscopy images of HPC/HNTs and LM pectin/HNTs films. The HNTs concentration is: top, $C_f = 10$ wt %; bottom, $C_f = 60$ wt %. The bar is 30 μm.

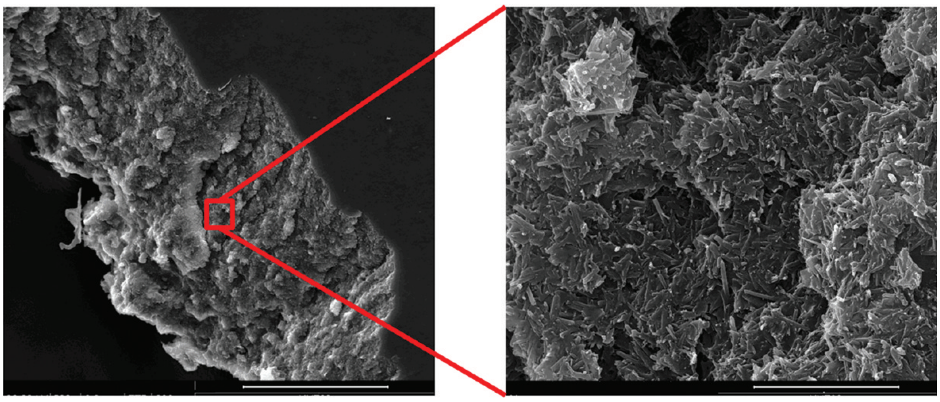

Figure 9. Scanning electron microscopy images of cross section of HPC/HNTs film at $C_f = 60$ wt %. The bar is 5 μm at the right-hand side and 100 μm at the left and side.

containing several biopolymers including pectin.[32] By comparing the volume drop and the contact area data, we conclude that both spreading and water absorption occur during the experiment.[32] A semiquantitative evaluation of the contributions from the spreading and the absorption can be done by fitting the ϑ versus τ curve as[32]

$$\vartheta = \vartheta_i \exp(k_\vartheta \tau^n) \tag{6}$$

where ϑ_i is the contact angle at $\tau = 0$, k_ϑ measures the process rate, and n assumes fractional values ascribable to the occurrence of absorption and spreading. Equation 6 successfully fitted our data, providing n values (Table 1) that reveal that both spreading and absorption take place; accordingly, $n = 0$ and 1 for pure absorption and pure spreading, respectively. The negative values of k_ϑ reveal the decrease in contact angle.

The general trends of ϑ_i versus C_f for both materials are rather intriguing (Figure 12). For LM pectin/HNT films, ϑ_i is a decreasing function of C_f, whereas for HPC/HNTs a peculiarity is exhibited by the ϑ_i versus C_f trend, which remarks a well-defined minimum at $C_f = 15$ wt %. The large differences between the behavior of LM pectin- and HPC-based films can be also easily evidenced by the drop images collected just after deposition. (See the examples in Figure 13.)

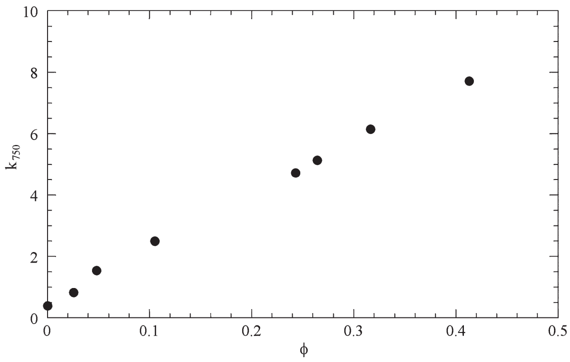

Figure 10. Dependence of the attenuation coefficient at 750 nm on the filler volume fraction for HPC mixed with HNTs.

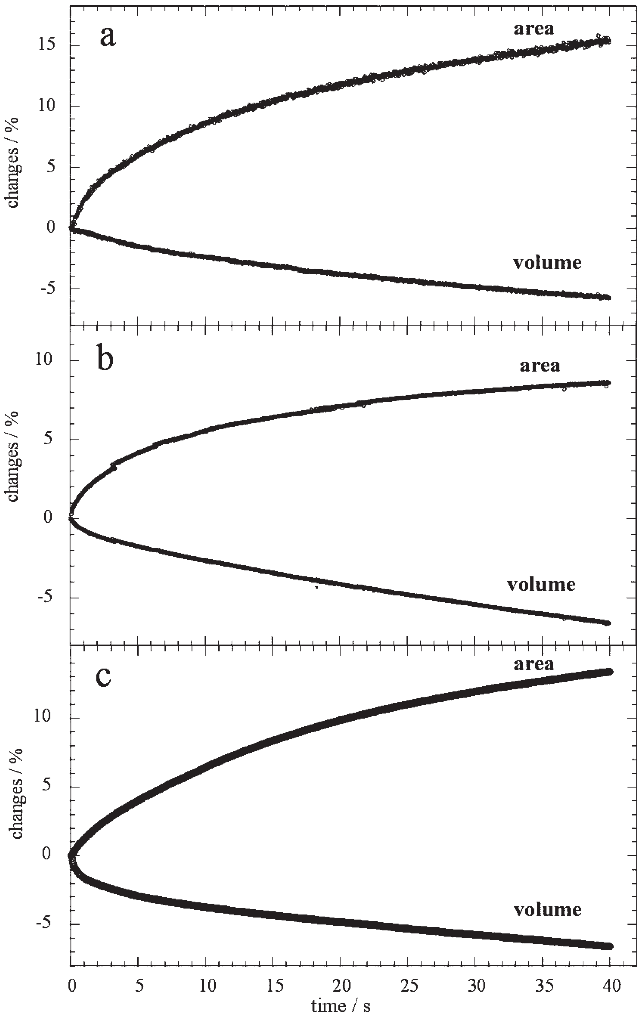

Figure 11. Water droplet volume and solid/liquid contact area evolution over time for HPC/HNTs at C_f = 0 wt % (a), 30 wt % (b) and 60 wt % (c).

The changes in ϑ_i can be related to the surface roughness or to the chemical hydrophilicity and therefore to the surface composition. Literature reports[33] ascribed the enhancement in the surface hydrophilicity and surface free energy to the surface enrichment of the nanofillers (synthetic layered silicate as well as octaammonium polyhedral oligomeric silsesquioxane) dispersed in polyamide-6. The spherulite superstructures generating a very rough surface were indicated to be responsible for the superhydrophobic properties of the polypropylene/HNT nanocomposite surface; that agrees with the well-known Wenzel model describing the contact angle on a rough surface, for which the surface hydrophobicity is strictly correlated to the surface roughness. Furthermore, Marmur[34] assessed that hydrophobic surfaces can be formed by hydrophilic substances if the roughness topography is multivalued.

Table 1. Fitting Parameters of Equation 6 Applied to the Contact Angle Data[a]

C_f	k_ϑ	n
	LM pectin	
0	−0.0103	0.425
9.88	−0.0118	0.547
29.56	−0.0152	0.431
60.27	−0.0103	0.665
	HPC	
0	−0.0296	0.482
5.36	−0.0330	0.399
9.85	−0.0076	0.555
14.60	−0.0059	0.661
20.29	−0.0279	0.475
30.01	−0.0283	0.453
50.02	−0.0204	0.380
60.33	−0.0192	0.559

[a] Units are: C_f, wt %; k_ϑ, s^{-n}. The errors are 1 and 0.3% on k_ϑ and n, respectively.

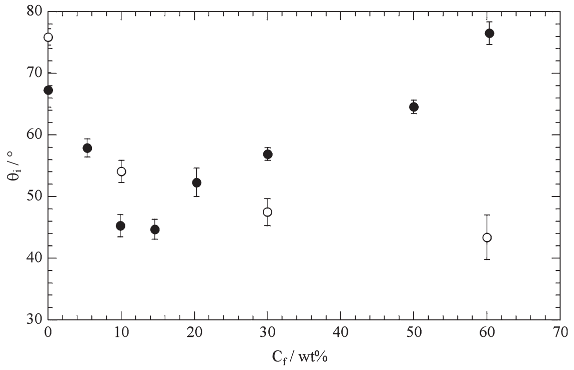

Figure 12. Dependence of the water contact angle at τ = 0 on the filler concentration for LM pectin/HNT (○) and HPC/HNT (●) composites.

DISCUSSION

The SEM images readily detected the difference on the surfaces and on the edges for the composite films of HPC and LM pectin. Moreover, TGA, dielectric, and wettability properties all indicated that they are affected by HNT loading. For the LM pectin/HNTs system, rather strong electrostatic interactions between the polymer and the nanofiller likely take place because of the presence of a certain number of carboxylic groups. This generates a sort of

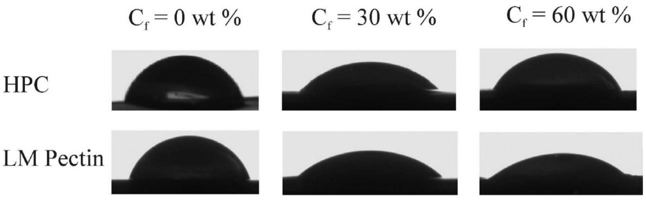

Figure 13. Images of water drops on films of biopolymer/HNTs at $\tau = 0$.

polymer network where the nanotubes are well-dispersed; once the percolation regime for the HNT content is approached, the cluster formation takes place.[14] In the HPC/HNTs films, electrostatic forces are absent; furthermore, the hydroxy-propyl groups cause the different morphology of the film. It likely occurs that HPC, due to the presence of the relatively hydrophobic hydroxypropyl groups, exhibits a smaller affinity toward HNTs; consequently, it generates a segregation between the HNTs and the polymer itself. In light of this picture, the other physicochemical properties can be understood.

From the dielectric spectroscopy, we evidenced that ν_{max} exhibits two different behaviors occurring in the low and high concentration regimes (Figure 2): low amounts of HNTs do not alter the characteristic relaxation time, whereas a further HNT addition generates a reduced mobility of the polymer, which is related to the polymer confinement at the surface layers of the sandwich-like structure. We observe the enhancement of the thermal stability of HPC in the low HNTs region and surprisingly the enhancement of the thermal degradation in the high HNTs region. Furthermore, the activation energy for the degradation process is in line with the degradation temperature trends and shows that low HNT amounts increase the energetic barrier, whereas high HNT amounts essentially cancel it, speeding up the degradation process. These peculiarities cannot be correlated with a change in the morphology of HPC/HNTs films at different HNTs loadings because SEM images (Figures 8 and 9) did not reveal significant differences. For the HPC/HNTs films, transparency measurements indicated that the cluster formation is inhibited, and SEM images show that the nanotubes are well-dispersed along the plane directions of the film in the entire concentration range and are well-compacted between the HPC layers. To obtain a compact HNTs layer in the film, a certain concentration is needed; in fact, even if the nanotubes are not present at the film surface they may not be enough to generate a layer. From simple geometrical considerations one calculates that at C_f = 10 wt % one may generate a HNTs layer of ca. 2 μm (only two times the nanotube length) if the thickness of 60 μm is considered for the film. On this basis, one can state that below that concentration the sandwich-like structure cannot exist because the HNT particle amount is low. Therefore, we argue that the HNTs layer is obtained above a certain C_f value and the sandwich-like structure makes available a reduced number of lumen able to incorporate volatile products generated by polymer. On the contrary, the homogeneous distribution of HNTs into the LM pectin matrix makes the nanofillers very good barriers, reinforcing the thermal stability of the films at high HNTs loadings.[14]

Finally, as concerns the wettability properties, the monotonic decrease of ϑ_i with C_f observed for the pectin-based materials is in agreement with the enhancement of the surface hydrophilicity caused by the HNT enrichment at the interface as shown by SEM micrographs (Figure 8). The contact angle of 10° for pure HNT was reported,[2] confirming its hydrophilic nature.

For the HPC/HNT films, the peculiar increase of ϑ_i starting at ca. C_f = 15 wt % is not ascribable to the roughness of the surface ruled out by the SEM micrographs but rather to the rearrangement of the polymer structure that exposes the hydrophobic moieties to the interface as a consequence of the interaction with the inner HNTs layer. The HPC-based materials generally provide faster spreading/absorption than the corresponding film based on LM pectin. The sandwich-like structure is responsible for this discrepancy because the surface of the film is essentially a polymer layer.

■ CONCLUSIONS

Films composed of HNTs and polymers from renewable resources were prepared and characterized from the physicochemical viewpoint. The nature of the biopolymer exercises a key effect on the morphology. The hydroxypropylcellulose-based material forms a sandwich-like structure where the nanoclays are buried by two polymer layers. The LM pectin-based material is highlighted by a homogeneous HNTs dispersion on both the surface as well as on the transverse film section. The different mesoscopic structures of the film regulate the physicochemical properties.

Controlling the nanotube allocation within a biopolymeric-based film can open the route to materials with interesting and tunable barrier and delivery properties useful for specific purposes.

■ ASSOCIATED CONTENT

Ⓢ Supporting Information. Water content and residual matter for HPC/HNTs films from TGA data analysis. Dependence of the attenuation coefficient on the wavelength and roughness of the films. Dielectric constant and dispersion factor as functions of the frequency for HPC/HNTs films. Water contact angle as a function of time. Activation energy data from FWO method. This material is available free of charge via the Internet at http://pubs.acs.org.

■ AUTHOR INFORMATION

Corresponding Author

*E-mail: giuseppe.lazzara@unipa.it. Fax: +39 091 590015. Phone: +39 091 6459851.

■ ACKNOWLEDGMENT

The work was financially supported by the University of Palermo and COFIN 2008 (prot. 2008RH3FCW_002). Applied Minerals (USA) is acknowledged for kindly providing the Halloysite sample.

■ REFERENCES

(1) Du, M.; Guo, B.; Jia, D. *Polym. Int.* **2010**, *59*, 574–582.
(2) Lvov, Y. M.; Shchukin, D. G.; Mohwald, H.; Price, R. R. *ACS Nano* **2008**, *2*, 814–820.
(3) Abdullayev, E.; Lvov, Y. *J. Mater. Chem.* **2010**, *20*, 6681–6687.
(4) Fix, D.; Andreeva, D. V.; Lvov, Y.; Shchukin, D. G.; Möhwald, H. *Adv. Funct. Mater.* **2009**, *19*, 1720–1727.
(5) Shchukin, D. G.; Lamaka, S. V.; Yasakau, K. A.; Zheludkevich, M. L.; Ferreira, M. G. S.; Mohwald, H. *J. Phys. Chem. C* **2008**, *112*, 958–964.
(6) Lvov, Y.; Price, R.; Gaber, G.; Ichinose, I. *Colloids Surf.* **2002**, *198–200*, 375–382.

(7) Pan, J.; Yao, H.; Xu, L.; Ou, H.; Huo, P.; Li, X.; Yan, Y. *J. Phys. Chem. C* **2011**, *115*, 5440–5449.

(8) Lin, Y.; Ng, K. M.; Chan, C. M.; Sun, G.; Wu, J. *J. Colloid Interface Sci.* **2011**, *358*, 423–429.

(9) Lecouvet, B.; Gutierrez, J. G.; Sclavons, M.; Bailly, C. *Polym. Degrad. Stab.* **2011**, *96*, 226–235.

(10) Zhou, C.; Du, X.; Liu, Z.; Mai, Y. W.; Ringer, S. *J. Mater. Sci.* **2011**, *46*, 446–450.

(11) Yuan, P.; Southon, P. D.; Liu, Z.; Green, M. E. R.; Hook, J. M.; Antill, S. J.; Kepert, C. J. *J. Phys. Chem. C* **2008**, *112*, 15742–15751.

(12) Tharanathan, R. N. *Trends Food Sci. Technol.* **2003**, *14*, 71–78.

(13) Yu, L.; Dean, K.; Li, L. *Prog. Polym. Sci.* **2006**, *31*, 576–602.

(14) Cavallaro, G.; Lazzara, G.; Milioto, S. *Langmuir* **2011**, *27*, 1158–1167.

(15) Voon, H.; Bhat, R.; Easa, A.; Liong, M.; Karim, A. *Food Bioprocess Technol.* **2010**, 1–9.

(16) Chang, P. R.; Xie, Y.; Wu, D.; Ma, X. *Carbohydr. Polym.* **2011**, *84*, 1426–1429.

(17) Xie, Y.; Chang, P. R.; Wang, S.; Yu, J.; Ma, X. *Carbohydr. Polym.* **2011**, *83*, 186–191.

(18) Giachi, G.; Capretti, C.; Macchioni, N.; Pizzo, B.; Donato, I. D. *J. Cult. Heritage* **2010**, *11*, 91–101.

(19) Guan, Y.; Zhang, Y.; Zhou, T.; Zhou, S. *Soft Matter* **2009**, *5*, 842–849.

(20) Pogodina, N.; Cerclé, C.; Avérous, L.; Thomann, R.; Bouquey, M.; Muller, R. *Rheol. Acta* **2008**, *47*, 543–553.

(21) Rachocki, A.; Markiewicz, E.; Tritt-Goc, J. *Acta Phys. Pol., A* **2005**, *108*, 137–145.

(22) Sudo, S. *J. Phys. Chem. B* **2011**, *115*, 2–6.

(23) Einfeldt, J.; Kwasniewski, A. *Cellulose* **2002**, *9*, 225–238.

(24) Fothergill, J. C. In *Dielectric Polymer Nanocomposites*; Nelson, J. K., Ed.; Springer: New York, 2010.

(25) Du, M.; Guo, B.; Jia, D. *Eur. Polym. J.* **2006**, *42*, 1362–1369.

(26) De Lisi, R.; Lazzara, G.; Milioto, S.; Muratore, N. *J. Therm. Anal. Calorim.* **2007**, *87*, 61–67.

(27) Lazzara, G.; Milioto, S.; Gradzielski, M.; Prevost, S. *J. Phys. Chem. C* **2009**, *113*, 12213–12219.

(28) Cavallaro, G.; Donato, I. D.; Lazzara, G.; Milioto, S. *J. Therm. Anal. Calorim.* **2011**, *104*, 451–457.

(29) Wang, S.; Tan, Z.; Li, Y.; Sun, L.; Li, Y. *J. Therm. Anal. Calorim.* **2008**, *92*, 483–487.

(30) Budrugeac, P.; Segal, E.; Perez-Maqueda, L. A.; Criado, J. M. *Polym. Degrad. Stab.* **2004**, *84*, 311–320.

(31) Vyazovkin, S.; Dranca, I.; Fan, X.; Advincula, R. *J. Phys. Chem. B* **2004**, *108*, 11672–11679.

(32) Farris, S.; Introzzi, L.; Biagioni, P.; Holz, T.; Schiraldi, A.; Piergiovanni, L. *Langmuir* **2011**, *27*, 7563–7574.

(33) Zhou, Q.; Pramoda, K. P.; Lee, J. M.; Wang, K.; Loo, L. S. *J. Colloid Interface Sci.* **2011**, *355*, 222–230.

(34) Marmur, A. *Langmuir* **2008**, *24*, 7573–7579.

Soft Matter

Dynamic Article Links

Cite this: *Soft Matter*, 2012, **8**, 3627

www.rsc.org/softmatter

Attached II

PAPER

Aqueous phase/nanoparticles interface: hydroxypropyl cellulose adsorption and desorption triggered by temperature and inorganic salts†

G. Cavallaro, G. Lazzara* and S. Milioto

Received 21st October 2011, Accepted 17th January 2012
DOI: 10.1039/c2sm07021a

The study highlighted the main forces driving the adsorption of hydroxypropyl cellulose (HPC) onto clay nanoparticles with a disk-like shape (Laponite RD). Modeling the isothermal titration calorimetry data provided the key thermodynamic properties, which enabled us to discuss the microscopic aspects contributing to the energetic and the entropic changes of the polymer adsorption at the nanoparticle/liquid interface. We evidenced that the process is strongly enthalpy-driven and that the interactions lead to constraints of the HPC configuration at interface. The functionalized nanoparticles enhanced the polymer solubility in water expanding the one-phase area of the binodal curve. Temperature and salts change the forces of adsorption and, furthermore, salts generate a dramatic reduction of the HPC solubility in water in the presence of Laponite RD.

Introduction

Over the last few years several polymers from natural resources or biocompatible have been investigated because their use in combination with other additives may form new structures with potential technological applications.[1–6] Designing new nanomaterials composed of biopolymer and nanoparticles environmental friendly is a challenging task. Within this issue, hydroxypropyl cellulose (HPC) assumes a particular interest. It is a biopolymer obtained from the chemical modification of the cellulose and, in particular, the propylene oxide is linked to the anhydroglucose hydroxyl groups. The physico-chemical behavior of HPC is well known based also on its rather high solubility in water although it is hydrophobically modified. HPC undergoes phase separation upon heating,[7] and it is able to form liquid crystals.[8] Interactions between HPC molecules at close separation were evidenced by means of the osmotic stress method coupled with X-ray scattering.[9] This polymer has been used in the consolidation of waterlogged woods and it was revealed very efficient even if optimization of the impregnation process was necessary.[10] HPC is used in preparing organic–inorganic nanocomposites because it ensures the stabilization and the homogeneous dispersions of inorganic salts.[11] The role of the solvent nature (water and ethanol) in the performance of the obtained films was investigated.[12] Finally, HPC assembled with poly(acrylic acid) onto nanoparticles provided long term stability microcapsules for controlled drug delivery applications.[5]

As concerns the nanoparticles, nanoclays are of some interest because they are environmentally friendly and available at low cost. Several studies have been devoted to the physico-chemical characterization of aqueous nanoclay dispersions in the presence of adsorbing species.[13–16] Laponite RD is a synthetic clay that forms charge-stabilized colloidal dispersion in water.[17] The net charge of a single particle is negative and it is due to the negatively charged faces and slightly positive edge.[17]

We thought that HPC may be adopted to functionalize surfaces of solid substrates through non-covalent forces and its interactions with Laponite RD may generate new materials. Being that HPC was approved by the United States Food and Drug Administration,[18] it is recurrent within the pharmaceutical technology and films of HPC have been designed accordingly.[19] Within this issue, we thought it would be interesting to perform a thermodynamic, structural and surface tension study on the aqueous mixtures of HPC and Laponite RD in dependence of the concentration of both the polymer and the nanofiller. Temperature and inorganic salts were selected as parameters to trigger the adsorption process. The thermodynamic properties were obtained from isothermal titration calorimetry and differential scanning calorimetry studies while the diffusion behaviour of the nanoparticles was described by the dynamic light scattering technique. Surface tension experiments evidenced the adsorption phenomenon occurring in the bulk phase.

Materials and methods

Chemicals

Hydroxypropyl cellulose (weight average molecular mass = 80 kg mol^{-1} and number average molecular mass = 10 kg mol^{-1}) and NaCl (99.999%) are Sigma products. KCl (99.99%) is from

---

Dipartimento di Chimica "S. Cannizzaro", Università degli Studi di Palermo, Viale delle Scienze, Parco D'Orleans II, Pad. 17, 90128 Palermo, Italy. E-mail: giuseppe.lazzara@unipa.it

† Electronic supplementary information (ESI) available. See DOI: 10.1039/c2sm07021a

Merck and LiCl (99.99%) is from Riedel-de-Hoën, AG. Laponite RD grade was a gift from Azelis Italia S.r.l. and it was used as received. It has the molecular formula[17] $Si_8(Mg_{5.45}Li_{0.4})O_{20}(OH)_4Na_{0.7}$ constituting the unitary cell of the disk-like clay platelet with a diameter of about 25 nm and a thickness of 1 nm. The molar mass of the Laponite RD unit cell is 764.55 g mol^{-1}. Water from reverse osmosis (Elga model Option 3) with a specific resistivity greater than 1 MΩ cm was used. The water content of 2.9 wt% for the polymer was determined by thermo-gravimetry.

Samples preparation

Laponite RD dispersion was prepared according to the literature procedure.[17] Briefly, nanoclay powder was added to water and the mixture was kept under stirring for at least 3 hours before the measurements. Aqueous hydroxypropyl cellulose (HPC) solution was prepared by mixing under vigorous stirring for *ca.* 2 hours a certain amount of polymer with water at 60 °C. The solution was left to equilibrate at room temperature under stirring overnight. The final polymer concentration was evaluated by weight.

Differential scanning calorimetry (DSC)

The micro-DSC III 106 (Setaram) under nitrogen flow in the range from 5 to 80 °C with a scan rate of 0.6 °C min^{-1} was used. The stainless steel (1 cm^3) sample cell contained *ca.* 500 mg of solution while the reference cell was filled with a comparable amount of water. The calibration was performed by using naphthalene.

For all the aqueous HPC solution in the absence and the presence of Laponite RD, a single endothermic phenomenon was observed and ascribed to the cloud point of HPC in agreement with the literature.[7,20] Examples of thermograms are collected in the ESI†. The cloud temperature (t_C) at the maximum of the peak as well as the corresponding enthalpy (ΔH_C) from the integration of the thermogram were determined. The baseline was subtracted according to the literature.[21] The measurements were carried out at a fixed HPC concentration by systematically changing the Laponite RD amount. The investigated solvent media are water and aqueous solutions of NaCl and KCl (both 5 mmol kg^{-1}). The uncertainty in t_C is ±0.1 °C and in ΔH_C is 3%.

Experiments performed on some dispersions in a week-range did not evidence time effects (data are in the ESI†).

Isothermal titration calorimetry (ITC)

The ITC experiments were performed by using the ultrasensitive nano-ITC200 calorimeter (MicroCal). The amount of approximately 40 μL of the water + HPC mixture was injected into the thermally equilibrated ITC cell (200 μL) containing the water + Laponite RD dispersion. Under the same experimental conditions, the dilution of the aqueous HPC solution and the Laponite RD dispersion with water were carried out. The temperature was changed from 5 to 45 °C. The effect of salt addition was investigated at 15 °C; namely, aqueous solutions of NaCl, KCl and LiCl (all 5 mmol kg^{-1}) were used as solvents. The concentration of 5 mmol kg^{-1} was chosen because, based on the phase diagram, larger salt amounts generate the nanoclay precipitation.[22]

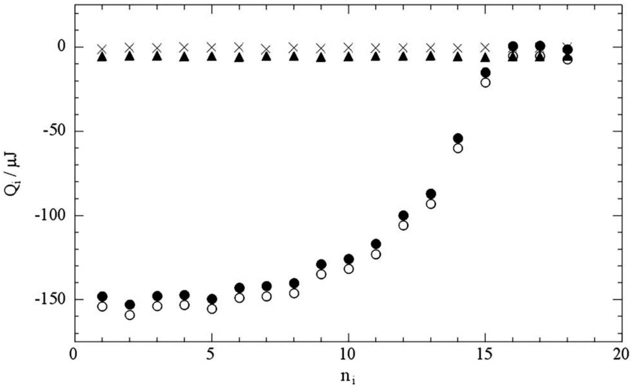

Fig. 1 Dependence on the number of injections of the heats of injection of the HPC solution into water (▲), of water into the Laponite RD dispersion (×), of the HPC solution into the Laponite RD dispersion (○) and heat of interaction (●) at 25 °C.

Fig. 1 illustrates an example of the enthalpic effects for a complete titration experimental set; namely, the dependence on the number of injections (n_i) of the heats of injection of the aqueous HPC solution into water (Q_{HPC}), of water into the aqueous Laponite RD dispersion (Q_L) and of the aqueous HPC solution into the aqueous Laponite RD dispersion ($Q_{HPC/L}$) is reported. Moreover, $Q_{HPC/L}$ corrected for the dilution effects (Q_{HPC} and Q_L) is also shown (Q_i). The heat of interaction per mole of HPC (ΔH_i) was calculated as $Q_i/(V_aM_P)$ being V_a the volume of each addition and M_P the polymer molarity. Both the dilution heats are slightly negative and almost negligible. Q_L is consistent with the negative dilution enthalpies of aqueous Laponite RD dispersion with water.[23]

Surface tension

A programmable tensiometer (KSV Sigma 70) equipped with a Wilhelmy plate was employed at 25.0 ± 0.1 °C. A concentrated polymer solution (being the solvent water or water + NaCl) was added to the corresponding solvent to obtain various polymer concentrations. Moreover, the presence of Laponite RD was investigated as detailed in the following. A concentrated polymer in the solvent (water or water + NaCl) was added to the Laponite RD dispersion in the corresponding solvent to obtain several polymer concentrations. The NaCl and Laponite RD concentrations are 5 and 0.4 mmol kg^{-1}, respectively. The additions of the polymer solution were done to cover a proper range of polymer/Laponite RD ratio based on the ITC experiments. The surface tension of each mixture was determined at the equilibrium. Each surface tension value is the average of three determinations and its precision is 0.1 dyne cm^{-1}.

Dynamic light scattering

The measurements were performed at 18.0 ± 0.1 °C in a sealed cylindrical scattering cell at a scattering angle of 90° by means of a Brookhaven Instrument apparatus composed of an BI-9000AT correlator and a He–Ne laser (75 mW) with a wavelength (λ) of 632.8 nm. The solvent was filtered by means of a Millipore filter with 0.45 μm pore size.

The field-time autocorrelation functions were well described by a mono-exponential decay function, which provides the decay rate (Γ) correlated to the apparent diffusion coefficient (D)

$$D = \Gamma/q^2 \tag{1}$$

where q is the scattering vector given by $4\pi n\lambda^{-1}\sin(\theta/2)$ being n the water refractive index and θ the scattering angle. The apparent hydrodynamic radius (R_h) was calculated by using the Stokes–Einstein equation and the water viscosity value. Examples of mono-exponential fitting are collected in the ESI†. The hydrodynamic radius of the Laponite RD in water agrees with the literature.[24,25]

Results

Isothermal titration calorimetry studies

Fig. 2a shows the effect of the polymer/Laponite RD mole ratio ($R_{\mathrm{HPC:L}}$) on the heat of interaction per mole of HPC (ΔH_i) from 5 to 45 °C. At a given temperature, the ΔH_i *vs.* $R_{\mathrm{HPC:L}}$ profile describes a sigmoidal curve that reaches null values at the highest $R_{\mathrm{HPC:L}}$ values. Upon increasing the temperature ΔH_i assumes more and more negative values generating sharper ΔH_i *vs.* $R_{\mathrm{HPC:L}}$ S-shaped curves; moreover, the inflection point of each trend is essentially independent of temperature.

The electrolyte generates relevant effects on the ΔH_i *vs.* $R_{\mathrm{HPC:L}}$ curves (Fig. 2b). The addition of NaCl shifts the enthalpic curve towards negative values while it does not alter the $R_{\mathrm{HPC:L}}$ at the inflection point. Differently, both KCl and LiCl shift the inflection point toward smaller $R_{\mathrm{HPC:L}}$ values and the observed heat effects are smaller than the corresponding data in water. These results reveal specificity of the interactions between the HPC and the Laponite RD triggered by the presence of electrolytes, which can alter the energetics of the adsorption process as well as the HPC/Laponite RD stoichiometry of interaction.

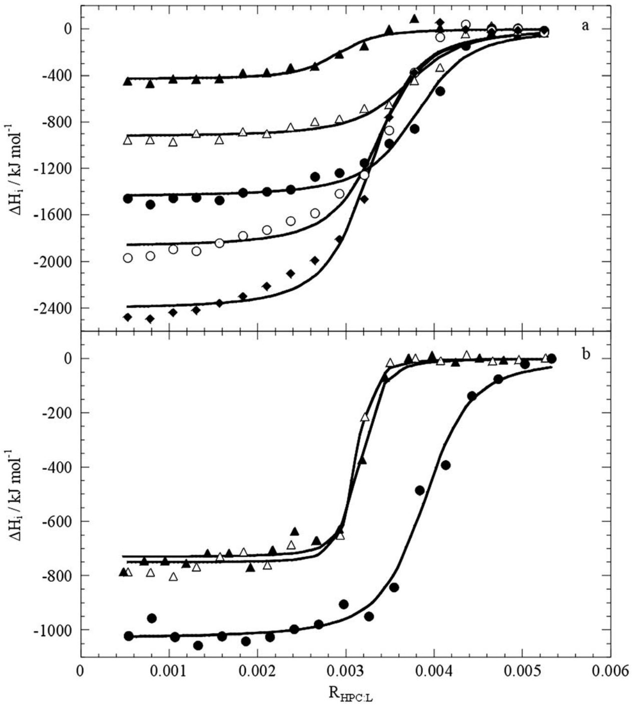

Fig. 2 Heat of interaction per mol of HPC as functions of the HPC/Laponite RD unit cell mole ratio in the absence (a) and the presence (b) of salts. (a) 5 °C (▲), 15 °C (△), 25 °C (●), 35 °C (○) and 45 °C (◆). (b) LiCl (▲), NaCl (●) and KCl (△), all 5 mmol kg^{-1} and 15 °C. Lines are best fits according to eqn (2)–(6).

The ΔH_i *vs.* $R_{\mathrm{HPC:L}}$ S-shaped curve reflects a single adsorption process interpretable by means of simple models, which have been revealed successful for the adsorption of macromolecules onto nanoparticles in water.[23,26,27] We assume that Laponite RD exhibits a total moles of adsorption sites per litre of water (S_t) given by[23]

$$S_t = Z[M_L] \tag{2}$$

where $[M_L]$ is the Laponite RD concentration in formula unit molarity and Z is the moles of sites contained in 1 mole of Laponite RD formula unit.

The equilibrium constant is

$$K_{\mathrm{ads}} = \frac{S_1}{[M_{\mathrm{pw}}]S_f} \tag{3}$$

where S_1 represents the moles of sites per litre of mixture occupied by the polymer, whereas S_f is the moles of free sites per litre of mixture; $[M_{\mathrm{pw}}]$ stands for unbound polymer molarity.

The injection heat for the i^{th} titration step is given by

$$Q_i = Q_j - Q_{j-1} + (Q_j + Q_{j-1})V_a/2V_c \tag{4}$$

For the j^{th} and $(j^{\mathrm{th}} - 1)$ states before and after the i^{th} addition step the corresponding Q_j and Q_{j-1} are

$$Q_j = [M_P]_j V_c \Delta H^\circ_{\mathrm{ads}} [X_{\mathrm{ads}}]_j \tag{5}$$

$$Q_{j-1} = [M_P]_{j-1} V_c \Delta H^\circ_{\mathrm{ads}} [X_{\mathrm{ads}}]_{j-1} \tag{6}$$

where $\Delta H^\circ_{\mathrm{ads}}$ is the enthalpy of adsorption per mole of polymer, V_c is the cell volume and X_{ads} is the fraction of adsorbed polymer controlled by the equilibrium constant.

Note that the third term at the right hand side of eqn (4) is the correction for the displaced volume.[28]

According to eqn (2)–(6) the experimental data (Fig. 2) were successfully fitted and provided K_{ads}, Z and $\Delta H^\circ_{\mathrm{ads}}$. The minimizing procedure was performed by means of the non-linear least-squares fitting based on the Levenberg–Marquardt algorithm.

The standard free energy and entropy for the adsorption process were calculated as:

$$\Delta G^\circ_{\mathrm{ads}} = -RT\ln K_{\mathrm{ads}},\ T\Delta S^\circ_{\mathrm{ads}} = \Delta H^\circ_{\mathrm{ads}} - \Delta G^\circ_{\mathrm{ads}} \tag{7}$$

From the Z value, the adsorbed amount of HPC (Z^*) per Laponite RD surface area was calculated by using the Laponite RD specific area of 200 m^2 g^{-1}.[24,29]

The adsorption of the polymer at the solid/liquid interface is entropy driven. As Fig. 3 shows, $\Delta S^\circ_{\mathrm{ads}}$ and $\Delta H^\circ_{\mathrm{ads}}$ compensate for each other, and their temperature slope is negative. Such a compensation is a real phenomenon related to the hydrophobic effect as proved by a statistical test[30,31] applied to our data. As

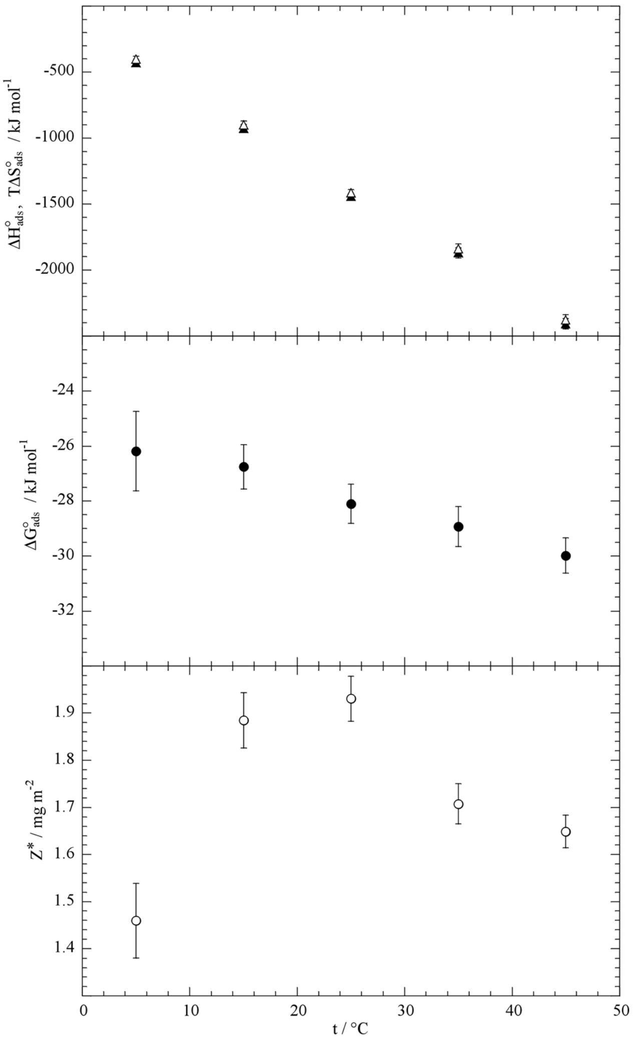

Fig. 3 Standard free energy (●), enthalpy (▲), entropy (△) and stoichiometry (○) for the HPC adsorption onto aqueous Laponite RD at various temperatures.

concerns Z^*, it exhibits a slight change with temperature with a maximum at 25 °C (Fig. 3).

The salts do not affect the mechanism of adsorption but they slightly enhance the adsorption process (see ΔG°_{ads} in Table 1) making the HPC less soluble in water.[9] Compared to the values in water, ΔH°_{ads} increases in the presence of LiCl and KCl, while it decreases in the presence of NaCl (Fig. 4). A similar trend was observed for the Z^* values (Table 1).

Table 1 Standard free energy and stoichiometry for the HPC adsorption onto Laponite RD in water and in the presence of LiCl, NaCl and KCl, all 5 mmol kg^{-1} and 15 °C[a]

	ΔG°_{ads}	Z^*
Water	−26.7 ± 0.8	1.88 ± 0.06
LiCl	−31.1 ± 0.9	1.60 ± 0.02
NaCl	−31.3 ± 0.6	1.97 ± 0.03
KCl	−32.4 ± 1.1	1.56 ± 0.02

[a] Units are: ΔG°_{ads}, kJ mol^{-1} and Z^*, mg m^{-2}.

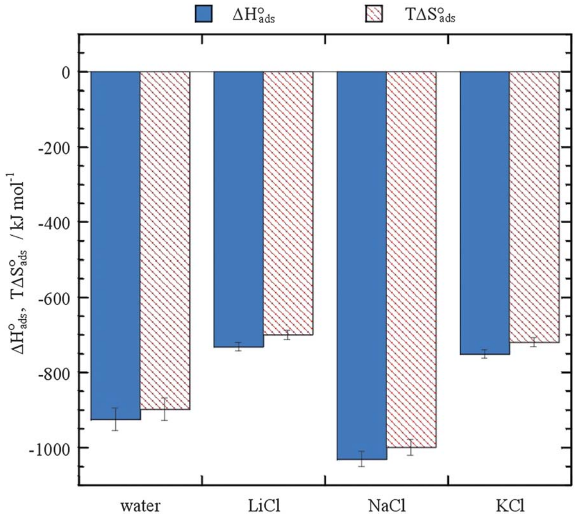

Fig. 4 Standard enthalpy and entropy for the HPC adsorption onto aqueous Laponite RD in the absence and the presence of LiCl, NaCl and KCl, all 5 mmol kg^{-1} and 15 °C.

Diffusion of aqueous Laponite RD in the presence of HPC

In the investigated HPC concentration regime, the scattering intensity of the polymer solution, in the absence of nanoparticles, was very low and it did not allow us to obtain a reliable correlation function to determine the HPC diffusion coefficient. The fact that Laponite RD can be easily monitored while HPC appears invisible is ascribable to the dispersed material–water contrast differences, given by the refractive indexes. In particular, for Laponite RD,[32] HPC[33] and water the refractive index values are 1.51, 1.34 and 1.33, respectively. Nevertheless, the results obtained for the aqueous Laponite RD/HPC mixtures are rather interesting. As Fig. 5 shows, the hydrodynamic radius (R_h) linearly increases with the $R_{HPC:L}$. Even if the polymer does not scatter much in water, one can ascribe such an increase to the polymer adsorption onto the solid surface. In fact, the Laponite RD particle covered by HPC has a slower dynamics than the bare Laponite RD and it maintains a sufficient scattering intensity. The maximum change in R_h is of *ca.* 20 nm and it is of the same order of magnitude of the variation observed[25] for adsorbing

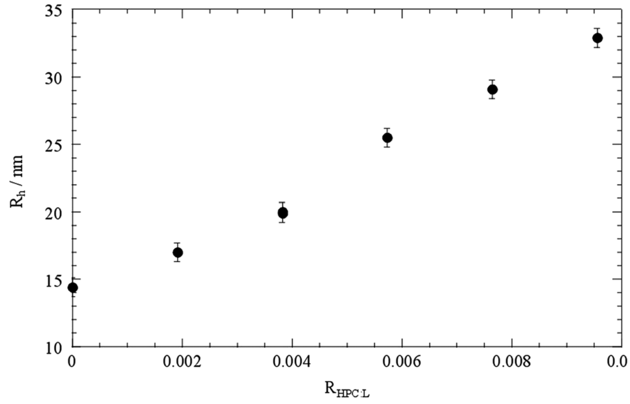

Fig. 5 Apparent hydrodynamic radius of HPC/Laponite RD mixtures in the aqueous phase as a function of their mole ratio.

poly(ethyleneglycols) with a molecular mass similar to the present HPC.

Differential scanning calorimetry studies

It is well known that HPC undergoes phase separation upon heating because the water cages surrounding the hydrophobic moieties of the polymer molecule melt.[6] The addition of Laponite RD generates a big effect on the cloud behavior of the polymer; namely, t_C increases describing a sigmoidal profile (Fig. 6), which indicates that the role of the Laponite RD on the HPC solubility is rather complex. The enlargement of the one-phase region in the presence of Laponite RD may be a consequence of the HPC adsorption onto the solid surface; in other words, the amount of free HPC is decreased and the solubility is increased. We also monitored the effect of the electrolytes and, in particular, NaCl and KCl were selected because they exhibited different adsorption behavior onto the Laponite RD surface. It is rather intriguing that the presence of just 5 mmol kg^{-1} of electrolytes generates a t_C which diminishes upon Laponite RD addition (Fig. 6). It appears that the electrolytes play a relevant salting out effect in the presence of Laponite RD because not only they cancel the improvement of the HPC solubility created by the nanoparticles but also make t_C lower than the value in water (Fig. 6).

Salts lower the HPC cloud-point transition temperature in water but at a concentration much larger than those investigated here.[9,20,34] Xia *et al.*[34] ascribed such an effect to the weakening of hydrogen bonding between HPC and water. The mechanism that salts act indirectly on HPC precipitation through its exclusion from the condensed phase was also invoked.[9,20,34] Our systems are rather complex and the presence of the nanoclay generates a more relevant salt effect on the HPC cloud behavior.

As concerns ΔH_C, it diminishes upon the nanoclay addition and the presence of Laponite RD 2.5 wt% reduces the enthalpy by one order of magnitude (Fig. 6). The electrolytes do not much alter ΔH_C whatever is their nature (Fig. 6). The ΔH_C change in the presence of Laponite RD is consistent with the reduced number of macromolecules that undergo the phase separation as a consequence of their interactions with the nanoparticles.

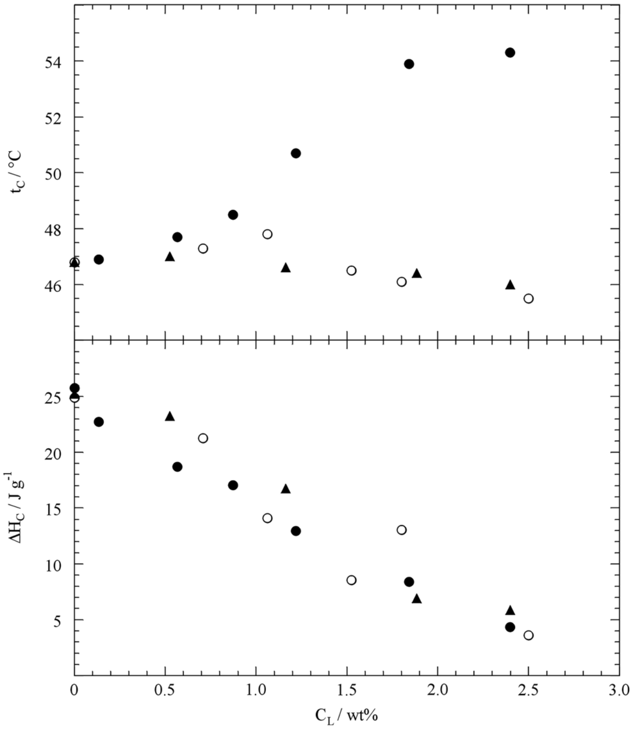

Fig. 6 Dependence on the Laponite RD concentration for temperature and enthalpy of the HPC phase separation in the absence (●) and the presence of NaCl 5 mmol kg^{-1} (○) and KCl 5 mmol kg^{-1} (▲).

Surface tension of the aqueous HPC solutions in the presence of Laponite RD and NaCl

To understand in a comprehensive manner the role played by the electrolyte and the nanoparticles on the HPC behaviour at the interface, the surface tension (γ) investigation was extended to the HPC + Laponite RD + NaCl + water mixtures by changing the polymer concentration (C_P, wt%) and keeping constant the concentrations of NaCl (5 mmol kg^{-1}) and Laponite RD (0.4 mmol kg^{-1}). For a comparison purpose, the HPC + water and HPC + NaCl + water mixtures as functions of C_P were also studied.

As Fig. 7a illustrates, HPC strongly lowers γ of water even at very low concentration and the values agree with the literature reports.[35] The presence of NaCl does not alter much γ values. The Gibbs equation applied to γ data of HPC in water and water + NaCl mixture allowed us to estimate the HPC surface

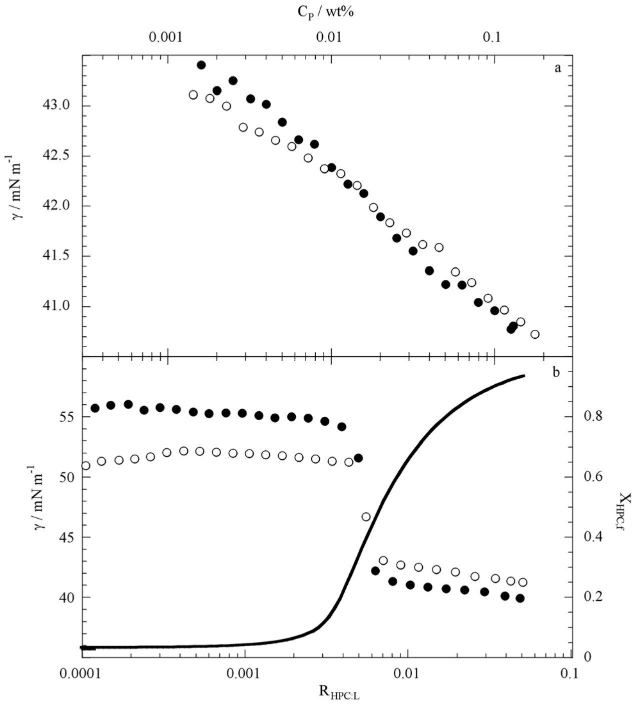

Fig. 7 Surface tension of aqueous HPC mixtures as a function of the polymer concentration: (a) the solvents are water (●) and water + NaCl (○); and (b) the solvents are water + Laponite RD (●) and water + Laponite RD + NaCl (○). $C_L = 0.033$ wt%; $m_{NaCl} = 5$ mmol kg^{-1}. The line is the fraction of non-adsorbed HPC calculated from ITC data (see text).

area (A_P), that is, 49.7 ± 1.3 and 61.1 ± 1.1 $m^2 g^{-1}$, respectively. From the model-projected surface areas[36] the A_P value of *ca.* 1800 $m^2 g^{-1}$ is obtained and therefore one can conclude that the polymer at the interface presents loops and tails to a large extent. Such a configuration agrees with the polymer hydrophilic nature. Similar conclusions were drawn[37] by surface light scattering experiments, which also showed that the HPC molecular mass does not play a relevant role. Moreover, we can state that the salt addition generates a slightly more flat polymer layer configuration than that observed in water. This result can be explained considering that the presence of NaCl reduces the HPC solubility in water because the salt apparently weakens the hydrogen bonding between HPC and water[34] and the polymer escapes from the solvent to the interface, consequently.

The Laponite RD addition is very intriguing (Fig. 7b) because it dramatically alters not only the γ values but also the shape of the γ *vs.* C_P trend. Namely, in the low C_P regime, it generates γ values larger than those in the corresponding solvent (water or water + NaCl) without Laponite RD. This finding is consistent with the HPC adsorption onto the Laponite RD surface, which lowers the polymer chemical potential in solution and therefore γ increases. Upon the polymer addition, γ suddenly decreases approaching a constant value that is close to the value in the absence of Laponite RD. As Fig. 7b shows, NaCl does not alter the γ *vs.* C_P trend in the presence of Laponite RD.

Discussion

The adsorption of a polymer at the solid/liquid interface involves a series of microscopic aspects that can differently contribute to the energetics of the entire process.

In particular, one observes the partial rupturing of the water–polymer and water–nanoparticle bonds and the formation of polymer–nanoparticle interactions. Given that $\Delta H^\circ_{ads} < 0$ (Fig. 3), the polymer–nanoparticle interactions are the dominant forces. This finding agrees with reports[23] on the adsorption of poly(ethylene-glycol), poly(propylene-glycol) and Pluronics onto Laponite RD. The entropy change, in principle, is the result of three contrasting effects: (i) the loss of configuration freedom of the polymer in the adsorbed state; (ii) the release of ions from the Laponite RD surface caused by the polymer adsorption and (iii) the water release (de-hydration) from the polymer. The strong entropy change confirms that the constraints of the polymer motion at the solid/liquid interface are the dominant entropic factors (Fig. 3). Nowicki[38] calculated that the polymer attached to the colloidal particle decreases its entropy. This result agrees with the R_h data that indicate a large number of contact points between the polymer and the nanoparticle. This result is peculiar for polymer adsorbed onto disk-like nanoparticles as also evidenced by neutron scattering experiments.[27,39] Differently, spherical nanoparticles lead to a hairy adsorbed polymer layer and in this case the adsorption was entropy driven.[40]

Temperature change affects the energetics of the adsorption process but the entropy–enthalpy compensation generates little changes in the ΔG°_{ads} with temperature. Concerning this aspect it is noteworthy to highlight the importance of direct measurements of thermodynamic properties. The issue on the comparability of the enthalpy derived from van't Hoff and calorimetric methods is still a debated matter.[41–43] In our case, based on the negative enthalpy change and the van't Hoff equation, one would expect a positive ΔG°_{ads} *vs.* temperature slope, that is opposite to the experimental findings (Fig. 3). The correlation of ΔG°_{ads} to temperature through the classical van't Hoff equation might be inappropriate because of the presence of supramolecular interactions (stoichiometry and polydispersity), which might be largely influenced by temperature variation. For the polymer/cyclodextrin inclusion complex formation, discrepancy between the enthalpies derived by the two methods was observed.[44] In our case, we found that the Z^* parameter is not constant (Fig. 3) and therefore the $\delta Z^*/\delta T$ contribution should be considered in the van't Hoff approach. Actually, this correction term cannot be rigorously calculated and, furthermore, if charged systems are considered (like Laponite RD) the $\delta Z^*/\delta T$ contribution can be the dominant effect due to the large pre-factor of the $\delta Z^*/\delta T$ derivative and the non-null derivative value[42] as observed here (Fig. 3). Nevertheless, it is straightforward that only the calorimetric experiments provide direct and unambiguous insights into the heat exchange occurring during a given process and this is particularly important for supramolecular associative processes in solution.[23,44–47]

As soon as the thermodynamics of the process in the bulk phase is well described, the aqueous phase/air interfacial properties can be quantitatively interpreted. The γ *vs.* C_P profile can be understood to the light of the fraction of free HPC in solution $X_{HPC,f}$ (calculated from the adsorption isotherm data). Fig. 7b illustrates that $X_{HPC,f}$ is nearly negligible at low C_P while it increases reaching a nearly unitary value at larger concentration. It is interesting that the shapes of the curves in Fig. 7b are rather similar and that to the sharp $X_{HPC,f}$ change corresponds the sharp γ decrease. From this evidence one deduces that the step-like change in the γ *vs.* C_P profile in the presence of Laponite RD reflects the saturation of the nanoparticles surface and that the polymer covering Laponite RD is not surface active or, at least, it is less surface active than the unbound polymer.

The salt addition might represent a strategy to control the structure of the HPC-covered Laponite RD. It is known that the HPC solvophilicity in water can be influenced by concentrated monovalent salts[9,20,34] and that the Laponite RD + water mixture is strongly sensitive to electrolytes.[22] We showed that the cloud point of HPC can be altered by adding the clay nanoparticles and that, compared to HPC in water, HPC in water + Laponite RD has a cloud behavior very sensitive to the salt addition.

The HPC adsorption isotherms in the presence of salts showed a peculiarity of NaCl (Table 1). This effect reflects neither the change of the hydrated ionic radii of the cations nor the chaotropic series. On the other hand one has to consider that the Laponite RD nanoparticles are charged because they release Na^+ ions from the disk-face surface into the aqueous phase. Thus, one may suppose that the NaCl effect is ascribable to the sodium common ion. To clarify this aspect one can calculate that under our experimental conditions and considering a charge of −700e for each disk,[22] the Laponite RD dissociation generates a sodium concentration in solution of *ca.* 4 mmol kg^{-1}. Being that this value is comparable to the concentration of the added salt, one expects that the ion release from Laponite RD is reduced in the presence of NaCl due to the common ion effect. To the light of this calculation one supposes a slightly small contribution of the Laponite RD dissociation to ΔH°_{ads}. Consequently, the decrease of ΔH°_{ads} in NaCl is explained as well as the opposite results of other salts for which the common ion effect cannot be invoked. The common ion phenomenon takes into account the Z^{*} values that evidence the NaCl peculiarity (Table 1). Accordingly, LiCl and KCl decrease the maximum amount of HPC adsorbed per Laponite RD cell unit mole while NaCl does not alter the stoichiometry of the adsorption process. The negligible influence of NaCl on the aqueous phase/air surface properties agrees with the unchanged polymer/Laponite RD stoichiometry upon NaCl addition as evidenced by ITC experiments.

Conclusions

The aim of the work was designing nanostructures in aqueous media that are inexpensive, biocompatible, environmentally friendly and advanced for potential specific purposes. Calorimetric experiments allowed us to determine the thermodynamics of the adsorption of a thermosensitive polymer HPC onto the nanoclay surface in aqueous solution. From the ITC data analysis it emerged that the adsorption process is favored and enthalpy driven. The HPC freedom at the nanoparticle/aqueous phase interface is reduced compared to that in the bulk phase. The knowledge of the adsorption equilibrium in the bulk allowed us to explain the air/solution interface properties. The role played by the salt addition is also interesting because the HPC cloud point in the presence of Laponite RD is highly affected and the polymer adsorption onto the nanoparticle is sensitive to the nature of the electrolyte showing a peculiarity for sodium ion that is the one released by Laponite RD.

The importance of direct measurements of the thermodynamic properties in supramolecular systems is remarked for a correct interpretation of the energetics of the involved processes.

We conclude that the nanoparticles functionalization triggered by temperature and/or inorganic salts opens up new routes for the control of the solid surfaces with the aim of obtaining smart materials.

Acknowledgements

The work was financially supported by the University of Palermo (Italy) and COFIN 2008 (Prot. 2008RH3FCW_002). Azelis Italia S.r.l. is acknowledged for kindly providing the Laponite RD sample.

References

1 G. Cavallaro, G. Lazzara and S. Milioto, *Langmuir*, 2011, **27**, 1158–1167.
2 G. Lazzara, S. Milioto, M. Gradzielski and S. Prevost, *J. Phys. Chem. C*, 2009, **113**, 12213–12219.
3 R. N. Tharanathan, *Trends Food Sci. Technol.*, 2003, **14**, 71–78.
4 M. Hassan-Nejad, J. Ganster, A. Bohn, M. Pinnow and B. Volkert, *Macromol. Symp.*, 2009, **280**, 123–129.
5 Y. Guan, Y. Zhang, T. Zhou and S. Zhou, *Soft Matter*, 2009, **5**, 842–849.
6 R. De Lisi, G. Lazzara, S. Milioto and N. Muratore, *J. Phys. Chem. B*, 2004, **108**, 1189–1196.
7 L. Robitaille, N. Turcotte, S. Fortin and G. Charlet, *Macromolecules*, 1991, **24**, 2413–2418.
8 I. W. Hamley, *Soft Matter*, 2010, **6**, 1863–1871.
9 J. Chik, S. Mizrahi, S. Chi, V. A. Parsegian and D. C. Rau, *J. Phys. Chem. B*, 2005, **109**, 9111–9118.
10 G. Giachi, C. Capretti, N. Macchioni, B. Pizzo and I. D. Donato, *J. Cult. Heritage*, 2010, **11**, 91–101.
11 I. Bobowska, P. Wojciechowski and T. Halamus, *Polym. Adv. Technol.*, 2008, **19**, 1860–1867.
12 J. Bajdik, J. Regdon, T. Marek, I. Eros, K. Suvegh and K. Pintye-Hòdi, *Int. J. Pharm.*, 2005, **301**, 192–198.
13 C. W. Chang, A. van Spreeuwel, C. Zhang and S. Varghese, *Soft Matter*, 2010, **6**, 5157–5164.
14 R. M. Guillermic, A. Salonen, J. Emile and A. Saint-Jalmes, *Soft Matter*, 2009, **5**, 4975–4982.
15 R. De Lisi, G. Lazzara, S. Milioto and N. Muratore, *Langmuir*, 2006, **22**, 8056–8062.
16 I. Boucenna, L. Royon, P. Colinart, M. A. Guedeau-Boudeville and A. Mourchid, *Langmuir*, 2010, **26**, 14430–14436.
17 S. L. Tawari, D. L. Koch and C. Cohen, *J. Colloid Interface Sci.*, 2001, **240**, 54–66.
18 J. Gao, G. Haidar, X. Lu and Z. Hu, *Macromolecules*, 2001, **34**, 2242–2247.
19 G. Cavallaro, D. I. Donato, G. Lazzara and S. Milioto, *J. Phys. Chem. C*, 2011, **115**, 20491–20498.
20 C. Bonnet-Gonnet, S. Leikin, S. Chi, D. C. Rau and V. A. Parsegian, *J. Phys. Chem. B*, 2001, **105**, 1877–1886.
21 D. Malakhov and M. Abou Khatwa, *J. Therm. Anal. Calorim.*, 2007, **87**, 595–599.
22 B. Ruzicka and E. Zaccarelli, *Soft Matter*, 2011, **7**, 1268–1286.
23 R. De Lisi, G. Lazzara, R. Lombardo, S. Milioto, N. Muratore and M. L. Turco Liveri, *Phys. Chem. Chem. Phys.*, 2005, **7**, 3994–4001.
24 R. De Lisi, G. Lazzara, S. Milioto and N. Muratore, *Chemosphere*, 2007, **69**, 1703–1712.
25 A. Nelson and T. Cosgrove, *Langmuir*, 2004, **20**, 10382–10388.
26 K. Chiad, S. H. Stelzig, R. Gropeanu, T. Weil, M. Klapper and K. Mullen, *Macromolecules*, 2009, **42**, 7545–7552.
27 R. De Lisi, M. Gradzielski, G. Lazzara, S. Milioto, N. Muratore and S. Prévost, *J. Phys. Chem. B*, 2008, **112**, 9328–9336.
28 J. Tellinghuisen, *Anal. Biochem.*, 2007, **360**, 47–55.
29 T. Kollár, Z. Kónya, I. Pálinkó and I. Kiricsi, *J. Mol. Struct.*, 2001, **563–564**, 417–420.
30 K. Sharp, *Protein Sci.*, 2001, **10**, 661–667.
31 R. R. Krug, W. G. Hunter and R. A. Grieger, *J. Phys. Chem.*, 1976, **80**, 2335–2341.
32 P. B. Laxton and J. C. Berg, *J. Colloid Interface Sci.*, 2006, **296**, 749–755.
33 A. Dupuis, N. Guo, Y. Gao, N. Godbout, S. Lacroix, C. Dubois and M. Skorobogatiy, *Opt. Lett.*, 2007, **32**, 109–111.
34 X. Xia, S. Tang, X. Lu and Z. Hu, *Macromolecules*, 2003, **36**, 3695–3698.
35 S. A. Chang and D. G. Gray, *J. Colloid Interface Sci.*, 1978, **67**, 255–265.
36 C. S. Gau, H. Yu and G. Zografi, *Macromolecules*, 1993, **26**, 2524–2529.
37 E. J. McNally and G. Zografi, *J. Colloid Interface Sci.*, 1990, **138**, 61–68.
38 W. Nowicki, *Macromolecules*, 2002, **35**, 1424–1436.
39 A. Nelson and T. Cosgrove, *Langmuir*, 2004, **20**, 2298–2304.
40 R. De Lisi, G. Lazzara, S. Milioto and N. Muratore, *Phys. Chem. Chem. Phys.*, 2008, **10**, 794–799.
41 J. B. Chaires, *Biophys. Chem.*, 1997, **64**, 15–23.
42 A. Holtzer and M. F. Holtzer, *J. Phys. Chem.*, 1974, **78**, 1442–1443.
43 P. Taboada, V. Mosquera, D. Attwood, Z. Yang and C. Booth, *Phys. Chem. Chem. Phys.*, 2003, **5**, 2625–2627.
44 R. De Lisi, G. Lazzara and S. Milioto, *Phys. Chem. Chem. Phys.*, 2011, **13**, 12571–12577.
45 M. Tiné, M. Alderighi, C. Duce, L. Ghezzi and R. Solaro, *J. Therm. Anal. Calorim.*, 2011, **103**, 75–80.
46 I. V. Terekhova, A. O. Romanova, R. S. Kumeev and M. V. Fedorov, *J. Phys. Chem. B*, 2010, **114**, 12607–12613.
47 C. De Stefano, A. Gianguzza, D. Piazzese, N. Porcino and S. Sammartano, *Biophys. Chem.*, 2006, **122**, 221–231.

Attached III

THE JOURNAL OF PHYSICAL CHEMISTRY C

Article

pubs.acs.org/JPCC

Exploiting the Colloidal Stability and Solubilization Ability of Clay Nanotubes/Ionic Surfactant Hybrid Nanomaterials

Giuseppe Cavallaro, Giuseppe Lazzara,* and Stefana Milioto

Department of Chemistry "S. Cannizzaro", University of Palermo, Viale delle Scienze, pad. 17, 90128 Palermo, Italy

Ⓢ *Supporting Information*

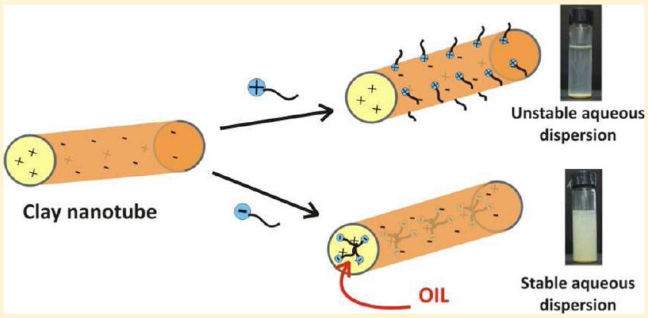

ABSTRACT: Halloysite clay nanotubes are functionalized by exploiting the different charges between the inner positive and the outer negative surfaces; accordingly, a selective adsorption is pursued by employing anionic and cationic surfactants. The obtained hybrid materials dispersed in aqueous phase are studied from the physicochemical viewpoint to investigate the colloidal stability that is a crucial parameter for applications. It is demonstrated that the adsorption of anionic surfactant into the HNTs lumen increases the net negative charge of the nanotubes enhancing the electrostatic repulsions and consequently the dispersion stability. The solubilization capability of these functionalized nanotubes toward hydrophobic compounds is demonstrated. This paper puts forward an easy strategy to prepare hybrid materials, like inorganic micelles, that can be used in water for solubilization and delivery of a hydrophobic compound by taking advantage of the sustainable and biocompatible properties.

■ INTRODUCTION

The demands of applications in several fields (pharmaceutical, optical, and environmental) have induced research in the past decade to manipulate the chemico-physical properties of nanostructures through the control of the chemistry of the constituents as well as the morphology of these structures. The functionalization of inorganic nanoparticles has been explored to improve the nanoparticles dispersal and properties in aqueous media.[1−3] Emerging nanoparticles are carbon nanotubes (CNTs) to which consistent research has been addressed; accordingly, in the past decade thousands of papers have been published with a continuous trend and several of them were devoted to the stabilization of aqueous CNTs dispersions.[4] Indeed, other interesting nanotubes that are promising components for various hybrid materials are represented by clays: imogolite[5] and natural halloysite[6] (HNTs). In recent papers,[6,7] Lvov stated that HNTs are cheap, abundant, durable, and biocompatible, but at the same time, they are not yet well investigated in view of exploring the chemistry of the inner and outer surfaces, which differ in the charge. The HNT external surface is composed of Si−O−Si groups, whereas the internal surface consists of a gibbsite-like array of Al−OH groups conferring the negative and positive charge at the outer and inner surfaces in a wide pH range in water.[6,8] HNTs are quite polydisperse in size; their length is between 0.1 and 2 μm, and the outer and inner diameters are ca. 30−50 and 1−30 nm, respectively.[6] In the past decade, the number of papers published within this topic is relatively low (ca. 100, half of which are from the last five years) compared to those dealing with the carbon nanotubes. Nevertheless, studies demonstrated the potential applications of these nanomaterials over different fields. The TiO_2/HNTs composite showed high photocatalytic activity on the degradation of methanol.[9] HNTs were used as nanoreactors for biomimetic reactions[10,11] and to synthesize insulated silver nanorods employed as antimicrobial additives for polymer composites.[12] The release control with end stoppers was exploited to obtain healing anticorrosion coatings.[13] HNTs was employed in the preparation of composites with humidity control ability.[14] The catalytic performance of Ru/HNTs was not comparable to that of Ru/carbon nanotubes but the natural HNTs make them advantageous being available at low price and abundant over the world.[15] The HNTs were magnetized with the view of separating them upon application of an external magnetic field, leading to a fast and selective recognition of contaminants from aqueous phases.[16] The inner and the outer surface chemistry of clay nanotubes were selectively modified, and the modified lumen adsorbed more ferrocene than the pristine nanotube leading to a new class of inorganic micelles.[17] Dispersions of HNTs in water were prepared and their stabilization was improved by adding polymers such as amylose,[18] DNA,[19] and pectin.[20] Even if a deep comprehension of the stabilization mechanism is absent, Shamsi et al.[19] claim that the DNA wraps the HNTs generating a steric barrier toward their aggregation in water and therefore the stabilization of the dispersion. Moreover, the preparation of HNTs/surfactant supramolecular

Received: August 10, 2012
Revised: September 11, 2012
Published: September 18, 2012

dx.doi.org/10.1021/jp307961q | *J. Phys. Chem. C* 2012, 116, 21932−21938

hybrids can lead to inorganic micelles that are, in principle, smart materials useful for solubilization and delivery of hydrophobic compounds. This route can be an alternative to the use of a polyelectrolyte/surfactant mixture to obtain self-assembled ones with a tuned structure and the required properties for specific applications.[21,22]

■ EXPERIMENTAL SECTION

Materials. Sodium dodecanoate (NaL), decyltrimethylammonium bromide (DeTAB), *n*-decane, and KCl are Sigma products. The structure of the surfactants are given in Chart 1.

Chart 1. Structural Formula for Sodium Dodecanoate (NaL) and Decyltrimethylammonium bromide (DeTAB)

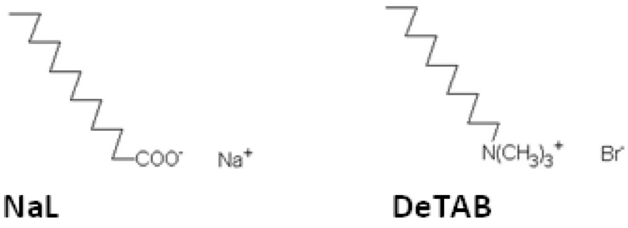

Halloysite nanotubes (HNTs) was a gift from Applied Minerals. All of the materials were used without further purification. Water from reverse osmosis (Elga model Option 3) with a specific resistivity greater than 1 MΩ cm was used.

Preparation of HNTs Functionalized with Surfactants. The aqueous solutions of NaL and DeTAB were prepared at 0.1 mol kg^{-1}, which roughly corresponds to 20 mg cm^{-3} in both cases. To a given aliquot of each surfactant solution was added a certain amount of HNTs. The obtained dispersion was magnetically stirred for ca. 48 h and left to equilibrate for ca. 10 days. The dispersions were centrifugated to separate the solid phase that was rinsed several times with water. The supernatant was dried at 80 °C by obtaining the solid phase. Both solids were investigated by means of thermogravimetric analysis (TG) to estimate the surfactant/HNTs ratio.

Methods. Turbidity experiments were performed on an Analytic Jena Specord S 600 BU at 600 nm using a quartz cuvette. To determine the kinetics of sedimentation, the HNTs and surfactant functionalized HNTs dispersions (1 wt %) were prepared and stirred vigorously for 15 s before the starting the experiment. The composition of the hybrid materials was $R_{\mathrm{S/HNTs}}$ = 0.09 weight ratio for NaL/HNTs and $R_{\mathrm{S/HNTs}}$ = 0.01 weight ratio for DeTAB/HNTs. FT-IR spectra were determined at room temperature in the spectral region 400–4000 cm^{-1} using a Frontier FT-IR spectrometer (Perkin-Elmer). The spectral resolution is 2 cm^{-1}. The dynamic light scattering (DLS) measurements were performed at a scattering angle of 90° by means of a Brookhaven Instrument apparatus composed of an BI-9000AT correlator and a He–Ne laser (75 mW) with a wavelength (λ) of 632.8 nm. The field-time autocorrelation functions were well described by a mono-exponential decay function, which provides the decay rate (Γ) of the single diffusive mode. For the translational motion,[23] the collective diffusion coefficient at a given concentration is $D_t = \Gamma/q^2$ where q is the scattering vector given by $4\pi n\lambda^{-1}\sin(\theta/2)$, where n is the water refractive index and θ is the scattering angle. ζ-potential measurements were carried out by means of a

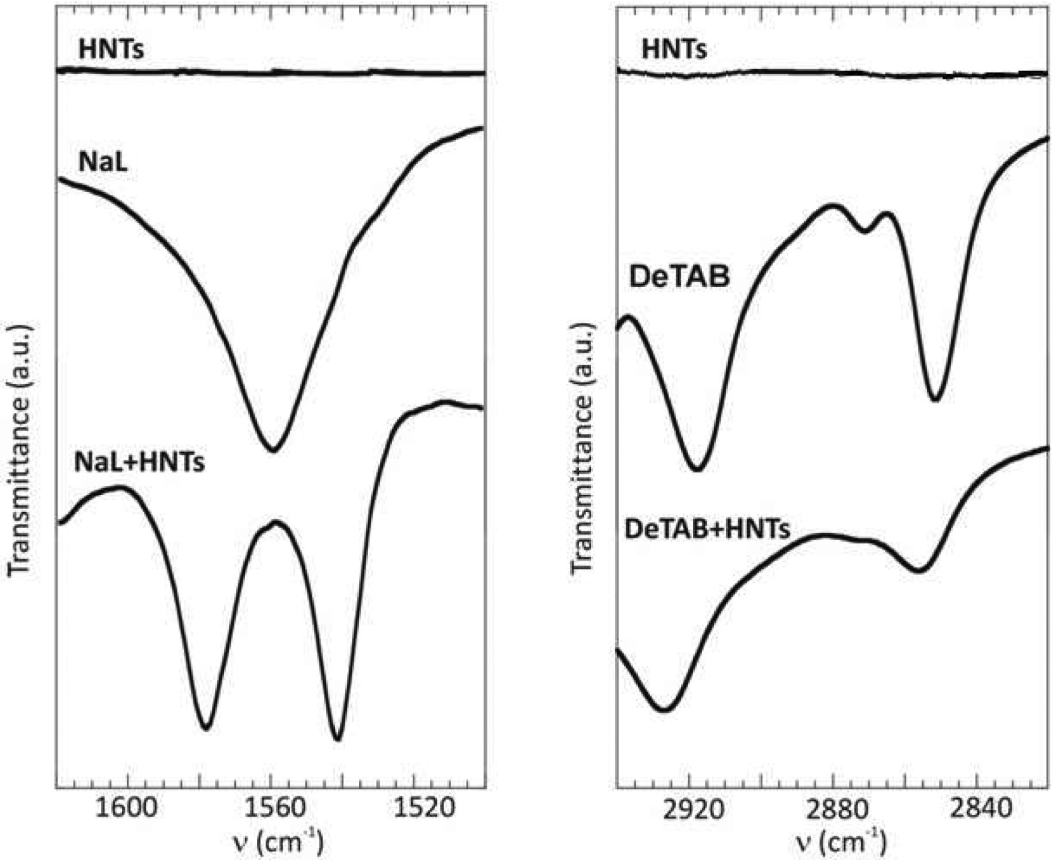

Figure 1. FTIR spectra of HNTs, surfactants, and surfactant + HNTs hybrid materials.

ZETASIZER NANO ZS90 (Malvern Instruments). For DLS and ζ-potential experiments the HNTs/surfactant ratios are NaL/HNTs ($R_{S/HNTs}$ = 1.78 weight ratio) and DeTAB/HNTs ($R_{S/HNTs}$ = 21.2 weight ratio). It has to be noted that the surfactant concentration in water is kept far below the critical micellar concentration reported in the literature.[24,25]

The functionalized nanotubes were imaged by using a microscope ESEM FEI QUANTA 200F. The HNTs/surfactant ratios for SEM measurements are same as above. Before each experiment, the sample was coated with gold in argon by means of an Edwards Sputter Coater S150A to avoid charging under electron beam.

The thermogravimetric analyses were done by using a Q5000 IR apparatus (TA Instruments) under the nitrogen flow of 25 $cm^3\ min^{-1}$ for the sample and 10 $cm^3\ min^{-1}$ for the balance at the heating rate of 10 °C min^{-1}. Temperature spanned from ambient to 900 °C. The surfactant/HNTs ratio was determined from the residual matter at 900 °C following a well established procedure in the literature.[20,26] Thermogravimetric volatilization of liquids method was used to determine the loading ability of functionalized and pristine HNTs toward decane. To this purpose, the dried powders were kept in pure decane for ca. 10 h under vacuum and then separated by centrifugation. The solid material was then dried on filter paper and analyzed.

The surface tension experiments were carried out by using a programmable tensiometer (KSV Sigma 70) equipped with a Wilhemy plate at 25.0 ± 0.1 °C. The platinum plate was lowered to the surface of the solution, and the downward force to the plate was measured. Surface tension was obtained as the force divided by the perimeter of the plate.[27] A concentrated surfactant solution was added to either water or aqueous HNTs dispersion to obtain various surfactant concentrations. Each surface tension value is the average of three determinations and its precision is 0.1 dyn cm^{-1}.

RESULTS AND DISCUSSION

We intend to design, prepare, and characterize Halloysite clay nanotubes (HNTs) functionalized with anionic and cationic surfactants, which are selectively adsorbed at the inner and the outer surface of the nanotube, respectively. The surface modification was done with the motivation of (1) controlling the colloidal stability of HNTs in aqueous media and (2) obtaining hybrid material with potential capability to solubilize hydrophobic compounds.

Adsorption of Surfactant onto Halloysite Nanotubes: Preparation of Inorganic Micelles. The inner positive and the outer negative surfaces of HNTs can be exploited for a selective functionalization operated by surfactants and therefore for a perfect tailoring of the structure/properties of the obtained hybrid material. To this aim we selected sodium dodecanoate (NaL) and decyltrimethylammonium bromide (DeTAB), which possess negative and positive head groups, respectively.

The FTIR measurements proved the surfactant adsorption onto the HNTs as they evidence the characteristic bands of surfactant and HNTs into the solid samples (see figure in ESI). Moreover, these experiments provided insights on the interactions between surfactant and HNTs. In the case of NaL (Figure 1), it is interesting to analyze the stretching band of the carboxylate group that for the pristine surfactant shows a single sharp peak at 1559.2 cm^{-1}, whereas for the NaL/HNTs mixture, the stretching of the carboxylate group is split into two peaks (1541.4 and 1578.1 cm^{-1}). It likely occurs that NaL entrapped into the lumen by attractive electrostatic forces interacts preferentially with one oxygen atom, and the delocalization of the negative charge along the carboxylate group of NaL is no longer present. Consequently, the band at 1541.4 cm^{-1} reveals the O−C stretching in the presence of the HNTs interactions, and the band at 1578.1 cm^{-1} is related to the stretching of C=O not interacting with the surface. As concerns DeTAB, the bands for the CH_2 asymmetric stretching mode and symmetric stretching mode[28] (at 2927 and 2855 cm^{-1}) are shifted to 2918 and 2851 cm^{-1}, respectively, (Figure 1) in the presence of HNTs. A similar effect was observed for cetyltrimethylammonium bromide intercalated into the gallery of montmorillonite clay and was related to the surfactant loading level and interlayer packing density.[29] Therefore, the molecular environment of the adsorbed DeTAB assumes a more solid-like packed feature.[30]

The ζ-potential experiments revealed interesting consequences of the adsorption of both surfactants onto HNTs. The net negative charge of HNTs in water generates the ζ-potential value of −19.4 mV in agreement with the literature.[31] DeTAB produces an inversion of the HNTs charge with a potential of +8.9 mV, whereas NaL enhances the negative ζ-potential up to −66.6 mV. These changes agree with the effective surfactant headgroup charge as positive alkylammonium bromide groups neutralize a certain number of negative sites of the external surface generating a total positive charge. The NaL entrapment into the HNTs lumen cancels out the inner positive charges and creates an increase in the total negative charge of HNTs; the latter new nanomaterials are expected to be stabilized in aqueous dispersion as a consequence of electrostatic repulsions.

The diffusion dynamics of functionalized HNTs in water evidenced clear differences between the two kinds of functionalized HNTs. The NaL/HNTs nanostructures present values for the average translational diffusion coefficients (D_t) close to those reported[20] for bare HNTs in water (9.4×10^{-13} $m^2\ s^{-1}$) indicating that they possess the same diffusion dynamic behavior in water of single diffusive nanotubes (Figure 2). The differences between the two hybrid systems can be explained by remembering that the DeTAB adsorption generates a dispersion with a stability lower than that based on NaL. Moreover, the tendency to form large aggregates in the presence of DeTAB is also favored by the presence of hydrophobic attractive interactions generated by the chains of the cationic surfactant adsorbed onto the HNTs outer surface. Going further, by considering the friction coefficient for a cylindrical object,[32] one can calculate the average number of HNTs assuming a certain geometry for the DeTAB/HNTs

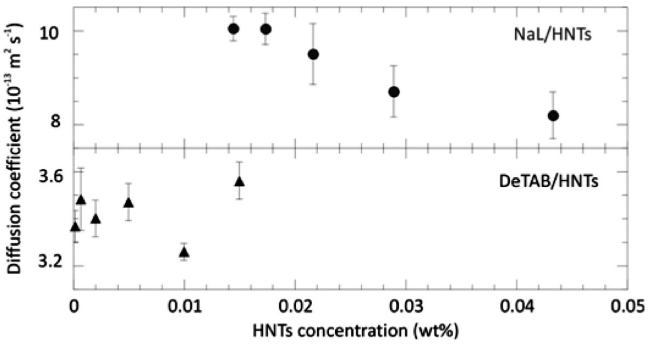

Figure 2. Diffusion coefficient as a function of the aqueous HNTs concentration in water of hybrid surfactant/HNTs.

system and the experimental D_t value. In particular, a diffusion coefficient 3 times smaller than those for a single nanotube (Figure 2) can be obtained by considering either an end-to-end arrangement of ca. five nanotubes or one nanotube surrounded by ca. three HNTs layers in a close compact side-by-side arrangement. Of course a combination of the two configurations is possible being the side-by-side arrangement the most likely case due to the hydrophobic interactions.

To quantify the adsorption efficiency, different amounts of HNTs (C_{HNTs}) were added to a given surfactant solution, and the surfactant/HNTs weight ratio ($R_{S/HNTs}$) in the solid phase, obtained from precipitation, was determined by means of thermogravimetric analysis (TG). The adsorbed amount for NaL is much larger than that for DeTAB (Figure 3) despite the larger outer surface area of the halloysite. Nevertheless, by simple geometric considerations based on the different charges of HNTs surface and the headgroup areas for DeTAB[33] (1.15 nm^2) and NaL[34] (0.1 nm^2) and assuming a monolayer adsorption of the cationic and anionic surfactant at the outer and inner surface, respectively, one calculates that the expected adsorbed amount of NaL is 3.5 times larger than that of DeTAB in agreement with our experimental results.

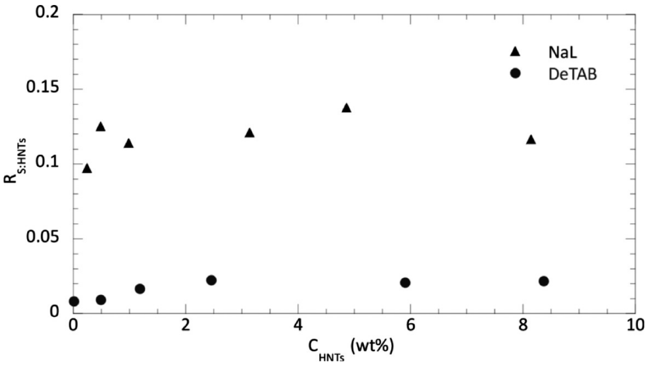

Figure 3. Surfactant/HNTs weight ratio in the solid phase separated from 0.1 *m* surfactant solution containing variable amounts of HNTs.

The adsorption of NaL and DeTAB onto the HNTs in aqueous dispersion was monitored also by means of surface tension experiments. In this case, a certain amount of HNTs was dispersed in water and the surface tension (γ) measured as a function of the surfactant concentration (Figure 4). The presence of HNTs generates an increase of γ that is consistent with the surfactant adsorption onto the HNTs surface and the consequent lower surfactant chemical potential in the aqueous phase. By comparing these curves with those in water, one can conclude that NaL is adsorbed more efficiently than DeTAB in agreement with the TG data.

Direct observation of the surface morphology of surfactant/HNTs materials was carried out by SEM (Figure 5). A fibrous mesoscopic structure is obtained for NaL/HNTs, whereas a compact material is imaged for DeTAB/HNTs. The NaL based sample showed very clearly the presence of several HNTs (Figure 5a,b) with sizes comparable to those observed for the pristine HNTs sample.[20] In the case of DeTAB, the HNTs presence at the surface is rare as only a few nanotubes have been imaged (Figure 5c,d). This result can be explained by assuming that HNTs are mainly hidden in the bulk of the DeTAB/HNTs material, and it is also in agreement with the smaller HNTs content in this composite as it is shown by the $R_{S/HNTs}$ values of 1.78 and 21.2 obtained for NaL/HNTs and DeTAB/HNTs, respectively, from TGA data.

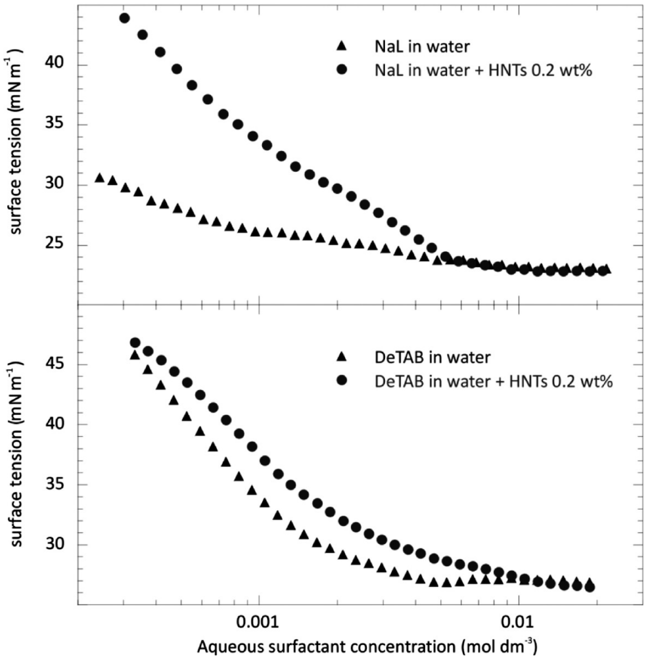

Figure 4. Surface tension as a function of the surfactant concentration in the absence and the presence of HNTs.

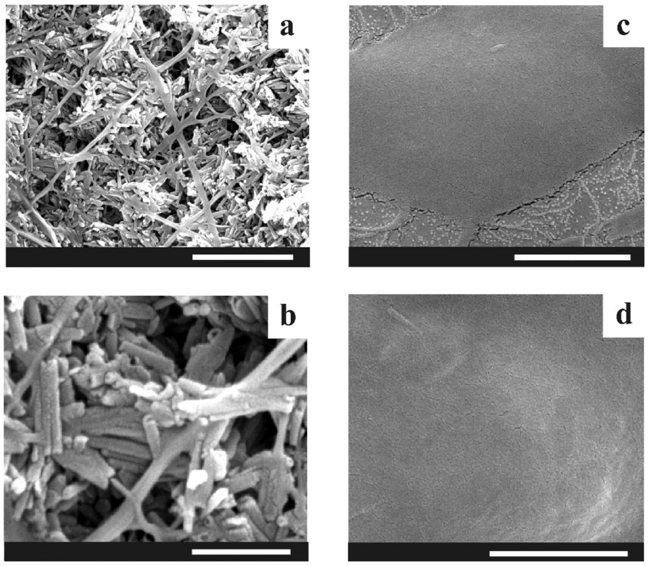

Figure 5. Scanning electron microscopy images of NaL/HNTs (a and b) and DeTAB/HNTs (c and d). The bars are 2 μm (a, c, and d) and 500 nm (b).

Based on all of the above results, HNTs charge distribution, and surfactant headgroup nature, one may define the consequent structure for the hybrid nanomaterials illustrated in Figure 6.

Properties of Functionalized Halloysite. The selective manipulation of HNTs allows us to modify the hydrophilic/hydrophobic character of the nanostructures which can be exploited for specific purposes. With this in mind, we explored (i) the stability of the hybrid nanomaterials in water and (ii) the adsorbent ability of pristine and functionalized HNTs toward a hydrophobic compound.

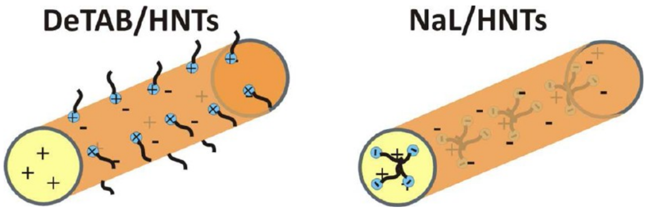

Figure 6. Illustration of the hybrid surfactant/HNTs materials.

i. Stability of Surfactant-Functionalized Halloysite Dispersion in Water. Obtaining stable HNTs dispersions in water is a crucial issue in view of their applications like nanocontainers, delivery systems, and so on. The aqueous phase obtained after equilibration of HNTs dispersions, in the presence of NaL and DeTAB both at 0.1 mol dm^{-3}, was investigated by TG to determine the eventual residual concentration of HNTs ($C_{HNTs,w}$). Data in Table 1 show that the HNTs amount dispersed in solution is significantly higher in the presence of NaL.

Table 1. Residual Concentration of HNTs in Aqueous Suspension ($C_{HNTs,w}$) in the Presence of Surfactants 0.1 *m* at Variable Stoichiometric Nanotubes Concentration (C_{HNTs})

	C_{HNTs} (wt %)	$C_{HNTs,w}$ (wt %)
NaL	1.60	0.18
	4.29	0.19
DeTAB	2.45	0.023
	4.16	0.023

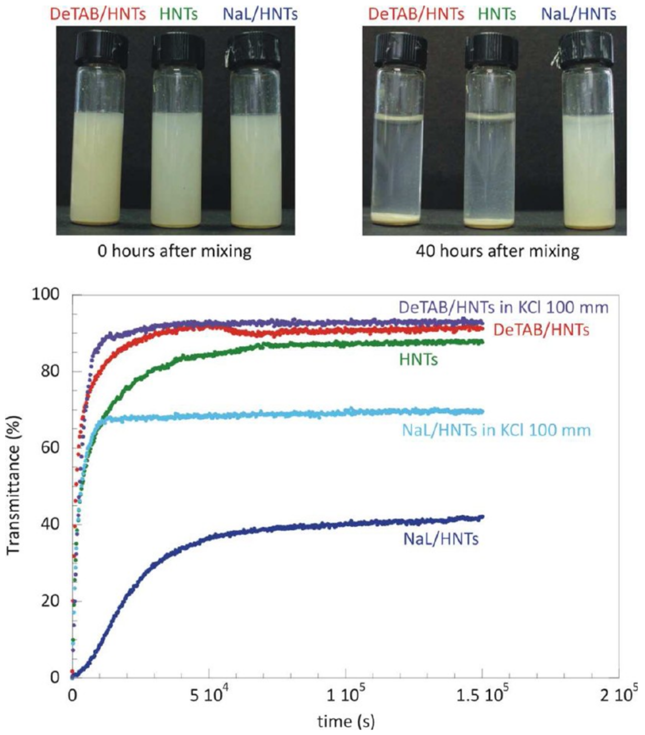

Figure 7. Photographs and transmittance as a function of time for HNTs and functionalized HNTs dispersions (1 wt %) in water and in a water + KCl mixture 100 m*m*.

To evaluate the mechanism controlling the stabilization of the dispersion, the kinetics of sedimentation of pristine and surfactant functionalized HNTs in water was studied by means of turbidimetry. Figure 7 shows that the sedimentation is highly influenced by the surfactant nature being strongly slowed down by NaL. The turbidity value after equilibration follows the order NaL > water > DeTAB indicating that the anionic surfactant is the proper and efficient stabilizing agent for the HNTs dispersion whereas DeTAB enhances the sedimentation.

The colloidal stability can be explained by considering the hydrophobic interactions as well as the electrostatic effects. As observed by DLS experiments, the DeTAB/HNTs system has the tendency to form aggregates due to the hydrophobic attractive interactions generated by the cationic surfactant adsorbed onto the HNTs outer surface. This phenomenon is absent in the presence of NaL that adsorbs at the HNTs lumen, and therefore, the NaL/HNTs dispersion stability in water is higher.

The electrostatic interactions evidenced by ζ-potential measurements lead to the same conclusions. Namely, the larger stability in the presence of NaL is explained in terms of enhancement of the repulsive electrostatic forces between NaL functionalized HNTs. Moreover, the lower ζ-potential value for the DeTAB based system agrees with the worst dispersion stability.

The DLVO theory establishes that the stability of a colloidal suspension depends on the balance between attractive van der Waals forces and electrostatic repulsion caused by the double layer surrounding each particle.[35] Therefore, both ζ-potential and width of the electric double layer contribute to the total repulsive force. Based on this theory one predicts that higher ionic strength leads to a screening of the electrostatic repulsion due to the contraction of the double layer width. This theory was successful in interpreting the dispersion stability of carbon nanotubes in aqueous media.[36,37]

To investigate the key role of the electrostatic interactions in controlling the stability of aqueous HNTs hybrid materials dispersions, we measured the turbidity under variable ionic strength conditions. NaL modified HNTs are strongly destabilized by KCl according to the salt screening effect. The DeTAB modified HNTs sedimentation is only slightly affected by the ionic strength because the system is already destabilized in water (Figure 7).

ii. Exploiting Surfactant-Functionalized Halloysite in Entrapping a Hydrophobic Compound. The sample of each nanostructure (dried powder) was equilibrated with pure decane; after separation, the solid material was analyzed by thermogravimetric volatilization method to monitor the eventual presence of decane. The volatilization rates (Figure 8) clearly illustrate that neither HNTs nor DeTAB/HNTs are able to entrap the decane, whereas NaL/HNTs incorporates the hydrophobic oil. The pristine HNTs have polar internal and external surfaces and therefore a low affinity to decane is expected. Comparing the structure of the two hybrid HNTs, it emerges that NaL/HNTs is the only one with a hydrophobic compartment evoking the formation of inorganic micelles (Figure 6). The confinement of the decane into the functionalized HNTs cavity can be confirmed by the temperature at the maximum volatilization rate (T_m). Our results show a T_m decrease of ca. 40 °C. According to the Gibbs−Thomson effect, a shift of T_m to a value lower than that of pure decane is expected in a confined environment. Therefore we conclude that most of the decane is confined inside the cavity of the NaL functionalized HNTs (ca. 7 wt %). Considering that the HNTs cavity is ca. 10% of the full volume, the large loading value

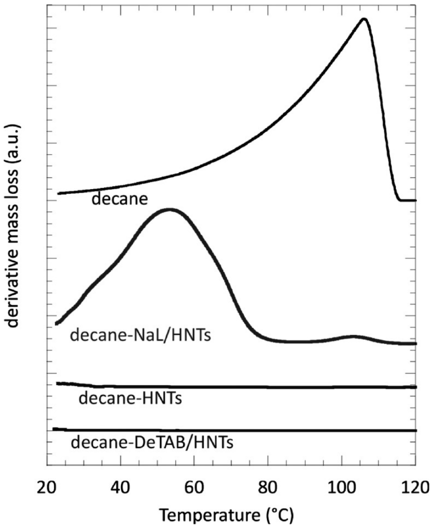

Figure 8. Volatilization rate as a function of temperature for decane and HNTs based materials after equilibration with decane.

indicates that all of the nanotubes are fully filled with decane. We observed that the NaL/HNTs mixture contains also a very small amount of the oil outside the cavity (ca. 0.3 wt %) as a small peak in the volatilization rate is observed at a temperature coincident with that observed for pure decane.

CONCLUSIONS

We prepared new hybrid nanomaterials by exploiting electrostatic forces between ionic surfactants with different headgroup charges and halloysite nanotubes. A physicochemical study straightforwardly proved the formation and the stability of these hybrid materials. We demonstrated that the adsorption of a negatively charged surfactant, even if it occurs at the inner surface of the HNTs, generates the higher stabilization effect of the nanotubes in water while either the cationic surfactant or the salt addition enhances the precipitation. The HNTs possess a net negative charge, as a result of the inner positive and the outer negative surface, and consequently, the selective adsorption of cationic or anionic surfactants can tune the electrostatic interactions between particles. The findings on the colloidal stability are consistent with the DLVO theory. In light of these results, one can asses that the same mechanism is behind the stabilization of HNTs aqueous dispersions by means of negative polyelectrolytes such as DNA[19] and pectin[20] and the extended knowledge of HNTs dispersion properties is fundamental for the applications. Namely, anionic polyelectrolytes can be loaded into the cationic lumen and the overall stability increases as demonstrated in this work.

The functionalization of HNTs with the anionic surfactant not only generates stable dispersions but also hybrid material with hydrophobic lumens. Due to this structure, this material behaves as a sponge, strongly increasing the adsorption capacity of HNTs toward *n*-decane.

We provided a valuable platform for the development of new strategies to prepare smart materials, like inorganic micelles, easily dispersible in water with a hydrophobic pocket for current and future solubilization and delivery applications.

ASSOCIATED CONTENT

Ⓢ Supporting Information

FTIR spectra of surfactants, HNTs, and surfactant + HNTs hybrid materials in the full frequency range. Autocorrelation functions for aqueous dispersion of the surfactant + HNTs composites. This material is available free of charge via the Internet at http://pubs.acs.org.

AUTHOR INFORMATION

Corresponding Author

*E-mail: giuseppe.lazzara@unipa.it. Fax: +39 091 590015. Phone: +39 091 23897962.

Notes

The authors declare no competing financial interest.

ACKNOWLEDGMENTS

The work was financially supported by the University of Palermo and COFIN 2008 (Prot. 2008RH3FCW_002). Applied Minerals Inc. (U.S.A.) is acknowledged for kindly providing the Halloysite sample.

REFERENCES

(1) Mout, R.; Moyano, D. F.; Rana, S.; Rotello, V. M. *Chem. Soc. Rev.* **2012**, *41*, 2539−2544.

(2) Cavallaro, G.; Lazzara, G.; Milioto, S. *Soft Matter* **2012**, *8*, 3627−3633.

(3) De Lisi, R.; Gradzielski, M.; Lazzara, G.; Milioto, S.; Muratore, N.; Prévost, S. *J. Phys. Chem. B* **2008**, *112*, 9328−9336.

(4) Ma, P. C.; Siddiqui, N. A.; Marom, G.; Kim, J. K. *Composites, Part A* **2010**, *41*, 1345−1367.

(5) Ma, W.; Yah, W. O.; Otsuka, H.; Takahara, A. *J. Mater. Chem.* **2012**, *22*, 11887−11892.

(6) Lvov, Y. M.; Shchukin, D. G.; Mohwald, H.; Price, R. R. *ACS Nano* **2008**, *2*, 814−820.

(7) Vergaro, V.; Abdullayev, E.; Lvov, Y. M.; Zeitoun, A.; Cingolani, R.; Rinaldi, R.; Leporatti, S. *Biomacromolecules* **2010**, *11*, 820−826.

(8) Abdullayev, E.; Joshi, A.; Wei, W.; Zhao, Y.; Lvov, Y. *ACS Nano* **2012**, *6*, 7216−7226.

(9) Wang, R.; Jiang, G.; Ding, Y.; Wang, Y.; Sun, X.; Wang, X.; Chen, W. *ACS Appl. Mater. Interfaces* **2011**, *3*, 4154−4158.

(10) Shchukin, D. G.; Sukhorukov, G. B.; Price, R. R.; Lvov, Y. M. *Small* **2005**, *1*, 510−513.

(11) Yah, W. O.; Xu, H.; Soejima, H.; Ma, W.; Lvov, Y.; Takahara, A. *J. Am. Chem. Soc.* **2012**, *134*, 12134−12137.

(12) Abdullayev, E.; Sakakibara, K.; Okamoto, K.; Wei, W.; Ariga, K.; Lvov, Y. *ACS Appl. Mater. Interfaces* **2011**, *3*, 4040−4046.

(13) Abdullayev, E.; Lvov, Y. *J. Mater. Chem.* **2010**, *20*, 6681−6687.

(14) Dong, F.; Wang, J.; Wang, Y.; Ren, S. *J. Mater. Chem.* **2012**, *22*, 11093−11100.

(15) Wang, L.; Chen, J.; Ge, L.; Zhu, Z.; Rudolph, V. *Energy Fuels* **2011**, *25*, 3408−3416.

(16) Pan, J.; Yao, H.; Xu, L.; Ou, H.; Huo, P.; Li, X.; Yan, Y. *J. Phys. Chem. C* **2011**, *115*, 5440−5449.

(17) Yah, W. O.; Takahara, A.; Lvov, Y. M. *J. Am. Chem. Soc.* **2011**, *134*, 1853−1859.

(18) Chang, P. R.; Xie, Y.; Wu, D.; Ma, X. *Carbohydr. Polym.* **2011**, *84*, 1426−1429.

(19) Shamsi, M. H.; Geckeler, D. V. *Nanotechnology* **2008**, *19*, 075604.

(20) Cavallaro, G.; Lazzara, G.; Milioto, S. *Langmuir* **2011**, *27*, 1158−1167.

(21) Hoffmann, I.; Heunemann, P.; Prévost, S.; Schweins, R.; Wagner, N. J.; Gradzielski, M. *Langmuir* **2011**, *27*, 4386−4396.

(22) Bilalov, A.; Leal, C.; Lindman, B. *J. Phys. Chem. B* **2004**, *108*, 15408−15414.

(23) Degiorgio, V.; Corti, M.; Giglio, M. *Light Scattering in Liquids and Macromolecular Solutions*; Plenum Press: New York, 1980.
(24) Kinzel, S.; Gradzielski, M. *Langmuir* **2008**, *24*, 10123−10132.
(25) De Lisi, R.; Lazzara, G.; Milioto, S.; Muratore, N. *Langmuir* **2004**, *20*, 9938−9944.
(26) Cavallaro, G.; Donato, D. I.; Lazzara, G.; Milioto, S. *J. Phys. Chem. C* **2011**, *115*, 20491−20498.
(27) Miller, C. A.; Neogi, P. *Interfacial Phenomena: Equilibrium and Dynamic Effects*; Marcel Dekker, Inc.: New York, 1985; Vol. *17*.
(28) Zhao, Z.; Tang, T.; Qin, Y.; Huang, B. *Langmuir* **2003**, *19*, 9260−9265.
(29) Zhu, J.; He, H.; Zhu, L.; Wen, X.; Deng, F. *J. Colloid Interface Sci.* **2005**, *286*, 239−244.
(30) Vaia, R. A.; Teukolsky, R. K.; Giannelis, E. P. *Chem. Mater.* **1994**, *6*, 1017−1022.
(31) Shi, Y.-F.; Tian, Z.; Zhang, Y.; Shen, H.-B.; Jia, N.-Q. *Nanoscale Res. Lett.* **2011**, *6*, 608.
(32) Garcia de la Torre, J.; Bloomfield, V. *Q. Rev. Biophys.* **1981**, *14*, 81−139.
(33) Feitosa, E.; Savério Brazolin, M. R.; Zumstein Georgetto Naal, R. M.; Perpétua Freire de Morais Del Lama, M.; Lopes, J. R.; Loh, W.; Vasilescu, M. *J. Colloid Interface Sci.* **2006**, *299*, 883−889.
(34) *Reactions And Synthesis In Surfactant Systems*; Texter, J., Ed.; CRC Press: Boca Raton, FL, 2001.
(35) Derjaguin, B. V.; Landau, L. D. *Acta Physicochim.* **1941**, *14*, 733−762.
(36) Wang, X.; Xia, T.; Ntim, S. A.; Ji, Z.; George, S.; Meng, H.; Zhang, H.; Castranova, V.; Mitra, S.; Nel, A. E. *ACS Nano* **2010**, *4*, 7241−7252.
(37) Heister, E.; Lamprecht, C.; Neves, V.; Tîlmaciu, C.; Datas, L.; Flahaut, E.; Soula, B.; Hinterdorfer, P.; Coley, H. M.; Silva, S. R. P.; McFadden, J. *ACS Nano* **2010**, *4*, 2615−2626.

J Therm Anal Calorim (2013) 112:383–389
DOI 10.1007/s10973-012-2766-8

Polyethylene glycol/clay nanotubes composites

Thermal properties and structure

**G. Cavallaro · R. De Lisi · G. Lazzara ·
S. Milioto**

Received: 18 July 2012 / Accepted: 12 October 2012 / Published online: 7 November 2012

Abstract Nanocomposites of poly(ethylene) glycol (PEG) 20000 filled with clay nanotubes (HNTs) were prepared. The thermal properties obtained from thermogravimetry and differential scanning calorimetry were correlated to the morphology imaged by scanning electron microscopy. Low amounts of HNTs generate compact structure while large amounts of HNTs create craters and voids. The decrease of polymer degradation temperature in the presence of large amount of nanoclay (ca. 80 wt%) is a consequence of the morphology at the mesoscale range. The thermal opposite effect observed in the HNTs low regime (up to ca. 20 wt%) is due to the gas entrapment into the nanoparticles lumen. The quantitative analysis of the PEG 20000 enthalpy of melting in the presence of HNTs allowed us to characterize the polymer adsorption onto the nanoclay surface.

Keywords Halloysite · Nanotube · PEG · Nanocomposite · TG · SEM · DSC

Introduction

Polymer–nanoclay composites are well known in the nanotechnology and engineering fields. These nanomaterials have attracted increased interest in recent years because of their improved properties with respect to the pristine polymer, and therefore, their designing may be a challenging task for applications in several fields. Batteries, [1] packaging films [2] and membranes for proton exchange [3] are some examples of potential applications.

In general, thermal properties of materials are crucial to establish their use in a certain field; a recent review [4] reported that several polymeric materials are disadvantageous because of fast degradation. Filling polymers with nanoclays may be a proper strategy to obtain a thermal stabilization of a polymer and it may produce new nanomaterials with tunable properties [5].

Among nanoclays, halloysite nanotubes (HNTs) are newly emerging fillers with interesting properties [6] and appealing perspectives [7]. Halloysite is a non-toxic [8] natural alluminosilicate with an unitary cell composed of $Al_2Si_2O_5(OH)_4{\cdot}2H_2O$ and a peculiar hollow tubular shape (the outer and inner diameters are ca. 30–50 and 1–30 nm, respectively) [6]. Cancer cell separation, bone implants, cosmetics, and controlled drug delivery [9] are interesting examples of HNTs medical applications. Well-dispersed HNTs into polypropylene [10] and polyamide [11] determined a thermal stabilization and a mechanical reinforcement of the polymer matrix. The macromolecule nature and the amount of filler play a key role on both the physicochemical properties of nanocomposites and their morphology [2, 12]. In this study, we investigated poly(ethylene) glycol (PEG) as polymeric matrix that is well known for its several applications and biocompatibility [13]. Keeping in mind [14] that PEGs may be used as consolidants of archaeological woods, their filling with HNTs may generate new advanced nanomaterials for Cultural Heritage applications. Moreover, the HNTs ability to entrap chemical species into the lumen was exploited to design anticorrosive films for metal protection [7].

Electronic supplementary material The online version of this article (doi:10.1007/s10973-012-2766-8) contains supplementary material, which is available to authorized users.

G. Cavallaro (✉) · R. De Lisi · G. Lazzara · S. Milioto
Dipartimento di Chimica "S. Cannizzaro", Università degli Studi di Palermo, Viale delle Scienze pad. 17, 90128 Palermo, Italy
e-mail: giuseppe.cavallaro@unipa.it

Calorimetry and thermal analysis are well-established techniques for diagnostics of art-work materials [15–17] because they have been revealed sensitive to even small intermolecular forces [18, 19]. We properly designed DSC and TG experiments to obtain direct information on the thermal behavior of these nanomaterials and, by means of suitable models, conclusions on the interactions at the mesoscopic scale were drawn [20, 21]. Performing experiments at variable heating rates (β) is fundamental for a correct interpretation of the mechanism behind the thermal response of a polymer [20, 22, 23].

Finally, the morphological insights from scanning electron microscopy combined with the thermal properties will elucidate the correlation between structure and properties.

Experimental

Materials

Polyethylene glycol (PEG) 20,000 g mol^{-1} is from Fluka. HNTs is a gift from Applied Minerals Inc. All the materials were used without further purification. Water from reverse osmosis (Elga model Option 3) with a specific resistivity higher than 1 MΩ cm was used.

Preparation of nanocomposites

The nanocomposites were prepared by the casting method [2, 12]. In brief, PEG 20,000 g mol^{-1} was solubilized in water under stirring at room temperature for 2 h. Then, an appropriate amount of HNTs was added to the polymer solution and kept under stirring over night. The well-dispersed aqueous mixture was poured into glass Petri dishes under vacuum to evaporate water until weight was constant.

The composition of nanofiller (C_{HNTs}) expressed as weight percent (g of filler/100 g of nanocomposite) was systematically changed.

Methods

Thermogravimetric analysis

The measurements were performed by means of the TGA Q5000 IR apparatus (TA Instruments) under nitrogen flow of 25 cm^3 min^{-1} for the sample and 10 cm^3 min^{-1} for the balance. The investigated temperature range was 25–900 °C at $\beta = 10$ °C min^{-1}. The sample weight was ca. 15 mg. The calibration was carried out by means of Curie temperature of nickel, cobalt, and their alloys standards. The degradation temperature (T_{d}) of PEG 20000 was taken at the peak of the first-order derivative curves of mass to time (DTG curves).

Experiments were also performed to determine the kinetics of degradation of the polymer into the nanocomposites. To this aim, the non-isothermal degradation was studied by changing β in a very large range (from 2.5 to 500 °C min^{-1}).

Differential scanning calorimetry

The enthalpy (ΔH_{m}) and the temperature (T_{m}) of melting for PEG 20000 were determined using the TA Instruments DSC (2920 CE) under nitrogen flow atmosphere (flow rate = 60 cm^3 min^{-1}) in the range from 0 to 80 °C at $\beta = 10$ °C min^{-1}. The used pans are in aluminum and contain ca. 5 mg of the compound. The calibration was carried out using indium standard. The T_{m} value was defined as the onset of the melting endothermic peak. Note that the ΔH_{m} value of PEG 20000 (199.6 J g^{-1}) is in a good agreement with the literature value (197.4 J g^{-1}) [21]. Furthermore, we investigated the kinetics of crystallization process under non-isothermal conditions by changing the cooling rate. To this purpose, the sample was heated to 90 °C and kept for 10 min to eliminate any previous thermal history; then, it was cooled down to 0 °C at 2.5, 5, 10, and 15 °C min^{-1}.

Scanning electron microscopy

The morphology of nanocomposites was studied using a microscope ESEM FEI QUANTA 200F. Before each experiment, the surface of the sample was coated with gold in argon by means of an Edwards sputter coater S150A to avoid charging under electron beam. Minimal electron dose condition was set to avoid damage of the sample.

Results and discussion

Microscopic structure of nanocomposites PEG 20000/HNTs

SEM micrographs of PEG 20000/HNTs nanocomposites showed that the filler concentration plays a crucial role in the microscopic structure of these materials (Fig. 1). In particular, for $C_{\mathrm{HNTs}} = 10$ wt% the material is compact with a rough surface where HNTs are clearly evident. The filler appears well dispersed into the polymer matrix on both the surface and the core of the material as the micrograph of the edge shows. The structure is consistent with the preferential interactions between polymer and nanofiller, and in particular with the HNTs external surface. This argument is based on the consideration that the entrapment of a macromolecule into the nanotube cavity would lead to confinement and, therefore, to a remarkable loss in configurational freedom of the polymer chain. On the other hand, the entrapment of molecules into the cavity is expected when preferential electrostatic interactions with the inner surface of HNTs are possible. This is, for instance, the case of poly(anions), such as pectin [2]. Moreover, it is reported that the incorporation of a non-ionic molecule into the HNTs cavity is obtained if vacuum is applied to facilitate the release of air from the lumen [24].

For $C_{\mathrm{HNTs}} = 50$ wt% the nanocomposite clearly appears less compact with several irregular craters (having a size of ca. 10 μm) present on both the surface and the edge. Such an open structure favors a faster gas diffusion trough the material.

Melting of PEG 20000 filled with HNTs

ΔH_{m} was determined for pristine polymer and nanocomposites to evaluate the effect of HNTs on the crystallinity of PEG 20000. The trend ΔH_{m} versus the reciprocal of polymer weight percent (C_{PEG}^{-1}), reported in Fig. 2, shows that ΔH_{m} decreases upon the addition of HNTs indicating a reduction of the polymer crystallinity. At a certain concentration ($C_{\mathrm{PEG}} = 20$ wt%) ΔH_{m} is no more affected by further HNTs addition. These results are interpreted by assuming that: (1) some segments of the adsorbed macromolecules are radiating away from the surface forming loops and tails; (2) the portion of polymer in contact with the HNTs surface cannot melt because of constraints due to the nanoclay anchoring; and (3) the unbound polymer in the nanocomposites behaves like the pristine one [20, 21, 25].

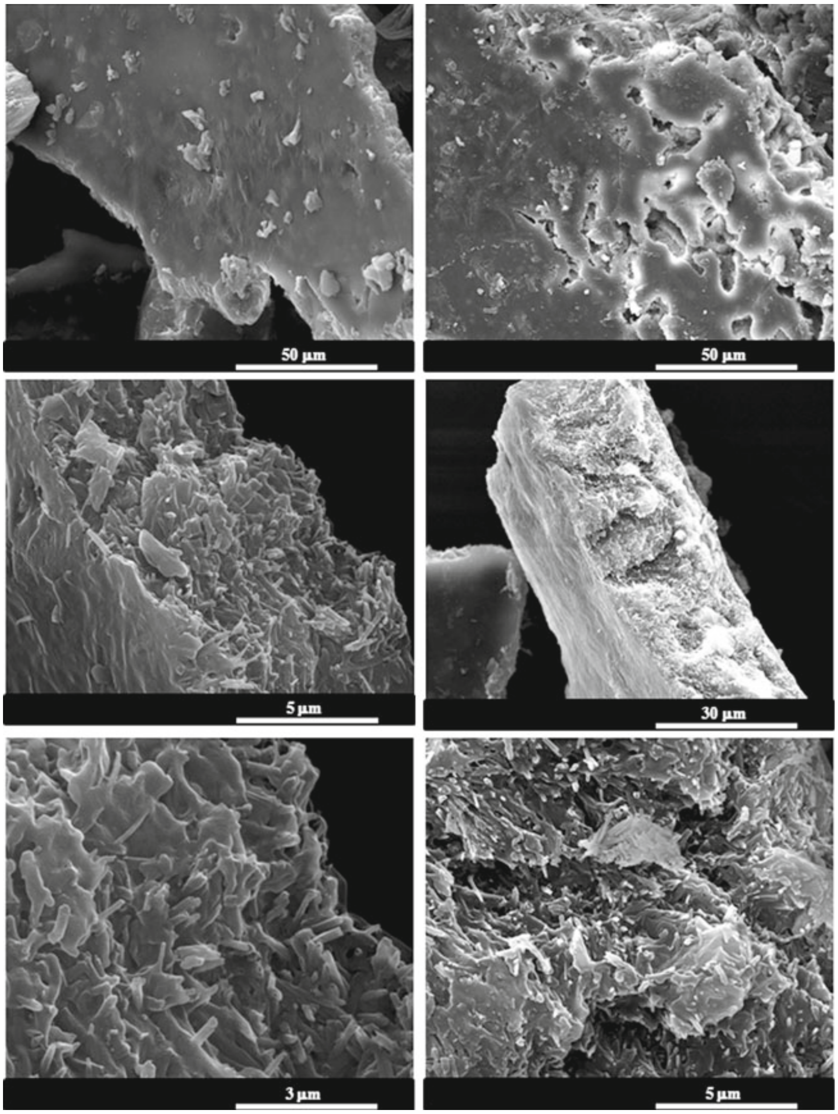

Fig. 1 Micrographies for nanocomposites at filler concentration (C_{HNTs}) of 10 wt% (*left hand side*) and 50 wt% (*right hand side*)

As a consequence ΔH_m can be expressed by the following equation:

$$\Delta H_m = x_f \Delta H_m^* + (1 - x_f)\, x_t \Delta H_m^* \quad (1)$$

where ΔH_m^* is the enthalpy of melting of pure PEG 20000, x_f is the fraction of the free polymer, and x_t is the fraction of the segments away from the HNTs surface with respect to the total adsorbed molecule. The x_t value is constant for a given system while x_f depends on both the composition of the nanocomposite and the C_{PEG} at the saturation point (cac). The largest amount of PEG 20000 (in g) that can be associated to 1 g of HNTs (ω) was calculated as cac/(100-cac). The ω and x_t values obtained from the fitting procedure of data in Fig. 2 are 0.351 and 0.47, respectively. These values are different than those of PEG 20000/laponite RD nanocomposites ($\omega = 0.301$, $x_t = 0.12$) [21] because of the diverse specific surface area (A_{sp}) of the two nanoclays. From geometric consideration, by assuming $\omega \propto A_{sp} \cdot x_t$ for a given polymer, we calculated that the ratio between the specific surface of laponite RD and that of HNTs is 3.4; that is very close to the value (3.0) obtained using the A_{sp} determined experimentally by BET measurements [26].

The addition of HNTs to PEG 20000 generates a monotonic decrease of T_m in the entire range of investigated composition (Fig. 2). Such a trend can be ascribed to a good dispersion of the nanofiller into the polymeric matrix [27, 28].

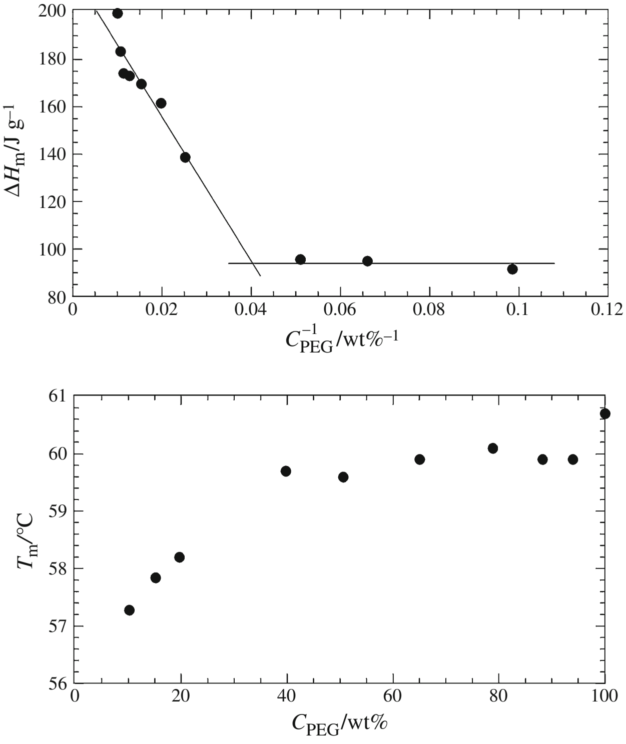

Fig. 2 Enthalpy (ΔH_m, *top*) and temperature (T_m, *bottom*) of melting as functions of PEG 20000 weight percent (C_{PEG}) for the nanocomposites

Non-isothermal crystallization of PEG 20000 filled with HNTs

DSC measurements at different cooling rates allowed us to investigate the role of HNTs on the crystallization kinetics of PEG 20000. Examples of DSC thermoanalytical curves for a nanocomposite (Fig. 3) evidence that the crystallization temperature (T_c) of the polymer is slightly higher at lower cooling rate. From this T_c shift, one can calculate the activation energy of crystallization (E_c) using the Kissinger approach [29].

The E_c values slightly decrease by increasing the C_{HNTs} from −250 kJ mol^{-1} to −440 kJ mol^{-1} (Table 1). These results can be understood by taking into account that generally E_c for a polymer depends on: (1) a negative contribution due to the diffusion of the polymer at the crystalline/amorphous interface [30] and (2) a positive contribution that reflects the energy requested for the nucleation of the polymer crystals. Our experimental data suggest that in the presence of the HNTs, the crystallization process is more diffusion controlled than in the pristine polymer.

Thermal degradation of nanocomposites PEG 20000/HNTs

TG experiments were performed to investigate the thermal degradation of nanocomposites in a wide range of composition by systematically changing C_{HNTs}. Figure 4 reports some examples of TG and DTG curves in the investigated temperature range obtained at $\beta = 10$ °C min^{-1}. The polymer resistance to thermal degradation is enhanced in the presence of HNTs up to a certain C_{HNTs}. This is clearly evidenced in the trend of T_d versus C_{HNTs} (Fig. 5), which exhibits a maximum at $C_{HNTs} \approx 20$ wt% with a thermal

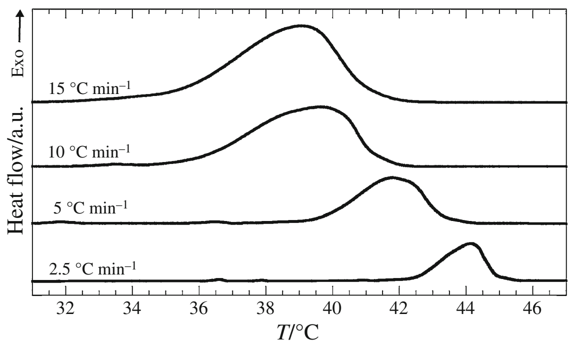

Fig. 3 DSC thermoanalytical curves of the crystallization at different cooling rates for the nanocomposite at the filler concentration of 6 wt%

Table 1 Activation energy of the PEG 20000 crystallization for pristine polymer and nanocomposites at different C_{HNTs}

C_{p} (wt%)	E_{c} (kJ mol^{-1})
100	-250 ± 14
93.96	-280 ± 30
88.20	-310 ± 30
50.58	-440 ± 90

enhancement of ca. 13 °C. At very large C_{HNTs}, T_{d} drops reaching values even 12 °C lower than the pristine polymer. The influence of inorganic nanofillers on the thermal degradation of polymeric matrix is correlated to the nature [10, 21, 25] and morphology [2, 20] of the nanoparticles and it is discussed in terms of barrier effects toward both mass and heat transports [12]. In general, the resistance to thermal stabilization is mainly due to a barrier effect toward the mass transport of the volatile products when the nanoparticles are well dispersed into the polymer matrix. The peculiar hollow tube morphology of HNTs can also generate the entrapment of degraded products into the lumen [10], and therefore, an increase of T_{d}. The TG data are well interpreted in the light of the morphological studies evidencing that at $C_{\mathrm{HNTs}} \approx$ 10 wt% (below the T_{d} maximum), the nanocomposite has a compact structure with the HNTs uniformly dispersed into the matrix while a further addition of HNTs (above the T_{d} maximum) generates a structural deterioration of the material with the presence of craters evidenced by SEM experiments. The decrease of the resistance to thermal degradation observed at high C_{HNTs} could be explained by this open structure that favors the diffusion of the volatile products of degradation as observed for PEGs/silica nanocomposites with a similar morphology [20].

Kinetic studies on the thermal degradation of PEG 20000

The non-isothermal thermal degradation kinetics of PEG 20000 was investigated by TG experiments under different β at $C_{\mathrm{HNTs}} = 0$, 35 and 80 wt%. DTG curves show that an increase of β causes a shift of the peak toward larger temperatures in agreement with the literature reports [31, 32]. The kinetic parameters of a process can be determined from non-isothermal data using many isoconversional procedures, such as KAS (Kissinger–Akahira–Sunose) [33], FWO (Flynn–Wall–Ozawa) [34], other integral methods [35, 36], and their combinations [37]. These methods provide the activation energy (E_{a}) without making any assumption on the reaction mechanism [38, 39]. We determined E_a for the degradation of PEG 20000 by means of KAS method, which is based on Eq. 2

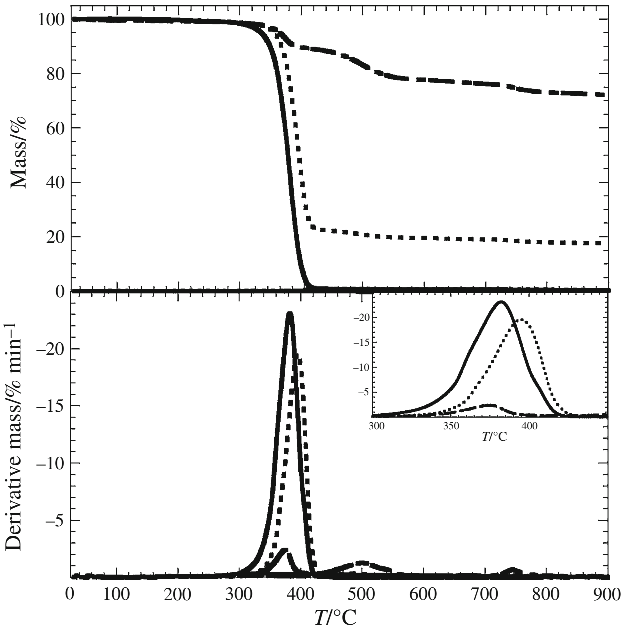

Fig. 4 TG and DTG curves obtained at $\beta = 10$ °C min^{-1} for pristine PEG 20000 (*solid lines*) and nanocomposites with the filler concentration of 20 wt% (*dotted lines*) and 90 wt% *dashed lines*)

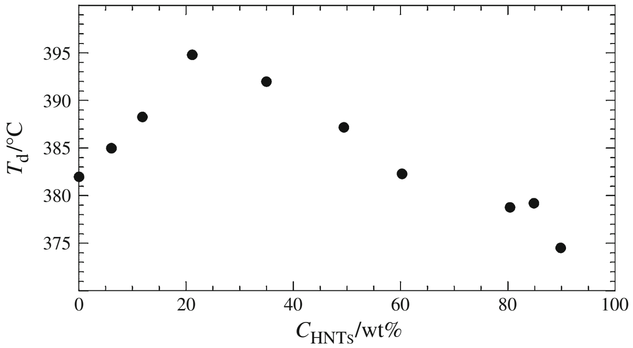

Fig. 5 PEG 20000 degradation temperature (T_{d}) as a function of filler concentration (C_{HNTs})

$$\ln\frac{\beta}{T^2} = \ln\frac{\mathrm{AR}}{E_{\mathrm{a}}g(\alpha)} - \frac{E_{\mathrm{a}}}{\mathrm{R}T} \qquad (2)$$

where $g(\alpha)$ is the integral conversion function, A is the pre-exponential factor while R is the gas constant, and T is the absolute temperature. The E_{a} values at each conversion degree (α) value are calculated from the slope of $\ln \frac{\beta}{T^2}$ versus $1/T$ plot. Data at $\beta > 20$ °C min^{-1} were excluded from this calculation because they are not under thermal equilibrium conditions. Figure 6 shows the dependence of E_{a} on α for pristine polymer and some nanocomposites. We observed that E_{a} is not constant with α, and this is an indication of complex mechanisms for the polymer degradation [40]. Even if the E_{a} variation with C_{HNTs} is quite small, in agreement with the T_{d} data, we observed that at

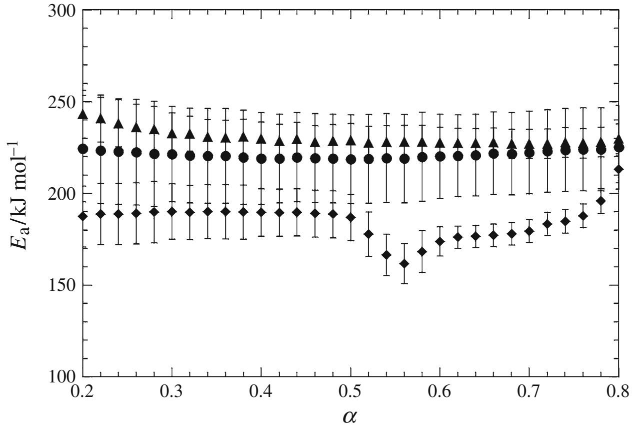

Fig. 6 Activation energy (E_a) of PEG 20000 thermal degradation as a function of the conversion degree (α) for pristine PEG 20000 (*filled circle*) and nanocomposites with filler concentration of 35 wt% (*filled triangle*) and 80 wt% (*filled diamond*) obtained from the KAS method

$C_{\text{HNTs}} = 35$ and 80 wt% the polymer thermal stability is likely enhanced and reduced, respectively.

Going further we focused on the thermal response under very fast heating ramp, which can provide information on the material behavior exposed to thermal shock. It has to be noted that the DTG curves present a shoulder at ca. 300 °C for $\beta = 100$, 250, and 500 °C min^{-1} generating a reduction of the initial onset temperature (T_i) for the polymer degradation. The time requested for the complete degradation (τ) is given by

$$\tau = \frac{\Delta T}{\beta} \tag{3}$$

where ΔT is the difference between the final and initial onset degradation temperature and corresponds to the temperature interval within the degradation takes place. For a given system, under thermal equilibrium conditions, τ depends only on β.

Therefore, the equilibrium ΔT value was extrapolated for $\beta \to 0$ and the trend τ versus β was calculated by means of Eq. 3 in the entire β range (data are reported in Supporting Information). One observes that the experimental τ data deviate from those computed in the higher β regime for all the investigated systems. The upper limit of β that allows thermal equilibration is shifted toward lower values in the presence of HNTs that is in agreement with the lower thermal conductivity of the clay compared to the polymer [41, 42].

Conclusions

Nanocomposites PEG 20000/HNTs were successfully prepared by casting method, and their thermal behavior was characterized by TG and DSC experiments. The bulk properties were correlated to the morphology of the materials obtained by SEM analysis. Small amounts of HNTs generate a compact nanomaterial, while larger amounts create the formation of craters and voids. These different morphologies at the mesoscale range were invoked to be responsible of the thermal degradation response of the polymer. Namely, the compact nanocomposite is thermally more stable than the pristine polymer while the opposite occurs in the high HNTs loading regime because of the more open structure. DSC measurements allowed us to characterize the polymer adsorption onto the HNTs surface. Combining PEG, which is well known in several fields such as consolidant for archaeological wood samples and drug delivery, and innovative biocompatible clay nanotubes may represent a new route to develop smart materials useful in advanced applications.

Acknowledgements The work was financially supported by PON Ricerca e competitività 2007–2013, asse 1 (Development of innovative technologies for the treatment of fluid wastes from shipping activities and for marine environment protection), the University of Palermo and COFIN 2009 (Prot. 2009T2WEAT). Applied Minerals (USA) is acknowledged for kindly providing the Halloysite sample. We are grateful to V. Bertolino for performing some TG and DSC measurements.

References

1. Reinholdt MX, Kirkpatrick RJ, Pinnavaia TJ. Montmorillonite-poly(ethylene oxide) nanocomposites: interlayer alkali metal behavior. J Phys Chem B. 2005;109:16296–303.
2. Cavallaro G, Lazzara G, Milioto S. Dispersions of nanoclays of different shapes into aqueous and solid biopolymeric matrices. Extended physicochemical study. Langmuir. 2011;27:1158–67.
3. Bébin P, Caravanier M, Galiano H. Nafion®/clay-SO3H membrane for proton exchange membrane fuel cell application. J Membr Sci. 2006;278:35–42.
4. Tharanathan RN. Biodegradable films and composite coatings: past, present and future. Trends Food Sci Technol. 2003;14:71–8.
5. Albdiry MT, Yousif BF, Ku H, Lau K. A critical review on the manufacturing processes in relation to the properties of nanoclay/polymer composites. J Compos Mater. 2012. doi:10.1177/0021998312445592.
6. Du M, Guo B, Jia D. Newly emerging applications of halloysite nanotubes: a review. Polym Int. 2010;59:574–82.
7. Lvov YM, Shchukin DG, Mohwald H, Price RR. Halloysite clay nanotubes for controlled release of protective agents. ACS Nano. 2008;2:814–20.
8. Vergaro V, Abdullayev E, Lvov YM, Zeitoun A, Cingolani R, Rinaldi R, Leporatti S. Cytocompatibility and uptake of halloysite clay nanotubes. Biomacromolecules. 2010;11:820–6.
9. Hughes AD, King MR. Use of naturally occurring halloysite nanotubes for enhanced capture of flowing cells. Langmuir. 2010;26:12155–64.
10. Du M, Guo B, Jia D. Thermal stability and flame retardant effects of halloysite nanotubes on poly(propylene). Eur Polym J. 2006;42:1362–9.
11. Lecouvet B, Gutierrez JG, Sclavons M, Bailly C. Structure-property relationships in polyamide 12/halloysite nanotube nanocomposites. Polym Degrad Stab. 2011;96:226–35.

12. Cavallaro G, Donato DI, Lazzara G, Milioto S. Films of halloysite nanotubes sandwiched between two layers of biopolymer: from the morphology to the dielectric, thermal, transparency, and wettability properties. J Phys Chem C. 2011;115:20491–8.
13. Zhang M, Li XH, Gong YD, Zhao NM, Zhang XF. Properties and biocompatibility of chitosan films modified by blending with PEG. Biomaterials. 2002;23:2641–8.
14. Donato D, Lazzara G, Milioto S. Thermogravimetric analysis. J Therm Anal Calorim. 2010;101:1085–91.
15. Duce C, Ghezzi L, Onor M, Bonaduce I, Colombini M, Tine' M, Bramanti E. Physico-chemical characterization of protein–pigment interactions in tempera paint reconstructions: casein/cinnabar and albumin/cinnabar. Anal Bioanal Chem. 2012;402: 2183–93.
16. Cavallaro G, Donato DI, Lazzara G, Milioto S. A comparative thermogravimetric study of waterlogged archaeological and sound woods. J Therm Anal Calorim. 2011;104:451–7.
17. Kučerík J, David J, Wetier M, Vala M, Vyňuchal J, Ouzzane I, Salyk O. Stability and physical structure tests of piperidyl and morpholinyl derivatives of diphenyl-diketo-pyrrolopyrroles (DPP). J Therm Anal Calorim. 2012;108:467–73.
18. De Lisi R, Giammona G, Lazzara G, Milioto S. Copolymers sensitive to temperature and pH in water and in water + oil mixtures: A DSC, ITC and volumetric study. J Colloid Interface Sci. 2011;354:749–57.
19. Lazzara G, Milioto S, Muratore N. Copolymer-cyclodextrin inclusion complexes in water and in the solid state. A physico-chemical study. J Phys Chem B. 2008;112:11887–95.
20. Lazzara G, Milioto S. Dispersions of nanosilica in biocompatible copolymers. Polym Degrad Stab. 2010;95:610–7.
21. De Lisi R, Lazzara G, Milioto S, Muratore N. Laponite clay in homopolymer and tri-block copolymer matrices. J Therm Anal Calorim. 2007;87:61–7.
22. Abate L, Blanco I, Bottino F, Di Pasquale G, Fabbri E, Orestano A, Pollicino A. Kinetic study of the thermal degradation of PS/MMT nanocomposites prepared with imidazolium surfactants. J Therm Anal Calorim. 2008;91:681–6.
23. Blanco I, Abate L, Bottino FA, Bottino P. Thermal degradation of hepta cyclopentyl, mono phenyl-polyhedral oligomeric silsesquioxane (hcp-POSS)/polystyrene (PS) nanocomposites. Polym Degrad Stab. 2012;97:849–55.
24. Abdullayev E, Price R, Shchukin D, Lvov Y. Halloysite tubes as nanocontainers for anticorrosion coating with benzotriazole. ACS Appl Mater Interfaces. 2009;1:1437–43.
25. Lazzara G, Milioto S, Gradzielski M, Prevost S. Small angle neutron scattering, X-ray diffraction, differential scanning calorimetry, and thermogravimetry studies to characterize the properties of clay nanocomposites. J Phys Chem C. 2009;113:12213–9.
26. Kollár T, Kónya Z, Pálinkó I, Kiricsi I. Intercalation of various oxide species in-between Laponite layers studied by spectroscopic methods. J Mol Struct. 2001;563–564:417–20.
27. Stefanescu EA, Schexnailder PJ, Dundigalla A, Negulescu II, Schmidt G. Structure and thermal properties of multilayered Laponite/PEO nanocomposite films. Polymer. 2006;47:7339–48.
28. Messersmith PB, Giannelis EP. Synthesis and barrier properties of poly(ε-caprolactone)-layered silicate nanocomposites. J Polym Sci A Polym Chem. 1995;33:1047–57.
29. Kissinger HE. Variation of peak temperature with heating rate in differential thermal analysis. J Res Natl Stand. 1956;57:217–21.
30. Turnbull D, Fisher JC. Rate of Nucleation in Condensed Systems. J Chem Phys. 1949;17:71–3.
31. Wang S, Tan Z, Li Y, Sun L, Li Y. A kinetic analysis of thermal decomposition of polyaniline/ZrO_2 composite. J Therm Anal Calorim. 2008;92:483–7.
32. Katsikas L, Popović IG. Improvement to the Flynn–Wall method of determining apparent activation energies of the thermal degradation of polymers†. J Phys Chem B. 2003;107:7522–5.
33. Kissinger H. Reaction kinetics in differential thermal analysis. Anal Chem. 1957;29:1702–6.
34. Flynn J, Wall LA. General treatment of the thermogravimetry of polymers. J Res Natl Bur Stand A Phys Chem. 1966;70:487–523.
35. Ortega A. A simple and precise linear integral method for isoconversional data. Thermochim Acta. 2008;474:81–6.
36. Wanjun T, Donghua C. An integral method to determine variation in activation energy with extent of conversion. Thermochim Acta. 2005;433:72–6.
37. Rotaru A, Gosa M. Computational thermal and kinetic analysis. Complete standard procedure to evaluate the kinetic triplet form non-isothermal data. J Therm Anal Calorim. 2009;97:421–6.
38. Budrugeac P, Segal E, Perez-Maqueda LA, Criado JM. The use of the IKP method for evaluating the kinetic parameters and the conversion function of the thermal dehydrochlorination of PVC from non-isothermal data. Polym Degrad Stab. 2004;84:311–20.
39. Rotaru A, Brătulescu G, Rotaru P. Thermal analysis of azoic dyes: Part I. Non-isothermal decomposition kinetics of [4-(4-chlorobenzyloxy)-3-methylphenyl](p-tolyl)diazene in dynamic air atmosphere. Thermochim Acta. 2009;489:63–9.
40. Criado J, Sánchez-Jiménez P, Pérez-Maqueda L. Critical study of the isoconversional methods of kinetic analysis. J Therm Anal Calorim. 2008;92:199–203.
41. Wang W, Yang X, Fang Y, Ding J, Yan J. Preparation and thermal properties of polyethylene glycol/expanded graphite blends for energy storage. Appl. Energy. 2009;86:1479–83.
42. Michot A, Smith DS, Degot S, Gault C. Thermal conductivity and specific heat of kaolinite: evolution with thermal treatment. J Eur Ceram Soc. 2008;28:2639–44.

Applied Clay Science 72 (2013) 132–137

Contents lists available at SciVerse ScienceDirect

Applied Clay Science

journal homepage: www.elsevier.com/locate/clay

Research paper

Alginate gel beads filled with halloysite nanotubes

G. Cavallaro, A. Gianguzza, G. Lazzara *, S. Milioto, D. Piazzese

Department of Chemistry "S. Cannizzaro", University of Palermo, Viale delle Scienze, Parco D'Orleans II, 90128 Palermo, Italy

ARTICLE INFO

Article history:
Received 6 July 2012
Received in revised form 27 November 2012
Accepted 3 December 2012
Available online 18 January 2013

Keywords:
Alginate
Halloysite
Hybrid gel beads
Adsorption

ABSTRACT

Novel hybrid gel beads with a well defined and controlled size formed by alginate biopolymer and halloysite (Hal) nanotubes were designed, prepared and characterized from the physico-chemical viewpoint. The thermogravimetry made it possible to determine the water content, the total as well as the local compositions of Hal into the gel beads. Dielectric spectroscopy evidenced that Hal reduced the fluctuation of ions. The SEM micrographs showed that the dried beads exhibit a rough surface, with pores in the micrometer range. In addition, the concentration of nanotubes was higher into the bead core at a higher overall loading. The performance of these materials was verified with the specific purpose of adsorbing crystal violet from aqueous phase. The alginate gel beads populated by Hal improved their ability to capture the dye so that they can have important implications in the enhancement of controlled adsorptions.

1. Introduction

Nanoparticles are widely used because of their unique properties related to the large surface/volume ratio. Their selection is done in reference to their nature (hydrophobic or hydrophilic), shape (spherical, disk-like or tubular), and specific surface area.

Halloysite (Hal) nanotubes are natural occurring clay minerals. The tubular structure shows typically the inner diameter from 15 to 100 nm, and the length from 500 to 700 nm (Lvov et al., 2008). Hal presents inner and outer hydroxyl groups, which are located between layers and on the surface of the nanotubes, respectively. These nanomaterials have hydrophilic character but, due to their size, they do not form kinetically stable dispersions in water. Recently, a large range of new exciting applications for these cheap and abundantly available natural clay minerals with nanoscale lumens were discovered and developed (Cornejo-Garrido et al., 2012; Kiani et al., 2011; Luo et al., 2011; Pasbakhsh et al., 2010; Vergaro et al., 2010; Xie et al., 2011). Hal is expected to be ideal materials for controlled or sustained release of substances, which may be encapsulated into the lumen. Similarly, the cyclodextrins, forming stable aqueous solutions, are used for this purpose being that they are able to generate inclusion complexes (Gradzielski et al., 2011; Lazzara and Milioto, 2008; Terekhova et al., 2010). Both hydrophobic and hydrophilic agents were encapsulated into the cavity of Hal after appropriate treatments of the surface (Shchukin et al., 2005). Halloysite nanotubes functionalized with polyelectrolyte multilayers loaded corrosion inhibitors, which may be released under a controlled way (Shchukin et al., 2008). A wide range of active agents and biopolymers interact with the external surface and the lumen of Hal (Cavallaro et al., 2011a, 2011b; Levis and Deasy, 2003; Lvov et al., 2002). Interestingly, a novel method was proposed for enhancing the capture of viable circulating tumor cells in a selectin-functionalized microtube by altering the surface topography with immobilized Hal (Hughes and King, 2010). Recently, inorganic micelles were prepared by the selective modification of the Hal cavity (Cavallaro et al., 2012).

These arguments straightforwardly prove the versatility and the potential use of Hal within several fields. The Hal encapsulation into matrices with dimensions of the order of millimeters may represent an advancement towards a multidisciplinary impact on many fields, like the environmental one, where new adsorbent materials are required to make efficient, effective and quantitative the removal of contaminants. Biopolymers as well as gel beads composed of polymers or polymer mixtures with sequestrant capabilities were proposed to capture contaminants from the aqueous phase (Escudero et al., 2009; Lin et al., 2005; Nurchi and Villaescusa, 2012; Peretz and Cinteza, 2008). Gel beads with controlled size can be obtained by mixing a solution of biopolymer containing carboxylate functional groups with Ca^{2+} that bridges the polymer chains generating an increase of the viscosity. Clay/polymer hybrid materials provided advanced drug delivery systems (Alcantara et al., 2010; Huang et al., 2012; Wang et al., 2009, 2010). The use of gel beads may render the process more efficient and practical; for instance, gel beads (with diameters of ca.1 mm) were revealed to be appropriate for use in a column system for heavy metal removal (Cao et al., 2010).

The aim of this work was at designing, preparing and characterizing from the physico-chemical view-point new gel beads of alginate filled with nanosized clay mineral with the motivation to design new nanomaterials at a low environmental impact being composed of Hal, that is environmental friendly, and alginate that is a biopolymer from natural resources. The adsorption capability of hybrid gel beads was investigated. To this aim crystal violet was selected because it is

---

* Corresponding author. Tel.: +39 091 238 97962; fax: +39 091 590015.
E-mail address: giuseppe.lazzara@unipa.it (G. Lazzara).

0169-1317/$ – see front matter © 2012 Elsevier B.V. All rights reserved.
http://dx.doi.org/10.1016/j.clay.2012.12.001

commonly used as additive for fertilizers, anti-freezes, detergents, and it has also some medical applications as antibacterial, antifungal, and anthelmintic (Docampo and Moreno, 1990).

2. Experimental

2.1. Materials

The alginic acid sodium salt (Mw = 70–100 kDa) and crystal violet (CV) are Sigma products. Halloysite (Hal) nanotubes are a gift from Applied Minerals Inc. The calcium chloride ($CaCl_2 \cdot 2H_2O$) is from Merck. All the materials were used without further purification. The water content of Hal is 1.1 mass% as determined by thermogravimetric analysis. This value was taken into account in the concentration calculations. Water was from reverse osmosis (Elga model Option 3) with a specific resistivity greater than 1 MΩ cm.

2.2. Preparation of gel beads

The sodium alginate solution (2 mass%) was prepared by dissolving the polymer in water under magnetic stirring for several hours at 60 °C. The alginate gel beads were prepared by using the dropping technique. Namely, with the aid of a peristaltic pump, a tube with a nozzle of 0.4 mm in diameter extruded the aqueous polymeric solution into an aqueous calcium chloride solution (0.1 mol dm^{-3}) which was gently stirred at room temperature. The distance from the nozzle to the surface of the calcium chloride solution was 5 cm. The beads stand in the $CaCl_2$ solution for several hours, afterwards they were washed with water until the excess of chloride ions was removed. This methodology was followed to prepare the hybrid gel beads composed of alginate and Hal; in this case, Hal was dispersed into the polymeric solution. The alginate/Hal mass ratios were 1:1, 2:1 and 2:3. Larger Hal concentrations were avoided to ensure the formation of a stable dispersion.

2.3. Methods

2.3.1. Dielectric spectroscopy

A Hewlett Packard impedance analyzer (HP 4294A) equipped with HP 16451B dielectric test fixtures was used at 25.0 ± 0.1 °C. The dielectric constant (ε_r) and the dispersion factor (tanδ) were measured in the frequency range from 50 kHz to 10 MHz. The sample thickness was 0.50 mm.

2.3.2. Thermogravimetry

A Q5000 IR apparatus (TA Instruments) under the nitrogen flow of 25 cm^3 min^{-1} for the sample and 10 cm^3 min^{-1} for the balance was used. The mass of each sample was ca. 10 mg and the heating rate was set at 10 °C min^{-1}. Two kinds of experiments were performed as described in the following. The first one was addressed to the determination of the water content of the hydrated gel beads and the temperature scanned from room temperature to 300 °C. The second one was aimed at determining the amount of the polymer and Hal present in the gel beads; to this purpose, the experiments were carried out on dried spherules heating up the sample from room temperature to 900 °C.

2.3.3. Scanning electron microscopy

The morphology of the composite gel beads was determined by using a microscope ESEM FEI Quanta 200F. Before each experiment, the gel beads were dried and the surface of the sample was coated with gold in argon by means of an Edwards Sputter Coater S150A to avoid charging under an electron beam. Minimal electron dose condition was set to avoid damage of the sample.

2.3.4. Spectrophotometry

The measurements were carried out at 25.0 ± 0.1 °C by using an Analytic Jena Specord S 600 BU. The spectra of absorbance were registered in the wavelength (λ) 420–800 nm range. The aqueous CV solution exhibits the maximum of the absorption band at 592 nm. The cuvettes in polystyrene material instead of those in the quartz were used to avoid errors caused by the dye sorption on the quartz walls. The determined molar extinction coefficient of CV in water is $(68 \pm 1) \times 10^3$ dm^3 mol^{-1} cm^{-1}.

The kinetics of adsorption of CV onto the adsorbents were followed over 60 h to estimate the equilibration time. In particular, a given amount of the adsorbent material (0.5 mg of pure Hal or 20 mg of hydrated gel beads) was added to 2 ml of aqueous dye solution 1×10^{-5} mol dm^{-3} and, under a gentle stirring, the absorbance of the dye was registered over time.

The percent of removed dye was calculated as $R_{\%} = 10^2(C_0 - C_t)/C_0$ where C_0 is the stoichiometric concentration while C_t is that at a given time. The alginate beads exhibit a constant $R_{\%}$ value after ca. 30 h and the presence of Hal hardly changes the adsorption kinetics.

Based on these studies, the dispersions were equilibrated for 1 week and the absorbance of the dye in the supernatant was measured. The adsorption of CV (1×10^{-5} mol dm^{-3}) onto pure Hal and gel beads was studied as a function of the adsorbent amount.

Examples of the spectra determined as functions of the wavelengths are reported in the Supplementary information.

The $R_{\%}$ value was calculated as $R_{\%} = 10^2(C_0 - C_e)/C_0$ where C_e is the value of the concentration at the equilibrium.

3. Results

3.1. Alginate gel beads filled with Hal

The formation of alginate gel beads occurs also in the presence of Hal. The gel beads' size is not significantly influenced by the Hal content while the transparency is reduced upon the addition of the clay mineral amount (Fig. 1).

Similarly, the size of the gel beads composed of chitosan and laponite are not affected by the addition of the nanoclay (Yang et al., 2011). The drops of the aqueous Hal/alginate dispersion in contact with the calcium chloride solution do not generate opalescence leaving transparent and homogeneous bulk electrolyte phase; therefore, one may deduce that Hal is fully incorporated into the beads' structure.

To verify this aspect, the gel beads were characterized by means of thermogravimetry that made it possible to determine the water content as well as the amount of Hal and biopolymer entrapped into the gel network. Fig. 2a shows the experimental Hal mass fraction in the dried gel beads (P_{Hal}) against the stoichiometric value calculated from the actual polymer and nanotube concentrations (P^o_{Hal}). The very good linear correlation between P_{Hal} and P^o_{Hal} shows that Hal is quantitatively entrapped into the gel beads and that the gel formation is faster than the Hal diffusion into the calcium chloride solution.

The Hal presence influences the gel beads' water content (WC), which decreases upon incorporating the clay mineral into the beads (Table 1).

The SEM micrographs show that the dried bead possesses a rough surface with pores in the micrometer range (Fig. 3a–c) that is similar to what was observed in the absence of Hal (Peretz and Cinteza, 2008).

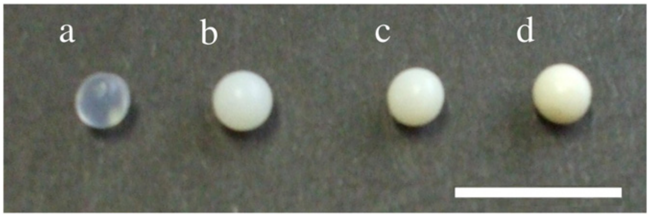

Fig. 1. Optical images for hybrid gel beads at variable Hal content: a, $P^o_{Hal} = 0$ mass%; b, $P^o_{Hal} = 33.2$ mass%; c, $P^o_{Hal} = 48.5$ mass%; d, $P^o_{Hal} = 60.2$ mass%. The bar is 1 cm.

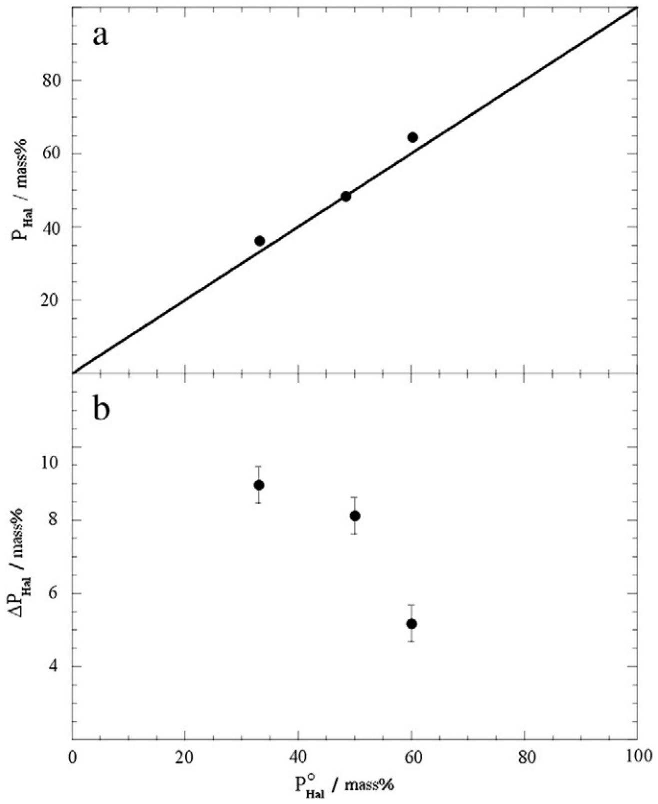

Fig. 2. Hal percent (a) and its relative variation between the core and the peel (b) of hybrid gel beads at various compositions.

In addition, the nanotubes appear at the bead surface even if they are well incorporated into the polymer network. Investigating the core structure of the dried gel bead (Fig. 3d–f), the Hal particles are more numerous than those at the surface. To better highlight this aspect, we carried out TGA experiments on samples collected from the core and the peel (1 mm thick) of the beads, respectively. The percentage variations of the Hal concentration in the core with respect to the outer peel (Fig. 2b) agree with the SEM results, which indicate an enrichment of Hal into the bead core; moreover, by increasing the Hal amount generates a more uniform distribution of the nanotubes through the gel beads. The higher content of Hal into the spherule core is ascribed to the presence of a larger amount of water where the functionalized nanotubes are well dispersed and stabilized.

Dielectric spectroscopy provides information on the molecular dynamics of systems by monitoring the relaxation processes. Polyelectrolyte solutions (Muller et al., 1974; Umemura et al., 1980; Van Der Touw and Mandel, 1974) show two relaxation processes in the regions of kHz and MHz, respectively. The low-frequency relaxation reflects either the oriental polarization of the polymer or the fluctuation of counterions bound along the polyelectrolytes. The high-frequency relaxation is related to the bound counterion fluctuation within the range of the correlation length along (Mandel and Odijk, 1984; Minakata and Imai, 1972) or perpendicular (Oosawa, 1971) to the polyelectrolyte. The gel beads showed a relaxation process in the MHz domain that is well identified as the maximum in the tanδ vs ν plot (Fig. 4) corresponding to the inflection point in the ε_r vs ν curve. Upon Hal addition the peak position is shifted toward lower frequencies but the general profile is not altered. The relaxation frequency at the maximum (ν_{max}) shows a linear decrease with P^{o}_{Hal} (Table 1) in agreement with a reduced ions fluctuation generated by the nanotubes. Finally, the steep increase of the dielectric constant at low frequencies can be related to ionomer multiplets forming large aggregates with high polarizability observed in gels based on polyelectrolytes (Osada and Khokhlov, 2002).

Table 1
Physico-chemical parameters of gel beads loaded with Hal.[a]

P^{o}_{Hal}	WC	ν_{max}
0	96.8	938
33.2	95.4	726
48.4	94.4	533
60.2	91.6	468

[a] Units are: P^{o}_{Hal} and water content (WC), wt.%; ν_{max}, kHz. Uncertainties are: ±0.1 mass% and ±5 kHz.

3.2. Adsorption studies

The trends of $R_{\%}$ vs the stoichiometric concentration of the adsorbent material (alginate + Hal, C_s) at the various Hal loading into the beads are shown in Fig. 5.

The monotonic profiles were fitted by assuming the availability of a certain number of equivalent adsorption sites (De Lisi et al., 2005, 2006) into the gel beads. The following equation was used

$$R_{\%} = 10^2 \frac{q_m C_s K(C_0 - C_{ads})}{[K(C_0 - C_{ads}) + 1]C_0} \tag{1}$$

where q_m is the maximum adsorbed amount of the dye per gram of adsorbent, C_s is the stoichiometric adsorbent concentration, C_0 and C_{ads} are the stoichiometric and the adsorbed dye concentrations, respectively, and K is the equilibrium constant for the adsorption process.

By remembering that $R_{\%} = 10^2 C_{ads}/C_0$, from Eq. (1) one obtains

$$C_{ads} = -\left\{ \left[{C_s}^2 K^2 {q_m}^2 + 2q_m C_s K(1 - KC_0) + K^2 {C_0}^2 + 2KC_0 \right]^{0.5} - q_m C_s K - K(C_0 - 1) \right\} / 2\,K. \tag{2}$$

Eqs. (1) and (2) which are applied to the experimental data provided the q_m and K parameters as functions of P^{o}_{Hal} collected in Table 2. The best fits are illustrated in Fig. 5.

The presence of Hal into the gel beads improves the adsorption process; q_m increases with P^{o}_{Hal} in agreement with the larger adsorption capability of the hybrid gel beads conferred by Hal. As concerns the K values, they are only slightly affected by Hal; notwithstanding, it is noteworthy that the dye affinity toward the hybrid beads is greater than that for the alginate gel beads.

For comparison, the adsorption isotherm of CV onto Hal was measured obtaining $(40.3 \pm 0.4) \cdot 10^4$ dm^3 mol^{-1} and 28 ± 3 mg g^{-1} for K and q_m, respectively.

4. Discussion

Gel beads present several advantages for controlled adsorption and release of substances (contaminants, drugs, and so on) thanks to the fact that they are easy to prepare, to collect and to dispose. With this in mind we loaded the alginate gel beads with efficient adsorbent nanotubes with the aim of obtaining new environmental friendly nanomaterials, which on one side have improved adsorption ability and on the other side make easy and practical the removal process.

The extended physico-chemical studies made it possible to extract significant and relevant insights on the versatility and novelty of the new designed nanomaterials.

The hybrid gel beads with well defined and controlled size (of the order of millimeters) were easily prepared owning to the stable dispersion of nanotubes in the presence of the polymer. According to the dissociation equilibrium of the alginic acid (Crea et al., 2009), under our experimental conditions (pH≈6), the biopolymer is present

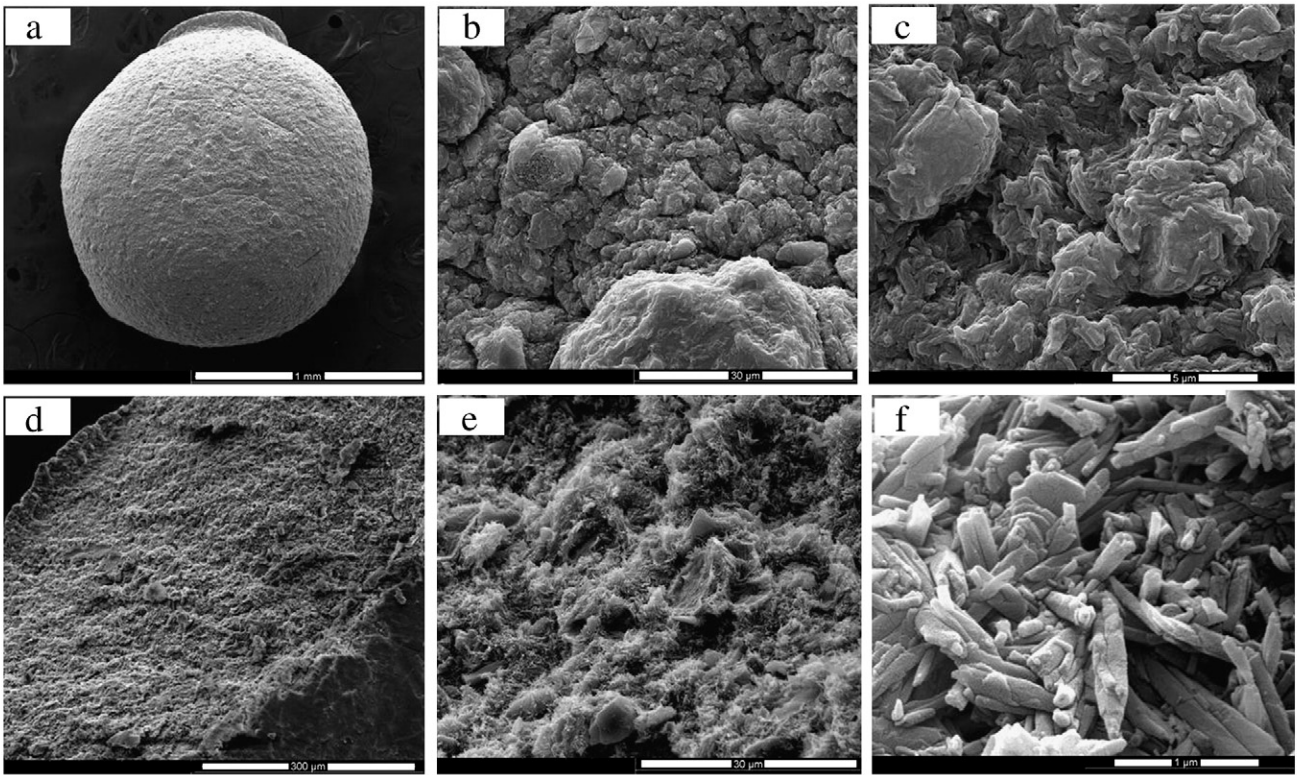

Fig. 3. Scanning electron microscopy images of gel beads loaded with Hal at $P^{o}_{Hal} = 33.2$ mass%. a, b, c refer to the surface; d, e, f refer to the core.

only in the dissociated form. The adsorption of the alginate ion can occur through two mechanisms: 1) the encapsulation of the carboxylate group into the lumen due to the interactions with the aluminol groups and 2) the dipole/dipole interactions between the uncharged siloxane and the hydroxyl groups of the biopolymer. The total net charge of the wrapped nanotube is more negative than the pristine nanotube as a result of the neutralization of the lumen positive charge. The chelant ability of the carboxylate groups towards the Ca^{2+} ions is not suppressed by the negative surface of the nanotubes which, indeed, can assume the role of bridges favoring the network formation. The key role of Hal is corroborated by the formation of gel beads under conditions where Hal is in excess with respect to the biopolymer (Hal/polymer mass ratio was as large as 3:2). Independent dielectric spectroscopy studies confirm such a picture, which describes an evident reduction of mobility of ions upon an increasing amount of Hal.

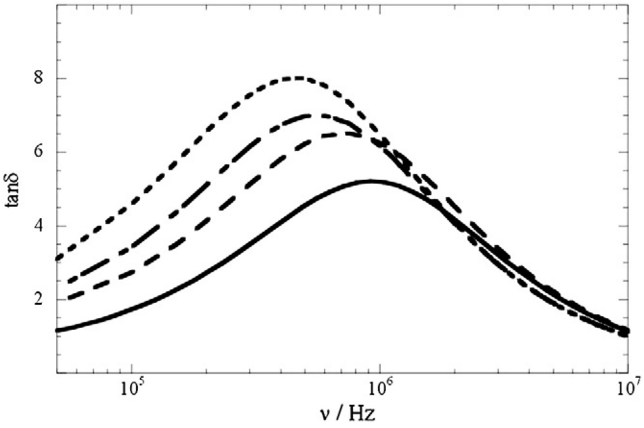

Fig. 4. Dispersion factor as a function of the frequency for hybrid gel beads with variable Hal content. (—), $P^{o}_{Hal} = 0$ mass%; (– –), $P^{o}_{Hal} = 33.2$ mass%; (- – -), $P^{o}_{Hal} =$ 48.5 mass%; (---), $P^{o}_{Hal} = 60.2$ mass%.

The ability of the hybrid nanomaterials was tested by studying the adsorption of the crystal violet dye. The good performance is exhibited by the change in the adsorption generated by the gel population with clay minerals. As Fig. 6 shows, Hal enhances the gel beads' ability in capturing CV; for instance, at the alginate/Hal mass ratio of 2:1, at $C_s = 0.25$ and 0.50 mass%, the $R_{\%}$ value is increased by ca. 55 and 45%, respectively. This sharp increase is even larger than that calculated by assuming the simple rule of mixtures (Fig. 6) and it proves that the combination of Hal and biopolymer generates synergistic effects in the adsorption properties of hybrid beads based on alginate.

The benefit of the nanofiller on the CV affinity towards the hybrid material reveals the key role of the interactions between CV and the Hal. To interpret the Hal effect, one has to consider that CV has the pK_a value of 1.0 and therefore under our experimental conditions (pH ≈ 6) the cationic form is dominant; in addition the external surface and the internal cavity of Hal are negatively and positively charged, respectively. Consequently, one can argue that electrostatic interactions between CV and the outer surface of Hal are present.

5. Conclusions

Novel materials were designed and prepared by encapsulating halloysite nanotubes into hydrogel composed of electrostatically cross-linked biopolymer network. The dynamics, the structure and the composition of the hybrid gel beads were well described through SEM, thermogravimetry and dielectric spectroscopy studies. These materials are promising for controlled adsorption/release applications where the tube lumen can be properly loaded with functional molecules. The

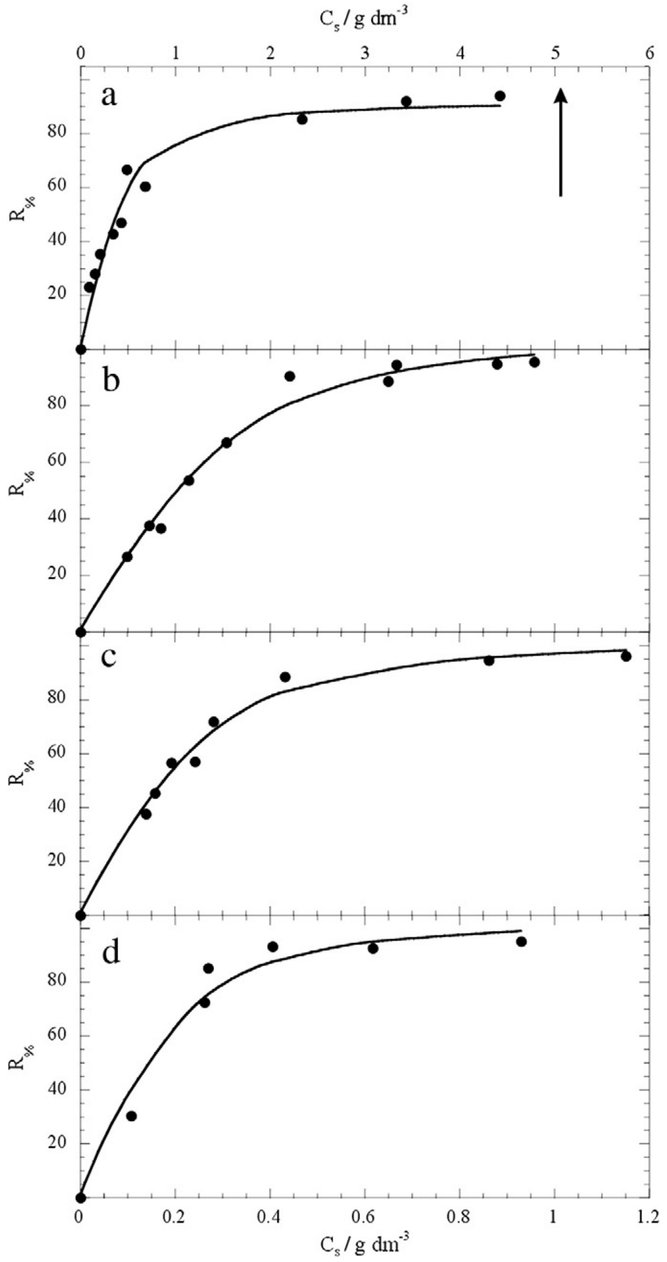

Fig. 5. Percent of removed CV as functions of the stoichiometric adsorbent material. a, $P^{o}_{Hal}=0$ mass%; b, $P^{o}_{Hal}=33.2$ mass%; c, $P^{o}_{Hal}=48.5$ mass%; d, $P^{o}_{Hal}=60.2$ mass%. Lines are best fits according to Eqs. (1)–(2).

advantages of using easy to handle and biocompatible gel beads are straightforward. The hybrid gel beads are very effective and efficient for removing positively charged dye from aqueous phase with enhanced properties compared to the unloaded gel beads.

Table 2
Physico-chemical parameters for the adsorption of dyes onto hybrid gel beads.[a]

P^{o}_{Hal}	K	q_m
0	$(39.3\pm0.8)\cdot10^4$	8.5 ± 1.0
33.2	$(42.4\pm0.6)\cdot10^4$	12.7 ± 1.0
48.4	$(41.7\pm0.6)\cdot10^4$	15.5 ± 1.1
60.2	$(42.9\pm1.7)\cdot10^4$	17 ± 3

[a] Units are: P^{o}_{Hal}, mass%; K, dm^3 mol^{-1}; q_m, mg g^{-1}.

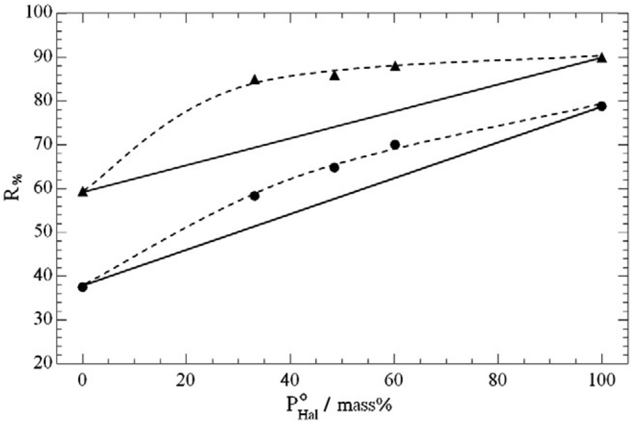

Fig. 6. Dependence on Hal concentration of percent of removed CV from aqueous phase calculated from data in Table 2. (●), $C_s=0.25$ mass% and (▲), $C_s=0.5$ mass%. Solid lines are calculated by rule of mixtures. Broken lines are guide for eyes.

Acknowledgments

The work was financially supported by PON Ricerca e Competitività 2007–2013, Asse 1 (Development of innovative technologies for the treatment of fluid wastes from shipping activities and for marine environment protection) and the University of Palermo. Applied Minerals Inc. (USA) is acknowledged for kindly providing the Halloysite sample.

Appendix A. Supplementary data

Dielectric constant as a function of the frequency for hybrid gel beads. UV–VIS spectra of CV as functions of wavelength for dispersions equilibrated with Hal. Percent of removed CV as a function of time. Adsorption isotherm of CV onto Hal.

Supplementary data to this article can be found online at http://dx.doi.org/10.1016/j.clay.2012.12.001.

References

Alcantara, A.C.S., Aranda, P., Darder, M., Ruiz-Hitzky, E., 2010. Bionanocomposites based on alginate-zein/layered double hydroxide materials as drug delivery systems. Journal of Materials Chemistry 2042, 9495–9504.

Cao, J., Tan, Y., Che, Y., Xin, H., 2010. Novel complex gel beads composed of hydrolyzed polyacrylamide and chitosan: an effective adsorbent for the removal of heavy metal from aqueous solution. Bioresource Technology 1017, 2558–2561.

Cavallaro, G., Donato, D.I., Lazzara, G., Milioto, S., 2011a. Films of halloysite nanotubes sandwiched between two layers of biopolymer: from the morphology to the dielectric, thermal, transparency, and wettability properties. Journal of Physical Chemistry C 11542, 20491–20498.

Cavallaro, G., Lazzara, G., Milioto, S., 2011b. Dispersions of nanoclays of different shapes into aqueous and solid biopolymeric matrices. Extended physicochemical study. Langmuir 273, 1158–1167.

Cavallaro, G., Lazzara, G., Milioto, S., 2012. Exploiting the colloidal stability and solubilization ability of clay nanotubes/ionic surfactant hybrid nanomaterials. Journal of Physical Chemistry C 116, 21932–21938.

Cornejo-Garrido, H., Nieto-Camacho, A., Gómez-Vidales, V., Ramírez-Apan, M.T., del Angel, P., Montoya, J.A., Domínguez-López, M., Kibanova, D., Cervini-Silva, J., 2012. The anti-inflammatory properties of halloysite. Applied Clay Science 57, 10–16.

Crea, F., De Stefano, C., Gianguzza, A., Pettignano, A., Piazzese, D., Sammartano, S., 2009. Acid–base properties of synthetic and natural polyelectrolytes: experimental results and models for the dependence on different aqueous media. Journal of Chemical & Engineering Data 542, 589–605.

De Lisi, R., Lazzara, G., Lombardo, R., Milioto, S., Muratore, N., Turco Liveri, M.L., 2005. Adsorption of triblock copolymers and their homopolymers at laponite clay/solution interface. Role played by the copolymer nature. Physical Chemistry Chemical Physics 723, 3994–4001.

De Lisi, R., Lazzara, G., Milioto, S., Muratore, N., 2006. Aqueous nonionic copolymer-functionalized laponite clay. A thermodynamic and spectrophotometric study to characterize its behavior toward an organic material. Langmuir 2219, 8056–8062.

Docampo, R., Moreno, S.N., 1990. The metabolism and mode of action of gentian violet. Drug Metabolism Reviews 22, 161–178.

Escudero, C., Fiol, N., Villaescusa, I., Bollinger, J.-C., 2009. Arsenic removal by a waste metal hydroxide entrapped into calcium alginate beads. Journal of Hazardous Materials 1642–3, 533–541.

Gradzielski, M., Lazzara, G., Prevost, S., 2011. Selectivity of cyclodextrins as a parameter to tune the formation of pseudorotaxanes and micelles supramolecular assemblies. a systematic SANS study. Soft Matter 7, 6082–6091.

Huang, X., Xiao, Y., Lang, M., 2012. Micelles/sodium-alginate composite gel beads: a new matrix for oral drug delivery of indomethacin. Carbohydrate Polymers 871, 790–798.

Hughes, A.D., King, M.R., 2010. Use of naturally occurring halloysite nanotubes for enhanced capture of flowing cells. Langmuir 2614, 12155–12164.

Kiani, G., Dostali, M., Rostami, A., Khataee, A.R., 2011. Adsorption studies on the removal of malachite green from aqueous solutions onto halloysite nanotubes. Applied Clay Science 541, 34–39.

Lazzara, G., Milioto, S., 2008. Copolymer–cyclodextrin inclusion complexes in water and in the solid state. A physic-chemical study. The Journal of Physical Chemistry. B 112, 11887–11895.

Levis, S., Deasy, P., 2003. Use of coated microtubular halloysite for the sustained release of diltiazem hydrochloride and propranolol hydrochloride. International Journal of Pharmaceutics 2531–2, 145–157.

Lin, Y.-B., Fugetsu, B., Terui, N., Tanaka, S., 2005. Removal of organic compounds by alginate gel beads with entrapped activated carbon. Journal of Hazardous Materials 1201–3, 237–241.

Luo, P., Zhang, J., Zhang, B., Wang, J., Zhao, Y., Liu, J., 2011. Preparation and characterization of silane coupling agent modified halloysite for CrVI removal. Industrial and Engineering Chemistry Research 5017, 10246–10252.

Lvov, Y., Price, R., Gaber, B., Ichinose, I., 2002. Thin film nanofabrication via layer-by-layer adsorption of tubule halloysite, spherical silica, proteins and polycations. Colloids and Surfaces A: Physicochemical and Engineering Aspects 198–2000, 375–382.

Lvov, Y.M., Shchukin, D.G., Mohwald, H., Price, R.R., 2008. Halloysite clay nanotubes for controlled release of protective agents. ACS Nano 25, 814–820.

Mandel, M., Odijk, T., 1984. Dielectric properties of polyelectrolyte solutions. Annual Review of Physical Chemistry 35, 75–108.

Minakata, A., Imai, N., 1972. Dielectric properties of polyelectrolytes. I. A study on tetra-n-butyl ammonium polyacrylate. Biopolymers 112, 329–346.

Muller, G., Van Der Touw, F., Zwolle, S., Mandel, M., 1974. Dielectric properties of poly L glutamic acid in salt free aqueous solutions. Biophysical Chemistry 23, 242–254.

Nurchi, V.M., Villaescusa, I., 2012. Sorption of toxic metal ions by solid sorbents: a predictive speciation approach based on complex formation constants in aqueous solution. Coordination Chemistry Reviews 2561–2, 212–221.

Oosawa, F., 1971. Polyelectrolytes. Marcel Dekker, New York.

Osada, Y., Khokhlov, A., 2002. Polymer Gels and Networks. Marcel Dekker, New York.

Pasbakhsh, P., Ismail, H., Fauzi, M.N.A., Bakar, A.A., 2010. EPDM/modified halloysite nanocomposites. Applied Clay Science 483, 405–413.

Peretz, S., Cinteza, O., 2008. Removal of some nitrophenol contaminants using alginate gel beads. Colloids and Surfaces A: Physicochemical and Engineering Aspects 3191–3, 165–172.

Shchukin, D.G., Sukhorukov, G.B., Price, R.R., Lvov, Y.M., 2005. Halloysite nanotubes as biomimetic nanoreactors. Small 15, 510–513.

Shchukin, D.G., Lamaka, S.V., Yasakau, K.A., Zheludkevich, M.L., Ferreira, M.G.S., Mohwald, H., 2008. Active anticorrosion coatings with halloysite nanocontainers. Journal of Physical Chemistry C 1124, 958–964.

Terekhova, I.V., Romanova, A.O., Kumeev, R.S., Fedorov, M.V., 2010. Selective Na$^+$/K$^+$ effects on the formation of α-cyclodextrin complexes with aromatic carboxylic acids: competition for the guest. The Journal of Physical Chemistry. B 114, 12607–12613.

Umemura, S., Hayakawa, R., Wada, Y., 1980. New method for simultaneous measurement of frequency spectra of complex dielectric constants of polyelectrolyte solutions. Biophysical Chemistry 113–4, 317–320.

Van Der Touw, F., Mandel, M., 1974. Dielectric increment and dielectric dispersion of solutions containing simple charged linear macromolecules. II. Experimental results with synthetic polyelectrolytes. Biophysical Chemistry 23, 231–241.

Vergaro, V., Abdullayev, E., Lvov, Y.M., Zeitoun, A., Cingolani, R., Rinaldi, R., Leporatti, S., 2010. Cytocompatibility and uptake of halloysite clay nanotubes. Biomacromolecules 113, 820–826.

Wang, Q., Zhang, J., Wang, A., 2009. Preparation and characterization of a novel pH-sensitive chitosan-g-poly acrylic acid/attapulgite/sodium alginate composite hydrogel bead for controlled release of diclofenac sodium. Carbohydrate Polymers 784, 731–737.

Wang, Q., Xie, X., Zhang, X., Zhang, J., Wang, A., 2010. Preparation and swelling properties of pH-sensitive composite hydrogel beads based on chitosan-g-poly acrylic acid/vermiculite and sodium alginate for diclofenac controlled release. International Journal of Biological Macromolecules 463, 356–362.

Xie, Y., Chang, P.R., Wang, S., Yu, J., Ma, X., 2011. Preparation and properties of halloysite nanotubes/plasticized *Dioscorea opposita* Thunb. starch composites. Carbohydrate Polymers 831, 186–191.

Yang, H., Hua, S., Wang, W., Wang, A., 2011. Composite hydrogel beads based on chitosan and laponite: preparation, swelling, and drug release behaviour. Iranian Polymer Journal 206, 479–490.

Attached VI

Journal of Environmental Chemical Engineering 1 (2013) 1252–1260

Contents lists available at ScienceDirect

Journal of Environmental Chemical Engineering

journal homepage: www.elsevier.com/locate/jece

Kinetic and equilibrium study for cadmium and copper removal from aqueous solutions by sorption onto mixed alginate/pectin gel beads

Salvatore Cataldo [a], Giuseppe Cavallaro [a], Antonio Gianguzza [a,*], Giuseppe Lazzara [a], Alberto Pettignano [a], Daniela Piazzese [a], Isabel Villaescusa [b]

[a] *Dipartimento di Fisica e Chimica, Università di Palermo, Viale delle Scienze, I-90128 Palermo, Italy*
[b] *Departament d'Enginyeria Química, Agrària i Tecnologia Agroalimentària, Universitat de Girona, Mª Aurelia Capmany 61, s/n, 17071 Girona, Spain*

ARTICLE INFO

Article history:
Received 20 June 2013
Received in revised form 4 September 2013
Accepted 16 September 2013

Keywords:
Alginate
Pectin
Gel beads
Adsorption
Metal removal

ABSTRACT

Kinetic and equilibrium studies have been carried out to evaluate Cd(II) and Cu(II) sorption from aqueous solution by calcium alginate and new synthesized hybrid calcium alginate/pectate gel beads with different alginate/pectate concentration ratios. Physical and chemical properties of the beads were characterized by different techniques (SEM, EDX, TGA). The best experimental pH conditions were selected on the basis of a study on the acid–base properties of pectin and alginate in aqueous solution and their ability to act as sequestering agents for copper(II) and cadmium(II) ions. Calcium released during the sorption process was determined in order to elucidate a possible ion exchange mechanism between calcium of the beads and metal ions in solution. Sorption kinetics and metal sorption capacity of gel beads were investigated in batch mode. Measurements of Cd^{2+}, Cu^{2+} and Ca^{2+} concentration were carried out by Inductively Coupled Plasma Optical Emission Spectroscopy (ICP-OES). Results obtained showed that for all the studied systems the sorption process follows a pseudo-second order kinetic model and the sorption rate increases when increasing pectin concentration in gel beads. The equilibrium data were fitted by using both Langmuir and Freundlich isotherms models. The highest copper and cadmium sorption yields were obtained for beads containing a mixture of 2% alginate and 2% pectate. Ion exchange is the major mechanism governing the sorption process though other mechanisms are also taking place.

Introduction

The possible use of low cost and environmental friendly materials to remove toxic metal ions from aqueous solutions has been widely investigated with the aim to set-up new sorption and biosorption technologies [1–7], alternative to the conventional electrochemical, flotation and precipitation treatments [8–14]. The most investigated sorbent materials are derived from natural biomass, especially fungi [15–18], algae [19–23], humic substances from soil [24] and byproducts from industrial processes, such as wood and food industries, agriculture, fishery and textile manufacturing [25–32]. Also some inorganic materials (zeolites, clays, etc.) are used for the same purpose [7,8,33,34]. These sorbent materials all exhibit characteristics of being low cost, causing low environmental impact, presenting high degradability, great availability and high sorption capacity towards metal ions [35–37]. The sorption ability of these materials is strictly related to their chemical composition containing high percentages of macromolecules with a great number of binding groups such as –O, –N, and –S donors [4,37] able to form stable species with the metal ions to be removed [38–40]. Several investigations have been carried out using a variety of materials for wastewaters and contaminated sites treatment. Reviews and textbooks cited in Refs. [1–8,36,37] give a general picture of potential sorbent materials used. In particular, algae and fruits have been widely tested as sorbents for metal removal, including copper and cadmium [19–23,30,41–47], from polluted aqueous solutions. Most of these studies refer to metal sorption capacity of raw materials and only few of them report results on the sorption by alginate and/or pectin in gel phase [41,45,48–53]. Alginic acid is a polysaccharide constituted by monomer units of mannuronic and guluronic acids [54,55]. It is the main component of brown algae where it is present up to 40% dry weight [56]. Pectin, mostly constituted by polygalacturonic acid with different extent of acetylation [57], is the main component of peel and pulp of several fruits. Both these materials are able to form hydrogels in the

---

[*] Corresponding author. Tel.: +39 09123897954.
E-mail address: antonio.gianguzza@unipa.it (A. Gianguzza).

2213-3437/$ – see front matter © 2013 Elsevier Ltd. All rights reserved.
http://dx.doi.org/10.1016/j.jece.2013.09.012

presence of small amounts of divalent cations, especially calcium ion [58,59]. The removal capacity of both these biopolymers can be attributed to the presence of several ligand carboxylic groups per molecule. Therefore, it can be assumed that they are the main responsible for the sorption process of metal ion by algae and fruits. For the above reasons we carried out the present study with the aim to test the removal capacity of cadmium(II) and copper(II) from aqueous solutions using directly alginate and pectin in gel phase. To that end, the biopolymers under investigation, mixed in various concentration ratios to form a new hybrid alginate/pectin sorbent material, were used as calcium gel beads which are more easily to handle and give more accurate results than the raw biomaterials. The sorption capacity of mixed materials was compared to that of calcium alginate beads, used as a reference material. Several studies report that ion exchange is the predominant mechanism in metal sorption by algal biomass [40,54,55,60] and a pseudo-second order kinetic model is generally used to describe the sorption process when the chemical sorption is the rate – controlling step [32,61]. In order to confirm the hypothesis, *i.e.*, if the sorption process occurs *via* ion exchange between calcium ion of sorbent materials and copper(II) or cadmium(II) ions present in the solution, the amount of calcium released by gel beads during the kinetic experiments was determined. The effect of contact time, initial metal concentration and different alginate/pectate concentration ratios on the kinetics of metal adsorption was investigated by batch experiments.

A pseudo second-order model was used to quantify the sorption capacity of gel materials under investigation. Both Langmuir and Freundlich isotherm models were used to fit the equilibrium data. A comparison with some results reported by different authors using the same models and similar experimental conditions is also given.

To obtain the best metal removal efficiency, the most suitable conditions of pH, ionic strength and medium of solutions containing the metal ion to be removed, were assessed on the basis of the results of previous speciation studies [62–64]. In these studies the acid–base properties of alginate [62,63] and pectin [64] and the ability of these polymers to bind copper(II) and cadmium(II) ions in aqueous solution were defined over a wide pH range.

Materials and methods

Chemicals

Cadmium(II), copper(II) and calcium(II) nitrate salts solutions were prepared by diluting standard (1000 mg L^{-1} in HNO_3 0.5 mol L^{-1}) Merck solutions. Commercial pectin, as potassium salt extracted by citrus peel, was supplied by Aldrich (lot. 077K1583). Commercial alginic acid (AA, molecular weight in the range 70–100 kDa), as sodium salt extracted from *Macrocystis pyrifera*, with an average content of mannuronic and guluronic acids of 61% and 39%, respectively, was supplied by Sigma (lot. 60K1443). Nitric acid and sodium hydroxide solutions used to adjust the pH of the metal ion standard solutions were prepared by diluting concentrated Fluka ampoules and standardized against sodium carbonate and potassium hydrogen phthalate, respectively. Calcium chloride dehydrate (Fluka) was used to prepare calcium alginate and mixed calcium alginate/pectate gel beads. All the solutions were prepared using freshly prepared CO_2-free ultra pure water ($\rho \geq 18$ MΩ cm) and grade A glassware.

Preparation and characterization of sorbent materials

Calcium alginate and mixed calcium alginate/pectate gel beads were prepared using the dropping technique. A peristaltic pump (GILSON, Minipuls 3) was used to dispense the suspension in a stirred reservoir containing 200 mL of a $CaCl_2$ 0.1 M solution used for gel formation. At the end of the dispensing tube a micropipette tip (yellow type 5–200 μL) cut out to get a final diameter of 1 mm was attached and positioned approximately 1 cm above the surface of the fixing solution. The beads formed were allowed to cure, under continuous stirring, in the same $CaCl_2$ solution for 24 h; they were rinsed three times with distilled water to ensure the removal of unbound calcium(II) ion. The following gel beads were prepared: 2% calcium alginate (Ca-*A*), 2% calcium alginate 1% calcium pectate (Ca-AP_1), 2% calcium alginate 1.5% calcium pectate (Ca-$AP_{1.5}$) and 2% calcium alginate 2% calcium pectate (Ca-AP_2).

To define the physico-chemical and mechanical properties of gel beads, different analysis were carried out. The density of gel beads was measured by a helium pycnometer (AccuPyc 1330) at $T = 20$ °C. A digital calliper (MITUTOYO, model 500-181-U) was used to measure the diameter of beads and the mean value was calculated on 50 beads together with the relative standard deviation. The water content was evaluated by Thermo Gravimetric Analysis using a Q5000 IR apparatus (TA Instruments). Experiments were carried out in a temperature range 25–300 °C, under the nitrogen flow of 25 $cm^3 min^{-1}$ for the samples and 10 $cm^3 min^{-1}$ for the balance. The weight of each sample was 10 mg and the heating rate was set at 10 °C min^{-1}. The mechanical resistance of gel beads was measured by using a Texture Analyser (model TA-XTS2i, Stable Micro Systems, England). This parameter represents the mean force necessary to generate the 10% compression on a bead placed under a cylinder probe P10 (Batch 2370, Stable Micro Systems, England). The measurements of mechanical resistance were repeated 40 times for each type of gel beads and the mean value was calculated together with the standard deviation. The morphology of sorbent materials was investigated by an electronic microscope ESEM FEI QUANTA 200F coupled with an EDX (Energy Dispersive X-ray spectroscopy) system. Before the analysis the gel beads were dried at $T = 105$ °C and their surface was coated with gold in the presence of argon by an Edwards Sputter Coater S150A in order to prevent charging under electronic beam. The electron beam was opportunely set in order to avoid the damage of the samples. SEM micrographs were registered within the micrometer range.

Experimental procedures for kinetic and equilibrium investigations

Batch kinetic experiments were carried out by placing twenty gel beads in Erlenmeyer flasks containing each one 15 mL of $Cu(NO_3)_2$ or $Cd(NO_3)_2$ salt solutions ($C_M{}^{2+} = 200$ mg L^{-1}) at room temperature and at pH ~ 5.5. The solutions were shacked for different time in the range 1–300 min by using an orbital Stuart Scientific-Rotator Drive STR4 (Instruments s.r.l., Bernareggio, MI) apparatus and then filtered with filters WHATMAN (grade 520 a1/2). No precipitation occurs during the filtration. The equilibrium study was also carried out by means of batch experiments, placing a variable number of spheres (from 5 to 100) in 25 mL of solution containing $Cu(NO_3)_2$ or $Cd(NO_3)_2$ at the same concentration and at the same experimental conditions as for kinetic experiments. The solutions were shaken for 24 h by using the same orbital rotator apparatus and then filtered. The residual concentration of metal ions (Cu^{2+}, Cd^{2+} and Ca^{2+}) in the filtrates from both kinetic and equilibrium experiments were determined by Inductively Coupled Plasma Optical Emission Spectroscopy (ICP-OES) using a Perkin Elmer Model Optima 2100 spectrophotometer equipped with auto-sampler (model AS-90).

The hydrogen ion concentration of the solutions was checked by a potentiometer (Metrohm, Model 654) equipped with a combined ISE-H^+ glass electrode (Ross type 8102). Metal adsorption and/or calcium release at different contact times t (q_t, μmol bead^{-1}) were calculated considering:

$$q_t = \frac{V(C_0 - C_t)}{n_{\text{beads}}} \quad (1)$$

where V, C_0 and C_t are the volume and the metal concentration in solution expressed as μmol L^{-1} at $t = 0$ and $t = t$, respectively. All sorption experiments were carried out in duplicate and the averaged results are presented.

Computer programs

Linear and non linear regression data analysis as well as the determination of kinetic and equilibrium parameters were carried out using Origin Professional 8.6 software.

Results and discussion

Characterization of sorbent materials

The results obtained for the characterization of sorbent materials investigated are reported in Table 1.

From the results shown in Table 1 the following considerations can be made. The density values of the mixed polymers gel beads (Ca-AP_1, Ca-$AP_{1.5}$ and Ca-AP_2) are similar (differences are within the experimental errors). The lowest density value was observed for calcium alginate gel beads (Ca-A).

The mechanical resistance of gel beads containing pectin (0.21–0.22 N/bead) is a little higher than that of Ca-A gel beads (0.19 N/bead). This can be evidently attributed to the higher concentration of biopolymers which contributes to make more compact the structure of the gel due to the higher number of cross-linking among the molecules of alginate, pectate and Ca^{2+} ions.

Micrographs from Scanning Electron Microscopy (SEM) analysis show wrinkled surfaces of gel beads with creases and pores, especially in the presence of Cd^{2+} and Cu^{2+} ions. This morphology may be attributed to the shrinkage of the beads at higher metal concentrations [59]. As an example, SEM surface micrographs of Ca-A and Ca-AP_2 biopolymers before and after contacting with 200 mg L^{-1} copper(II) and cadmium(II) solutions for 48 h are depicted in Figs. 1 and 2, respectively.

All the sorbent materials investigated show analogous behavior. As pointed out before, SEM analysis was coupled with EDX measurements which allow to obtain semi-quantitative results on the metal content in the different dried gel beads.

EDX results, reported in Table 2, clearly show that calcium percentage in gel beads lowers when the calcium–biopolymer system is in contact with the solutions containing cadmium(II) or copper(II) ions. In particular, the loss of calcium ion from mixed Ca-AP_2 gel beads is comparable with the amount of copper(II) or cadmium(II) ions adsorbed by the sorbent material.

This evidence supports the hypothesis according to which ion exchange is the main mechanism governing the metal ions removal from aqueous solution by pectin–alginate biopolymers in gel phase.

Preliminary speciation analysis

The sorption process mechanism is based on the possibility that metal ions present in solution interact with carboxylic binding groups of polymer biomaterials to form stable species. In order to facilitate this interaction and to obtain the best metal sorption performance, the most suitable experimental conditions of solutions were fixed on the basis of a speciation analysis previously carried out on the Cu–Cd/alginate/pectate systems in aqueous solution [62–64]. The results of speciation analysis showed that a pH value of about 5.5 is the most appropriate one to avoid or minimize the hydrolysis of metal ions under investigation as well as the protonation of biopolymers. Moreover, at this pH, fairly stable metal complex species are formed with alginate and pectate, as confirmed by the following formation constants values: $\log K_{\text{Cu-AA}} = 3.626$ and $\log K_{\text{Cd-AA}} = 3.072$ [63]; $\log K_{\text{Cu-Pect}} = 5.278$ and $\log K_{\text{Cd-Pect}} = 3.636$ [64] in $NaNO_3$, at $I = 0.1$ mol L^{-1} and $T = 25$ °C. As expected, copper(II) complex species formed with both alginate and pectate are more stable than the corresponding species of cadmium(II).

Kinetic study of cadmium(II) and copper(II) sorption and calcium(II) release by gel beads

Kinetics of Cd(II) and Cu(II) sorption onto the beads and Ca(II) released from alginate/pectate gel beads can be appropriately described by a pseudo second order rate law according to the following equation [61]:

$$\frac{dq_t}{dt} = k_2(q_e - q_t)^2 \quad (2)$$

where q_e and q_t are the values of the amount of metal ion (Cd^{2+} or Cu^{2+}) adsorbed (μmol bead^{-1}) at equilibrium and at different contact times (t), respectively; k_2 is the pseudo-second order rate coefficient (μmol^{-1} min^{-1} bead).

The integrated form of Eq. (2) for the boundary conditions ($t = 0$ to $t = t$ and $q_t = 0$ to $q_t = q_t$) is:

$$\frac{1}{q_e - q_t} = \frac{1}{q_e} + k_2 t \quad (2a)$$

that can be rearranged to obtain:

$$q_t = \frac{t}{1/k_2 q_e^2 + t/q_e} \quad (2b)$$

By fitting the experimental data to Eq. (2b), the second order rate constant (k_2) and q_e were determined. The values of both parameters for Cu(II) and Cd(II) sorption onto Ca-A, Ca-AP_1, Ca-$AP_{1.5}$ and Ca-AP_2 systems and the corresponding calcium release are reported in Tables 3 and 4. The plots of q_t as function of t for cadmium(II) and copper(II) sorption and calcium(II) release are

Table 1
Physico-chemical and mechanical properties of gel beads.

Properties	Gel beads			
	Ca-A	Ca-AP_1	Ca-$AP_{1.5}$	Ca-AP_2
Bead diameter (mm)	3.45 ± 0.05[a]	3.75 ± 0.06[a]	4.18 ± 0.05[a]	4.16 ± 0.04[a]
Bead density (g/mL)[b]	1.023 ± 0.003	1.031 ± 0.002	1.032 ± 0.002	1.035 ± 0.003
Dry weight of one bead (mg)	0.7 ± 0.1	0.9 ± 0.1	1.1 ± 0.1	1.3 ± 0.1
Water content (%)	97.3	97.2	95.4	95.3
Mechanical resistance (N/bead)	0.19 ± 0.02	0.22 ± 0.02	0.21 ± 0.02	0.21 ± 0.02

[a] ±Std. dev.

[b] Density of wet gel beads at $T = 20$ °C.

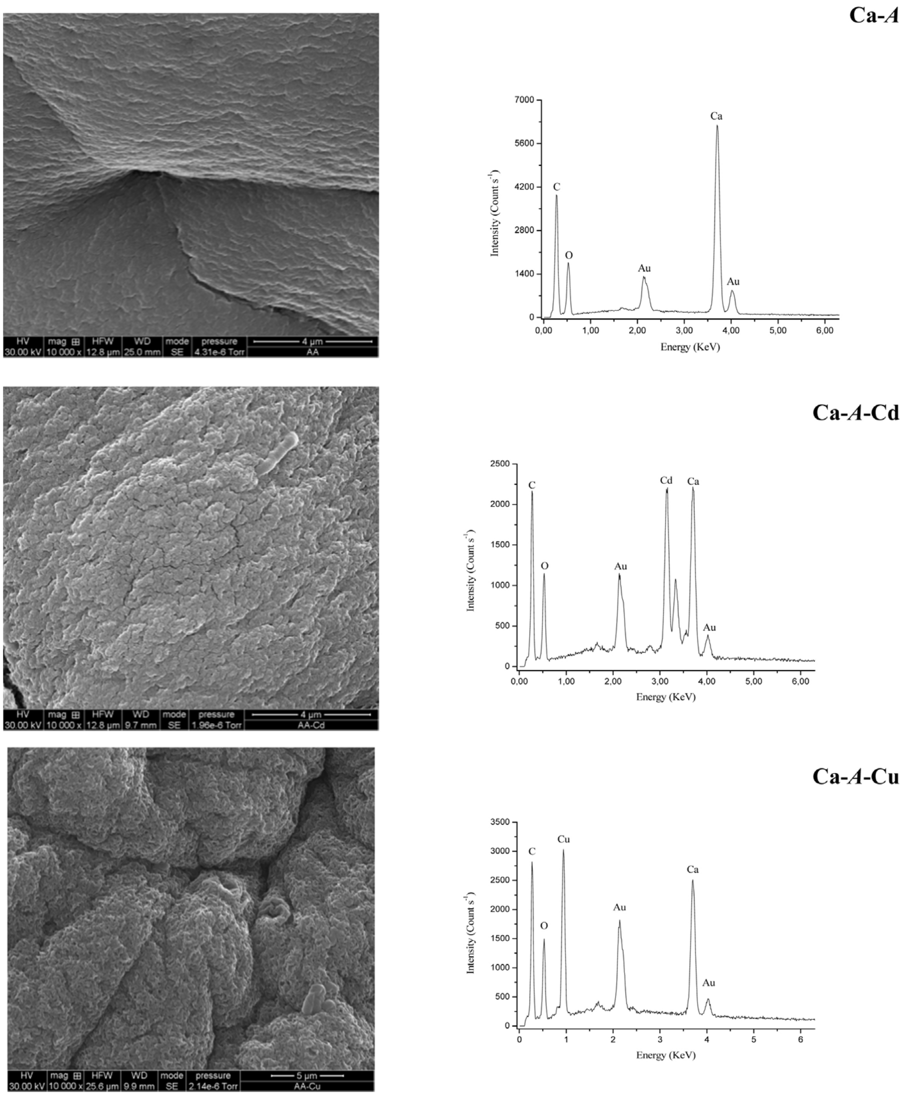

Fig. 1. Scanning electron microscopy images at 10000× of magnification and EDX spectra of Ca-A before and after sorption of Cd^{2+} or Cu^{2+} ions.

shown in Figs. 3 and 4 for all the systems investigated, including calcium alginate (Ca-*A*) polymer gel used here as a reference sorbent material. As expected, the removal ability of the simple calcium alginate gel beads is less than that of the mixed alginate/pectate gel beads, especially when the pectin concentration in mixed gel beads increases according to the following sorption ability trend: Ca-AP_1 < Ca-$AP_{1.5}$ < Ca-AP_2. The quite high values of correlation coefficients R^2 show that the pseudo-second order model fits satisfactorily to the experimental data for all the systems examined.

The higher amount of Cu^{2+} adsorbed as compared with Cd^{2+} (see the q_e values in Tables 3 and 4) is in accordance with the stability trend of complex species formed by alginate and pectate with the two metal ions in aqueous solution (see Section "Preliminary speciation analysis").

Since alginate and pectate are used as calcium salts in gel phase, it is presumable that the removal process of metal ions from solution occurs *via* ion exchange between calcium of gel beads and metal ions present in solution.

With the aim to check this hypothesis, the kinetics of the release of Ca^{2+} ion in solution by the different gel beads was also investigated, in the presence and in absence of Cu^{2+} and Cd^{2+} ions, under the same experimental conditions. The results of this investigation are shown in Figs. 3b and 4b (presence of Cu(II) and Cd(II) ions) and Fig. 5 (absence of Cu(II) and Cd(II) ions). The kinetic parameters are reported in Tables 3 and 4.

The amount of Ca^{2+} ion released by the alginate and hybrid alginate/pectate gel beads in distilled water is very low as confirmed by the values of q_e calculated: $q_{e\ \mathrm{ca}^{2+}\ \mathrm{release}} = 0.001 \pm 0.001,\ 0.008 \pm 0.001,\ 0.012 \pm 0.002$ and 0.016 ± 0.003 μmol bead^{-1} for *Ca-A*, *Ca-AP_1*, *Ca-$AP_{1.5}$* and *Ca-AP_2* gel beads, respectively.

The results obtained confirm the above hypothesis. Indeed, the amount of Ca^{2+} released by gel beads increases in the presence of metal ions (Cu^{2+} or Cd^{2+}) in solution; for example, the kinetic parameter q_e for the calcium release by Ca-AP_1 gel beads is: $q_{e\ \mathrm{release\ of\ ca}^{2+}} = 0.80$ and 0.008 μmol bead^{-1} in presence and in absence of Cu^{2+}, respectively.

In general, the amount of copper(II) or cadmium(II) adsorbed is slightly higher than the calcium(II) released by gel beads. This apparently anomalous behavior may be attributed to other factors, such as, for example, the presence of other calcium-free binding groups present in the alginate and pectate structure [65].

The low variation of pH (within ± 0.2 log units), monitored by potentiometry during the kinetic experiments, lets us to affirm that: (i) no hydrolysis of metal ions in solution occurs, and (ii) the release of Ca^{2+} from gel beads partially depends on the ion exchange with H^+ and, therefore, it must be mostly attributed to the ion exchange with metal ions present in solution.

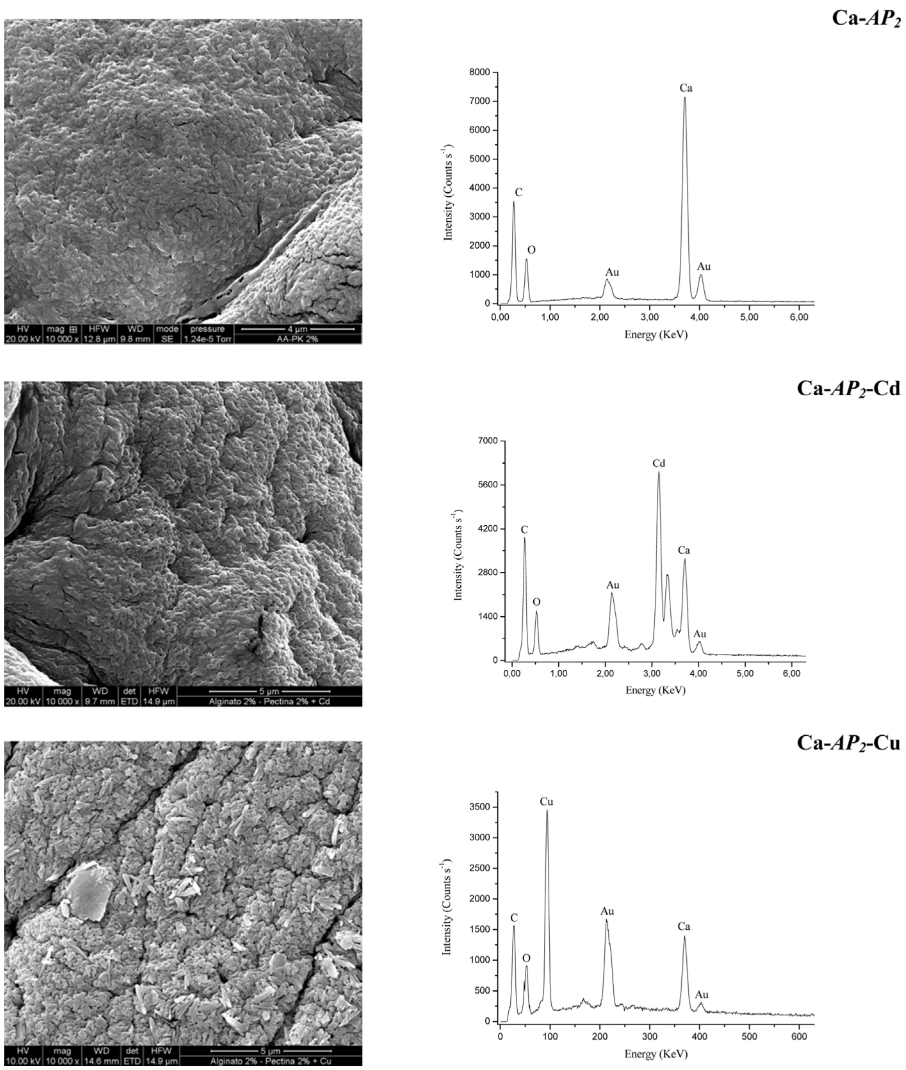

Fig. 2. Scanning electron microscopy images at 10000× of magnification and EDX spectra of Ca-AP_2 before and after sorption of Cd^{2+} or Cu^{2+} ions.

Isotherms for Cd^{2+} and Cu^{2+} sorption by gel beads

Equilibrium data were analyzed using Langmuir and Freundlich isotherm models. According to the Langmuir model, the sorption is assumed as a chemical process occurring on homogeneous binding sites of the sorbent material and is generally expressed by the following non-linear equation:

$$q_e = \frac{q_{\max} K_L C_e}{1 + K_L C_e} \qquad (3)$$

where q_e (μmol bead^{-1}) is the metal concentration adsorbed by gel beads at equilibrium; $q_{\max}$ (μmol bead^{-1}) represents the monolayer sorption capacity of the sorbent; K_L (L mg^{-1}) is the Langmuir constant that provides information on the sorption process free energy; C_e (mg L^{-1}) is the metal ion concentration in solution.

The Freundlich isotherm model is an empirical relationship based on the assumption that the sorption process takes place on the surface of sorbent by heterogeneous sites with different heat of sorption. The Freundlich isotherm model is expressed by the following exponential equation:

$$q_e = K_F C_e^{1/n} \qquad (4)$$

where K_F (μmol L mg^{-1} bead^{-1}) is the Freundlich constant related to the sorption capacity and $1/n$ is an empirical parameter correlated to the sorption intensity depending on the heterogeneity of sorbent material. The Langmuir and Freundlich isotherm plots for the sorption of Cu^{2+} and Cd^{2+} by Ca-*A*, Ca-AP_1, Ca-$AP_{1.5}$ and Ca-AP_2 are reported in Figs. 6 and 7. The values of parameters for Langmuir and Freundlich models are given in Table 5. From the plot of Fig. 6 and also considering the correlation coefficient values R^2, the Langmuir model seems to fit the equilibrium data slightly better than the Freundlich model.

In Fig. 8 the $q_{\max}$ values obtained for copper(II) and cadmium(II) sorption by using Langmuir model (Eq. (3)) are plotted *vs.* the percentage of pectin in gel beads. As can be seen, the sorption capacity of gel beads shows a linear increase when increasing the pectin percentage. According to the experimental conditions used

Table 2
Weight percentage (wt%) of elements in gel beads surface by semi-quantitative EDX analysis.

	C	O	Ca	Cd	Cu
Ca-*A*	33.08	14.92	51.99		
Ca-*A*/Cd	24.56	13.04	25.14	25.01	
Ca-*A*/Cu	28.61	15.16	25.47		30.76
Ca-AP_2	29.96	12.62	58.42		
Ca-AP_2/Cd	26.51	10.73	21.99	40.75	
Ca-AP_2/Cu	21.88	12.75	19.66		45.71

Table 3
Pseudo-second order kinetic parameters for Cu^{2+} sorption into and Ca^{2+} release from alginate and alginate/pectin gel beads at pH = 5.5 and at room temperature.

Sorbent	Parameters for Cu^{2+} sorption			Parameters for Ca^{2+} release		
	q_e[a]	k_2[b]	R^2	q_e[a]	k_2[b]	R^2
Ca-*A*	0.73 ± 0.02	0.66 ± 0.15	0.8666	0.64 ± 0.01	0.54 ± 0.08	0.9469
Ca-AP_1	0.84 ± 0.02	0.48 ± 0.08	0.9243	0.80 ± 0.02	0.26 ± 0.04	0.9539
Ca-$AP_{1.5}$	0.96 ± 0.02	0.35 ± 0.04	0.9669	0.84 ± 0.02	0.27 ± 0.04	0.9633
Ca-AP_2	1.03 ± 0.03	0.55 ± 0.11	0.8660	0.90 ± 0.02	0.28 ± 0.04	0.9595

[a] μmol bead^{-1}.
[b] μmol^{-1} min^{-1} bead.

Table 4
Pseudo-second order kinetic parameters for Cd^{2+} sorption into and Ca^{2+} release from alginate and alginate/pectin gel beads at pH = 5.5 and at room temperature.

Sorbent	Parameters for Cd^{2+} sorption			Parameters for Ca^{2+} release		
	q_e[a]	k_2[b]	R^2	q_e[a]	k_2[b]	R^2
Ca-*A*	0.63 ± 0.01	0.74 ± 0.09	0.9502	0.43 ± 0.01	1.05 ± 0.16	0.9365
Ca-AP_1	0.75 ± 0.02	0.46 ± 0.08	0.9229	0.76 ± 0.03	0.21 ± 0.04	0.9403
Ca-$AP_{1.5}$	0.82 ± 0.02	0.38 ± 0.07	0.9216	0.77 ± 0.02	0.22 ± 0.04	0.9450
Ca-AP_2	0.89 ± 0.02	0.36 ± 0.05	0.9549	0.79 ± 0.03	0.23 ± 0.04	0.9357

[a] μmol bead^{-1}.
[b] min^{-1} μmol^{-1} bead.

in this work, this relationship can be expressed by the equation:

$$q_{\max} = q_{\max(\text{Ca-}A)} + \gamma P_x \qquad (5)$$

where $q_{\max(\text{Ca-}A)}$ is the maximum sorption capacity exhibited by calcium alginate beads towards Cu^{2+} or Cd^{2+} ions; γ is an empirical parameter (equal to 0.549 ± 0.006 and 0.795 ± 0.003 for copper and cadmium, respectively) accounting for the correlation between sorption capacity and P_x is the percentage of pectin in gel beads.

Literature analysis and data comparisons

Relatively few studies have been carried out on cadmium and copper sorption by alginate and pectate gel only [48–53,59,66–72], *i.e.* in absence of other molecules or substances encapsulated inside or mixed. Results reported show much discrepancies owing to the different experimental conditions used, such as pH, initial metal concentration, size and dry weight of gel

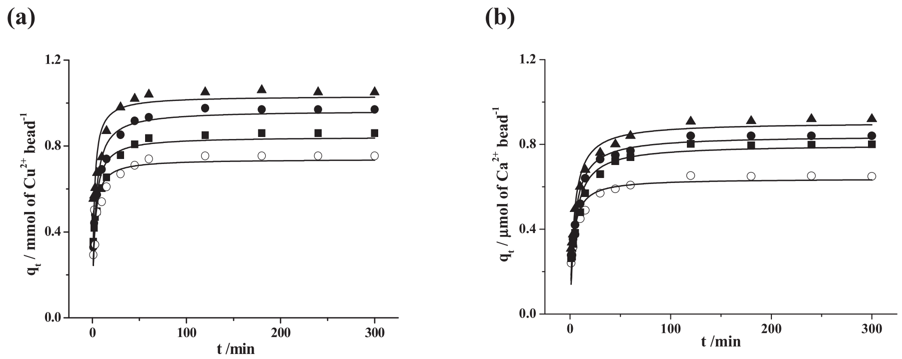

Fig. 3. Kinetics of Cu^{2+} sorption (3a) and Ca^{2+} release (3b) by alginate [Ca-*A* (○)] and alginate/pectate [Ca-AP_1 (■); Ca-$AP_{1.5}$ (●); Ca-AP_2 (▲)] gel beads at room temperature (initial pH = 5.5; initial metal concentration 200 mg L^{-1}).

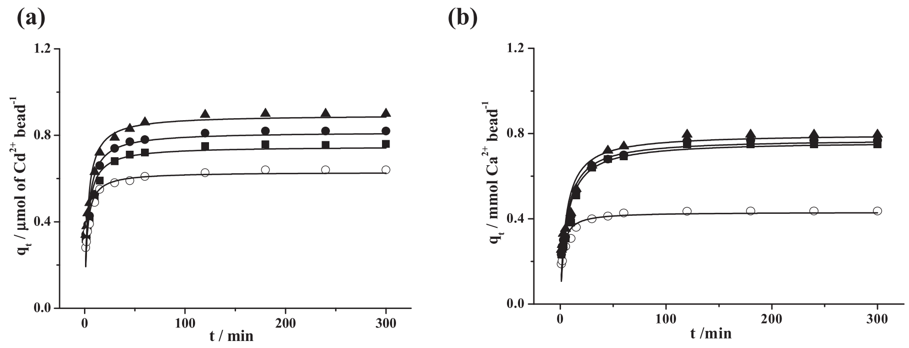

Fig. 4. Kinetics of Cd^{2+} sorption (4a) and Ca^{2+} release (4b) by alginate [Ca-*A* (○)] and alginate/pectate [Ca-AP_1 (■); Ca-$AP_{1.5}$ (●); Ca-AP_2 (▲)] gel beads at room temperature (pH = 5.5; initial metal concentration 200 mg L^{-1}).

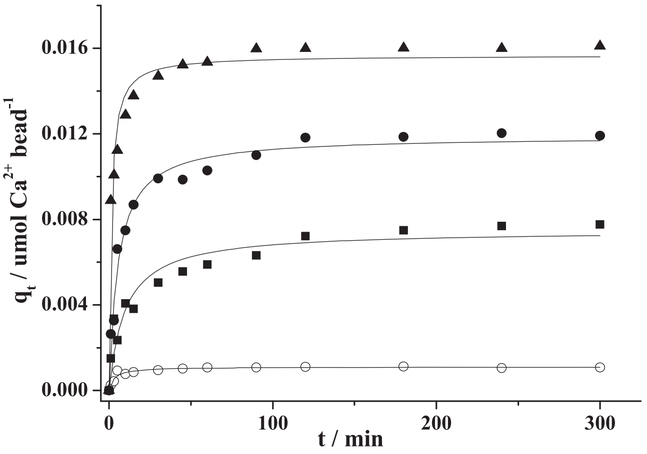

Fig. 5. Kinetics of Ca^{2+} release [µmol of Ca^{2+} released/bead] by alginate [Ca-*A* (○)] and alginate/pectate [Ca-AP_1 (■); Ca-$AP_{1.5}$ (●); Ca-AP_2 (▲)] gel beads in absence of Cu(II) and Cd(II) ions, at room temperature and pH = 5.5.

beads and the amount of sorbent biomaterial. The large heterogeneity of data reported in the literature is confirmed by the values of q_{max} (expressed as mmol g^{-1}) found by the different authors for copper and cadmium adsorption onto calcium alginate gel beads, ranging between 1.20 and 2.04 for copper [49,50,52,68,69] and between 0.21 and 2.09 for cadmium [50,52,66–68,70,71]. Moreover, no studies are reported in the literature on the sorption by mixed alginate/pectate gel material. Therefore, no direct comparison can be made between the literature data and the results obtained in this work using a new hybrid calcium alginate/pectate gel system. A rough comparison can be made only between the results on the sorption capacity of calcium alginate beads towards the two metal ions by considering, as far as possible, the similarity of experimental conditions and models used by the different authors. Papageorgiou et al. [52] reported a q_{max} = 2.09 and 1.50 mmol g^{-1} at pH 4.5 for sorption onto calcium alginate gel beads of Cd^{2+} and Cu^{2+} ions, respectively. Deze et al. [68] found, at the same pH and for the same metal ions, q_{max} = 1.53 and 1.78 mmol g^{-1}. Chen et al. [49] found for cadmium ion a q_{max} = 2.04 mmol g^{-1} at pH = 4. These results are the more close to those obtained in this work, *i.e.* q_{max} = 2.44 and 2.71 mmol g^{-1} for cadmium and copper sorption by calcium alginate gel beads, respectively, at pH = 5.5. In particular, a fairly good accordance can be noted between the q_{max} values found for cadmium ion. As pointed out before, the differences can be attributed to the different experimental conditions used, with particular reference to pH values.

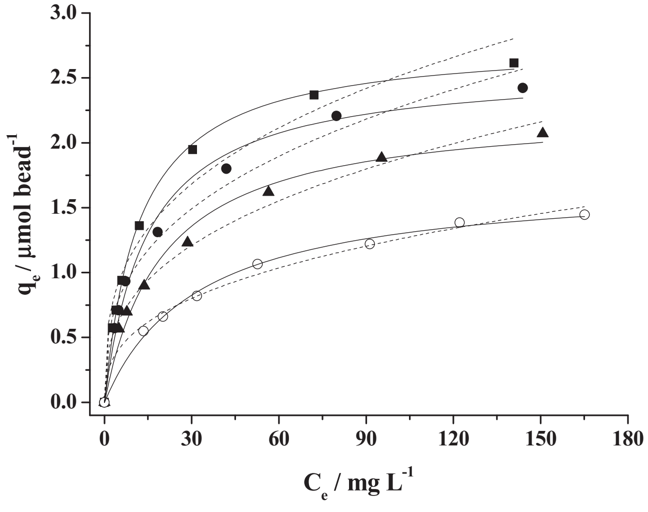

Fig. 6. Langmuir (full line) and Freundlich (dotted line) isotherm plots for the sorption of Cd^{2+} by Ca-*A* (○), Ca-AP_1 (▲), Ca-$AP_{1.5}$ (●), Ca-AP_2 (■) at room temperature (pH = 5.5; initial metal concentration 200 mg L^{-1}; contact time: 24 h).

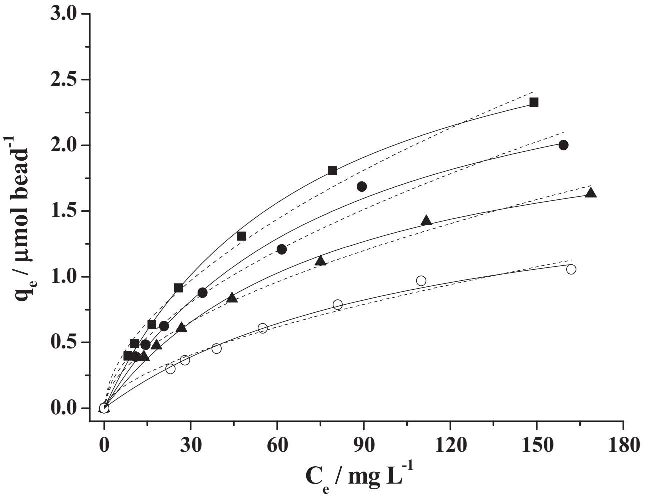

Fig. 7. Langmuir (full line) and Freundlich (dotted line) isotherm plots for the adsorption of Cu^{2+} by Ca-*A* (○), Ca-AP_1 (▲), Ca-$AP_{1.5}$ (●), Ca-AP_2 (■) at room temperature (pH = 5.5; initial metal concentration 200 mg L^{-1}; contact time: 24 h).

Table 5
Sorption isotherm parameters of Cadmium (II) and Copper(II) by alginate and alginate/pectate gel beads at room temperature.

Sorbent	Langmuir model		Freundlich model	
Cadmium(II)				
Ca-*A*	q_{max}[a]	1.71 ± 0.05[c]	K_F	0.23 ± 0.02[c]
	K_L[b]	0.031 ± 0.002	n	2.7 ± 0.2
	R^2	0.9958	R^2	0.96286
Ca-AP_1	q_{max}	2.27 ± 0.09	K_F	0.35 ± 0.03
	K_L[b]	0.049 ± 0.006	n	2.8 ± 0.1
	R^2	0.98819	R^2	0.98174
Ca-$AP_{1.5}$	q_{max}	2.58 ± 0.09	K_F	0.46 ± 0.05
	K_L	0.068 ± 0.001	n	2.9 ± 0.2
	R^2	0.98820	R^2	0.99020
Ca-AP_2	q_{max}	2.79 ± 0.04	K_F	0.55 ± 0.08
	K_L	0.083 ± 0.004	n	3.0 ± 0.3
	R^2	0.99796	R^2	0.98992
Copper(II)				
Ca-*A*	q_{max}	1.9 ± 0.1	K_F	0.05 ± 0.01
	K_L	0.009 ± 0.001	n	1.6 ± 0.1
	R^2	0.99335	R^2	0.97809
Ca-AP_1	q_{max}	2.39 ± 0.09	K_F	0.10 ± 0.01
	K_L	0.012 ± 0.001	n	1.82 ± 0.08
	R^2	0.99698	R^2	0.99326
Ca-$AP_{1.5}$	q_{max}	3.06 ± 0.19	K_F	0.11 ± 0.02
	K_L	0.012 ± 0.001	n	1.7 ± 0.1
	R^2	0.99227	R^2	0.98281
Ca-AP_2	q_{max}	3.4 ± 0.1	K_F	0.14 ± 0.02
	K_L	0.014 ± 0.001	n	1.76 ± 0.09
	R^2	0.99750	R^2	0.99068

[a] µmol $bead^{-1}$.
[b] L mg^{-1}.
[c] Std. dev.

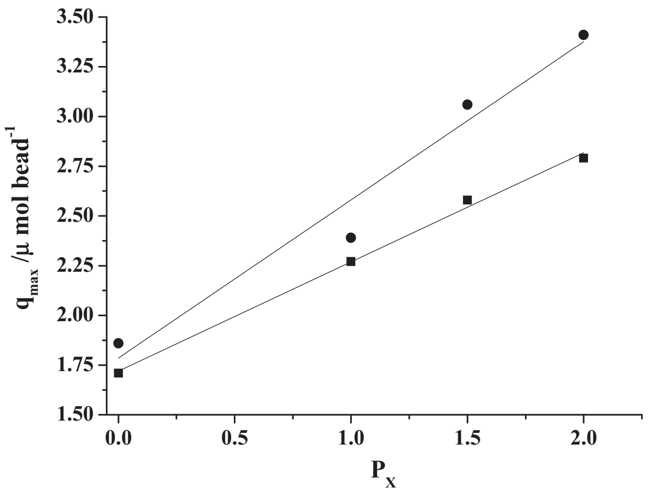

Fig. 8. Dependence of q_{max} [according to Eq. (3)] on pectin percentage for Cu^{2+} (●) and Cd^{2+} (■) sorption at room temperature and pH = 5.5.

Conclusions

New mixed alginate/pectate sorbent materials were used in gel phase for cadmium(II) and copper(II) removal from aqueous solutions. Physical and mechanical properties of these materials were characterized by different techniques, such as thermogravimetrical analysis and SEM–EDX.

The sorption process of Cd(II) and Cu(II) ions from solution by mixed alginate/pectate gel beads at different concentration ratios was evaluated on the basis of kinetic and equilibrium studies.

The results obtained from kinetic investigations show that: (i) the removal of cadmium(II) and copper(II) ions from the solution occurs prevalently by ion exchange with calcium(II) ion present in the gel beads and useful correlations were found between the amount of Cu^{2+} and/or Cd^{2+} absorbed and the Ca^{2+} released; (ii) the sorption ability of mixed alginate/pectin gel beads is higher in comparison with the calcium alginate polymer gel; (iii) the sorption process follows a pseudo second-order kinetic model and the sorption capacity increases with the increasing of pectin percentage in the mixed alginate/pectate gel system, according to the trend Ca-AP_2 > Ca-$AP_{1.5}$ > Ca-AP_1; (iv) the Langmuir isotherm model fits equilibrium data better than the Freundlich model.

The results of preliminary speciation analysis [62–64] allowed us to assess the pH value of about 5.5 as the most appropriate one (i) to avoid or minimize the hydrolysis of metal ions under investigation as well as the protonation of biopolymers, (ii) to favor the formation of stable metal–biopolymer complex species. The higher stability of copper species in comparison with cadmium species, as shown by aqueous speciation analysis, is confirmed also by the sorption trend (Cu > Cd) obtained using the biopolymers in gel phase.

A literature data analysis was made on the cadmium and copper sorption by calcium alginate and a comparison of results obtained in this work was also given. No results are reported in the literature on the metal sorption by the mixed alginate/pectin gel system investigated in this work.

The results obtained from this study show that the hybrid alginate/pectate system in gel phase, never before tested, can be considered a good material to be used as low cost and environmental friendly sorbent for cadmium(II) and copper(II) removal from aqueous solution.

Acknowledgments

The authors S.C., A.G., G.L., A.P., and D.P. carried out this work thanks to a grant from the project "Development of innovative technologies for the treatment of fluid wastes from shipping activities and for marine environment protection" (PON02_00153_2849085 "Ricerca e competitività 2007–2013, asse 1").

References

[1] J. Wase, C. Forster, Biosorbents for Metal Ions, Taylor & Francis, Padstow, GB, 1997
[2] B.W. Atkinsons, F. Bux, H.C. Kasan, Considerations for application of biosorption technology to remediate metal contaminated industrial effluents, Water SA 24 (1998) 129–135.
[3] B. Volesky, Sorption and Biosorption, BV Sorbex Inc., Montreal, St. Lambert, Quebec, Canada, 2003.
[4] G.M. Gadd, Biosorption: critical review of scientific rationale, environmental importance and significance for pollution treatment, J. Chem. Technol. Biotechnol. 84 (2009) 13–28.
[5] M. Gavrilescu, Removal of heavy metals from the environment by biosorption, Eng. Life Sci. 4 (2004) 219–232.
[6] A. Singh, C.K. Ramesh, O.P. Ward, Advances in Applied Bioremediation, Springer Verlag, Berlin Heidelberg, 2009.
[7] J. Wang, C. Chen, Biosorbents for heavy metals removal and their future, Biotechnol. Adv. 27 (2009) 195–226.
[8] Y.-F. Zhou, R.J. Haynes, Sorption of heavy metals by inorganic and organic components of solid wastes: significance to use of wastes as low-cost adsorbents and immobilizing agents, Crit. Rev. Environ. Sci. Technol. 40 (2010) 909–977.
[9] F. Fu, Q. Wang, Removal of heavy metal ions from wastewaters: a review, J. Environ. Manage. 92 (2011) 407–418.
[10] T.A. Kurniawan, G.Y.S. Chan, W.-H. Lo, S. Babel, Physico-chemical treatment techniques for wastewater laden with heavy metals, Chem. Eng. J. 118 (2006) 83–98.
[11] K. Juttner, U. Galla, H. Schmieder, Electrochemical approaches to environmental problems in the process industry, Electrochim. Acta 45 (2000) 2575–2594.
[12] A.I. Zouboulis, K.A. Matis, Removal of metal ions from dilute solutions by sorptive flotation, Crit. Rev. Environ. Sci. Technol. 27 (1997) 195–235.
[13] D. Zamboulis, E.N. Peleka, N.K. Lazaridis, K.A. Matis, Metal ion separation and recovery from environmental sources using various flotation and sorption techniques, J. Chem. Technol. Biotechnol. 86 (2011) 335–344.
[14] A.E. Lewis, Review of metal sulphide precipitation, Hydrometallurgy 104 (2010) 222–234.
[15] A. Kapoor, T. Viraraghavan, Fungal biosorption – an alternative treatment option for heavy metal bearing wastewaters: a review, Bioresour. Technol. 53 (1995) 195–206.
[16] R. Gupta, P. Ahuja, S. Khan, R.K. Saxena, H. Mohapatra, Microbial biosorbents: meeting challenges of heavy metal pollution in aqueous solutions, Curr. Sci. India 78 (2000) 967–973.
[17] Y. Sag, Biosorption of heavy metals by fungal biomass and modeling of fungal biosorption: a review, Sep. Purif. Rev. 30 (2001) 1–48.
[18] R. Dhankhar, A. Hooda, Fungal biosorption – an alternative to meet the challenges of heavy metal pollution in aqueous solutions, Environ. Technol. 32 (2011) 467–491.
[19] A.A. Hamdy, Biosorption of heavy metals by marine algae, Curr. Microbiol. 41 (2000) 232–238.
[20] Y. Liu, Q. Cao, F. Luo, J. Chen, Biosorption of Cd^{2+}, Cu^{2+}, Ni^{2+} and Zn^{2+} ions from aqueous solutions by pretreated biomass of brown algae, J. Hazard. Mater. 163 (2009) 931–938.
[21] S. Ahmady-Asbchin, Y. Andres, C. Gerente, P. Le Cloirec, Natural seaweed waste as sorbent for heavy metal removal from solution, Environ. Technol. 30 (2009) 755–762.
[22] C.J. Tien, Biosorption of metal ions by freshwater algae with different surface characteristics, Process Biochem. 38 (2002) 605–613.
[23] T.A. Davis, B. Volesky, A. Mucci, A review of the biochemistry of heavy metal biosorption by brown algae, Water Res. 37 (2003) 4311–4330.
[24] M. Drastik, F. Novak, J. Kucerik, Origin of heat-induced structural changes in dissolved organic matter, Chemosphere 90 (2013) 789–795.
[25] A. Bhatnagar, M. Sillanpää, Utilization of agro-industrial and municipal waste materials as potential adsorbents for water treatment – a review, Chem. Eng. J. 157 (2010) 277–296.
[26] V.M. Nurchi, I. Villaescusa, Agricultural biomasses as sorbents of some trace metals, Coord. Chem. Rev. 252 (2008) 1178–1188.
[27] N. Miralles, M. Martinez, A. Florido, I. Casas, N. Fiol, I. Villaescusa, Grape stalks waste as low cost biosorbents: an alternative for metal removal from aqueous solutions, Solvent Extr. Ion. Exch. 26 (2008) 261–270.
[28] D. Sud, G. Mahajan, M.P. Kaur, Agricultural waste material as potential adsorbent for sequestering heavy metal ions from aqueous solutions – a review, Bioresour. Technol. 99 (2008) 6017–6027.
[29] U. Kumar, M. Bandyopadhyay, Sorption of cadmium from aqueous solution using pretreated rice husk, Bioresour. Technol. 97 (2006) 104–109.
[30] S. Schiewer, S.B. Patil, Pectin-rich fruit wastes as biosorbents for heavy metal removal: equilibrium and kinetics, Bioresour. Technol. 99 (2008) 1896–1903.

[31] A. Bhatnagar, M. Sillanpaa, Applications of chitin- and chitosan-derivatives for the detoxification of water and wastewater – a short review, Adv. Colloid Interf. Sci. 152 (2009) 26–38.

[32] Y.S. Ho, G. McKay, D.A.J. Wase, C.F. Forster, Study of the sorption of divalent metal ions on to peat, Adsorpt. Sci. Technol. 18 (2000) 639–650.

[33] F. Arias, T. Kanti Sen, Removal of zinc metal ion (Zn^{2+}) from its aqueous solution by kaolin clay mineral: a kinetic and equilibrium study, Colloid Surf. A 348 (2009) 100–108.

[34] G. Cavallaro, A. Gianguzza, G. Lazzara, S. Milioto, D. Piazzese, Alginate gel beads filled with halloysite nanotubes, Appl. Clay Sci. 72 (2013) 132–137.

[35] S.E. Bailey, T.J. Olin, M. Bricka, D.D. Adrian, A review of potentially low-cost adsorbents for heavy metals, Water Res. 33 (1999) 2469–2479.

[36] S. Babel, T.A. Kurniawan, Low-cost adsorbents for heavy metals uptake from contaminated water: a review, J. Hazard. Mater. 97 (2003) 219–243.

[37] V.O. Arief, K. Trilestari, J. Sunarso, N. Indraswati, S. Ismadji, Recent progress on biosorption of heavy metals from liquids using low cost biosorbents: characterization, biosorption parameters and mechanism studies, Clean Soil Air Water 36 (2008) 937–962.

[38] V.M. Nurchi, G. Crisponi, I. Villaescusa, Chemical equilibria in wastewaters during toxic metal ion removal by agricultural biomass, Coord. Chem. Rev. 254 (2010) 2181–2192.

[39] V.M. Nurchi, I. Villaescusa, Sorption of toxic metal ions by solid sorbents: a predictive speciation approach based on complex formation constants in aqueous solution, Coord. Chem. Rev. 256 (2011) 212–221.

[40] I. Twardowska, J. Kyziol, Sorption of metals onto natural organic matter as a function of complexation and adsorbent–adsorbate contact mode, Environ. Int. 28 (2003) 783–791.

[41] P. Harel, L. Mignot, J.P. Sauvage, G.A. Junter, Cadmium removal from dilute aqueous solution by gel beads of sugar beet pectin, Ind. Crop. Prod. 7 (1998) 239–247.

[42] M.A. Hashim, K.H. Chu, Biosorption of cadmium by brown, green, and red seaweeds, Chem. Eng. J. 97 (2004) 249–255.

[43] P. Lodeiro, J.L. Barriada, R. Herrero, M.E. Sastre de Vicente, The marine macroalga *Cystoseira baccata* as biosorbent for cadmium(II) and lead(II) removal: kinetic and equilibrium studies, Environ. Pollut. 142 (2006) 264–273.

[44] D. Lu, Q. Cao, X. Li, X. Cao, F. Luo, W. Shao, Kinetics and equilibrium of Cu(II) adsorption onto chemically modified orange peel cellulose biosorbents, Hydrometallurgy 95 (2009) 145–152.

[45] Y.N. Mata, M.L. Blazquez, A. Ballester, F. Gonzalez, J.A. Munoz, Optimization of the continuous biosorption of copper with sugar-beet pectin gels, J. Environ. Manage. 90 (2009) 1737–1743.

[46] V.J.P. Vilar, C.M.S. Botelho, J.P.S. Pinheiro, R.F. Domingos, R.A.R. Boaventura, Copper removal by algal biomass: biosorbents characterization and equilibrium modelling, J. Hazard. Mater. 163 (2009) 1113–1122.

[47] J.L. Zhou, P.L. Huang, R.G. Lin, Sorption and desorption of Cu and Cd by macroalgae and microalgae, Environ. Pollut. 101 (1998) 67–75.

[48] J. Chen, F. Tendeyong, S. Yiacoumi, Equilibrium and kinetic studies of copper ion uptake by calcium alginate, Environ. Sci. Technol. 31 (1997) 1433–1439.

[49] J.P. Chen, L. Wang, Characterization of a Ca-alginate based ion-exchange resin and its applications in lead, copper, and zinc removal, Sep. Sci. Technol. 36 (2001) 3617–3637.

[50] Y.N. Mata, M.L. Blazquez, A. Ballester, F. Gonzalez, J.A. Munoz, Biosorption of cadmium, lead and copper with calcium alginate xerogels and immobilized *Fucus vesiculosus*, J. Hazard. Mater. 163 (2009) 555–562.

[51] S.K. Papageorgiou, F.K. Katsaros, E.P. Kouvelos, N.K. Kanellopoulos, Prediction of binary adsorption isotherms of Cu^{2+}, Cd^{2+} and Pb^{2+} on calcium alginate beads from single adsorption data, J. Hazard. Mater. 162 (2009) 1347–1354.

[52] S.K. Papageorgiou, E.P. Kouvelos, F.K. Katsaros, Calcium alginate beads from *Laminaria digitata* for the removal of Cu^{2+} and Cd^{2+} from dilute aqueous metal solutions, Desalination 224 (2008) 293–306.

[53] L. Singh, A.R. Pavankumar, R. Lakshmanan, G.K. Rajarao, Effective removal of Cu^{2+} ions from aqueous medium using alginate as biosorbent, Ecol. Eng. 38 (2012) 119–124.

[54] T.A. Davis, F. Llanes, B. Volesky, G. Diaz-Pulido, L. McCook, A. Mucci, A ^{1}H-NMR study of Na-alginates extracted from *Sargassum* spp. in relation to metal biosorption, Appl. Biochem. Biotechnol. 110 (2003) 75–90.

[55] T.A. Davis, F. Llanes, B. Volesky, A. Mucci, Metal selectivity of *Sargassum* spp. and their alginates in relation to their α-L-guluronic acid content and conformation, Environ. Sci. Technol. 37 (2003) 261–267.

[56] Alginate Products for Scientific Water Control, Kelco, San Diego, CA, 1987.

[57] R.H. Walter, The Chemistry and Technology of Pectin (Food Science and Technology), 1st ed., Academic Press, San Diego, CA, 1991.

[58] M.A.V. Axelos, J.F. Thibault, The chemistry of low-methoxyl pectin gelation, in: R.H. Walter (Ed.), The Chemistry and Technology of Pectin (Food Science and Technology), Academic Press Inc., San Diego, CA, 1991, pp. 109–118.

[59] T. Gotoh, K. Matsushima, K. Kikuchi, Adsorption of Cu and Mn on covalently cross-linked alginate gel beads, Chemosphere 55 (2004) 57–64.

[60] S. Cataldo, A. Gianguzza, A. Pettignano, I. Villaescusa, Mercury(II) removal from aqueous solution by sorption onto alginate, pectate and polygalacturonate calcium gel beads: a kinetic and speciation based equilibrium study, React. Funct. Polym. 73 (2013) 207–217.

[61] Y.S. Ho, A.E. Ofomajia, Pseudo-second order model for lead ion sorption from aqueous solutions onto palm kernel fiber, J. Hazard. Mater. 129 (2006) 137–142.

[62] C. De Stefano, A. Gianguzza, D. Piazzese, S. Sammartano, Modelling of proton and metal exchange in the alginate biopolymer, Anal. Bioanal. Chem. 383 (2005) 587–596.

[63] C. De Stefano, A. Gianguzza, A. Pettignano, S. Sammartano, S. Sciarrino, On the complexation of Cu(II) and Cd(II) with polycarboxyl ligands: potentiometric studies with ISE-H^{+}, ISE-Cu^{2+} and ISE-Cd^{2+}, J. Chem. Eng. Data 55 (2010) 714–722.

[64] S. Cataldo, A. Gianguzza, A. Pettignano, D. Piazzese, S. Sammartano, Complex formation of copper(II) and cadmium(II) with pectin and polygalacturonic acid in aqueous solution: an ISE-H^{+} and ISE-Me^{2+} electrochemical study, Int. J. Electrochem. Sci. 7 (2012) 6722–6737.

[65] N. Fiol, C. Escudero, J. Poch, I. Villaescusa, Preliminary studies on Cr(VI) removal from aqueous solution using grape stalk wastes encapsulated in calcium alginate beads in a packed bed up-flow column, React. Funct. Polym. 66 (2006) 795–807.

[66] M.Y. Arica, Y. Kacar, O. Genc, Entrapment of white-rot fungus *Trametes versicolor* in Ca-alginate beads: preparation and biosorption kinetic analysis for cadmium removal from an aqueous solution, Bioresour. Technol. 80 (2001) 121–129.

[67] G. Bayramoglu, A. Denizli, S. Bektas, M. Yakup Arica, Entrapment of *Lentinus sajor-caju* into Ca-alginate gel beads for removal of Cd(II) ions from aqueous solution: preparation and biosorption kinetics analysis, Microchem. J. 72 (2002) 63–76.

[68] E.G. Deze, S.K. Papageorgiou, E.P. Favvas, F.K. Katsaros, Porous alginate aerogel beads for effective and rapid heavy metal sorption from aqueous solutions: Effect of porosity in Cu^{2+} and Cd^{2+} ion sorption, Chem. Eng. J. 209 (2012) 537–546.

[69] O. Guven, N. Ceyhan, E. Manav, Utilization in alginate beads for Cu(II) and Ni(II) adsorption of an exopolysaccharide produced by *Chryseomonas luteola* TEM05, World J. Microbiol. Biotechnol. 21 (2005) 163–167.

[70] M. Jain, V.K. Garg, K. Kadirvelu, Cadmium(II) sorption and desorption in a fixed bed column using sunflower waste carbon calcium-alginate beads, Bioresour. Technol. 129 (2013) 242–248.

[71] Y. Kacar, C. Arpa, S. Tan, A. Denizli, O. Genc, M.Y. Arica, Biosorption of Hg(II) and Cd(II) from aqueous solutions: comparison of biosorptive capacity of alginate and immobilized live and heat inactivated *Phanerochaete chrysosporium*, Process Biochem. 37 (2002) 601–610.

[72] F. Veglio, A. Esposito, A.P. Reverberi, Copper adsorption on calcium alginate beads: equilibrium pH-related models, Hydrometallurgy 65 (2002) 43–57.

Attached VII

Polymer Degradation and Stability 98 (2013) 2529–2536

Contents lists available at ScienceDirect

Polymer Degradation and Stability

journal homepage: www.elsevier.com/locate/polydegstab

Sustainable nanocomposites based on halloysite nanotubes and pectin/polyethylene glycol blend

Giuseppe Cavallaro, Giuseppe Lazzara*, Stefana Milioto

Department of Physics and Chemistry, Università degli Studi di Palermo, Viale delle Scienze, Pad. 17, 90128 Palermo, Italy

ARTICLE INFO

Article history:
Received 25 July 2013
Received in revised form
6 September 2013
Accepted 15 September 2013
Available online 25 September 2013

Keywords:
Thermal stability
TGA
Halloysite
Nanocomposite

ABSTRACT

This study was focused on the preparation and characterization of biofilms based on pectin/polyethylene glycol 20000 (PEG) blend and halloysite nanotubes (HNTs). The obtained blends loaded with a natural nanoclay are proposed as sustainable alternative to the polymers produced from non-renewable resources such as fossil fuels. Properties of technological interest have been monitored and they were correlated to the structural features of the nanocomposites. It turned out that the wettability of the films can be tuned by changing the composition and the distribution of HNTs into the material as well as the surface roughness. The tensile properties of the blend are enhanced by the presence of the nanoclays. The PEG crystallinity is reduced by the nanoparticles and preserved if a certain amount of pectin is added.

This work represents a starting point to develop new green composite material, which can be used for purposes such as in packaging, by employing the strategy of adding plasticizers and fillers within a full biocompatible approach.

1. Introduction

The largely used petroleum based plastics in several fields, such as in packaging, generates a relevant environmental impact in urban areas because of their non degradability. The disposal of plastic wastes by incineration produces an increase of carbon dioxide and, in some cases, toxic products which contribute to the global warming and the city pollution.

To the light of this situation, nowadays there is a growing interest on the development of biodegradable materials, sustainable alternative to the plastics produced from fossil fuel. Researchers have focused their attention on biopolymers and clay nanoparticles as renewable resources to process innovative green materials, such as polymer blends and bionanocomposites.

Pectin is a biodegradable polymer which is used to develop smart green materials useful for specific purposes. Blend based on pectin and chitosan may be used as carrier of pharmaceutical products [1]. Biofilms based on pectin and starch can be potentially employed in the food conservation because of their good mechanical properties [2] and oxygen barrier capability [3]. Gelatin-pectin films showed improved tensile characteristics and water resistance than the pristine polymers [4].

Polyethylene glycol (PEG) is a biocompatible, nontoxic polymer with good water solubility. It is an efficient plasticizer for biopolymers and nanocomposites. The mechanical properties of chitosan were improved by the addition of an appropriate amount of PEG [5,6]. The PEG content (C_{PEG}) is crucial to determine the effectiveness of the plasticization; a decrease of the glass transition temperature (T_g) of Poly(lactic acid) (PLA) was observed in polymer blends with $C_{PEG} = 20$ wt% [7]. PLA/PEG blends with C_{PEG} up to 30 wt% showed a decrease of the elongation at the break point [8] and an increase of T_g [9] because of the phase separation of PEG in the composite system.

Filling a polymer blend with clay nanoparticles represents an alternative route to develop new nanomaterials with unique properties from the physico-chemical view point [10–12].

Among the clay nanoparticles, halloysite nanotubes (HNTs) are newly promising filler. The size of HNTs is rather polydisperse ranging between 0.1 and 2 μm while the outer and inner diameters are ca. 30–50 nm and 1–30 nm, respectively [13]. The biocompatibility of HNTs makes these nanoparticles appropriate to develop composite materials with appealing perspective in several applications, such as biotechnology [14–17], water decontamination [18,19], anticorrosive coatings [20,21] and packaging [22,23]. Composite materials with humidity control ability were prepared by using HNTs as filler [24].

---

* Corresponding author. Tel.: +39 3284279554.
E-mail address: g.lazzara@unipa.it (G. Lazzara).

0141-3910/$ – see front matter © 2013 Elsevier Ltd. All rights reserved.
http://dx.doi.org/10.1016/j.polymdegradstab.2013.09.012

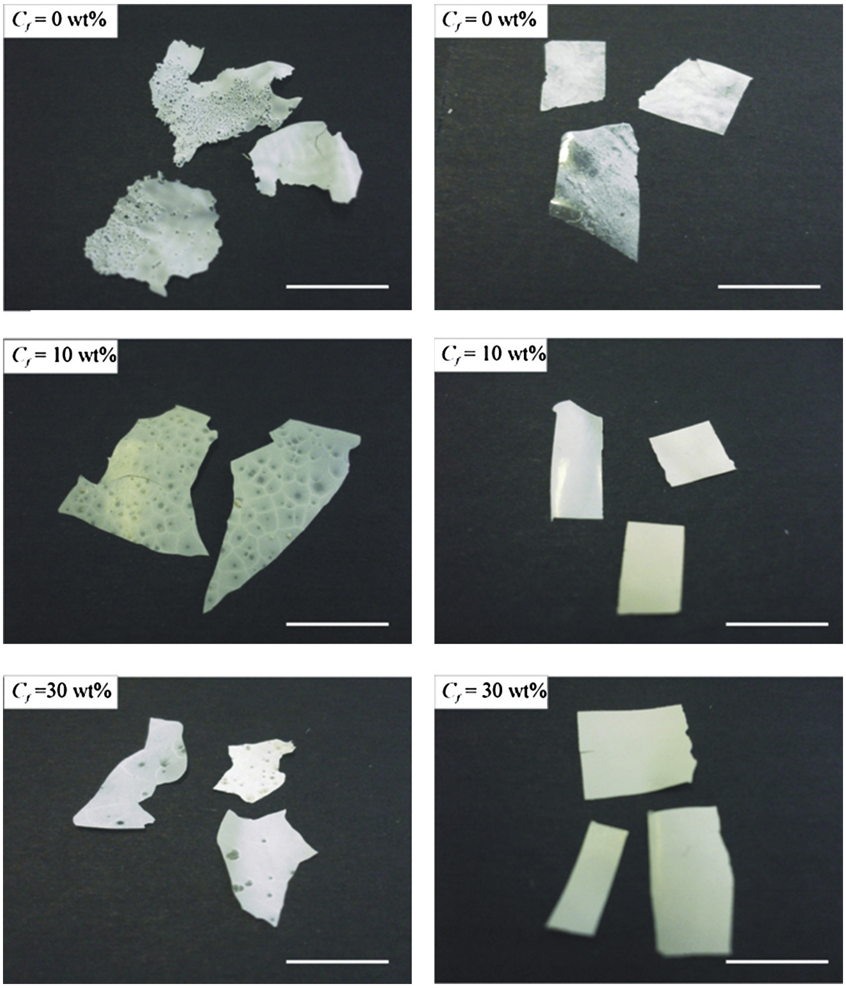

Fig. 1. Photos of bionanocomposites at variable C_f for $R_{pp} = 1$ (on the left) and $R_{pp} = 4$ (on the right). The bar is 10 mm.

Literature reports that the addition of HNTs prevents the cracking in the drying latex films [25]. Filling pectins with HNTs caused an improvement of the thermal and the mechanical properties in a large clay loading regime. [23] The hydroxypropylcellulose/HNTs showed an enhancement of the polymer degradation temperature only for small nanoclay concentration, while the peculiar sandwich-like structure observed at the high filler loading caused a thermal destabilization [22]. It was observed [26] that PEG/HNTs is thermally more stable than the pristine polymer in the low filler regime where the nanomaterial presents a compact morphology, while the opposite thermal behavior occurred over the high HNTs loading region because of the more open structure.

Furthermore, it is known that the physical properties of blend polymers [27] and nanocomposites [26,28] depend on their supramolecular morphology that is controlled by the crystallization process in melt processing for crystalline and semicrystalline polymers. In many cases the nucleation and the overall crystallization may be enhanced by the presence of nanofillers which act as a nucleating agent [28]. Nevertheless, it was found that for plasticized PEG/PLA/cloisite nanocomposites [29] and for the PEG/halloysite nanotubes (HNTs) nanocomposites [26] the nanoclay did not play such a role.

In this work, we prepared blend films based on pectin and PEG 20000 as precursors of new plasticized bionanocomposites containing also HNTs. All biofilms were extensively investigated from the physico-chemical view point by determining the thermal and mechanical properties, the wettability and the water uptake behavior. The morphological study was crucial to explain the nanomaterial features.

The acquired knowledge represents a basic point for designing new hybrid sustainable materials.

2. Experimental

2.1. Materials

Pectin (degree of methyl esterification, 24%, Mw = 30–100 kg mol^{-1}), halloysite nanotubes ($Al_2Si_2O_5(OH)_4 \cdot 2H_2O$, HNTs) are from Aldrich. Polyethylene glycol (PEG) 20,000 g mol^{-1} is from Fluka. All the materials were used without further purification. Water from reverse osmosis (Elga model Option 3) with a specific resistivity greater than 10^5 Ω m was used.

Table 1
The water contact angle at $\tau = 0$ for pectin, PEG 20000 and the pectin/PEG 20000 blend ($R_{pp} = 4$).

	θ_i (°)
Pectin[a]	75 ± 1
PEG 20000	28 ± 1
Pectin/PEG 20000 ($R_{pp} = 4$)	80 ± 2

[a] From Ref. [22].

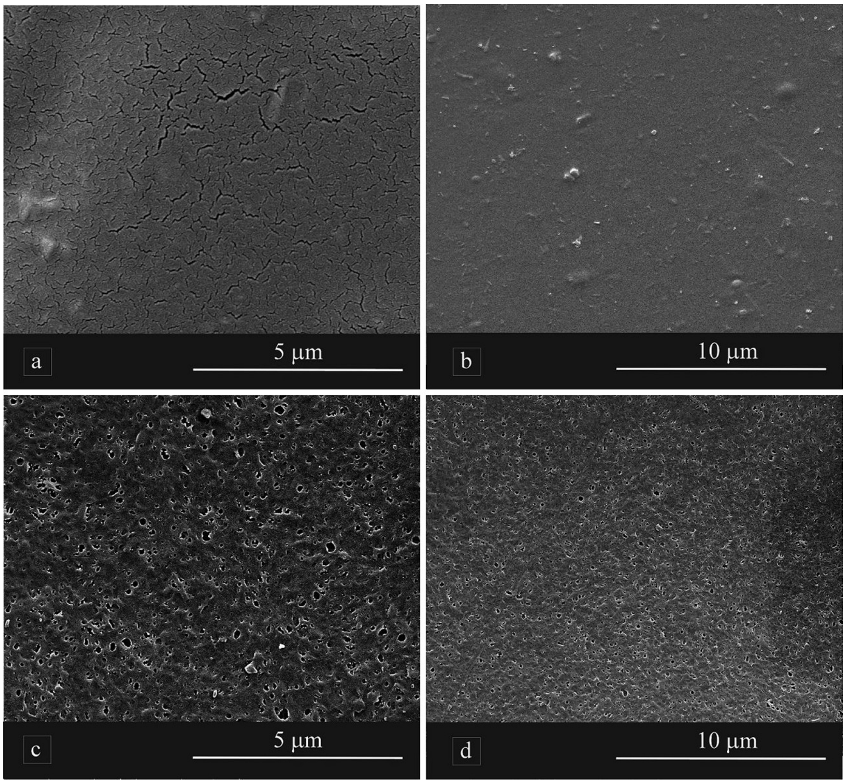

Fig. 2. Scanning electron microscopy images for surface of pristine pectin (a,b) and pectin/PEG 20000 blend with $R_{pp} = 4$ (c,d).

2.2. *Preparation of bionanocomposites*

We prepared a 2 wt % aqueous pectin solution under stirring at 70 °C. Then, an appropriate amount of plasticizer (PEG 20000) and nanofiller (HNTs) were added to the pectin solution and kept under stirring over night. The well dispersed aqueous mixture was poured into glass Petri dishes under vacuum at 35 °C to evaporate water until weight was constant and to obtain biofilms with a thickness of ca. 60 μm. We selected the weight ratio pectin/PEG 20000 (R_{pp}) values of 1 and 4. The composition of nanofiller (C_f) expressed as weight percent (grams of HNTs/100 g of plasticized nanocomposite) was systematically varied.

The prepared bionanocomposites evidenced clear macroscopic differences. As Fig. 1 shows, the nanomaterials with $R_{pp} = 1$ appear fragile and with several voids, while those with $R_{pp} = 4$ exhibit compact mechanical features.

2.3. *Methods*

2.3.1. *Contact angle measurements*

Contact angle studies were performed by means of an optical contact angle apparatus (OCA 20, Data Physics Instruments) equipped with a video measuring system having a high-resolution CCD camera and a high-performance digitizing adapter. SCA 20 software (Data Physics Instruments) was used for data acquisition. Rectangular (5 cm × 2 cm) films were fixed on top of a plane solid support and kept flat throughout the analysis. The contact angle (θ) of water in air was measured by the sessile drop method by gently placing a droplet of 6 ± 0.5 μL onto the surface of the film. Temperature was set at 25.0 ± 0.1 °C for the support and the injecting syringe as well. Images were collected 25 times per second, starting from the deposition of the drop to 60 s. The evolution of θ, the volume (V) and the surface area (A) of droplet was monitored using a software-assisted image-processing procedure. A minimum of 5 droplets were examined for each film sample. Only the biofilms with $R_{pp} = 4$ were analyzed.

2.3.2. *Scanning electron microscopy*

The morphology of nanocomposites was studied using a microscope ESEM FEI QUANTA 200F. Before each experiment, the surface of the sample was coated with gold in argon by means of an Edwards Sputter Coater S150A to avoid charging under electron

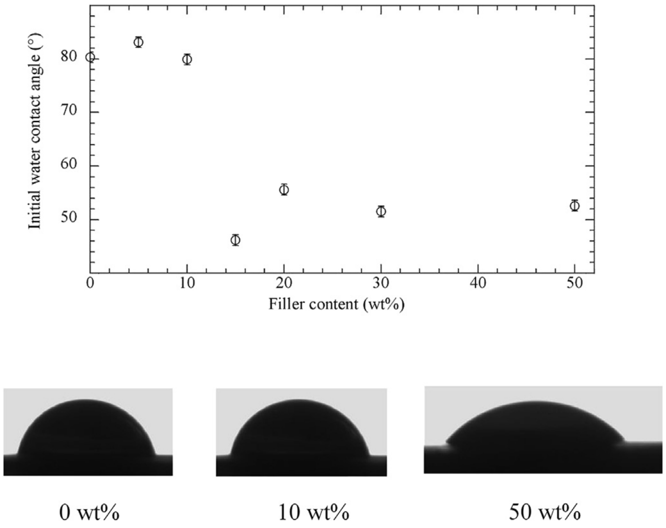

Fig. 3. Top: the water contact angle extrapolated at $\tau = 0$ as a function of the filler content for bionanocomposites with $R_{pp} = 4$. Bottom: optical images of water drops just after the deposition on bionanocomposites with $R_{pp} = 4$ and variable filler content.

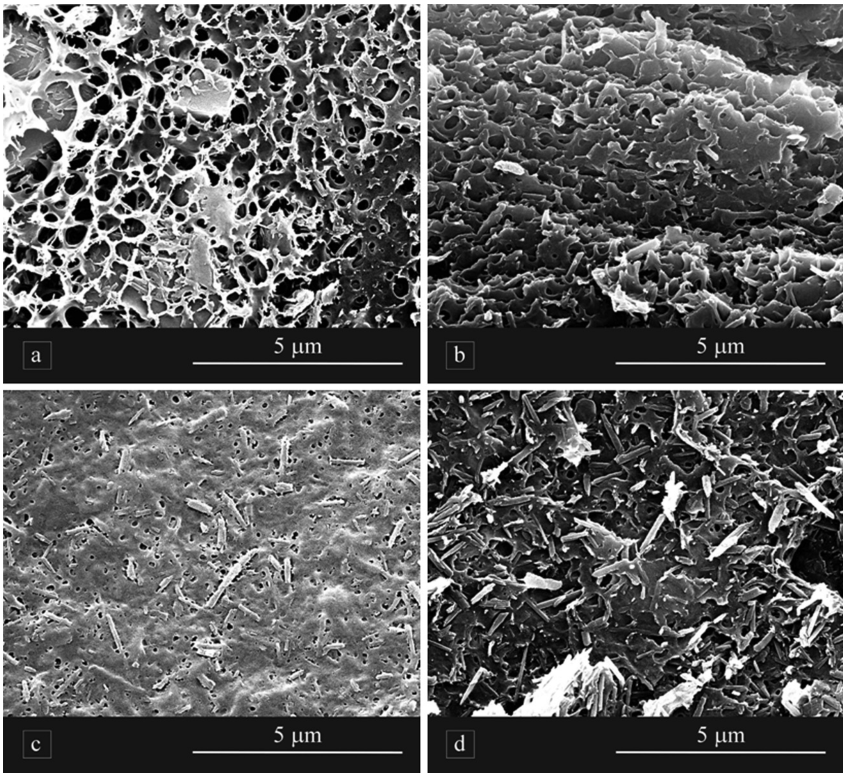

Fig. 4. Scanning electron microscopy images of surface (a,c) and cross section (b,d) of bionanocomposites with $R_{pp} = 4$. The filler content is: top, $C_f = 10$ wt%; bottom, $C_f = 30$ wt%.

beam. The measurements were carried out in high vacuum mode ($<6 \times 10^{-4}$ Pa) for simultaneous secondary electron, the energy of the beam was 30 kV and the working distance was 10 mm. Minimal electron dose condition was set to avoid damage of the sample.

2.3.3. Water uptake

The water uptake (*WU*) experiments were done on the rectangular films with the same dimensions used for DMA measurements. The samples were supposed to be thin enough so that the molecular diffusion was considered to be one dimensional.

Samples were first dried under vacuum at 25 °C for ca. 2 h. After weighing, they were conditioned at certain relative humidity (*RH%*) in a climate chamber. To obtain a stable equilibrium *RH%* of 33, 75 and 97% saturated salt solutions of $MgCl_2$, NaCl and K_2SO_4 were used. The temperature of the climate chamber was set at 25.0 ± 0.5 °C. The samples were removed after two weeks and weighed (±0.00001 g). The *WU* % of the films was calculated as follows:

$$WU\% = 100 \times (M_t - M_0)/M_t \quad (1)$$

where M_0 and M_t are the weights of the sample before and after two weeks exposure to a certain *RH%*, respectively.

2.3.4. Tensile properties

Tensile properties were determined by means of DMA Q800 instrument (TA Instruments). For all mechanical measurements, the samples were films of rectangular shape (10.00 mm × 6.00 mm × 0.060 mm). Tensile tests were performed with a stress ramp of 1 MPa min^{-1} at 26.0 ± 0.5 °C. We determined the values of the elastic modulus (E), the tensile strength (defined as the tensile stress at which the material fractures (σ_r)) and the percent elongation at break ($\varepsilon_{\%}$). Each nanocomposite was measured five times and the average values are reported.

The characteristics of the bionanocomposites with $R_{pp} = 1$ did not allow us to perform tensile experiments (Fig. 1).

2.3.5. Thermogravimetry

The experiments were performed by means of a Q5000 IR apparatus (TA Instruments) under the nitrogen flow of 25 cm^3 min^{-1} for the sample and 10 cm^3 min^{-1} for the balance. The weight of each sample was ca. 10 mg. The calibration was carried out by means of Curie temperature of standards (nickel, cobalt and their alloys). The measurements were conducted by heating the sample from room temperature to 900 °C with a rate of 10 °C min^{-1}. The degradation temperature of pectin (T_{d1}) and PEG 20000 (T_{d2}) were taken at the maximums of the first order derivative curves of mass loss to temperature (DTG curves). Examples of DTG curves are reported in the ESI.

The thermal degradation of pectin (ca. 240 °C) and PEG 20000 (390 °C) are well resolved in all bionanocomposites. The materials with very high HNTs content clearly showed a DTG peak at ca. 490 °C due to the expulsion of the two water molecules from the nanoclay interlayer. At very large C_f, DTG curve exhibited (see ESI) a peak at ca. 180 °C and a shoulder at ca. 340 °C, which are probably correlated to PEG 20000 thermal degradation.

Table 2
Water uptake values at different relative humidity.

WU% (*Rh* = 33%)	*WU%* (*Rh* = 75%)	*WU%* (*Rh* = 97%)
Pectin		
3.6 ± 0.7	8.2 ± 0.8	14 ± 2
Pectin/PEG 20000 ($R_{pp} = 4$)		
1.3 ± 0.3	5.0 ± 0.9	8 ± 1
Pectin/PEG 20000/HNTs ($R_{pp} = 4$, $C_f = 50.52$)		
1.3 ± 0.1	4.7 ± 0.8	7 ± 1

2.3.6. Differential scanning calorimetry

The differential scanning calorimeter TA Instrument 2920 CE was used under nitrogen flow atmosphere (flow rate $= 60$ cm^3 min^{-1}). The apparatus was calibrated with indium. The used pans are in aluminum and contain ca. 5 mg of the compound. The enthalpy (ΔH_m) and the temperature (T_m) of melting for PEG 20000 were determined by the experiments performed in the range 0–90 °C with a heating rate of 10 °C min^{-1}. The T_m and ΔH_m values were defined as the onset and the area of the melting endothermic peak, respectively. The ΔH_m values were calculated per gram of PEG 20000 in the composite material. Moreover, we studied the kinetics of crystallization process of PEG 20000 under non-isothermal conditions by changing the cooling rate. To this aim, the sample was heated to 90 °C and kept for 10 min to eliminate any previous thermal history; then, it was cooled down to 0 °C at 2.5, 5, 10 and 15 °C min^{-1}.

3. Results and discussion

3.1. Morphology, wettability and water uptake of bionanomaterials

The wettability of pectin/PEG blend film ($R_{pp} = 4$) and the corresponding bionanocomposites at variable C_f was determined.

For all biofilms, both V and θ decrease with time (τ) while A increases (see ESI). These values indicate that both spreading and water absorption occur during the measurements as reported for several biopolymers [30] and bionanocomposites based on pectin [22]. Farris et al. [30] analyzed the θ vs τ trends with an exponential function to extrapolate the θ value at $\tau = 0$ s (θ_i). Examples of the best fits are given in ESI. We observed that the PEG 20000 addition caused a small but significant increase (ca. 5°) of θ_i despite the PEG 20000 hydrophilic nature (Table 1). Hydrophobic surfaces can be formed by hydrophilic substances if the roughness of the surface is enhanced [31]. For composite materials, the presence of an hydrophilic additive into a matrix can generate an increase of θ_i because the surface composition is modified [22]. To the light of these insights the peculiar effect generated by PEG 20000 on the wettability of the biomaterial is ascribable to the increase of the surface roughness. This hypothesis is confirmed by SEM images (Fig. 2) showing that the surface of the pectin/PEG 20000 blend is very rough with many craters (size of ca. 2 μm), while the pectin surface is smooth.

More intriguing appears the wettability of the bionanocomposites. The general trend of θ_i vs C_f (Fig. 3) shows that over the low filler loading regime ($C_f \leq 10$ wt%), θ_i is nearly equal to that of the blend; for $C_f > 10$ wt% θ_i sharply decreases in agreement with the enhancement of the surface hydrophilicity. Such a phenomenon is straightforwardly evidenced by the drop images collected after just the deposition (Fig. 3). These results can be univocally understood in the light of the morphological study (Figs. 4 and 5) by taking into account the factors influencing the surface properties: 1) the roughness; and 2) the population of HNTs at the interface. Fig. 4 shows that for $C_f = 10$ wt%, the surface of bionanocomposite is still rough, with the presence of craters (size of ca. 2 μm), burying the HNTs. The SEM micrography of the transverse section shows that the filler is confined along the edges of the biofilm. For $C_f = 30$ wt% the surface roughness appears decreased and the HNTs are homogeneously dispersed on the surface as well as along the edges. Thus, the strong decrease of θ_i observed over the HNTs high loading region is explained by both the enrichment of the nanoclay at the interface and the reduction of the roughness because these morphological changes simultaneously contribute to enhance the surface hydrophilicity of the biofilms.

To the surface properties is correlated the tendency of the materials to incorporate water from environmental moisture that is of relevant interest for applicative purposes of biopolymers [32–34]; with this in mind, water uptake experiments were performed on the blend and the bionanocomposite film with $R_{pp} = 4$ and after

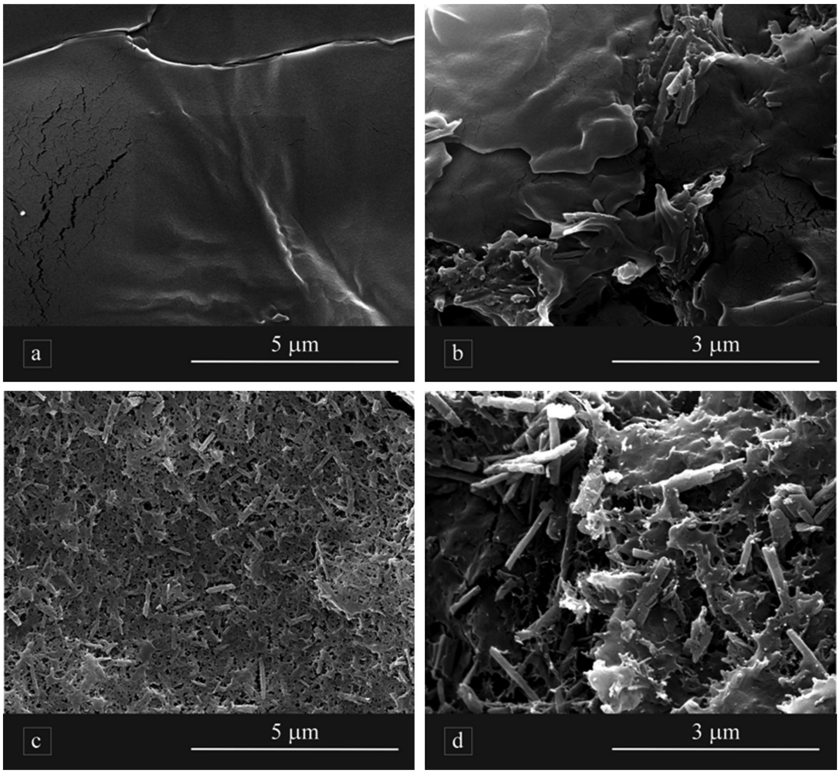

Fig. 5. Scanning electron microscopy images of surface (a,c) and cross section (b,d) of bionanocomposites with $R_{pp} = 1$. The filler content is: top, $C_f = 10$ wt%; bottom, $C_f = 30$ wt%.

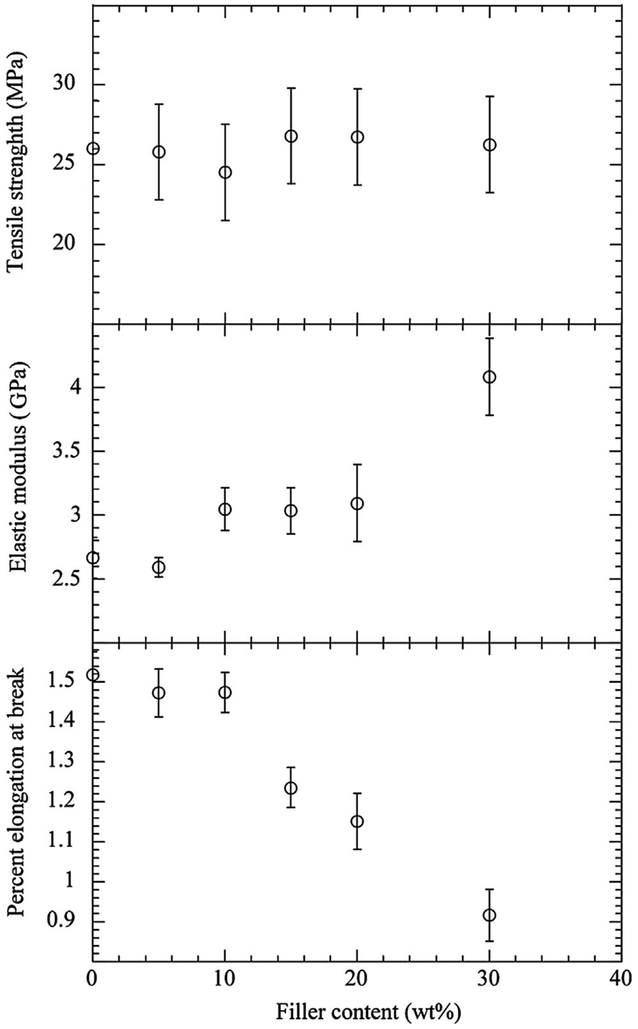

Fig. 6. Tensile properties of bionanocomposites with $R_{pp} = 4$ as function of filler content.

conditioning at variable *RH%* (Table 2). We observed that the *WU%* values of the pectin/PEG 20000 blend are lower than those for the pectin. The addition of large amount of HNTs to the blend generated biomaterials with unaltered *WU%* in spite of the hydrophilic nature of the nanoclay that is promising for applications in several field such as coatings for food conservation.

3.2. Tensile properties of bionanocomposites

The plasticization of pectin with PEG 20000 changed the tensile properties of the biopolymer. A similar result was also observed for chitosan/PEG 20000 blends [6]. The addition of PEG 20000 ($R_{pp} = 4$) generated a slight improvement of E (ca. 10%) with respect to the pristine polymer [23], while both σ_r and $\varepsilon\%$ decreased.

The effect of HNTs on the tensile properties of the blend pectin/PEG 20000 ($R_{pp} = 4$) films was investigated. Some examples of the stress–strain curves for plasticized bionanocomposites at variable C_f are reported in the ESI. The E increase upon HNTs addition (Fig. 6) is a clear indication of the good dispersion of the filler into the polymer matrix as reported for other plasticizes polymer/clay composites [35–38]. In fact, the uniform distribution of HNTs into the nanocomposite enhances the affinity and the adhesion of the polymers to the filler surface. The highest E value was observed for $C_f = 30$ wt% (the increase was of 50% respect to the blend film pectin/PEG 20000 ($R_{pp} = 4$) and of ca. 75% respect to the pristine pectin) [23].

The tensile strength is not influenced by the nanoclay while $\varepsilon\%$ decreases with C_f as reported in literature for starch/poly vinyl alcohol/Montmorillonite nanocomposites [35]. The latter finding was explained in terms of clay–polymer interactions that avoid the sliding of polymer chains against each other.

Finally, bionanocomposites with $R_{pp} = 1$ were not studied by DMA because of their high fragility. Such a loss mechanical strength is consistent with the morphology at the mesoscopic scale. In fact, for $C_f = 30$ wt% and $R_{pp} = 1$ a phase separation and a formation of globules (size of ca. 10 μm) take place at the interface generating an inhomogeneous and fractured surface (Fig. 7). For the sample at $C_f = 30$ wt% and $R_{pp} = 4$, HNTs are uniformly dispersed at the surface that appears rather compact (Fig. 7).

3.3. Thermal characterization of bionanomaterials

The thermal degradation and crystallization behavior of the materials were also determined. Both T_{d1} and T_{d2} in the pectin/PEG 20000 blends have similar values to those of the pristine polymers. Fig. 8 reports the effect of the filler on the degradation temperatures of both polymers for bionanocomposites. T_{d1} increases in the presence of HNTs with a larger slope for $R_{pp} = 4$. This finding corroborates with the reports [23] that the HNT lumen can encapsulate the pectin degradation products delaying the mass transport. Of course, such a phenomenon is enhanced by increasing the pectin concentration. Furthermore, the thermal stabilization of the biopolymer agrees with the good dispersion of the filler into the polymeric matrix [39–41]. The degradation of pectin ($T_{d1} < T_{d2}$)

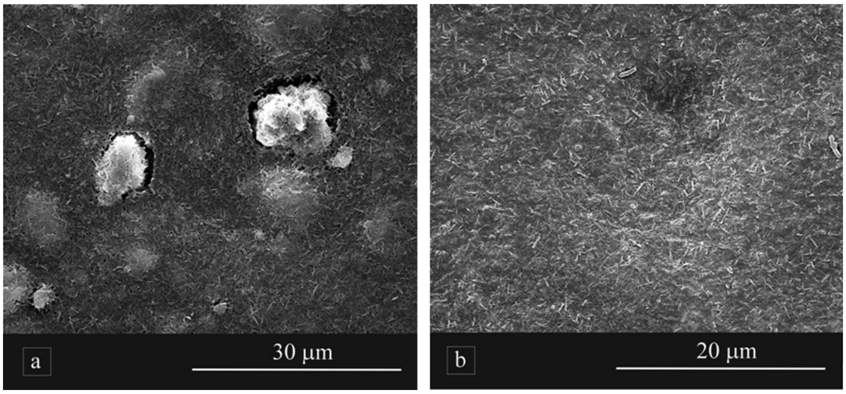

Fig. 7. Scanning electron microscopy images of bionanocomposites at $C_f = 30$ wt% with $R_{pp} = 1$ (a) and 4 (b).

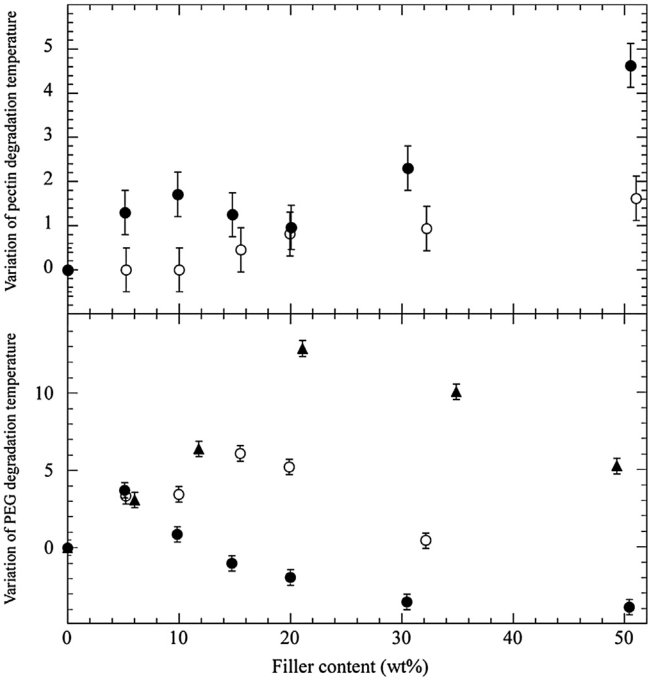

Fig. 8. Variation of the degradation temperature of the pectin (top) and PEG 20000 (bottom) as function of the filler content for bionanocomposites with $R_{pp} = 0$ (▲), $R_{pp} = 1$ (○) and $R_{pp} = 4$ (●). Data at $R_{pp} = 0$ are from Ref. [26].

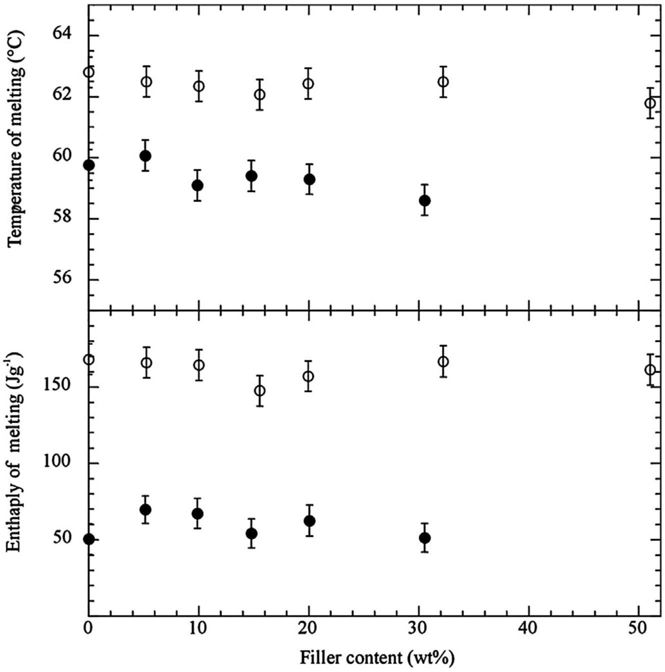

Fig. 9. Temperature (top) and enthalpy (bottom) of PEG 20000 melting as function of the filler content for bionanocomposites with $R_{pp} = 1$ (○) and $R_{pp} = 4$ (●).

influences the thermal stability of PEG 20000. As Fig. 8 illustrates, while the T_{d2} vs C_f profile remains unchanged, the maximum is shifted towards lower values upon the pectin addition. The PEG 20000 thermal destabilization generated by the pectin proves that the HNTs hollows are no more available to incorporate the PEG 20000 degradation products.

The crystallinity of the blend may derive from PEG 20000 having a certain degree of crystallinity. Such a property was evaluated by studying the melting process through the DSC. The ΔH_m values (Table 3) of the blends indicate that the interactions with the pectin reduce the crystallinity fraction of the PEG 20000. This effect is more important with the R_{pp} increase. Literature reports that the addition of electrolytes to the PEGs generate a decrease of the polymer crystallinity [42].

The addition of HNTs to the blends essentially did not modify the crystallinity of PEG 20000 as the ΔH_m and T_m values of all the bionanocomposites show (Fig. 9). It was demonstrated that the interactions between PEG 20000 and HNTs reduce the polymer crystallinity [26] so that one may conclude that competitive processes of HNTs/pectin and HNTs/PEG 20000 interactions take place and that the interactions of pectin with the nanoclay surface appears privileged. The crystallization process of PEG 20000 was studied under non-isothermal conditions. The crystallization temperature (T_c) for all of the nanocomposites decreased linearly with the cooling rate (see Figure in ESI). The T_c values extrapolated at null heating rates are reported as functions of the nanofiller amount (Fig. 10). It has to be noted that the nanotubes did not influence the crystallization temperature of PEG 20000 in the presence of pectin while the opposite occurs if HNTs/PEG 20000 is considered [26]. Therefore, one can conclude that the pectin protects the nanoparticles and the melting and crystallization properties of PEG 20000 in the blend nanocomposites are preserved.

Table 3
Temperature and enthalpy of PEG 20000 for pectin/PEG 20000 blends and pristine PEG 20000.

	ΔH_m (J g^{-1})	T_m (°C)
Pectin/PEG 20000 ($R_{pp} = 1$)	168.4	62.8
Pectin/PEG 20000 ($R_{pp} = 4$)	50.5	59.8
PEG 20000	199.4[a]	60.8[a]

[a] From Ref. [26].

4. Conclusions

We prepared biofilms based on pectin/PEG 20000 blend filled with inorganic natural nanoparticles. Halloysite nanotubes (HNTs) are very promising in material science because, besides the interesting properties conferred by the peculiar hollow tubular shape, they are largely available and at low cost. The obtained nanocomposite blends represents a sustainable alternative to the plastic materials synthesized from fossil fuels. The structural features are tunable and therefore a variety of materials with controlled properties were obtained. A comprehensive characterization of the

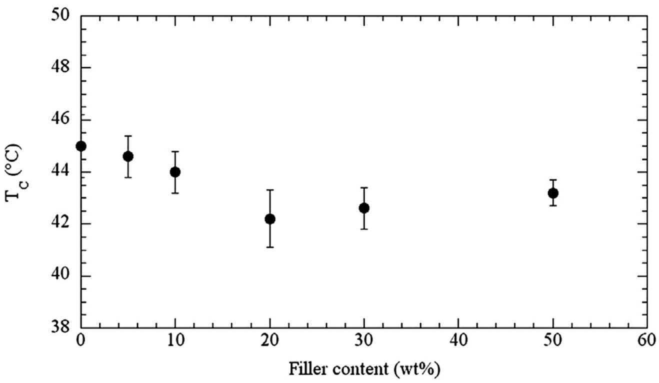

Fig. 10. PEG 20000 crystallization temperature at null cooling rate for Pectin/PEG 20000/HNTs bionanocomposites at $R_{pp} = 1$.

materials was carried out through wettability, water uptake, crystallinity, thermal degradation and tensile properties, which were correlated to the mesoscopic structure.

With this study we successfully propose to employ the strategy widely used for polymeric materials, such as the addition of plasticizers and inorganic fillers, with a green biocompatible approach.

Acknowledgments

The work was financially supported by the University of Palermo, PRIN 2010–2011 (prot. 2010329WPF) and FIRB 2012 (prot. RBFR12ETL5).

Appendix A. Supplementary data

Supplementary data related to this article can be found online at http://dx.doi.org/10.1016/j.polymdegradstab.2013.09.012.

References

[1] Ghaffari A, Navaee K, Oskoui M, Bayati K, Rafiee-Tehrani M. Eur J Pharm Biopharm 2007;67:175–86.
[2] Coffin DR, Fishman ML, Ly TV. J Appl Polym Sci 1996;61:71–9.
[3] Coffin DR, Fishman ML. J Appl Polym Sci 1994;54:1311–20.
[4] Farris S, Schaich KM, Liu L, Cooke PH, Piergiovanni L, Yam KL. Food Hydrocoll 2011;25:61–70.
[5] Wang Q, Dong Z, Du Y, Kennedy JF. Carbohydr Polym 2007;69:336–43.
[6] Gunbas ID, Aydemir Sezer U, Gülce İz S, Deliloğlu Gürhan İ, Hasirci N. Ind Eng Chem Res 2012;51:11946–54.
[7] Ozkoc G, Kemaloglu S. J Appl Polym Sci 2009;114:2481–7.
[8] Hu Y, Hu YS, Topolkaraev V, Hiltner A, Baer E. Polymer 2003;44:5711–20.
[9] Ljungberg N, Wesslén B. Polymer 2003;44:7679–88.
[10] Tharanathan RN. Trends Food Sci Technol 2003;14:71–8.
[11] Alcantara ACS, Aranda P, Darder M, Ruiz-Hitzky E. J Mater Chem 2010;20:9495–504.
[12] Ruiz-Hitzky E, Aranda P, Darder M, Fernandes FM. In: Bergaya Faïza, Lagaly Gerhard, editors. Developments in clay science, vol. 5. Elsevier; 2013. p. 721–41.
[13] Lvov YM, Shchukin DG, Mohwald H, Price RR. ACS Nano 2008;2:814–20.
[14] Yah WO, Xu H, Soejima H, Ma W, Lvov Y, Takahara A. J Am Chem Soc 2012;134:12134–7.
[15] Yah WO, Takahara A, Lvov YM. J Am Chem Soc 2011;134:1853–9.
[16] Vergaro V, Abdullayev E, Lvov YM, Zeitoun A, Cingolani R, Rinaldi R, et al. Biomacromolecules 2010;11:820–6.
[17] Liu M, Wu C, Jiao Y, Xiong S, Zhou C. J Mater Chem B 2013;1:2078–89.
[18] Cavallaro G, Gianguzza A, Lazzara G, Milioto S, Piazzese D. Appl Clay Sci 2013;72:132–7.
[19] Cavallaro G, Lazzara G, Milioto S. J Phys Chem C 2012;116:21932–8.
[20] Abdullayev E, Price R, Shchukin D, Lvov Y. ACS Appl Mater Interfaces 2009;1:1437–43.
[21] Abdullayev E, Lvov Y. J Mater Chem 2010;20:6681–7.
[22] Cavallaro G, Donato DI, Lazzara G, Milioto S. J Phys Chem C 2011;115:20491–8.
[23] Cavallaro G, Lazzara G, Milioto S. Langmuir 2011;27:1158–67.
[24] Dong F, Wang J, Wang Y, Ren S. J Mater Chem 2012;22:11093–100.
[25] Qiao J, Adams J, Johannsmann D. Langmuir 2012;28:8674–80.
[26] Cavallaro G, Lisi R, Lazzara G, Milioto S. J Therm Anal Calorim 2013;112:383–9.
[27] He Y, Fan Z, Hu Y, Wu T, Wei J, Li S. Eur Polym J 2007;43:4431–9.
[28] Durmus A, Ercan N, Soyubol G, Deligöz H, Kaşgöz A. Polym Compos 2010;31:1056–66.
[29] Gumus S, Ozkoc G, Aytac A. J Appl Polym Sci 2012;123:2837–48.
[30] Farris S, Introzzi L, Biagioni P, Holz T, Schiraldi A, Piergiovanni L. Langmuir 2011;27:7563–74.
[31] Marmur A. Langmuir 2008;24:7573–9.
[32] Kučerík J, Průšová A, Rotaru A, Flimel K, Janeček J, Conte P. Thermochim Acta 2011;523:245–9.
[33] Mlčoch T, Kučerík J. J Therm Anal Calorim 2013:1–9.
[34] Průšová A, Šmejkalová D, Chytil M, Velebný V, Kučerík J. Carbohydr Polym 2010;82:498–503.
[35] Tang X, Alavi S. J Agric Food Chem 2012;60:1954–62.
[36] Ali SS, Tang X, Alavi S, Faubion J. J Agric Food Chem 2011;59:12384–95.
[37] Chivrac F, Pollet E, Dole P, Avérous L. Carbohydr Polym 2010;79:941–7.
[38] Lee J-H, Jung D, Hong C-E, Rhee KY, Advani SG. Compos Sci Technol 2005;65:1996–2002.
[39] Lecouvet B, Gutierrez JG, Sclavons M, Bailly C. Polym Degrad Stab 2011;96:226–35.
[40] Blanco I, Cicala G, Latteri A, Mamo A, Recca A. J Therm Anal Calorim 2013;112:375–81.
[41] Blanco I, Bottino FA. Polym Compos 2013;34:225–32.
[42] Singh T, Bhat SV. Bull Mater Sci 2003;26:707–14.

Journal of Colloid and Interface Science 417 (2014) 66–71

Contents lists available at ScienceDirect

Journal of Colloid and Interface Science

www.elsevier.com/locate/jcis

Halloysite nanotube with fluorinated lumen: Non-foaming nanocontainer for storage and controlled release of oxygen in aqueous media

Giuseppe Cavallaro, Giuseppe Lazzara *, Stefana Milioto, Giovanni Palmisano, Filippo Parisi

Department of Physics and Chemistry, Università degli Studi di Palermo, Viale delle Scienze, pad. 17, 90128 Palermo, Italy

ARTICLE INFO

Article history:
Received 9 October 2013
Accepted 10 November 2013
Available online 20 November 2013

Keywords:
Halloysite
Nanoclay
Fluorinated surfactant
Gas solubilization

ABSTRACT

Halloysite clay nanotubes were selectivity modified by adsorbing perfluoroalkylated anionic surfactants at the inner surface. The modified nanotubes formed kinetically stable dispersions due to the enhanced electrostatic repulsions exercised between the particles. We proved that the modified nanotubes can be used as non-foaming oxygen nanocontainers in aqueous media. The gas release from supersaturated dispersions can be controlled by external stimuli and system composition. In conclusion, we managed to put forward an easy strategy to develop smart materials from natural nanoclays, which can endow important applications like the storage and delivery of gas.

1. Introduction

Covalent or non-covalent nanoparticle modification is a well known strategy to design new target properties. Sustainable nanoparticles are represented by clays available with different shapes, sizes and surface chemical properties. Most common clay nanoparticles possess a nanolayered morphology, such as kaolin and montmorillonite. Notwithstanding, there are natural nanoclays with hollow tubular shape [1,2] of great scientific interest due to potential applications. Promising nanoclays as nanocontainers with controlled release properties are imogolite [1] and natural halloysite (HNT) [2]. Besides the interesting properties, imogolite presents a certain toxicity [3]. Halloysite mineral is well known [4] since 1946 but its application in smart sustainable materials has been proposed only a few years ago [2]. HNT is abundant, durable and biocompatible and, furthermore, it is cheap compared to synthetic nanomaterials with similar morphology. HNT is generated by rolling-up a kaolin sheet with a still unknown mechanism; its size ranges between 0.5 and 1 μm in length and between 15 and 100 nm in the inner diameters [2].

The different chemistry of the inner and the outer surfaces makes HNT a tremendous tool. Being that the external surface is composed of Si—O—Si groups and the internal surface of a gibbsite-like array of Al–OH groups, the aqueous acid–base equilibria confer negative and positive charges, at the outer and inner surfaces respectively, in a wide pH range [5,6]. Consequently, selective adsorption of ionic species may strategically control the charge. The hydrophobic modification of HNT lumen with anionic surfactant stabilized successfully nanotubes in water [7] as a consequence of canceling the positive charges at the surface due to the entrapment of the anionic molecule into the HNT lumen generating a large net negative charge. Nanotube applications have been proposed for controlled release in healing anticorrosion [8,9], water purification [10], polymer composites [11,12] and antimicrobial coatings [13]. The covalent modification of the inner surface generated HNT able to incorporate more ferrocene than pristine nanoclay [14]. To the light of the phase behaviors of HNT dispersion, those nanoparticles are considered strategic for fabrication of long-range ordered nano-objects [15]. Thus, development of tube-like materials with tunable properties is one of the most scientific challenges.

We report the modification of HNT lumen by incorporating perfluoroalkylated anionic surfactants. This was done with the intent at obtaining rather stable colloidal dispersions in water with enhanced oxygen solubilization ability. Fluorinates are well established for chemical and biological inertness, fire extinguishing and flame retardant materials [16]. Finally, fluorinated biocompatible surfactants have been proposed as oxygen carriers in biomedical applications [17].

2. Experimental section

2.1. Materials

Halloysite nanotubes (HNTs) and kaolin are Sigma products. Perfluorooctanoic acid (PFC8H), Perfluoroheptanoic acid (PFC7H)

---

* Corresponding author.
E-mail address: giuseppe.lazzara@unipa.it (G. Lazzara).

0021-9797/$ - see front matter © 2013 Elsevier Inc. All rights reserved.
http://dx.doi.org/10.1016/j.jcis.2013.11.026

and Perfluoropentanoic acid (PFC5H) from Fluka were crystallized from carbon tetrachloride and dried at room temperature. Their sodium salts (NaPFC8, NaPFC7 and NaPFC5) were prepared by neutralization with an aqueous sodium hydroxide solution. The products were crystallized twice from an ice-cold solution and dried in a vacuum oven at 60 °C for at least 4 days before their use. The structure of the surfactants is given in Chart 8.

Water from reverse osmosis (Elga model Option 3) with a specific resistivity greater than 1 MΩ cm was used.

2.2. Preparation of surfactants functionalized HNTs

To aqueous surfactant solutions (0.1 mol kg^{-1}) 0.02 g cm^{-3} of HNTs was added. The obtained dispersions were magnetically stirred for ca. 1 day. Afterward, they were taken in a vacuum oven at 50 °C and at 100 mbar overnight. The solid was separated by centrifugation and rinsed several times with water until the surface tension of the supernatant was close to the value for pure water (ca. 72 mN m^{-1}). This ensures the absence of unbound surfactant. All of the solids dried at 80 °C were investigated by means of thermogravimetric analysis (TG) to estimate the surfactant loading into the HNT lumen.

2.3. Methods

ζ-potential and dynamic light scattering (DLS) measurements were carried out by means of a Zetasizer NANO-ZS (Malvern Instruments). The field-time autocorrelation functions were well described by a single decay, which provides the decay rate (Γ) of the diffusive mode. For the translational motion, the collective diffusion coefficient at a given concentration is $D_t = \Gamma/q^2$ where q is the scattering vector given by $4\pi n\lambda^{-1}\sin(\theta/2)$ being n the water refractive index, λ the wavelength (632.8 nm) and θ the scattering angle (173°).

The functionalized nanotubes were imaged by using a microscope ESEM FEI QUANTA 200F. The measurements were carried out in high vacuum mode ($<6 \times 10^{-4}$ Pa) for simultaneous secondary electron, the energy of the beam was 30 kV and the working distance was 10 mm. Before each experiment, the sample was coated with gold in argon by means of an Edwards Sputter Coater S150A to avoid charging under electron beam.

The thermogravimetric analyses were done by using a Q5000 IR apparatus (TA Instruments) under the nitrogen flow of 25 cm^3 min^{-1} for the sample and 10 cm^3 min^{-1} for the balance at the heating rate of 10 °C min^{-1}. Temperature spanned from ambient to 900 °C. The surfactant:HNT ratio was determined from the residual mass by taking into account for the water content as reported in the literature [16,12].

The densities ($\pm 1 \times 10^{-6}$ g cm^{-3}) and speed of sound (± 0.1 m s^{-1}) of the liquid dispersion were determined at 25.000 ± 0.001 °C by using a density and sound velocity meter (DSA 5000 M, Anton Paar).

The specific volume of pristine or modified HNTs (v_{sp}) was calculated as follows

$$v_{sp} = 1/d - 10^2(d - d_0)/(C_S \times d \times d_0) \tag{1}$$

where d and d_0 are the dispersion and water densities, respectively; C_S is the concentration of solid material into the dispersion in g/100 g of solvent. The isentropic compressibility coefficients of the dispersions (β) were obtained as $100/(u^2 \times d)$ being u the ultrasonic velocity of the dispersion. The specific isentropic compressibility (k_s) was calculated using the following equation.

$$k_s = v_{sp}\beta + 10^2(\beta - \beta_0)/(C_S \times d_0) \tag{2}$$

where β_0 is the isentropic compressibility coefficients of water and the other symbols have the same meaning as above.

The sedimentation volume of pristine and modified HNTs was determined by using tubes of borosilicate glass with an inner diameter of ca. 2.3 mm and length of ca. 125 mm. The tubes were filled with the dispersion and left to equilibrate in vertical position. Two phases were observed, an upper transparent phase and a lower milk-like phase. The transparent upper phase is water according to the density value. On this basis, the concentration of either HNTs or functionalized HNTs in the lower phase (C_{LP}) was determined as $C_{LP} = C_S/R_{LP:T}$, where C_S is the stoichiometric initial concentration of material in water, $R_{LP:T}$ is the V_{LP}/V_T ratio being V_T and V_{LP} the total and the lower phase volumes, respectively. The tubes were imaged and $R_{LP:T}$ was estimated from the height of the meniscus in the capillary by using an image analyzer software (ImageJ 1.43u).

The oxygen desaturation curves were obtained by using a HD22559.2 apparatus (Delta Ohm). Water, HNT and modified HNT aqueous dispersions (ca. 15 cm^3) were saturated with oxygen by bubbling the pure gas for ca. 1 h. The oxygen concentration was registered every 2 min. The experiments were carried out under static conditions and under magnetic stirring at 1250 rpm. The oxygen concentration was normalized for the solubility of the gas in water, $[O_2]_{sat}$, at the experimental conditions (25 °C and 1 atm).

3. Results and discussion

The alumina inner surface of the nanotube was selectively modified with perfluorinated anionic surfactants rendering the total charge of the nanotube significantly changed. The as prepared hybrid nanotubes exhibit an enhancement of stability in water and a core to successfully entrap oxygen in aqueous media.

3.1. Physico-chemical characterization of functionalized Halloysite nanotubes

The amount of surfactant adsorbed onto the HNT (Table 1) was estimated from the thermogravimetric analysis from the residual mass by taking into account for the water content as reported in the literature [16,12]. These values are far below the maximum loading ability of HNTs being that the hollow cavity represents ca. 10% of the nanoclay volume. By assuming an adsorbed surfactant monolayer and considering 760 m^2 g^{-1} for the occupied area of NaPFC8 at the alumina/water interface [19], one calculates the surfactant loading of 0.90 wt% that is in straightforward agreement with the experimental value (Table 1). These calculations cannot be extended to NaPFC7 and NaPFC5 because, to the best of our knowledge, no adsorption data at the alumina/water interface are available; nevertheless, it is expected a behavior rather comparable in terms of area per molecule if an extended chain configuration is considered [19]. From experimental loading data one can conclude that NaPFC7 and NaPFC5 did not fully cover the HNT lumen.

Table 1
Surfactant loading, diffusion coefficient and ζ-potential for HNT/surfactant hybrid materials[a].

	Surfactant loading	$D° \times 10^{12}$	ζ-potential
HNT		1.5; 0.94[b]	−21; −19.6[b]
HNT/NaPFC5	0.29	1.2	−27
HNT/NaPFC7	0.62	1.0	−29
HNT/NaPFC8	0.86	0.90	−32

[a] Units are: surfactant loading, wt%; $D°$, m^2 s^{-1}; ζ, mV. Errors are: surfactant loading, 4%; $D°$, 5%; ζ, 4%.

[b] From Ref. [7].

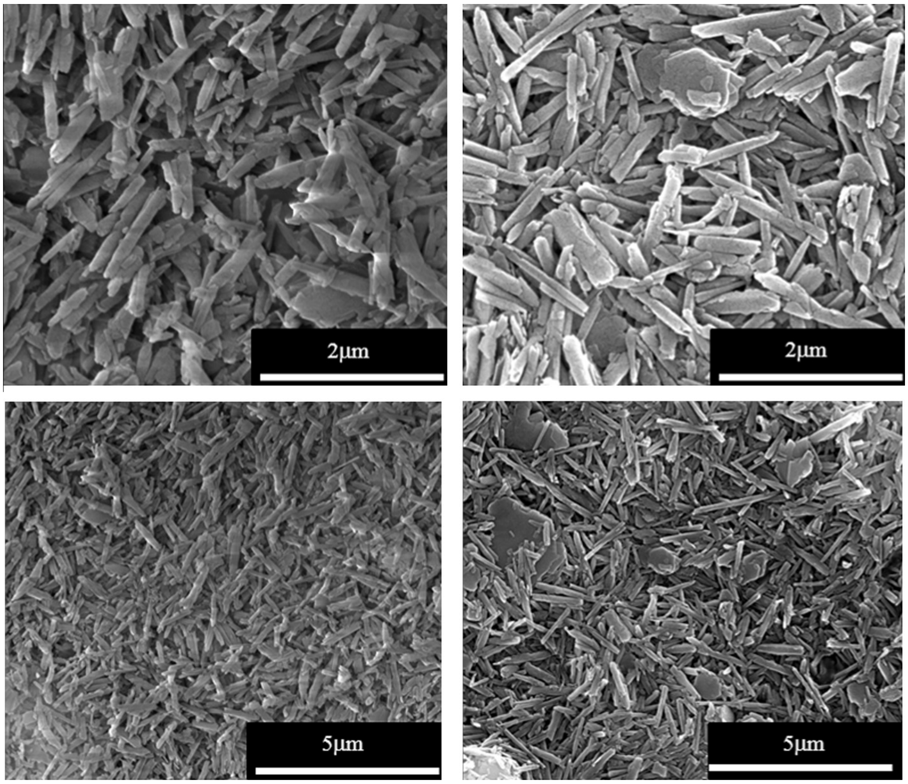

Fig. 1. Scanning electron micrographs of HNT/NaPFC5 (left hand side) and HNT/NaPFC8 (right hand side).

The SEM micrographs (Fig. 1) showed that the tubular shape of halloysite is preserved after the adsorption of perfluorinated surfactants and the characteristic lengths are comparable to those observed for the pristine HNT samples in agreement with the monolayer formation [18]. The dried samples did not show any orientation of the anisotropic particles ruling out preferential interactions. This aspect is fundamental as far as the aqueous dispersions stability is concerned.

To shed more light to this aspect, the translational diffusion coefficient and the charge of the hybrid materials were determined in dilute aqueous dispersions. The measurements were carried out at various contents of the dispersed material but the concentration effect was negligible. The diffusion coefficient ($D°$) and the ζ-potential (ζ) extrapolated at infinite dilution are reported in Table 1. The data show that the hybrid materials did not aggregate in water and they diffuse as single nanotubes. The ζ-potential data (Table 1) indicate that the net negative charge of the nanotubes is raised up by the surfactant adsorption in agreement with the neutralization of the positive charges of the inner surface.

To definitely rule out the presence of aggregates and to evidence eventual particle–particle interactions, the specific volume (v_{sp}) and the isentropic compressibility (k_s) of HNT and HNT/NaPFC8 dispersed in water were determined (Fig. 2). Both v_{sp} and k_s are linearly dependent on the concentration of the material and can be fitted according to the Mc-Millan-Mayer approach

$$v_{sp} = v° + B_v C_S \quad k_s = k° + B_k C_S \tag{3}$$

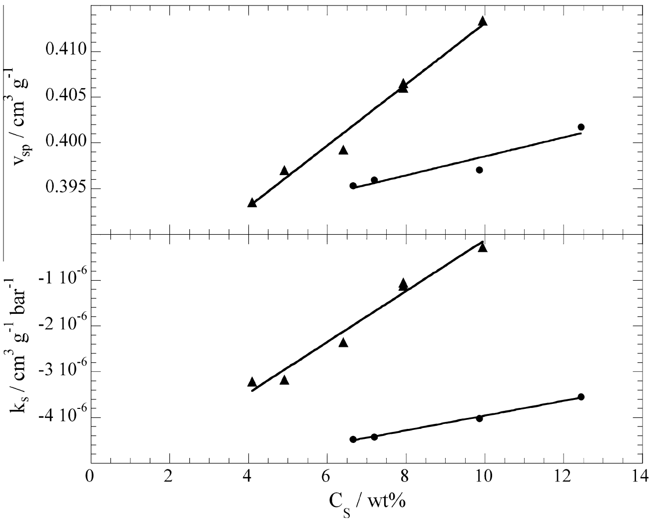

Fig. 2. Specific volume and isoentropic compressibility for aqueous dispersion of HNT (●) and HNT/NaPFC8 hybrid materials (▲) as a function of concentration.

Table 2
Volume and compressibility data[a].

	HNT	HNT/NaPFC8
$v°$	0.388 ± 0.002	0.380 ± 0.002
B_v	(1.0 ± 0.2) × 10^{-4}	(3.3 ± 0.2) × 10^{-4}
$k°$	−(5.57 ± 0.07) × 10^{-6}	−(5.7 ± 0.3) × 10^{-6}
B_k	(1.62 ± 0.08) × 10^{-8}	(5.6 ± 0.5) × 10^{-8}

[a] Units are: $v°$, cm^3 g^{-1}; $k°$, cm^3 g^{-1} bar^{-1}; B_v, cm^3 g^{-2} kg; B_k, cm^3 g^{-2} kg bar^{-1}.

where $v°$ and $k°$ are the specific volume and compressibility at infinite dilution, respectively, while B_v and B_k are the particle–particle interaction parameters for volume and compressibility, respectively. Within the experimental errors, the properties extrapolated at infinite dilution do not reflect differences between HNT and the hybrid material (Table 2). By using the surfactant loading from Table 1, the $v°$ value for NaPFC8 (0.458 cm^3 g^{-1}) [20] and HNT, one can calculate v° for the composite material by means of the rule of mixtures. As a result, the change in $v°$ for HNT/NaPFC8 with respect to the value for HNT is predicted to be less than 0.1% in agreement with the experimental findings. As concerns the particle–particle interaction parameters it is reported [21] that hydrophobic forces provide negative values for B_v while the electrostatic interactions render the water molecules less compressible [21] so that, B_v and B_k are expected to be positive. Therefore one may deduce that the nanoparticle-nanoparticle electrostatic interactions are enhanced in the hybrid material in agreement with the ζ-potential results.

3.2. Sedimentation volume of pristine and functionalized Halloysite nanotubes

The sedimentation of the clay nanotubes assumes a key role in understanding the colloidal stability. To quantitatively explore such a phenomenon, concentrated dispersions of pristine and functionalized HNT in water were prepared and left to equilibrate in a glass tube. After 1 week, two phases were clearly identified; namely, a bottom milk-like phase and an upper transparent phase. The systems remained unaltered for 6 months at least. The lower phase is the sedimentation volume and its value increased with the initial total concentration of the material as examples shown in Fig. 3. For most concentrated samples, the upper transparent phase was not observed at all. It is noteworthy that such a peculiar sedimentation was not observed for kaolin, which possesses the same chemical composition as HNT but a sheet-like morphology. In such a case a complete sedimentation even at 8 wt%, the maximum concentration investigated for HNT, was observed. Different morphologies confer different properties to the particles.

The sedimentation volume is a very complex parameter; nevertheless, at least in water, it is controlled by the repulsive forces exercised between particles [22]. For instance, the electrostatic repulsions are caused by the double layer surrounding each particle and the particle charge. Consequently, if the particles repel to each other they remain independent until they reach the closest packing, which will represent the concentration in the sedimentation volume. If the particles do not strongly repel to each other, they are sticking together generating a smaller sedimentation volume.

Fig. 4 shows the dependence of $R_{LP:T}$ on the stoichiometric concentration of the nanotubes. For all of the investigated systems, we observed a linear increase in $R_{LP:T}$ up to the limit of 1, beyond which it is constant. These data indicate that the sedimentation does not take place over the concentrated regime regardless of the presence and the nature of the surfactant. From the inverse of the positive slope of the linear trends shown in Fig. 4, we calculated the concentrations of the lower phase (C^*_{LP}), which are reported in Table 3. Such values are a sort of critical concentration above which the dispersion is stable because the highest packing of the nanotubes is approached and shorter distances between the nanoparticles are hindered by the electrostatic repulsions. The

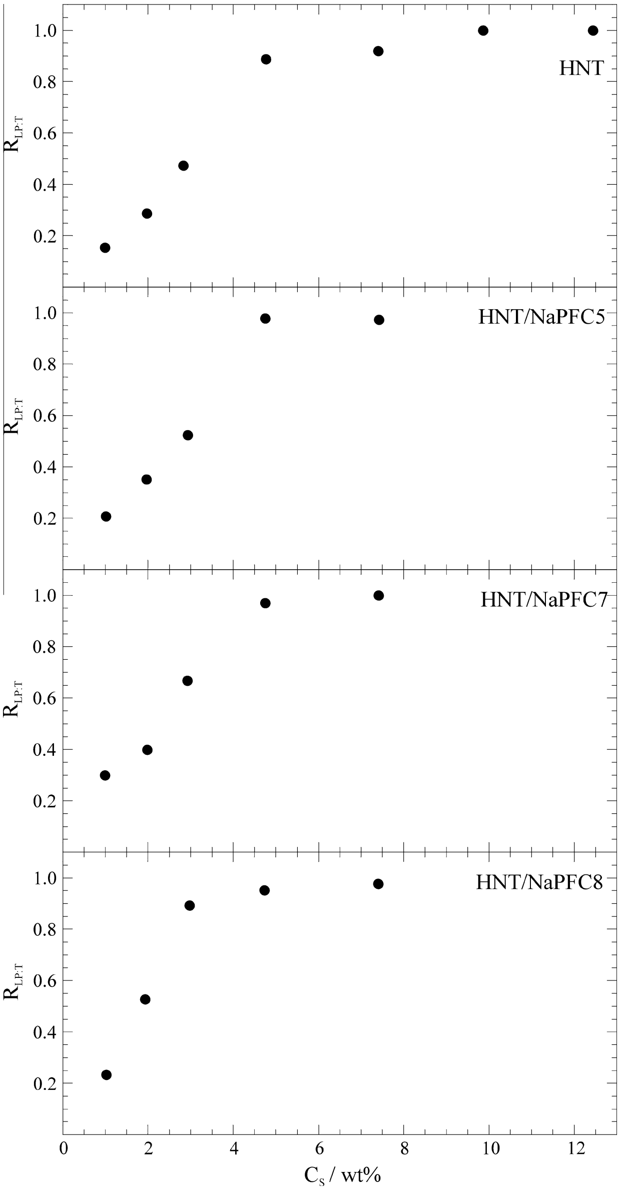

Fig. 4. Dependence of the ratio between the volume of lower phase and total volume on stoichiometric concentration of the dispersed material.

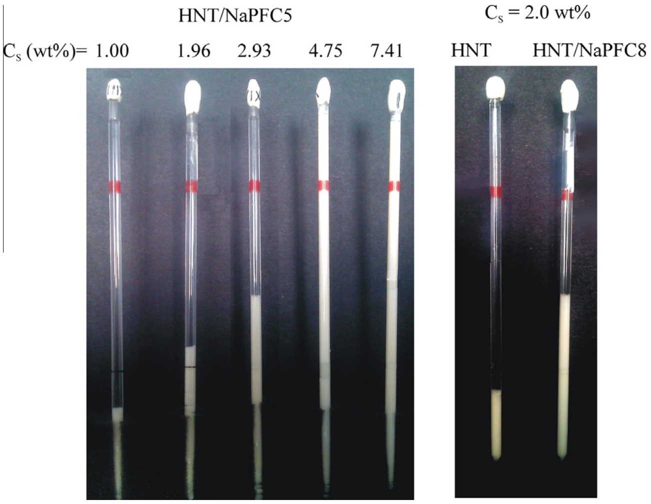

Fig. 3. Optical images of sedimentation volume in glass tubes. The tube length is 125 mm.

Table 3
Critical concentration of the lower phase for HNT and HNT/surfactant hybrid materials in water[a].

	C^*_{LP}
HNT	6.3
HNT/NaPFC5	5.4
HNT/NaPFC7	4.3
HNT/NaPFC8	3.8; 4.5[b]

[a] Units are: C^*_{LP}, wt%. Error for C^*_{LP} is less than 3%.

[b] In KCl 0.1 mol kg^{-1}.

C^{*}_{LP} is highly altered by the presence of the anionic surfactant (Table 3) that is in agreement with the large net charge of the hybrid HNT compared to pristine HNT.

Although a quantitative interpretation of this phenomenon from a microscopic view-point might be very challenging we thought it would be interesting to compare the experimental C^{*}_{LP} with the computed value. This was done by assuming a simple cubic model and a contact distance given by the average length of the nanotubes (see Fig. 5). Briefly, when the concentration generates some overlapping, the rotation of each individual nanoparticle becomes restricted and the cylinders are entangled [23]. From such a geometrical model, one obtains the critical volume fraction φ^{*} for cylinders

$$\varphi^{*} = \pi R^{2}/L^{2} \tag{4}$$

where R and L are the external radius and the length of the nanotubes (Fig. 5). By introducing in Eq. (4) the average outer radius (73 nm) and the length (770 nm) of HNT [18], the φ^{*} value of 0.028 was obtained. By taking into account for the specific volume of HNT (Table 2) the C^{*}_{LP} value of 6.9 wt% was calculated. An excellent agreement between the computed and the experimental (Table 3) values of pristine nanotubes was found. On this basis one can state that the sedimentation volume of HNTs is driven by hard-cylinder interactions, and the aqueous dispersion looks stable when the contact distance between nanoparticles is approached.

As concerns the hybrid materials, ζ-potential data evidenced an increase in the net charge in the modified HNT. Therefore, the particle–particle repulsive interactions shift to longer range increasing the closest average distance between the functionalized nanoparticles. This description explains the C^{*}_{LP} decrease for functionalized HNTs. It is noteworthy the straight correlation between C^{*}_{LP} and the amount of loaded surfactant into the hybrid material (Fig. 6). This reveals that each mole of adsorbed surfactant neutralizes an equivalent number of positive charges of the nanotubes inner surface generating a linear increase in the net negative charge of HNT and therefore longer range interactions. To highlight the significance of the electrostatic forces on the sedimentation behavior, 0.1 mol kg^{-1} of KCl was added to the 2.97 wt% NaPFC8/HNT dispersion. The determined C^{*}_{LP} increases in agreement with the reduction in the mean distance between particles generated by the salt screening effect, as expected by the DLVO theory, for which higher ionic strength screens electrostatic repulsions due to the contraction of the double layer width [24].

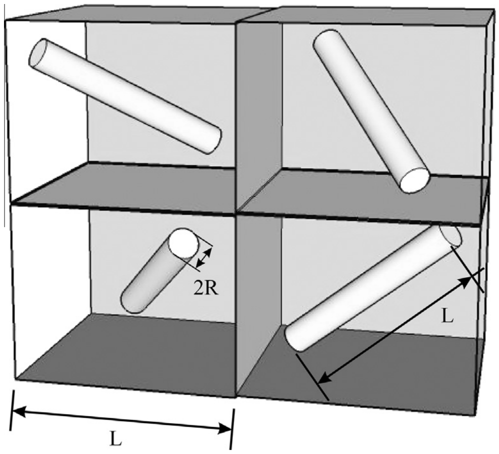

Fig. 5. Sketch representation of the simple cubic model for the interpretation of the sedimentation volume.

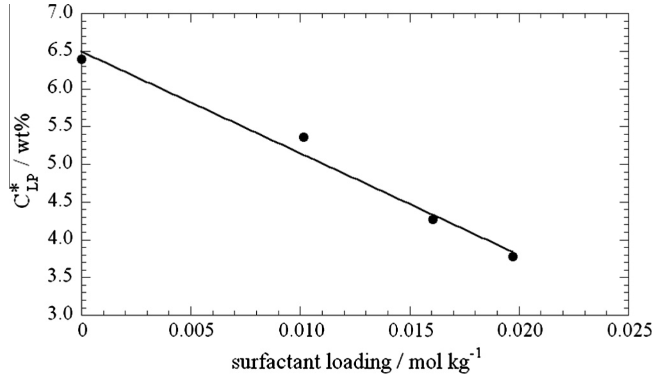

Fig. 6. Critical concentration as a function of the surfactant loading for HNT hybrid materials.

3.3. Hybrid HNT/surfactant: non-foaming nanoreservoir for oxygen storage

The nanotubes with highly hydrophobic cores might allow encapsulation of molecules of interest within fields like nanotechnology, drug delivery and gas storage. These prepared hybrid materials can be promising as oxygen nanoreservoir in aqueous media being that fluorinated solvents are able to solubilize large amount of gas. To explore this perspective, aqueous dispersions of both HNT and HNT/NaPFC8 (2.0 wt%) were saturated with oxygen and left to equilibrate with air under two very different situations, i.e. vigorous stirring (1250 rpm) and static conditions. For comparison purposes, experiments in pure water were also carried out. In case of fluorinated surfactant based HNT, foam was not generated during the gas bubbling as well as during stirring conditions in contrast to solution containing conventional fluorinated micelles. As concerns the results collected under stirring (Fig. 7A), an induction time is required before the O_2 concentration starts to monotonically decrease to reach the equilibrium. The induction time follows the order water < HNT < HNT/NaPFC8 (Table 4). Moreover, the time dependence of the O_2

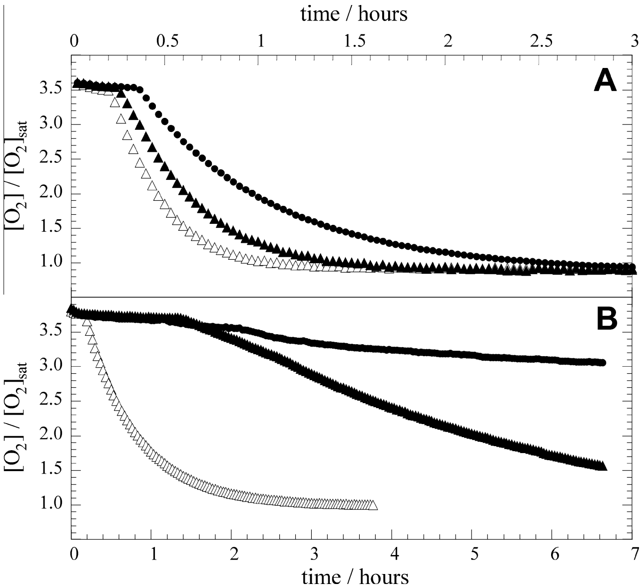

Fig. 7. Oxygen concentration as a function of time in water (Δ), in aqueous dispersions of HNT (▲) and HNT/NaPFC8 (●). Data collected under magnetic stirring at 1250 rpm (A) and under static conditions (B).

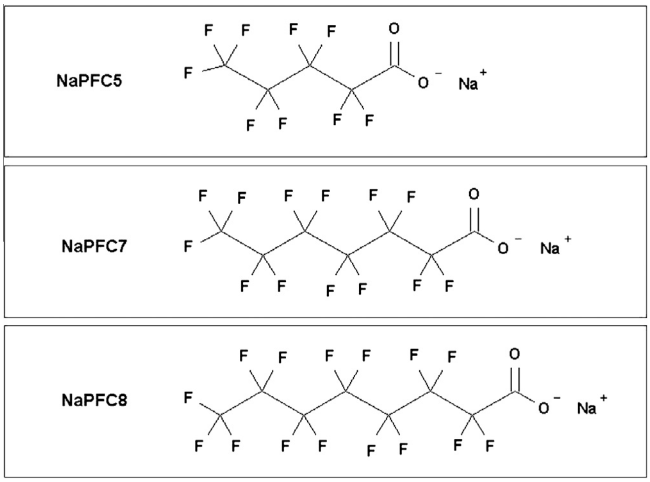

Chart 8. Structure of the fluorinated surfactants.

Table 4
Parameters for oxygen release from supersaturated systems[a].

	Induction time	$t_{1/2}$
Under stirring condition		
Water	12	31
Water/HNT	14	42
Water/HNT/NaPFC8	22	68
Under static condition		
Water	11	37
Water/HNT	83	242
Water/HNT/NaPFC8	126	>400

[a] Units are min for induction time and $t_{1/2}$. Error is ± 2 min.

concentration in the aqueous phase is rather smooth in the presence of HNT/NaPFC8. From the curves in Fig. 7A the time required for the O_2 concentration to halve its initial value ($t_{1/2}$) was calculated and reported in Table 4. The $t_{1/2}$ value for HNT/NaPFC8 (twice that for pure water) shows that the hybrid material behaves like an O_2 reservoir that releases the gas in water over time to contrast the desaturation of the aqueous dispersion resulting an efficient tool in retarding the O_2 desaturation.

The key role played by the nanotubes on the oxygen release under static situation is impressive (Fig. 7B). The kinetics of oxygen release from water is essentially unchanged compared to the result under stirring as the $t_{1/2}$ values prove (Table 4). On the contrary, both HNT and HNT/NaPFC8 are efficient in keeping the supersaturation state. Nevertheless, after 6 h the HNT dispersion released ca. 50% of O_2 while the hybrid nanotubes showed an oxygen loss of ca. 10%. This peculiar condition is well described by both the induction and the $t_{1/2}$ values that follow the order water < HNT ≪ HNT/NaPFC8 (Table 4). The strong enhancement of oxygen entrapment ability of the modified lumen is generated by the presence of only 0.86 wt% of surfactant, which corresponds to the concentration value of 5×10^{-5} mol kg^{-1} that is two order of magnitude smaller than the sodium perfluorooctanoate critical micellar concentration (0.05 mol kg^{-1}) [25].

In conclusion, the presence of a fluorinated cavity generates excellent performances of the hybrid material in incorporating oxygen. In response to external stimuli (namely stirring rate) the material exhibits purposefully oxygen release.

4. Conclusions

We prepared hybrid nanotubes by selectively adsorbing perfluorinated anionic surfactants. These nanomaterials were highly stable (at least for six months) in water due to the key role played by the electrostatic repulsions. This kinetics stability makes them of interest for applications. The peculiar hollow tubular morphology hydrophobized with perfluorinated chains endows their use as nanocontainers to entrap apolar compounds. We proved that these nanohybrid materials are excellent reservoirs for oxygen in water and exhibit gas release under controlled situations in response to external stimuli. In conclusion, we provided an easy processing and facile surface modification to prepare sustainable and biocompatible materials promising for gas delivery applications.

Acknowledgments

The work was financially supported by the University of Palermo, PRIN 2010–2011 (prot. 2010329WPF), FIRB 2012 (prot. RBFR12ETL5) and PON 2007–2013 STI-TAM.

Appendix A. Supplementary material

Supplementary data associated with this article can be found, in the online version, at http://dx.doi.org/10.1016/j.jcis.2013.11.026.

References

[1] W. Ma, W.O. Yah, H. Otsuka, A. Takahara, J. Mater. Chem. 22 (2012) (1892) 11887–11892.
[2] Y.M. Lvov, D.G. Shchukin, H. Mohwald, R.R. Price, ACS Nano 2 (2008) 814–820.
[3] W. Liu, P. Chaurand, C. Di Giorgio, M. De Méo, A. Thill, M. Auffan, et al., Chem. Res. Toxicol. 25 (2012) 2513–2522.
[4] D.M.C. Macewan, Nature 157 (1946) 159–160.
[5] V. Vergaro, E. Abdullayev, Y.M. Lvov, A. Zeitoun, R. Cingolani, R. Rinaldi, et al., Biomacromolecules 11 (2010) 820–826.
[6] E. Abdullayev, A. Joshi, W. Wei, Y. Zhao, Y. Lvov, ACS Nano 6 (2012) 7216–7226.
[7] G. Cavallaro, G. Lazzara, S. Milioto, J. Phys. Chem. C 116 (2012) (1938) 21932–21938.
[8] E. Abdullayev, Y. Lvov, J. Mater. Chem. 20 (2010) 6681–6687.
[9] G.L. Li, Z. Zheng, H. Möhwald, D.G. Shchukin, ACS Nano 7 (2013) 2470–2478.
[10] Y. Zhao, E. Abdullayev, A. Vasiliev, Y. Lvov, J. Colloid Interface Sci. 406 (2013) 121–129.
[11] S.A. Hashemifard, A.F. Ismail, T. Matsuura, J. Colloid Interface Sci. 359 (2011) 359–370.
[12] G. Cavallaro, D.I. Donato, G. Lazzara, S. Milioto, J. Phys. Chem. C 115 (2011) 20491–20498.
[13] E. Abdullayev, K. Sakakibara, K. Okamoto, W. Wei, K. Ariga, Y. Lvov, ACS Appl. Mater. Interfaces 3 (2011) 4040–4046.
[14] W.O. Yah, A. Takahara, Y.M. Lvov, J. Am. Chem. Soc. 134 (2011) 1853–1859.
[15] Z. Luo, H. Song, X. Feng, M. Run, H. Cui, L. Wu, et al., Langmuir 29 (2013) 12358–12366.
[16] P.J. Crowley, Pestic. Sci., in: M. Hudlicky, A. E. Pavlath (Eds.), American Chemical Society, Washington DC, 1995, vol. 53, 1998, pp. 263–263.
[17] V. Ćirkva, R. Polák, O. Paleta, K. Kefurt, J. Moravcová, M. Kodíček, et al., Carbohydr. Res. 339 (2004) 2177–2185.
[18] G. Cavallaro, G. Lazzara, S. Milioto, Langmuir 27 (2011) 1158–1167.
[19] L. Nordstierna, I. Furó, P. Stilbs, Langmuir 22 (2006) 7969–7974.
[20] S. Milioto, R. Crisantino, R.D. Lisi, A. Inglese, Langmuir 11 (1995) 718–724.
[21] A. Soto, A. Arce, M.K. Khoshkbarchi, Biophys. Chem. 74 (1998) 165–173.
[22] H. Freundlich, A.D. Jones, J. Phys. Chem. 40 (1935) 1217–1236.
[23] A.M. Wierenga, A.P. Philipse, Langmuir 13 (1997) 4574–4582.
[24] B.V. Derjaguin, L.D. Landau, Acta Physicochim. 14 (1941) 733–762.
[25] R. De Lisi, G. Lazzara, S. Milioto, N. Muratore, Phys. Chem. Chem. Phys. 5 (2003) 5084–5090.

Attached IX

ACS APPLIED MATERIALS & INTERFACES
Research Article
www.acsami.org

Modified Halloysite Nanotubes: Nanoarchitectures for Enhancing the Capture of Oils from Vapor and Liquid Phases

Giuseppe Cavallaro, Giuseppe Lazzara,* Stefana Milioto, Filippo Parisi, and Vincenzo Sanzillo

Dipartimento di Fisica e Chimica, Università degli Studi di Palermo, Viale delle Scienze, pad. 17, 90128 Palermo, Italy

Supporting Information

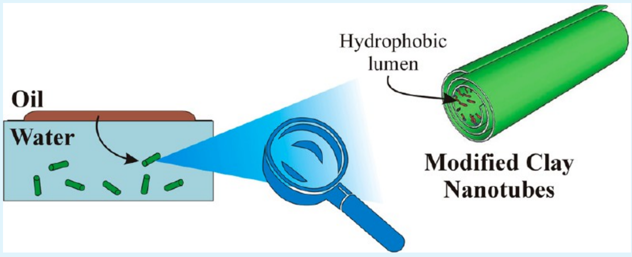

ABSTRACT: We prepared hybrid halloysite nanotubes (HNT/sodium alkanoates) in which the inner cavity of the nanoclay was selectively modified. Physicochemical studies evidenced the interactions between HNT and sodium alkanoates, ruled out clay exfoliation, quantified the amount of the loaded substance, and showed an increase of the total net negative charge, allowing us to obtain rather stable aqueous nanoclay dispersions. These dispersions were exploited as inorganic micelles to capture hydrocarbon and aromatic oils in the vapor and liquid states and were revealed to be nonfoaming but very efficient in encapsulating oils. Here, we have fabricated biocompatibile and low-cost inorganic micelles that can be exploited for industrial applications on a large scale.

KEYWORDS: *halloysite, gas absorption, inorganic micelles, hydrocarbon solubilization*

INTRODUCTION

For a long time, clay minerals, which are present in all types of sediments and sedimentary rocks, have been an object of scientific interest. Among them are the nanoclays, like imogolite and halloysite that both have a hollow tubular shape, which have a particular relevance for materials design. Imogolite, $Al_2SiO_3(OH)_4$, possesses an external diameter of ca. 25 Å and an internal diameter of ca. 10 Å.[1] In spite of its interesting structure, imogolite shows a certain toxicity, which may limit its applications.[2] Halloysite nanotubes (HNTs), $Al_2Si_2O_5(OH)_4\cdot 2H_2O$, possess a coil structure with an external diameter of ca. 50 nm and an internal diameter of ca. 15 nm. The different chemistry at each surface offers the opportunity to control the selective interaction with ionic molecules.[3,4] Recent studies proved that HNTs are ecological, biocompatible, and dispersible in water even at very high concentrations where they can form liquid crystalline phases.[5,6] HNTs are abundant all over the world and consequently are available at low cost. All of these features (i.e., chemical structure and sustainable cost and biocompatibility) make HNTs very appealing for several purposes. Two main application fields can be identified. The first one concerns the use of HNTs as an additive for polymers to increase the mechanical resistance and to confer an active response ability to external stimuli.[7−11] The second one deals with the suitability of the HNT cavity for catalysis[12] and drug release.[6] In this case, the modification of the HNT internal surface[13,14] was tuned to promote the affinity between nanotubes and target molecules. Very few studies are available on the enhanced solubilization of hydrophobic compounds exhibited by a modified HNT cavity.[14,15]

In fact, the preparation of organic/inorganic hybrid materials based on HNTs may be of interest in terms not only because of their sustainability and eco-compatibility but also because they satisfy the demands of several applications. The modification of HNTs is an attractive and big challenge, with the goal being (1) to produce rather stable dispersions for applications where nanocontainers and nanocarriers are required to oppose the sedimentation of pristine HNTs and (2) to direct molecular species into the internal space to fabricate the desired nanostructures for the purposes of interest.

In this work, we designed, prepared, and physicochemically characterized HNT/sodium alkanoates hybrids. Because their inner surface is positively charged and external surface is negatively charged over a wide pH range,[6] we chose anionic compounds to make a selective hydrophobic modification to the cavity. Among various anionic surfactants, we selected sodium alkanoates obtained from the neutralization of fatty acids, which are biocompatible. Moreover, these surfactants are available with different hydrophilic−hydrophobic balances. We employed sodium undecanoate, sodium dodecanoate, and sodium tetradecanoate to tune and manipulate the degree of the hydrophobicity of the nanotubes core. Thermogravimetry, SEM, and FTIR spectroscopy were used to define the composition and morphology of the as-prepared hybrid materials. Dynamic light scattering, ζ potential, and turbidimetry allowed us to investigate the stability of their aqueous dispersions. These hybrids successfully entrap aliphatic and aromatic hydrocarbons, prototypes of hydrophobic contaminants and solvents, from gas and liquid phases. The developed biocompatible inorganic micelles are appealing for industrial

Received: October 23, 2013
Accepted: December 6, 2013

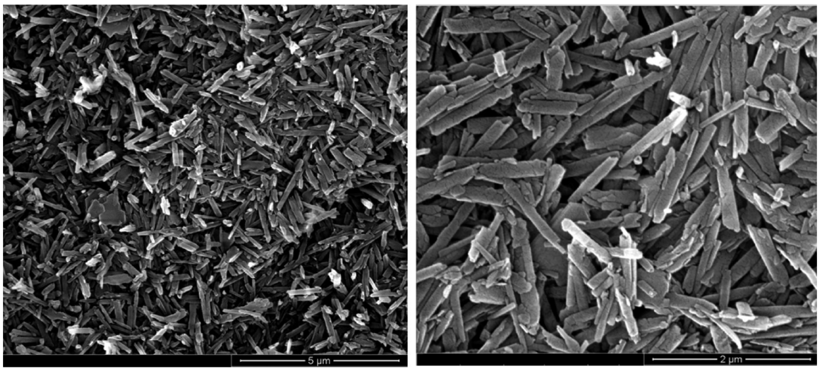

Figure 1. SEM micrographs for HNT/NaC12.

applications such as detergency. At the same time, they might play the role of conventional micelles, which is well-known to enhance oil solubilization, and inorganic builders. Intriguingly, these nanohybrids are nonfoaming, and although they are very efficient, they contain a surfactant concentration below the critical concentration at which the detergent ability emerges.

MATERIALS AND METHODS

Halloysite nanotubes (HNTs), sodium undecanoate (NaC11), sodium dodecanoate (NaC12), sodium tetradecanoate (NaC14), and toluene were from Aldrich, and *n*-decane was from Fluka. All of the products were used as received. Water from reverse osmosis (Elga model option 3) with a specific resistivity higher than 1 MΩ cm was used.

Preparation of Functionalized Nanotubes. Aqueous surfactant solutions were prepared by dissolving 5 g of surfactant (NaC11 or NaC12) in 250 cm^3 of water. Then, 5 g of HNT were added, and the obtained dispersion was magnetically stirred for 48 h at 20 °C. Successively, the dispersion was centrifuged to recover the functionalized material. The latter was washed with water several times until the water used in the washing reached the surface tension value of pure water (72 mN m^{-1}). This procedure ensures that eventually free surfactant is no longer present and that the encapsulated surfactant is not released at least within 1 month. The same procedure was followed for NaC14, but because of its low solubility in water (330.8 mg dm^{-3}), the HNT was added by maintaining the same HNT/surfactant weight ratio as for other surfactants and dissolving 0.075 g of NaC14 into 250 cm^3 of water.

Thermogravimetry (TGA). Experiments were performed using a Q5000 IR apparatus (TA Instruments) under a nitrogen flow of 25 cm^3 min^{-1} for the sample and 10 cm^3 min^{-1} for the balance. The explored temperature interval ranged between 25 and 900 °C at a heating rate of 10 °C min^{-1}. By recording the temperature dependence of mass loss (TG), the first-order differentiation curves of mass loss to temperature (DTG) were determined. The decomposition temperature (T_d) was taken at the maximum of the DTG peaks. The percentages of moisture loss at 120 °C (MD_{120}) and of the residual matter at 900 °C (MR_{900}) were determined from the TG curves.

IR Spectroscopy. The IR spectra were registered at ambient temperature in the range between 500 and 4000 cm^{-1} using an FT-IR spectrometer (Frontier, PerkinElmer). The spectral resolution was 2 cm^{-1}. Each sample was prepared with KBr.

Dynamic Light Scattering (DLS). The measurements were performed at 18.0 ± 0.1 °C in a sealed cylindrical scattering cell at a scattering angle of 90° using a Brookhaven Instrument apparatus composed of an BI-9000AT correlator and a He–Ne laser (75 mW) at a wavelength (λ) of 632.8 nm.

Dispersions were prepared by using water filtered by a Millipore filter with a 0.45 μm pore size.

For all of the systems, the field-time autocorrelation functions were well-described by a monoexponential decay function, which provides the decay rate (Γ) correlated to the apparent diffusion coefficient $D = \Gamma/q^2$, where $q = 4\pi n\lambda^{-1}\sin(\theta/2)$ is the scattering vector in which n is the refractive index of water and θ is the scattering angle.

ζ Potential. ζ-Potential measurements were carried out with of a Zetasizer Nano-ZS (Malvern Instruments) at 25.0 ± 0.1 °C.

Turbidimetry. The transmittance as a function of time of the aqueous dispersions of HNT/NaC11, HNT/NaC12, HNT/NaC14, and HNT (1% w w^{-1}) was measured at 25.0 ± 0.1 °C using an Analytic Jena Specord S 600 BU UV–vis spectrophotometer. The experiments were performed at a wavelength of 600 nm, where no absorption bands were detected.

Isotherm of Adsorption. The ability of HNT/NaC11, HNT/NaC12, and HNT/NaC14 to entrap toluene dissolved in water was monitored in the following way. Different amounts of HNT/surfactant were added to a fixed quantity of water saturated with toluene. The dispersions were stirred and equilibrated for 1 week. The concentration of residual toluene was determined by measuring the absorption spectra at 25.0 ± 0.1 °C at wavelengths between 190 and 600 nm using an Analytic Jena Specord S 600 BU, with toluene presenting a peak at 261 nm.

Surface Tension. A programmable tensiometer (KSV Sigma 70) equipped with a Wilhelmy plate was employed at 25.0 ± 0.1 °C. Each surface tension value is the average of three determinations, and its precision is 0.05 dyn cm^{-1}. The amount of *n*-decane was chosen so that it would form a film on the water surface of ca. 1 mm and would be ca. 0.4 g of *n*-decane per 100 g of water. Before each measurement, the system was gently stirred for 2 min.

Scanning Electron Microscopy (SEM). The morphology of the obtained materials was studied using an ESEM FEI QUANTA 200F microscope. Before each experiment, the surface of the sample was coated with gold in argon by means of an Edwards sputter coater S150A to avoid charging under the electron beam. The measurements were carried out in high-vacuum mode ($<6 \times 10^{-4}$ Pa) for simultaneous secondary electron, the energy of the beam was 30 kV, and the working distance was 10 mm. Minimal electron dose conditions were used to avoid damage to the sample.

RESULTS AND DISCUSSION

Physicochemical Studies of HNT/Surfactant in the Solid State. We prepared the hybrid HNT/surfactant materials by developing an easy strategy to ensure that both the inner cavity was modified with anionic surfactant by allowing an ionic exchange and that the prepared materials were free of unadsorbed surfactant. The physicochemical characterization evidenced the success of the procedure.

As occurs for clays with a lamellar structure, like kaolin, the surface modification with the surfactants may result in clay exfoliation,[16] which in the specific case of halloysite may induce a derolling coil with the loss of the hollow cylinder mesostructure. Because of this possibility, we performed SEM micrographs of HNT/NaC12 and HNT/NaC14, which were

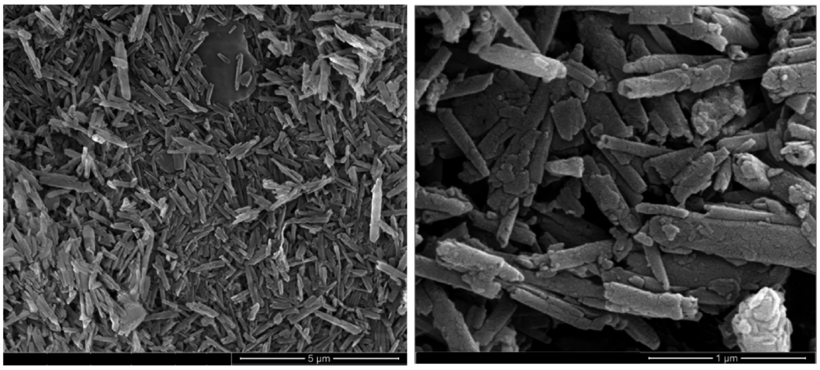

Figure 2. SEM micrographs for HNT/NaC14.

selected because of their larger surfactant content (Figures 1 and 2).

The images show nanotubes with dimensions comparable to those of pristine HNTs.[17] This means that the surfactant adsorption does not alter the tubular morphology. Moreover, the hollow cavity is preserved in the composite materials.

Once we ascertained that the nanotubes maintained their original shape during the fabrication of the hybrid materials, TGA analysis was done to make a quantitative computation of the amount of surfactant loaded into the lumen. To this end, preliminary thermograms of pure surfactants were determined (see the Supporting Information). The thermograms of the hybrid materials are very similar to that of pristine HNTs with the exception of the mass loss present over a range of temperatures, which is characteristic of surfactant degradation (Figure 3).

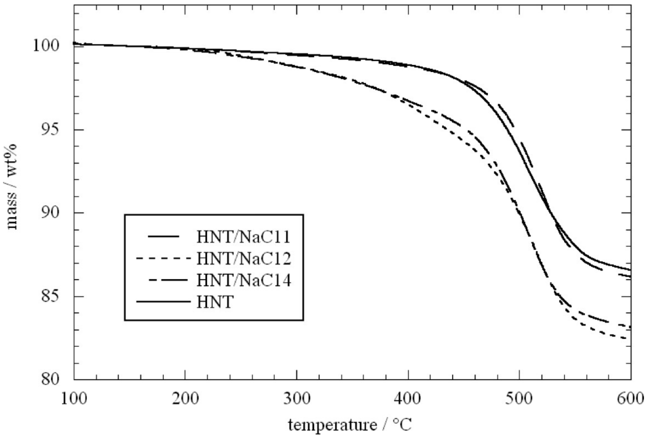

Figure 3. Thermograms of pristine and modified HNT.

The percent of surfactant in the composite (C_s) was calculated by using the rule of mixtures[17,18] once the mass loss of the pure components were known and by taking into account the water content calculated as the mass loss up to 150 °C. In particular, the residual masses at 600 °C were used because the surfactant degradation can be considered complete. The results are reported in Table 1.

It is noteworthy that anionic surfactant has to be loaded into the positive HNT lumen.[14] The negative charge on the HNT outer surface definitely rules out the adsorption of the negatively charged surfactants. The maximum loading value expected from the cavity size is ca. 10%.[3] The data in Table 1 show that for all of the surfactants this value is never reached, indicating the presence of void space in the hollow cavity. If one assumes that the adsorbed surfactant generates a monolayer, then by considering the average specific area of the inner surface[19] (6.9 m^2 g^{-1}) and the occupied area of the surfactant at the water/alumina interface[20] (0.41 nm^2 $molecule^{-1}$) a loading value of 1.2 wt % is calculated. From these results, one may deduce that NaC11 likely forms a monolayer in the lumen, whereas NaC12 and NaC14 generate structure that require larger amounts of surfactant.

Table 1. Percent of Water and Surfactant in the HNTs Cavity

materials	C_s (wt %)[a]	C_w (wt %)[a]
HNT/NaC11	1.4	1.2
HNT/NaC12	8.0	0.5
HNT/NaC14	6.6	1.0

[a] The error is ±0.1 wt %.

The IR spectra of the hybrid materials exhibit characteristic bands of the two single components (spectra are reported in the Supporting Information) and evidence the presence of interactions between the surfactant and HNT.

The band of the symmetric stretching of $-CH_2-$ in NaC11 and NaC14 is shifted toward larger values in the presence of nanotubes (Table 2). Such an effect was ascribed to the packing of the surfactant tails intercalated into the layers of HNTs.[14] It is noteworthy that the stretching of C=O undergoes substantial variations in the case of the hybrid materials. For both surfactants, the stretching undergoes a shift of ca. 80 cm^{-1}, revealing interactions between the charged head of the surfactant and the opposite charge of the inner surface of the HNT. Similar changes were found for organic acids adsorption onto aluminum hydroxide, and they were explained by the formation of C−O−Al.[21]

Table 2. Stretching Values of the Surfactants and the Hybrid Materials

materials	CH_2 symmetric stretching (cm^{-1})	CH_2 asymmetric stretching (cm^{-1})	C=O stretching (cm^{-1})
NaC11	2848	2923	1559
HNT/NaC11	2853	2923	1641
NaC14	2848	2921	1559
HNT/NaC14	2851	2921	1633

In summary, we have prepared hybrid materials of cylindrical shape containing a hydrophobic cavity.

Stability of Aqueous HNTs/Surfactants Dispersions. Diffusion coefficients of HNT/NaC11, HNT/NaC12, and HNT/NaC14 in water as functions of the concentration of dispersed material were determined. The diffusion coefficient values are practically concentration-independent (see the Supporting Information) and follow the order HNT/NaC14 > HNT/NaC11 > HNT/NaC12. The HNT/NaC12 nanostructures present values for the translational average diffusion at infinite dilution ($D°$ in Table 3) close to that reported for pristine HNTs in water.[17]

Table 3. Diffusion Coefficient and ζ Potential for HNT/Surfactant Hybrid Materials

materials	$D° \times 10^{12}$ ($m^2\ s^{-1}$)	ζ potential (mV)
HNT	0.94[a]	−19.4[a]
HNT/NaC11	1.04 ± 0.01	−28.3 ± 0.4
HNT/NaC12	0.88 ± 0.02	−25.3 ± 0.2
HNT/NaC14	1.13 ± 0.03	−34.0 ± 0.7

[a] From ref 14.

The increase of $D°$ for HNT/NaC14 and HNT/NaC11 compared to the value of pristine HNTs demonstrates a larger mobility of these systems as a consequence of the functionalization. Such an increase cannot be ascribed to the reduction of the size of the nanoparticles, which is ruled out by the SEM experiments, but rather to the increment of the repulsions between the modified nanotubes because of the increase of the total charge. Insight into the charge of the modified nanotubes was provided by ζ-potential measurements. The data in Table 3 show that the incorporation of anionic surfactant into the lumen generated a larger net negative charge of the HNT. It is noteworthy that the change of ζ potential with the nature of the incorporated surfactant follows $D°$. These findings predict a better colloidal stability of the hybrid materials compared to the pristine nanotubes because of the low tendency to aggregate and the increased electrostatic repulsions between the particles.

To evaluate the mechanism controlling the dispersions stabilization, sedimentation experiments were done for pristine and functionalized HNTs in water using turbidimetry.

Figure 4 shows that the sedimentation is strongly slowed by the surfactant. The turbidity follows the same order as $D°$ and ζ potential, namely, the higher the $D°$ values and the more negative ζ potential, the more stable is the dispersion. These results prove that modification by means of anionic surfactants is an efficient strategy for the stabilization of HNTs dispersions; on the contrary, cationic surfactants generate destabilization, enhancing the sedimentation.[14] The colloidal stability may also be confirmed by electrostatic effects because of the increment of the total net negative charge of the nanotube as a consequence of the neutralization of the positive charges of the inner surface subsequent to the surfactant adsorption.

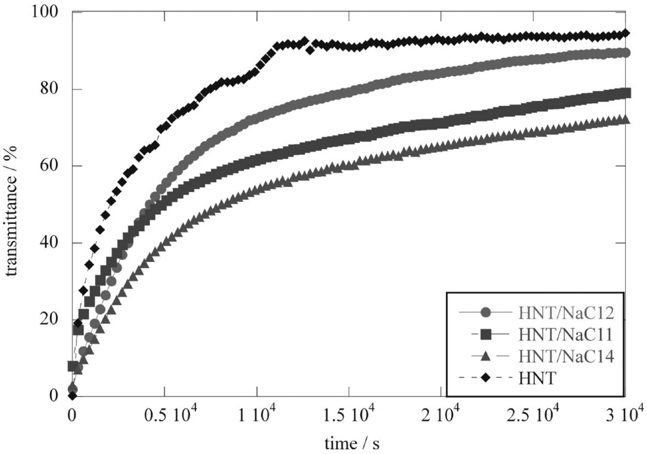

Figure 4. Transmittance at 600 nm as a function of time of pristine and modified HNT in water (1 wt %).

It should be noted that the colloidal stability of modified HNTs is not strictly correlated to the loading degree (Table 1) for HNT/NaC12 and HNT/NaC14. However, the very high surfactant content into the lumen of close to 10% indicates the formation of surfactant self-organized structures in the cavity, for example, like double-layers that maintain the counterions and do not contribute to the charge increase of the nanoparticle and consequently to its electrostatic stabilization.

To study the crucial role of the electrostatic forces in controlling the stability of the aqueous dispersions of the hybrid HNTs, turbidity measurements were carried out at variable ionic strength. As the data in Figure 5 show, the modified nanotubes are highly destabilized by KCl because of the screening effect on the repulsive electrostatic forces between the nanoparticles.

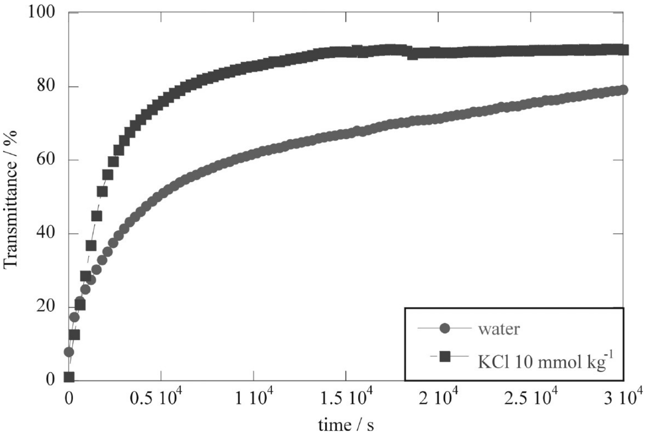

Figure 5. Transmittance at 600 nm as a function of time of HNT/NaC11 (1 wt %) in water and in KCl (10 mmol kg^{-1}).

This result agrees with the DLVO theory, which predicts that the stability of a colloidal system depends on both the attractive van der Waals forces and the electrostatic repulsive forces of the double layer surrounding each particle.[22] This theory envisages that a large ionic strength generates a screening of the electrostatic repulsions because of the reduction of the double layer.

Inorganic Micelles Based on HNT for Encapsulating Oils. The structure as well as the chemistry of the HNTs makes them rather versatile. The goal of the selective modification of the inner surface is to obtain nanomaterials with controlled sizes and shapes with an enhanced hydrophilic surface and a hydrophobic core that may be exploited for encapsulation of molecular species to be removed from aqueous phases, to be delivered and released under control, and so on. In our work, we selected *n*-decane and toluene, which are organic compounds of environmental interest. *n*-Decane is an aliphatic hydrocarbon that is nearly immiscible with water[23] (its solubility is 1.7×10^{-7} mol kg^{-1}), whereas toluene is an aromatic hydrocarbon sparingly soluble in water[24] (its solubility is 5×10^{-3} mol kg^{-1}). These nanohybrid materials will be employed as inorganic micelles to capture such compounds, and they will be examined in the solid state as well as in the aqueous dispersions.

Capturing Capability of n-Decane. We studied this hydrocarbon in the vapor and liquid phases, because its solubility in water is negligible. The HNT and the HNT/surfactant powders were equilibrated in a desiccator saturated with *n*-decane vapors at a controlled temperature. The amount of entrapped *n*-decane was determined by TGA.

As Figure 6 shows, all of the materials exhibit a significant amount of adsorbed *n*-decane (grams of *n*-decane per 100 g of solid, Q_{ads}), which increases with temperature.

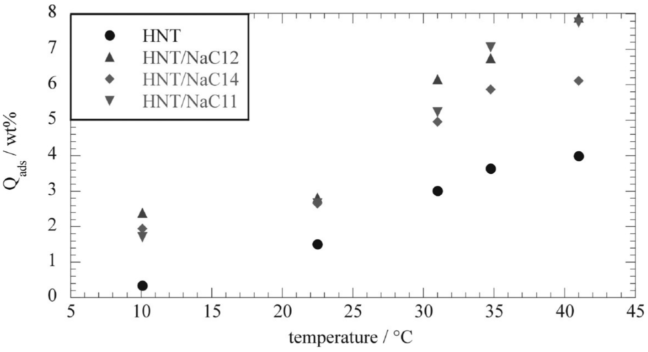

Figure 6. Quantity of *n*-decane adsorbed per 100 g of adsorbent as the temperature is changed.

From the data in Figure 6, one may argue that the hydrophobization of the HNT cavity improves the adsorption ability of the nanotubes and that this effect is independent of the alkyl chain length of the surfactant up to 30 °C. At higher temperatures, the hybrid materials containing NaC11 and NaC12 appear more efficient, which is rather surprising. Such a peculiar finding may be associated with two factors: (1) the change of the vapor pressure with temperature and consequently the *n*-decane concentration in the gas phase with temperature and (2) the temperature dependence of the equilibrium constant of adsorption. In the investigated temperature range, the vapor pressure (P_{vap}) was calculated by means of the Antoine equation.[25] The results demonstrate that the percent of *n*-decane volume in the vapor phase changes from 0.05 to 0.2 vol % upon changing the temperature from 10 to 42 °C. Indeed, the thermodynamic property, which correctly and properly evidences the affinity of gaseous *n*-decane toward the solid phase, is represented by the adsorption constant (K_{ads}) calculated as

$$K_{ads} = Q_{ads}/P_{vap} \tag{1}$$

The K_{ads} values for all of the investigated systems are illustrated in Figure 7.

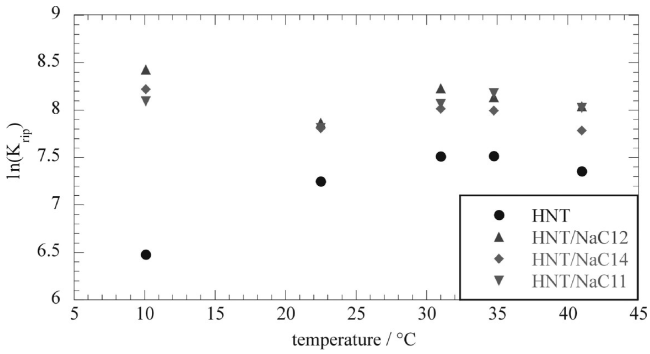

Figure 7. Adsorption constant of gaseous *n*-decane onto the solid substrate as a function of temperature.

Temperature plays a negligible role on K_{ads} for all of the hybrid systems. The pristine nanotubes exhibit an affinity toward *n*-decane that is rather small at low temperatures and is definitely smaller than that of the hybrid materials. It is surprising that the adsorption ability of the hybrid materials does not depend on the alkyl chain length of the surfactants. This result is straightforward to comprehend if one considers that the thermodynamic properties reveal the interactions exercised between the molecule and its environment in a state of equilibrium.[26] In fact, in spite of the amount of surfactant as well as the surfactant-tail-dependent structures formed in the lumen, the structures nature remains unaltered (anhydrous and with properties similar to the hydrocarbons). Therefore, one may conclude that HNT/NaC11 exhibits affinity toward gaseous *n*-decane in the same manner as HNT/NaC14 even though it contains a surfactant amount that is six times smaller than that in HNT/NaC14. This result assumes a particular relevance for the potential uses of these materials as far as their cost benefit is concerned.

The liquid *n*-decane in contact with the aqueous phase mimes the case of an aquifer contaminated by light non-aqueous-phase liquids. The first experiments involved an aqueous phase with dispersed pristine HNTs (5 wt %) and a film of *n*-decane (0.4 wt %). Afterward, HNT/NaC14 and HNT/NaC11 replaced the pristine HNTs. The *n*-decane/nanomaterials ratio was selected from Q_{ads} data. In all cases, the surface tension as a function of time was measured under gentle stirring and a controlled temperature. The results are illustrated in Figure 8.

The S-shaped trend registered for HNT/NaC14 is peculiar, which exhibits a value of around 50 mN m^{-1} because of the presence of *n*-decane at the interface; for 7.5 h thereafter, it sharply increases, reaching the value of water (72 mN m^{-1}). It is important to note that even very small amounts of *n*-decane at the interface drammatically lower the surface tension to a value of ca. 50 mN m^{-1}. Therefore, such a jump reveals a disappearance of *n*-decane that may be attributed to evaporation and/or its entrapment into the hydrophobic cavity of the nanotube. The experiment in the presence of pristine HNTs revealed a nearly constant surface tension value of at least ca. 50 mN m^{-1} for 10 h. Thus, one may state that the transferring of liquid *n*-decane to the aqueous nanotubes takes place only in the presence of NaC14 surfactant loaded into the lumen. However, such a process is strongly dependent on the alkyl chain length of the surfactant because HNT/NaC11 (Figure 8) behaves like pristine HNTs.

From all of the experiments one may conclude that (1) *n*-decane at the interface does not evaporate over the experimental time window, (2) the adsorption onto the native HNTs is negligible, and (3) the efficiency of the hybrid HNT/surfactant material is specific to the surfactant tail. In particular, the higher NaC14 surfactant loading produces complex structures in the lumen of HNTs that possess a more hydrophobic nature than the NaC11 monolayer. These structures may control the water capillary phenomenon into

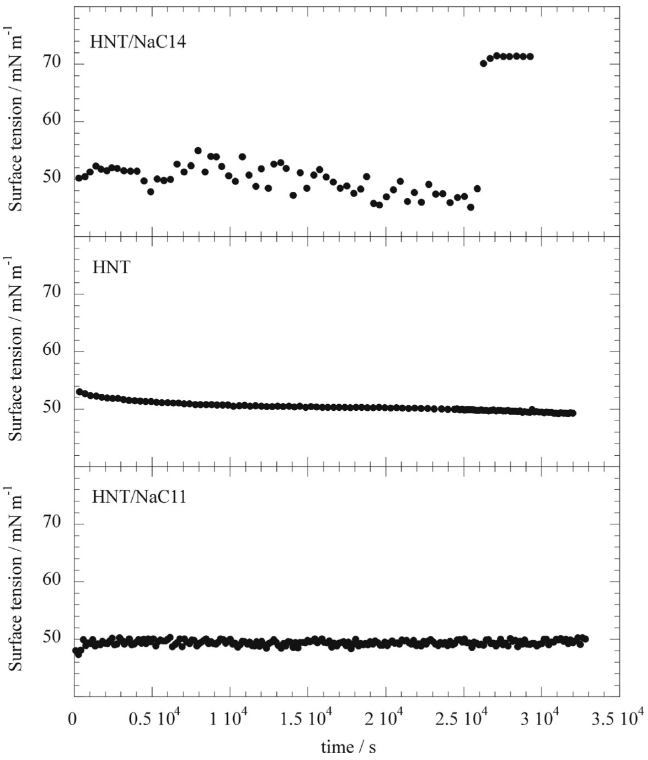

Figure 8. Surface tension as a function of time for aqueous HNT, HNT/NaC11, and HNT/NaC14 dispersions in the presence of an *n*-decane film.

the void space of nanotubes that is expected to be more important as the surfactant content becomes smaller. This behavior compared to that exhibited by the hybrid materials toward *n*-decane in the vapor phase indicates the relevant role played by the aqueous solvent in the transferring process.

Capturing Capability of Toluene. The inorganic micelles were also tested for their ability to entrap toluene solubilized in water at a concentration lower than its solubility. Figure 9 shows the difference of the removed toluene by the hybrid material with respect to the pristine HNT (ΔR). The surfactant tail tuned the affinity toward the oil; accordingly, higher alkyl chain surfactants exhibited a higher affinity toward toluene. Furthermore, the HNT/NaC11 system does not improve the encapsulation properties of HNTs at all. In spite of the loaded amount of NaC12 into the HNTs lumen being slightly larger than that of NaC14, HNTs/NaC14 exhibits a larger solubilizing power, indicating that the formed complex structures, likely double layers, possess a hydrophobicity established by the alkyl chain length.

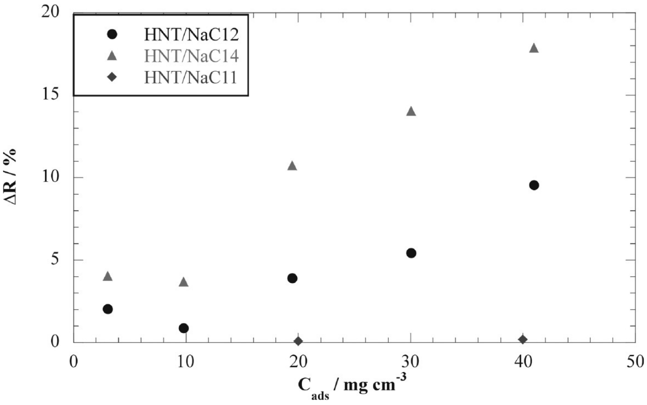

Figure 9. Toluene removal efficiency from aqueous dispersions of HNT/NaC11, HNT/NaC12, and HNT/NaC14 calculated as a percentage increment with respect to the removal obtained by pristine HNT as a function of hybrid material concentration.

These results are in line with those obtained for the liquid *n*-decane solubilization, corroborating the findings that the surfactant monolayer of HNT/NaC11 possesses a somewhat hydrophilic character, which is likely due to the presence of water, whereas the more complex surfactant structures of HNT/NaC12 and HNT/NaC14 behave like conventional micelles. The impact and the significance that conventional micelles assume in various applications is well-known, for instance, the surfactant-enhanced aquifer remediation, solubilization, delivery, and release of drugs, and so on. Consequently, it is interesting to compare the solubilization power of such inorganic micelles with that of sodium alkanoates micelles in water. To this end, the concentration of the surfactant (molarity scale) into the inorganic micelles was calculated from the total concentration of the hybrid solid and the loading values (Table 1). For the most concentrated dispersion (40 mg cm^{-3}) of the hybrid materials with the highest surfactant content (HNT/NaC12), we obtained a surfactant concentration of 0.014 mol dm^{-3}. This value is rather intriguing as it is about one-half of the critical micellar concentration (cmc) value of NaC12 in water.[27] Keeping in mind that conventional surfactants enhance the solubility of oils in water only above the cmc[26] where micelles take place, we can conclude that we successfully exploited the peculiar morphology of HNTs to prepare sustainable inorganic micelles with remarkable affinity toward oils that are sparingly soluble in water.

■ CONCLUSIONS

We developed a simple strategy to fabricate successfully HNT/surfactant materials by the selective modification of the nanotubes inner cavity with anionic, hydrogenated surfactants with different length tails.

The objective of the selective functionalization was aimed at obtaining nanomaterials with an enhanced hydrophilic surface and a hydrophobic core. The net negative charge of the hybrid nanotubes allowed us to obtain stable colloids. The hydrophobization of the nanotube cavity was exploited for the entrapment of hydrocarbons, both aliphatic and aromatic, which can be removed from the aqueous and gas phases. In our work, interestingly, we proved that although the amount of loaded surfactant into the hybrid materials is lower than the surfactant critical micellar concentration the hybrid materials very efficiently behave like inorganic micelles for encapsulating oils.

■ ASSOCIATED CONTENT

Ⓢ Supporting Information

Diffusion coefficient HNT/NaC11, HNT/NaC12, and HNT/NaC14 in water as a function of concentration, FTIR spectra of NaC11 and HNT/NaC11, and thermograms of NaC11, NaC12, and NaC14. This material is available free of charge via the Internet at http://pubs.acs.org.

■ AUTHOR INFORMATION

Corresponding Author

*E-mail: giuseppe.lazzara@unipa.it.

Notes

The authors declare no competing financial interest.

ACKNOWLEDGMENTS

The work was financially supported by the University of Palermo, PRIN 2010-2011 (prot. 2010329WPF), FIRB 2012 (prot. RBFR12ETL5), and PON 2007-2013 STI-TAM.

REFERENCES

(1) Cradwick, P. D. G.; Farmer, V. C.; Russell, J. D.; Masson, C. R.; Wada, K.; Yoshinaga, N. *Nature, Phys. Sci.* **1972**, *240*, 187−189.

(2) Liu, W.; Chaurand, P.; Di Giorgio, C.; De Méo, M.; Thill, A.; Auffan, M.; Masion, A.; Borschneck, D.; Chaspoul, F.; Gallice, P.; Botta, A.; Bottero, J.-Y.; Rose, J. *Chem. Res. Toxicol.* **2012**, *25*, 2513−2522.

(3) Lvov, Y. M.; Shchukin, D. G.; Mohwald, H.; Price, R. R. *ACS Nano* **2008**, *2*, 814−820.

(4) Sciascia, L.; Turco Liveri, M. L.; Merli, M. *Appl. Clay Sci.* **2011**, *53*, 657−668.

(5) Luo, Z.; Song, H.; Feng, X.; Run, M.; Cui, H.; Wu, L.; Gao, J.; Wang, Z. *Langmuir* **2013**, *29*, 12358−12366.

(6) Vergaro, V.; Abdullayev, E.; Lvov, Y. M.; Zeitoun, A.; Cingolani, R.; Rinaldi, R.; Leporatti, S. *Biomacromolecules* **2010**, *11*, 820−826.

(7) Shchukin, D. G.; Lamaka, S. V.; Yasakau, K. A.; Zheludkevich, M. L.; Ferreira, M. G. S.; Mohwald, H. *J. Phys. Chem. C* **2008**, *112*, 958−964.

(8) Abdullayev, E.; Price, R.; Shchukin, D.; Lvov, Y. *ACS Appl. Mater. Interfaces* **2009**, *1*, 1437−1443.

(9) Abdullayev, E.; Lvov, Y. *J .Mater. Chem.* **2010**, *20*, 6681−6687.

(10) Abdullayev, E.; Sakakibara, K.; Okamoto, K.; Wei, W.; Ariga, K.; Lvov, Y. *ACS Appl. Mater. Interfaces* **2011**, *3*, 4040−4046.

(11) Lvov, Y.; Abdullayev, E. *Prog. Polym. Sci.* **2013**, *38*, 1690−1719.

(12) Shchukin, D. G.; Sukhorukov, G. B.; Price, R. R.; Lvov, Y. M. *Small* **2005**, *1*, 510−513.

(13) Yah, W. O.; Takahara, A.; Lvov, Y. M. *J. Am. Chem. Soc.* **2012**, *134*, 1853−1859.

(14) Cavallaro, G.; Lazzara, G.; Milioto, S. *J. Phys. Chem. C* **2012**, *116*, 21932−21938.

(15) Yah, W. O.; Takahara, A.; Lvov, Y. M. *J. Am. Chem. Soc.* **2011**, *134*, 1853−1859.

(16) Sidheswaran, P.; Bhat, A. N.; Ganguli, P. *Clays Clay Miner.* **1990**, *38*, 29−32.

(17) Cavallaro, G.; Lazzara, G.; Milioto, S. *Langmuir* **2011**, *27*, 1158−1167.

(18) Cavallaro, G.; Donato, D. I.; Lazzara, G.; Milioto, S. *J. Phys. Chem. C* **2011**, *115*, 20491−20498.

(19) Abdullayev, E.; Joshi, A.; Wei, W.; Zhao, Y.; Lvov, Y. *ACS Nano* **2012**, *6*, 7216−7226.

(20) Ruths, M.; Sjöblom, J.; Blokhus, A. M. *J. Colloid Interface Sci.* **1991**, *145*, 108−112.

(21) Guan, X. H.; Chen, G. H.; Shang, C. *J. Environ Sci.* **2007**, *19*, 438−443.

(22) Derjaguin, B. V.; Landau, L. D. *Acta Physicochim. URSS* **1941**, *14*, 733−762.

(23) Mackay, D.; Shiu, W. Y. *J. Phys. Chem. Ref. Data* **1981**, *10*, 1175−1199.

(24) Neely, B. J.; Wagner, J.; Robinson, R. L.; Gasem, K. A. M. *J. Chem. Eng. Data* **2008**, *53*, 165−174.

(25) Carruth, G. F.; Kobayashi, R. *J. Chem. Eng. Data* **1973**, *18*, 115−126.

(26) De Lisi, R.; Lazzara, G.; Milioto, S.; Muratore, N. *J. Colloid Interface Sci.* **2006**, *300*, 368−374.

(27) De Lisi, R.; Lazzara, G.; Milioto, S.; Muratore, N. *Phys. Chem. Chem. Phys.* **2003**, *5*, 5084−5090.